SIMULATION AND CONSTRUCTION OF LUMINESCENT SOLAR CONCENTRATOR

By

LO CHIN KIM

A master thesis submitted to the Department of Electrical and Electronic Engineering, Faculty of Engineering and Science,
Universiti Tunku Abdul Rahman,
in partial fulfillment of the requirements for the degree of
Master of Engineering Science
November 2011

ABSTRACT

SIMULATION AND CONSTRUCTION OF LUMINESCENT SOLAR CONCENTRATOR

Lo Chin Kim

A new hybrid algorithm was developed which can take into account both the contribution from direct sunlight and diffuse light from the atmosphere. After developing the hybrid algorithm, verification of the simulation result was performed by constructing a small LSC sample to measure the emission from the LSC edge using a spectrometer, and then comparing the measured spectrum to the simulated spectrum. Difference in total irradiance between measurement and simulation was found to be less than 18%, thus proving that the simulation model can predict the LSC performance with reasonable accuracy.

The effect of different installation orientations of Luminescent Solar Concentrators (LSC) were studied using the newly developed hybrid simulation algorithm. The LSC was placed under simulated direct and diffuse sunlight illumination at different time on 1 March 2011, at Kuala Lumpur, Malaysia (Latitude: 3° 08', North. Longitude: 101° 42', East) where the sun position and irradiance change with time in that day. The spectral irradiance graphs of direct and diffuse sunlight at different time were generated using the software SMARTS (Simple Model of the Atmospheric Radiative Transfer of Sunshine) developed by National Renewable Energy Laboratory.

Besides, LSC samples were constructed in small size of 10cm×5cm×0.5cm for spectral irradiance measurement from its edge, and in large size of 100cm×50cm×2.5cm where solar cells were attached to its edge. The LSC samples were constructed using unsaturated polyester resin (UP) co-polymer with methyl methacrylate (MMA) added with dye and cured in a mold with the desired dimension in room temperature. To test the performance of the large sample, a high power light source with large enough illumination area and controllable power output was built, using an array of 500W halogen lamps connected to a variable autotransformer (Variac), which controls the input power supplied to the halogen lamps.

ACKNOWLEDGEMENT

I would like to thank my supervisor Ir. Dr. Lim Yun Seng and my co-supervisor Prof. Dr. Faidz bin Abd Rahman for their direction, assistance, and guidance. In particular, Ir. Dr. Lim Yun Seng's numerous recommendations and suggestions have been invaluable for the project.

I also wish to thank Mr. Tan Seng Gee, who have taught me knowledge on all the material properties. Thanks are also due to Mr Ho Kok Wai, Senior Laboratory Assistant, and Encik Wan Ilham Shah Bin Wan Hasan, Assistant Laboratory Manager, for their assistance.

Lastly, I offer my deepest regards and blessings to all of those who supported me in any respect during the completion of the project.

APPROVAL SHEET

This dissertation/thesis entitled "**SIMULATION AND CONSTRUCTION OF LUMINESCENT SOLAR CONCENTRATOR**" was prepared by LO CHIN KIM and submitted as partial fulfillment of the requirements for the degree of Master of Engineering Science at Universiti Tunku Abdul Rahman.

Approved by:

____

(Ir. Dr. LIM YUN SENG) Date:…………………..

Professor/Supervisor

Department of Electrical and Electronic Engineering

Faculty of Engineering and Science

Universiti Tunku Abdul Rahman

____

(Prof. Dr. FAIDZ BIN ABD RAHMAN) Date:…………………..

Professor/Co-supervisor

Department of Electrical and Electronic Engineering

Faculty of Engineering and Science

Universiti Tunku Abdul Rahman

FACULTY OF ENGINEERING AND SCIENCE

UNIVERSITI TUNKU ABDUL RAHMAN

Date: __________________

SUBMISSION OF THESIS

It is hereby certified that LO CHIN KIM (ID No: 09UEM09112) has completed this thesis entitled "SIMULATION AND CONSTRUCTION OF LUMINESCENT SOLAR CONCENTRATOR" under the supervision of Ir. Dr. LIM YUN SENG (Supervisor) from the Department of Electrical and Electronic Engineering, Faculty of Engineering and Science, and Prof. Dr. FAIDZ BIN ABD RAHMAN (Co-Supervisor)* from the Department of Elecrical and Electronic Engineering, Faculty of Engineering and Science.

I understand that University will upload softcopy of my thesis in pdf format into UTAR Institutional Repository, which may be made accessible to UTAR community and public.

Yours truly,

____

(LO CHIN KIM)

DECLARATION

I hereby declare that the dissertation/thesis is based on my original work except for quotations and citations which have been duly acknowledged. I also declare that it has not been previously or concurrently submitted for any other degree at UTAR or other institutions.

Name _____LO CHIN KIM_____

Date _____26 August 2011_____

TABLE OF CONTENTS

LIST OF TABLES

LIST OF FIGURES

LIST OF NOTATIONS

Physical constants

c	Speed of light in free space	k	Boltzmann constant
h	Planck constant	q	Elementary charge constant
n_{air}	Refractive index of air		

LSC properties

L	Length of LSC	n	Refractive index of LSC
W	Width of LSC	T	Temperature
D	Thickness of LSC	I_l	Incident light spectrum
Q_e	Luminescent quantum efficiency	σ_e	Absorption cross section of dye
N	Number of luminescent dye particles per unit volume	σ_a	Absorption cross section of LSC sample

Simulation

λ	Radiation wavelength	θ	Polar angle
ν	Radiation frequency	ϕ	Azimuthal angle
$\Phi(\lambda)$	Spectral photon flux (wavelength domain)	$I(\nu)$	Spectral photon flux (frequency domain)
$E(\lambda)$	Spectral irradiance (wavelength domain)	λ_{em_peak}	Emission peak wavelength
σ_{meas}	Measured absorption cross section	I_{em_peak}	Emission peak intensity
σ_{eff}	Effective absorption cross section	$\Delta\lambda_p$	Mismatch in emission peak wavelength
λ_p	Absorption peak wavelength	ΔI_p	Mismatch in emission peak intensity

Ray-tracing model

P_{rad}	Radiant power	M_θ	Number of discrete θ
$L(\lambda)$	Spectral radiance	M_φ	Number of discrete φ
Ω	Solid angle	M_y	Number of discrete points along y direction
r	Position vector	M_z	Number of discrete points along z direction

Thermodynamic model

$B(\nu)$	Luminescent brightness	μ	Photon chemical potential
$I_E(\nu)$	Escaped flux	R	Reflection coefficient
$I_T(\nu)$	Trapped flux	θ_C	Critical angle
Ω_C	Solid angle extended by an escape cone		

CHAPTER 1

INTRODUCTION

A luminescent solar concentrator (LSC) is a transparent plate doped with luminescent material. The luminescent material absorbs sunlight and convert to luminescence which is guided toward the plate edge where solar cells are attached to. Electricity is then generated by the solar cells. This thesis presents the construction procedure of a LSC in large surface area of 100cm x 50cm, as well as the simulation model to study the LSC performance under different installation orientation, which takes into account of different solar irradiance and direction throughout the day.

Recent focus of the research on the topic of LSC is on achieving higher power conversion efficiency: by discovering and testing on the new material for LSC, especially the luminescent material, or using a novel LSC design. However, the main issue in the solar industry is on the higher price of electricity generation compared to the other sources of energy. Therefore it would be more interesting for the solar industry to answer the following questions regarding the use of LSC:

1. How would be the cost of electricity (cost/kWh) generated by the solar cells attached to the edge of an actual LSC in large dimension under sunlight throughout the day?
2. What is the procedure to construct a LSC with large surface area with minimum construction cost?

To answer the two questions above, the objectives of the research project documented in this thesis is therefore set as:

1. To develop a simulation model for LSC which is able to take into account both the direct sunlight and diffuse sunlight, and has a reasonably fast simulation time.
2. To model the LSC in simulation and study the effect of its orientation on its performance.
3. To calculate the possible reduction in cost per electricity generation (cost/kWh) by using LSC.
4. To design a low-cost LSC construction procedure for LSC with large surface area.

In this thesis, an introduction to the LSC and a brief review on the recent development of LSC is included in the subsequent chapter. The next chapter presents the procedure on the construction of LSC sample with large surface area using mirror as the mold. The sample quality and suggested ways to improve it will be discussed as well in that chapter. For the measurement of the LSC sample, a light source is then constructed which has a large illumination area and adjustable light intensity.

A simulation model with the name hybrid algorithm is then developed, with the necessary background theory introduced in the literature review section. Full detail of the simulation algorithm will be presented in Chapter 4. Verification of the hybrid algorithm is then performed by making a real sample, setting up an experiment, then measure the irradiance spectrum from LSC edge and finally compare the result to the simulation result.

Next, the simulation code has been improved to trace more light rays to the sun for higher accuracy and shorter simulation time. The trapped incident sunlight is further separated into those coming from direct and diffuse sunlight for a better understanding on the light spectrum received by solar cells.

Finally, a study on the LSC installation orientation which includes simulation of the actual sun irradiance spectrum and direction from another simulation software called Simple Model of the Atmospheric Radiative Transfer of Sunshine (SMARTS). Solar cell simulation is also included for electrical power output and energy output calculation.

CHAPTER 2

LITERATURE REVIEW

The luminescent solar concentrator (LSC) consists of a transparent plate doped with luminescent materials, such as laser/organic dyes, semiconductor quantum dots, rare earth materials, and semiconductor polymers. Incident sunlight is first absorbed by the luminescent materials, then re-emitted at different wavelength and guided to the edge of solar concentrator by total internal reflection. Solar cells are attached to the edges of the transparent plate to convert the trapped radiation to electricity. The cost of such a photo-voltaic system can be cheaper than ordinary PV panels, due to the low fabrication cost of LSCs and smaller solar cells at the edges. Figure 2.1 shows a diagram of the simplest type of luminescent solar concentrator.

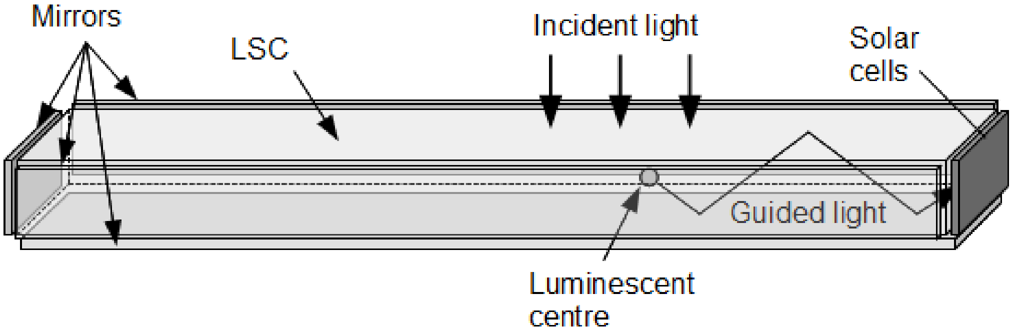

Figure 2.1: Luminescent Solar Concentrator

The LSCs have several advantages over conventional geometric solar concentrator. Complicated solar tracking system is unnecessary in LSCs. Furthermore, the LSC can collect both direct as well as diffuse sunlight, and the large surface area of LSC allow solar heat to be dispersed across the surface. Another benefit of the LSCs is that it can be integrated into buildings and hence generating electricity very near to the electrical distribution network. On the other hand, conventional geometric solar concentrators are usually installed in a remote area with no obstacle of sunlight. Therefore, several technical issues can be avoided by the integration of LSCs, such as power losses during transmission, voltage rise issues, etc.

The luminescent solar concentrator (LSC) is a non-imaging optical device that can concentrate sunlight onto a small area of solar cells to generate electricity. In this way, the large area of solar cells required in a standard flat-plate PV panel can be replaced by an inexpensive concentrator, hence reducing the cost of the module (in cost per watt) and also of the solar power (in cost per kilowatt-hour) (Rowan *et al.*, 2008).

The LSC typically consists of a polymer plate doped with a luminescent material, with solar cells attached to the plate edges. Higher efficiency can be achieved by matching the peak quantum efficiency of the solar cells to the peak emission of the concentrator. Several types of luminescent materials can be used in the LSC, such as laser dyes or organic dyes, semiconductor quantum dots (Barnham *et al.*, 2000), rare earth materials (Werts *et al.*, 1997), and semiconducting polymers (Sholin *et al.*, 2007). To further improve the efficiency of LSC, materials such as photonic layers (Rau *et al.*, 2005) and liquid crystals (Debije *et al.*, 2007) have also been used to reduce the losses in the LSC.

Several challenges are faced in LSC development, due to the limitation of the luminescent materials and the matrix materials used to fabricate the devices. There are four main criteria that should be met by the LSC materials (Rowan *et al.*, 2008):

1. Absorption of all wavelengths < 950nm with high absorption coefficients and an emission peak near wavelength of 1000nm.
2. Minimum re-absorption losses due to overlap of absorption and emission spectra.
3. Near-unity fluorescence quantum yield.
4. Long-term stability under the exposure of sunlight.

Typically one specific luminescent material satisfies some of the criteria above, but does not posses all the required characteristics. Therefore it is most likely to be a combination of different luminescent materials that can provide an optimized solution.

For LSC with device conversion efficiencies of 4%, the annual energy yield of 41.3 kWh/m^2 was reported based on ray-tracing simulation, which is 4.7 times lower than that of a state-of-the-art silicon solar cell (Van Sark *et al.*, 2008a). Cost per unit area of LSC with polymer plate-to-PV ratio of 1:15, is only 35% of that of a conventional PV (Bende *et al.*, 2008). High efficiencies of 6.9% was reported using a combination of different luminescent materials with spectrally matched solar cells (Goldschmidt *et al.*, 2009).

A reduction of re-absorption losses is reported using LSC with cylindrical design which was used together with a linear geometrical concentrator to focus sunlight onto the LSC, based on ray-tracing simulation (Bose *et al.*, 2009). Besides, it has been shown that the edge power output can be increased by 15% by introducing an organic selectively-reflecting mirror, which redirect light emitted to the surface of LSC to the edge with an efficiency of about 35% (Debije *et al.*, 2009). Diffusive reflector at the backside of LSC has also been shown to increase the module efficiency (Pravettoni *et al.*, 2009). Power conversion efficiency of 7.1% was achieved by the state-of-the-art LSC at the time of writing (Slooff *et al.*, 2008).

Finally, an estimated power conversion efficiencies of 6.8% is reported in (Currie *et al.*, 2008) by using different LSC design, in which a layer of thin film of organic dye molecules was deposited onto a layer of glass.

2.1 Luminescent Solar Concentrator Modelling

Modelling of the LSC have been done in two different approaches: Thermodynamic modelling (Chatten *et al.*, 2006) and ray-tracing modelling (Gallagher *et al.*, 2004). The thermodynamic modelling is a detailed balance model which is based on the radiative energy transfer between mesh points in the concentrator, and the ray-tracing modelling is a model which tracks every incoming photon and determines its fate (Van Sark *et al.*, 2008b). Both thermodynamic and ray-trace modelling provide useful tools for optimizing the performance of LSC and predicting the electrical output.

A LSC simulation model is developed from the existing thermodynamic model. Therefore a short review on the related background theory related to the thermodynamic model is presented in the following sub-chapters for the ease of reference.

2.2 Radiative Transfer Theory

Radiative transfer theory (RTT) describes quantitatively the way radiant energy is transferred through media that absorb, scatter, or emit radiation. It originated in astrophysics and later has been applied in the field of atmospheric physics and remote sensing.

The theory was first developed in a simple phenomenological way based on heuristic principle of classical radiometry as described by Chandrasekhar in his publication (Chandrasekhar, 1950). It has been criticized for its phenomenological character, lack of solid physical background, and unknown range of applicability. However, later progress in studies of its statistical wave content resulted in a much better understanding of its physical foundation and made it a corollary of the statistical electromagnetics (Tiggelen and Skipetrov, 2003).

Various ways to introduce the radiative transfer theory were also found, including a direct derivation from Maxwell's equation to get radiative transfer equation under certain approximations, or by means of a stocastic model where the radiative transfer equation was regarded as the differential equation for a Markov process's potential (Kanschat *et al.*, 2009).

In the following subchapters, coordinate systems, basic variables involved in the radiative transfer theory and radiative transfer equation are discussed and introduced using the simpler and intuitive phenomenological way as described in the publication (Chandrasekhar, 1950).

2.2.1 Coordinate Systems

Two types of coordinate systems are used in this thesis: cartesian coordinate system and spherical coordinate system.

Cartesian coordinate system defines the location of a point as (x,y,z). The values of x,y,z are the distances from the origin along the x-axis, y-axis and z-axis respectively, as shown in Figure 2.2.

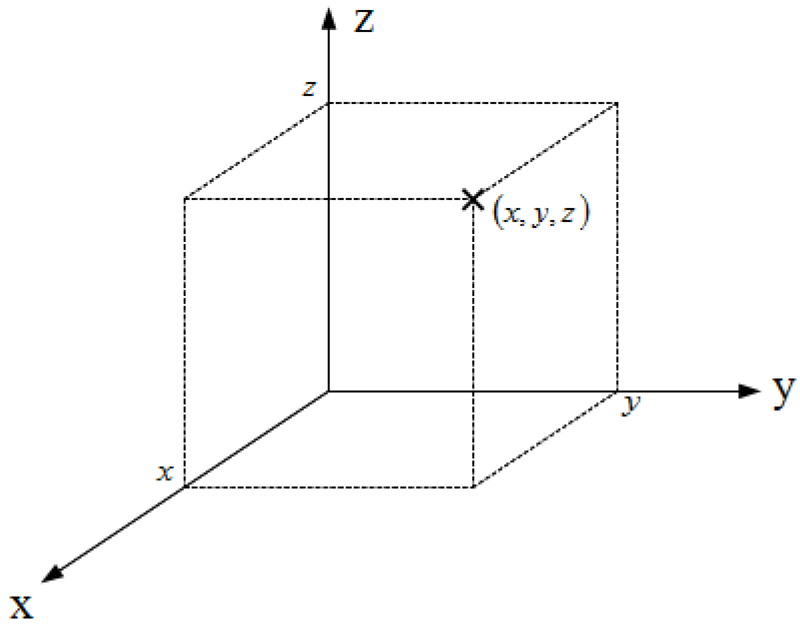

Figure 2.2: Cartesian coordinate system

As shown in Figure 2.3, a vector can be expressed in Cartesian coordinate as

$$\mathbf{P} = \begin{bmatrix} P_x \\ P_y \\ P_z \end{bmatrix} = P_x\,\hat{\mathbf{x}} + P_y\,\hat{\mathbf{y}} + P_z\,\hat{\mathbf{z}} \tag{2.1}$$

Where $\hat{\mathbf{x}}, \hat{\mathbf{y}}, \hat{\mathbf{z}}$ are unit vectors with unity magnitude and pointing from the origin to x-axis, y-axis and z-axis respectively.

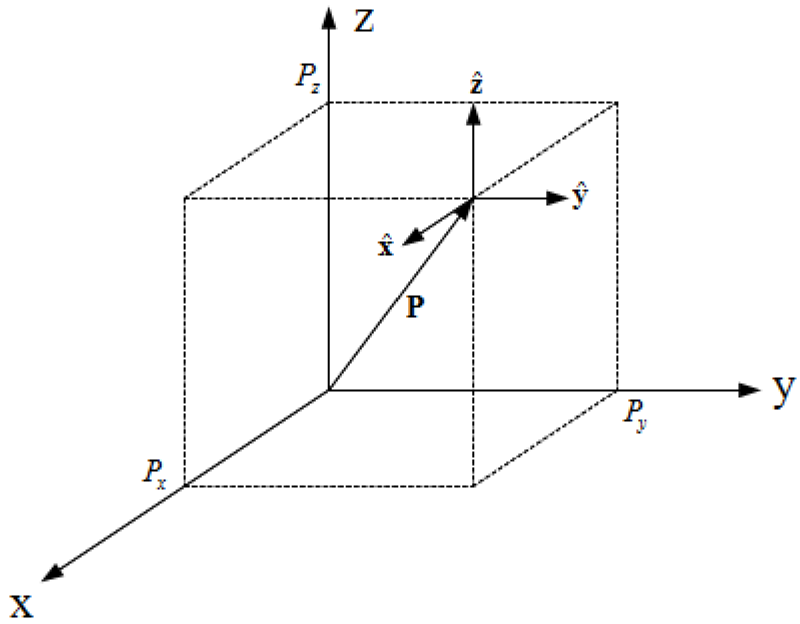

Figure 2.3: Vector in Cartesian coordinate system

Spherical coordinate system defines the location of a point as (r,θ,ϕ). The value r represents the distance from origin to the point, θ represents the angle from the z-axis to the line connecting the point and the origin, ϕ represents the angle from the x-axis to the line connecting the origin and the projection of the point on xy-plane as shown in Figure 2.4.

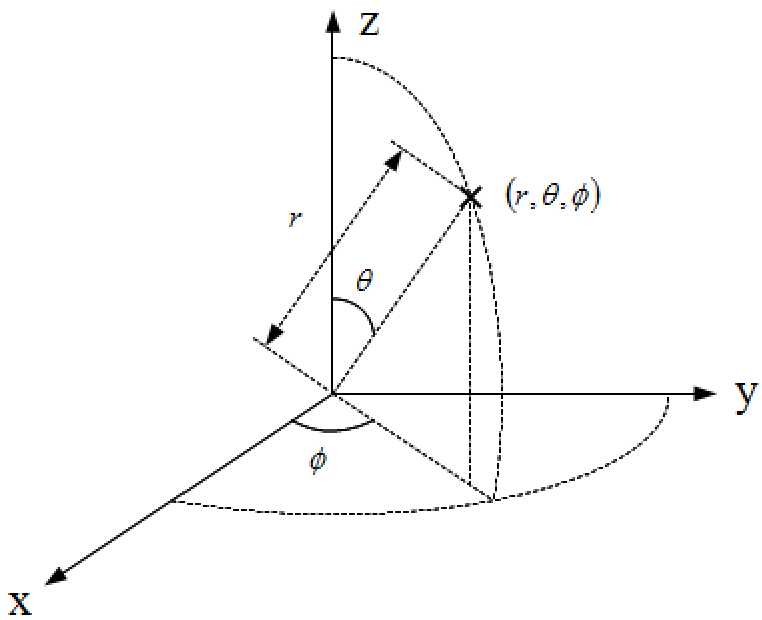

Figure 2.4: Spherical coordinate system

A vector in spherical coordinate, as shown in Figure 2.5 can be written as

$$\mathbf{P} = \begin{bmatrix} P_r \\ P_\theta \\ P_\phi \end{bmatrix} = P_r\,\hat{\mathbf{r}} + P_\theta\,\hat{\boldsymbol{\theta}} + P_\phi\,\hat{\boldsymbol{\varphi}} \tag{2.2}$$

Where $\hat{\mathbf{r}}$, $\hat{\boldsymbol{\theta}}$, $\hat{\boldsymbol{\varphi}}$ are unit vector with direction as shown in Figure 2.5.

Spherical coordinate and Cartesian coordinate are related by:

$$\begin{aligned} x &= r\sin\theta\cos\phi \\ y &= r\sin\theta\sin\phi \\ z &= r\cos\theta \end{aligned} \tag{2.3}$$

Or inversely,

$$\begin{aligned} r &= \sqrt{x^2+y^2+z^2} \\ \theta &= \cos^{-1}\left(\frac{z}{\sqrt{x^2+y^2+z^2}}\right) \\ \phi &= \tan^{-1}\left(\frac{y}{x}\right) \end{aligned} \tag{2.4}$$

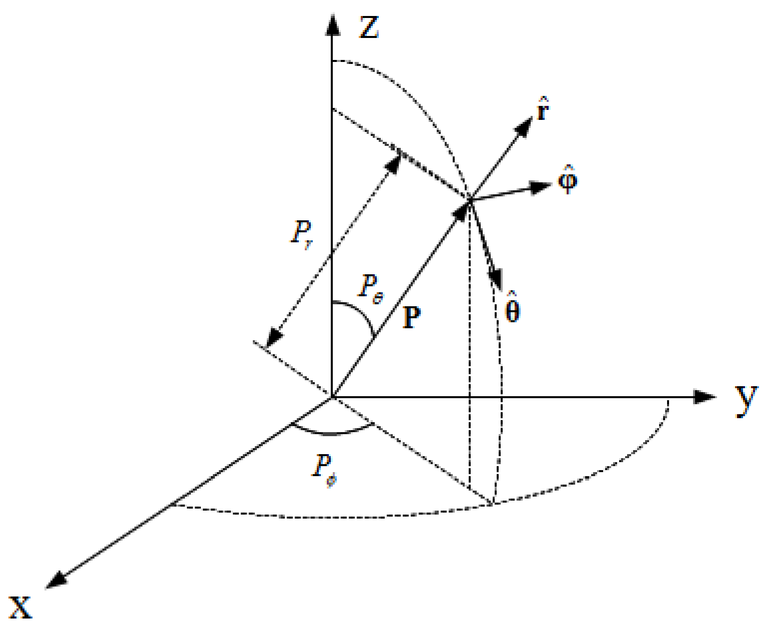

Figure 2.5: Vector in spherical coordinate system

2.2.2 Solid Angle

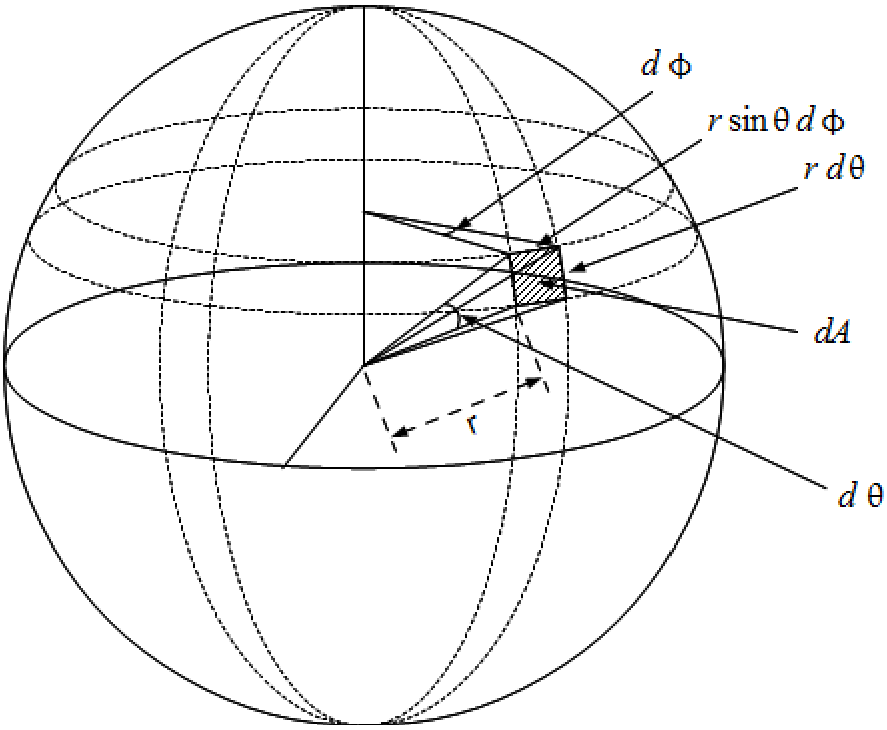

Figure 2.6: Definition of solid angle

The solid angle is defined as the ratio of the area A cut out from a sphere's surface to square of the sphere's radius. The solid angle is represented by Ω in Eq. 2.5 and its unit is steradians (sr).

$$\Omega = \frac{A}{r^2} \tag{2.5}$$

In differential form,

$$d\Omega = \frac{dA}{r^2} \tag{2.6}$$

As shown in Figure 2.6, the differential area can be written as

$$dA = r^2 \sin\theta \; d\theta \; d\phi \tag{2.7}$$

Substitute Eq. 2.7 into Eq. 2.6,

$$d\Omega = \sin\theta \, d\theta \, d\phi \tag{2.8}$$

Where,

dΩ = Differential solid angle (sr),

θ = Inclination angle in spherical coordinate (radian),

ϕ = Azimuth angle in spherical coordinate (radian).

2.2.3 Specific Intensity

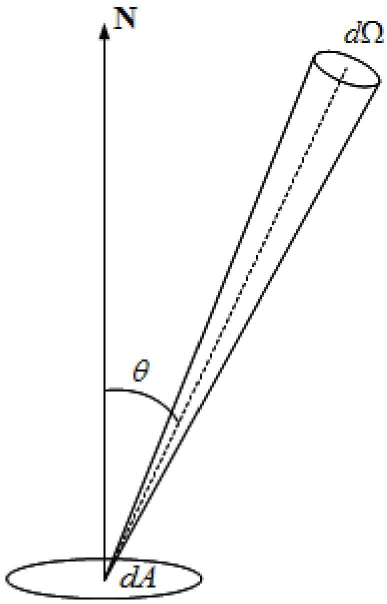

Figure 2.7: Definition of specific intensity

Refer to Figure 2.7, specific intensity of radiation, L(υ) (Chandrasekhar, 1950; Thomas and Stamnes, 1996) is defined as

$$d^4E = L(\nu)\cos\theta \, dA \, d\Omega \, dt \, d\nu \tag{2.9}$$

Where,

L(υ) = Specific intensity or spectral radiance (W m^{-2} sr^{-1} Hz^{-1}),

d^4E = Infinitesimal energy transferred to dA through dΩ (J),

dA = Infinitesimal area that receive radiation energy through dΩ (m^2),

dΩ = Infinitesimal solid angle within which the radiation transfer is confined (sr),

dt = Infinitesimal time interval where the radiation energy transfer takes place (s),

dν = Infinitesimal range of frequency of the radiation (Hz),

θ = Angle between radiation direction and surface normal of dA (radian).

The radiation transfer as illustrated in Figure 2.7 is also known as a pencil of radiation (Chandrasekhar, 1950).

2.2.4 Radiative Transfer Equation

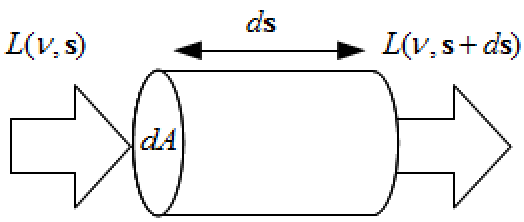

Figure 2.8: Definition of radiative transfer equation

Consider a radiation traveling in an infinitesimal cylindrical element of cross section dA and height d**s** (as shown in Figure 2.8) (Chandrasekhar, 1950).

$$dL(\nu) = L(\nu, \mathbf{s} + d\mathbf{s}) - L(\nu, \mathbf{s}) = -\kappa(\nu, \mathbf{s})\rho(\mathbf{s})L(\nu)d\mathbf{s} + \frac{j(\nu)}{4\pi}d\mathbf{s} \qquad (2.10)$$

Where,

dL(ν) = Differential change of specific intensity after traveling a distance d**s** (W m^{-2} sr^{-1} Hz^{-1}),

d**s** = Differential distance of travel (m),

κ(ν,**s**) = Mass absorption coefficient (m^2 kg^{-1}),

ρ(**s**) = Mass density (kg m^{-3}),

j(ν) = Volume emissivity (W m^{-3} Hz^{-1}),

The mass absorption coefficient is

$$\kappa(\nu,\mathbf{s}) = \frac{N(\mathbf{s})\,\sigma(\nu,\mathbf{s})}{\rho(\mathbf{s})} \qquad (2.11)$$

Where,

N(**s**) = Number density of particle (m^{-3}),

σ(ν,**s**) = Absorption cross section per particle (m^2)

In general, the quantity N(**s**)σ(ν,**s**) varies with the physical condition of the medium of radiation transfer (Thomas and Stamnes, 1996). However, N does not vary with location in this thesis since the dye particles are always distributed evenly throughout the medium, while σ is assumed to be a function of frequency only.

Rewrite Eq. 2.10 by substituting Eq. 2.11 into Eq. 2.10,

$$\frac{dL(\nu,\mathbf{s})}{d\mathbf{s}} = -N\sigma(\nu)L(\nu,\mathbf{s}) + \frac{j(\nu,\mathbf{s})}{4\pi} \qquad (2.12)$$

Define the source intensity (dye emission) of the medium as

$$L_s(\nu,\mathbf{s}) = \frac{1}{N\sigma(\nu)}\frac{j(\nu,\mathbf{s})}{4\pi} \qquad (2.13)$$

Where,

L_s(υ,**s**) = Source intensity, having the same unit as the specific intensity (W m^{-2} sr^{-1} Hz^{-1})

Therefore, Eq. 2.12 can be written as,

$$\frac{1}{N\sigma(\nu)}\frac{dL(\nu,\mathbf{s})}{d\mathbf{s}} = -L(\nu,\mathbf{s}) + L_s(\nu,\mathbf{s}) \tag{2.14}$$

Define the optical depth, τ, as,

$$d\tau = N\sigma(\nu)\,d\mathbf{s} \tag{2.15}$$

Substitute Eq. 2.15 into Eq. 2.14,

$$\frac{dL(\nu,\tau)}{d\tau} = -L(\nu,\tau) + L_s(\nu,\tau) \tag{2.16}$$

2.2.5 Two-stream approximation

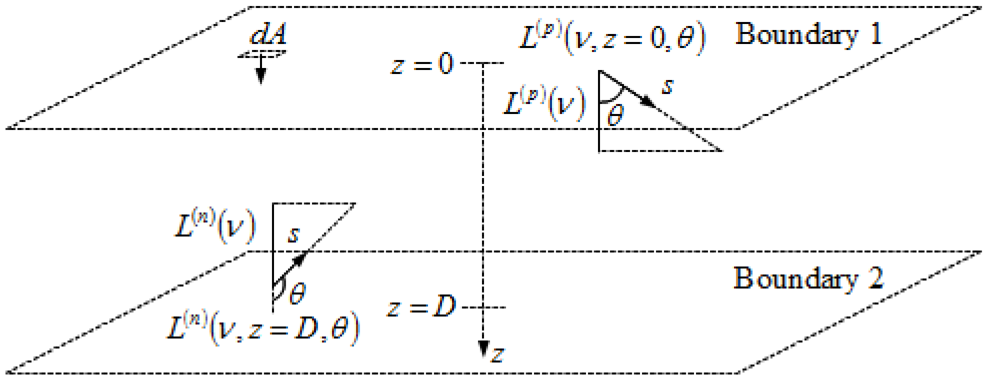

Figure 2.9: Plane layer between two infinite boundaries

A plane layer between two infinite boundaries is shown in Figure 2.9 (Siegel and Howell, 1972). Physical conditions in the medium between the boundary 1 and boundary 2 vary in one dimension (along z-axis) only. The path direction is given by the angle θ measured from the positive z direction. The superscript (p) and (n) correspond to directions with positive or negative cos θ respectively, so that $L^{(p)}(\nu)$ corresponds to $0 \le \theta \le \pi/2$ and $L^{(n)}(\nu)$ to $\pi/2 \le \theta \le \pi$.

From Figure 2.9, for $0 \le \theta \le \pi/2$,

$$s = \frac{z}{\cos\theta} \quad \forall\, 0 \le \theta \le \frac{\pi}{2} \tag{2.17}$$

So,

$$ds = \frac{dz}{\cos\theta} \quad \forall\, 0 \le \theta \le \frac{\pi}{2} \tag{2.18}$$

Therefore, from Eq. 2.15,

$$d\tau = N\sigma(\nu)\, ds = \frac{N\sigma(\nu)\, dz}{\cos\theta} \quad \forall\, 0 \le \theta \le \frac{\pi}{2} \tag{2.19}$$

For $\pi/2 \le \theta \le \pi$,

$$s = \frac{-z}{\cos(\pi - \theta)} \quad \forall\, \frac{\pi}{2} \le \theta \le \pi \tag{2.20}$$

$$s = \frac{z}{\cos\theta} \quad \forall\, \frac{\pi}{2} \le \theta \le \pi \tag{2.21}$$

Therefore,

$$d\tau = N\sigma(\nu)\, ds = \frac{N\sigma(\nu)\, dz}{\cos\theta} \quad \forall\, \frac{\pi}{2} \le \theta \le \pi \tag{2.22}$$

Substitute Eq. 2.19 and Eq. 2.22 into Eq. 2.16,

$$\frac{\cos\theta}{N\sigma(\nu)} \frac{\partial L^{(p)}(\nu, z, \theta)}{\partial z} = -L^{(p)}(\nu, z, \theta) + L_s^{(p)}(\nu, z, \theta) \quad \forall\, 0 \le \theta \le \frac{\pi}{2} \tag{2.23}$$

$$\frac{\cos\theta}{N\sigma(\nu)} \frac{\partial L^{(n)}(\nu, z, \theta)}{\partial z} = -L^{(n)}(\nu, z, \theta) + L_s^{(n)}(\nu, z, \theta) \quad \forall\, \frac{\pi}{2} \le \theta \le \pi \tag{2.24}$$

Eq. 2.23 and Eq. 2.24 are two coupled differential equations derived from Eq. 2.16 with appropriate substitution. The ordinary differential with respect to τ becomes partial differential with respect to z since the specific intensity now depends on the spatial and angular variables z and θ.

In the case of radiative transfer between two infinite parallel plane, two-stream approximation can be applied. The authors of the publication (Chatten *et al.*, 2001) applied the method of Schwarzschild and Milne which is the most simple two-stream approximation, also known as the hemispheric constant method as described in the publication (Meador and Weaver, 1980).

In Schwarzschild's method, the specific intensity $L^{(p)}(\nu,z,\theta)$ and $L^{(n)}(\nu,z,\theta)$ from Eq. 2.23 and Eq. 2.24 are assumed to be independent on the direction θ.

Therefore Eq. 2.23 and Eq. 2.24 can be simplified to

$$\frac{\cos\theta}{N\sigma(\nu)}\frac{\partial L^{(p)}(\nu,z)}{\partial z} = -L^{(p)}(\nu,z) + L_s^{(p)}(\nu,z,\theta) \quad \forall\ 0 \le \theta \le \frac{\pi}{2} \tag{2.25}$$

$$\frac{\cos\theta}{N\sigma(\nu)}\frac{\partial L^{(n)}(\nu,z)}{\partial z} = -L^{(n)}(\nu,z) + L_s^{(n)}(\nu,z,\theta) \quad \forall\ \frac{\pi}{2} \le \theta \le \pi \tag{2.26}$$

Integrate with respect to solid angle, Ω, over the regions $0 \le \theta \le \pi/2$ and $\pi/2 \le \theta \le \pi$ respectively for the two equations,

$$\begin{aligned}&\int_0^{2\pi}\int_0^{\pi/2} \frac{\cos\theta\sin\theta}{N\sigma(\nu)}\frac{\partial L^{(p)}(\nu,z)}{\partial z}\,d\theta\,d\phi \\ &\quad = \int_0^{2\pi}\int_0^{\pi/2} -L^{(p)}(\nu,z) + L_s^{(p)}(\nu,z,\theta)\sin\theta\,d\theta\,d\phi\end{aligned} \tag{2.27}$$

$$\begin{aligned}&\int_0^{2\pi}\int_{\pi/2}^{\pi} \frac{\cos\theta\sin\theta}{N\sigma(\nu)}\frac{\partial L^{(n)}(\nu,z)}{\partial z}\,d\theta\,d\phi \\ &\quad = \int_0^{2\pi}\int_{\pi/2}^{\pi} -L^{(n)}(\nu,z) + L_s^{(n)}(\nu,z,\theta)\sin\theta\,d\theta\,d\phi\end{aligned} \tag{2.28}$$

Eq. 2.27 and Eq. 2.28 can be solved by substituting the emission from luminescent particles into the source intensity $L_s^{(p)}$ and $L_s^{(n)}$.

The thermodynamic model was derived from radiative transfer equations in term of spectral photon flux, which is denoted by I(ν) in this thesis. It is related to the specific intensity or spectral radiance by,

$$L(\nu) = I(\nu) \cdot h\nu \tag{2.29}$$

Where,

L(ν) = Specific intensity or spectral radiance (W m^{-2} sr^{-1} Hz^{-1}),

I(ν) = Spectral photon flux (Photons s^{-1} m^{-2} sr^{-1} Hz^{-1}),

ν = Radiation frequency (Hz),

h = Planck's constant (J s).

Substitute Eq. 2.29 into Eq. 2.27 and Eq. 2.28,

$$\begin{aligned}&\int_0^{2\pi}\int_0^{\pi/2} \frac{\cos\theta \sin\theta}{N\sigma(\nu)} \frac{\partial I^{(p)}(\nu,z)}{\partial z}\, d\theta\, d\phi \\ &= \int_0^{2\pi}\int_0^{\pi/2} -I^{(p)}(\nu,z) + I_s^{(p)}(\nu,z,\theta) \sin\theta\, d\theta\, d\phi\end{aligned} \tag{2.30}$$

$$\begin{aligned}&\int_0^{2\pi}\int_{\pi/2}^{\pi} \frac{\cos\theta \sin\theta}{N\sigma(\nu)} \frac{\partial I^{(n)}(\nu,z)}{\partial z}\, d\theta\, d\phi \\ &= \int_0^{2\pi}\int_{\pi/2}^{\pi} -I^{(n)}(\nu,z) + I_s^{(n)}(\nu,z,\theta) \sin\theta\, d\theta\, d\phi\end{aligned} \tag{2.31}$$

Where the term hν has been taken out and canceled from both side of the equations since it is independent on the integration variables.

2.2.6 Local Thermal Equilibrium and Detailed Balance Principle

Yablonovitch derived a generalized brightness theorem (Yablonovitch, 1980) for the equilibrium of a radiation field brightness and the electronic degrees of freedom of the molecule. The luminescent brightness from the luminescent particles derived by Yablonovitch is

$$B(\nu, \mu(z)) = \frac{8\pi n^2 \nu^2}{c^2} \frac{1}{e^{[h\nu - \mu(z)]\beta} - 1} \tag{2.32}$$

Where,

$B(\nu,\mu(z))$ = Luminescent brightness (photons s^{-1} m^{-2} Hz^{-1}),

n = Refractive index (dimensionless quantity),

ν = Frequency of radiation (Hz),

c = Speed of light in free space (m s^{-1}),

h = Planck constant (J s),

$\mu(z)$ = Photon chemical potential (J),

β = 1/kT (J^{-1}),

k = Boltzmann constant (J K^{-1}),

T = Temperature (K)

The source intensity for plane layers in (photons s^{-1} sr^{-1} m^{-2} Hz^{-1}) can be expressed using luminescent brightness in Eq. 2.32 by assuming the luminescent particles emit light isotropically in all direction,

$$I_s(\nu, z, \theta) = \frac{B(\nu, \mu(z))}{4\pi} \tag{2.33}$$

Using detailed balance argument, from the viewpoint of an individual molecule, radiative equilibrium occurs when its net upward transition rate exactly balance its rate of spontaneous emission at each frequency (Yablonovitch, 1980). Therefore, the photon chemical potential μ will be determined by the steady-state balance of the upward and downward transition. Therefore, the detailed balance equation is given by,

$$\int \sigma_e(\nu)\left[\iint I(\nu, z)\sin\theta \, d\theta \, d\phi\right] d\nu = \int \frac{\sigma_e(\nu)}{Q_e} B(\nu, z) \, d\nu \tag{2.34}$$

2.2.7 Application of Radiative Transfer Equation and Detailed Balance Principle in LSC Simulation (Thermodynamic Model)

Substituting Eq. 2.33 as the source intensity into Eq. 2.30 and Eq. 2.31 and then further separating the equations into escaping and trapped photon fluxes forms 4 integro-differential equations. After performing the double integration, followed by simplification and substitution, forms the 4 differential equations in the thermodynamic two-flux model. Substitution of variables is required because the forward and backward, escaped and trapped fluxes are defined as the net photon fluxes integrated over their respected solid angle in the thermodynamic two-flux model (Chatten *et al.*, 2001). Solution for the 4 differential equations can be found in the cited paper and the detailed algorithm and all equations involved will be presented in Chapter 4.2.1.

2.3 Solar Cell Modelling

Solar cell electrical performance can be modeled accurately for a flat-band pn homojunction solar cell using single-diode model or two-diode model. Single diode model is introduced in this thesis for its simplicity. The solar cell equation from the model is given by,

$$I = I_{ph} - I_0\left[\exp\left(\frac{V + IR_s}{AV_T}\right) - 1\right] - \frac{V + IR_s}{R_{sh}} \tag{2.35}$$

Where,

I = Solar cell output current (A),

V = Solar cell output voltage (V),

I_{ph} = Photo-generated current (A),

I_0 = Diode saturated current (A),

R_s = Lumped series resistance (Ω),

R_{sh} = Lumped shunt resistance (Ω),

A = Diode quality factor,

$$V_T = \frac{kT_s}{e} \tag{2.36}$$

k = Boltzmann constant ($J\ K^{-1}$),

e = Elementary charge constant (C),

T_s = Temperature of the solar cell (K).

The diode saturated current in the model is derived from the semiconductor theory for diode, where the photo-generated current can be found by integrating the multiplication of spectral irradiance received by the solar cell and its internal quantum efficiency, with respect to wavelength (Yang *et al.*, 2008).

CHAPTER 3

LOW-COST CONSTRUCTION METHOD FOR LSC WITH SOLAR CELLS ATTACHED TO ITS EDGE

A low-cost LSC construction procedure, where solar cells are attached to its edge during the LSC construction, is proposed in this chapter. The most basic planar LSC design is used as a demonstration of the proposed procedure. Novelty of the proposed procedure are:

1. Cheaper unsaturated polyester resin (UP) is used together with methyl methacrylate (MMA) monomer as co-monomer to increase the optical transmission of UP.
2. Material cost for mold is minimized because bottom and side mirrors are used directly as the mold, hence avoiding additional cost for mold material. The additional mold material cost could increase the LSC construction cost significantly since the cured UP often left a significant amount of residual on the mold after demolding, which causes the mold to be reuseable only for a limited number of times before it is contaminated with too much residual.

Advantages of the proposed procedure includes:

1. Construction cost is minimized with the use of mirrors to construct the mold.
2. The raw materials, UP resin, MMA monomer and silicon solar cells are commercially available.

3. Short construction time for one LSC.
4. Specialized equipment, such as vacuum chamber with high volume for degassing is not required.
5. Highly specialized skill worker is not required.

The proposed procedure will be discussed in detail in this chapter, together with all the materials and equipment used. A 100cm x 50cm x 2.5cm LSC was built using the proposed procedure, with solar cells total area of 47.5cm x 11cm attached slanted at one of the LSC shorter edge. Next, a light source with large illumination area and variable intensity control was constructed for the measurement on the constructed LSC.

3.1 LSC Materials and Design

The materials to construct the LSC, material for the mold, solar cell, and equipment involved in the construction process are listed in Table 3.1.

Table 3.1. Materials and equipment used in the construction of LSC.

LSC material:	
Type of material	Material name
Transparent host material	Unsaturated polyester resin (Reversol P-9133LG, a mixture of unsaturated polyester and styrene)
Co-monomer	Methyl methacrylate
Luminescent dye	Rhodamine 6G (dye content ~95%, from Sigma Adrich)
Curing agent for UP resin	Methyl Ethyl Ketone Peroxide, solution in dimethyl phthalate (Buthanox M-50 from Akzo Nobel)
Mold material:	

Ordinary back surface glass mirrors	
Solar cell:	
Silicon solar cells	
Equipment:	
Electronic balance	
Magnetic stirrer	

3.2 Construction of LSC with Solar Cells Attached to One Edge

The procedure of LSC construction is separated into 2 stages: construction of the mold using mirrors and the actual LSC construction procedure. Several attempts were made to construct a LSC with minimized bubble content and no undissolved dye particles. The proposed LSC construction method is the best solution found among several other attempts to achieve that.

It was found hard to disperse the dye particles in the UP resin properly in a short time without leaving undissolved dye particles in it due to high viscosity of the UP resin which causes the process to be slow even with vigorous stirring. The proposed procedure first disperse the dye molecules inside MMA monomer solution which has much lower viscosity with the aid of magnetic stirrer. Only properly dispersed part is then added into the unsaturated polyester resin, where the rest is added with MMA monomer solution again and repeat the stirring process. It therefore reduce the overall stirring time required to prepare the UP resin with luminescent dye and MMA monomer.

LSC bubble content was controlled by allowing the prepared UP resin for degassing under room temperature and room atmospheric pressure. Air trapped inside the high viscosity UP resin can come out from the surface slowly when it was left inside the container for a period of time. Minimum amount of time for degassing process was determined from a trial and error method for the proposed procedure. Detail of the proposed procedure is listed in the following 2 sub-chapters.

3.2.1 Construction of Mold using Mirrors

Steps for the construction of mold are:

1. Put the bottom mirror on a table with its reflective surface facing upward.
2. Stick the side mirrors at the edge of the bottom mirror using silica gel, where all side mirrors have their reflective surfaces facing inside.
3. Solder the connection wires to the solar cells connection terminals.
4. Test the quality of connection using an ammeter, where solar cell is exposed under ambient light. Small current in the range of micro ampere should be recorded from the ammeter.
5. Stick the solar cells on the bottom mirror and edge mirror at one of its shorter edge.
6. Make sure terminals of all the connection wires not connected to the solar cells are left outside the mold during LSC curing process.

3.2.2 Procedure of LSC Construction

Procedure of LSC construction

1. Measure the mass of a small container (m_{con2}).

2. Add in and measure the mass of required dye excluding the tare mass of the small container (m_{dye}).
3. Add MMA into the small container.
4. Cover the small container and stir the dye+MMA solution using magnetic stirrer for 2 hours.
5. Measure the weight of a big container (m_{con1}).
6. Add UP resin to the big container and measure its mass excluding the tare mass of the big container (m_{up}).
7. After the stirring process finish, measure the mass of the dye+MMA solution and the small container (m_{mma1}).
8. Pour the dye+MMA solution into UP resin carefully. Precipitate of dye particles which does not disperse in MMA is left in the small container.
9. Measure the leftover mass (m_{left1}).
10. Add MMA into the small container again.
11. Cover the small container and stir the dye+MMA solution using magnetic stirrer for 10 minutes.
12. Stir the dye+MMA+UP resin using a plastic stick while the stirring process in the previous step is ongoing.
13. Repeat steps 7-12 until all required amoung of MMA is added into the UP resin. Pour all dye+MMA including all precipitate of dye particles, if any, for the last batch of solution. Subsequent mass of dye+MMA solution are m_{mma3}, m_{mma4}, ... and those of leftover are m_{left3}, m_{left4},...
14. Wait for 10 minutes for debubbling/degassing of UP resin.
15. Measure the mass of UP curing agent (m_{m50}).

16. Add the curing agent into the UP resin.

17. Wait for 10 minutes again for degassing.

18. Pour the UP resin into the mold.

19. Wait for 3 hours of UP resin curing process before moving the mold.

3.3 LSC Sample Quality

Figure 3.1: LSC sample with solar cells attached to the shorter edge.

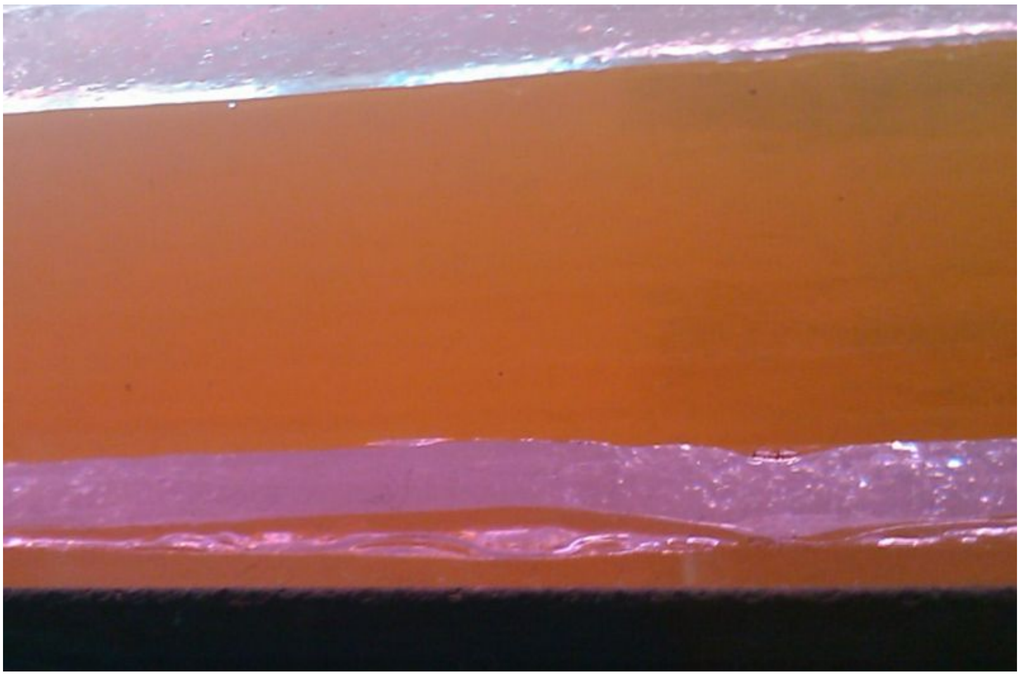

Figure 3.2: Reflection of ambient light from the bottom mirror of LSC sample can be seen at its edge, no scattering from bubble or large undissolved dye particles were observed.

A LSC sample (Figure 3.1) was made using the procedure described in the previous sub-chapter. No bubble or undissolved dye particles were visually observed in the constructed LSC sample, as shown in Figure 3.2. The actual percentage of MMA co-monomer in unsaturated polyester resin and the dye concentration in the LSC were calculated from the actual measurement, as listed in Table 3.2.

Table 3.2. Measured variables of the LSC sample with their corresponding accuracy.

Measured variables	Formula	Values	Accuracy
m_{con1}	Direct measurement	1082 g	±1 g
m_{con2}	Direct measurement	4.06 g	±0.01 g
m_{dye}	Direct measurement	0.16 g	±0.01 g
m_{up}	Direct measurement	13999 g	±1 g
m_{mma1}	Direct measurement	86.45 g	±0.01 g
m_{left1}	Direct measurement	4.93 g	±0.01 g
m_{mma2}	Direct measurement	72.47 g	±0.01 g
m_{left2}	Direct measurement	6.99 g	±0.01 g
m_{mma3}	Direct measurement	69.69 g	±0.01 g
m_{left3}	Direct measurement	5.21 g	±0.01 g
m_{mma4}	Direct measurement	59.03 g	±0.01 g
m_{left4}	Direct measurement	4.15 g	±0.01 g
$m_{addedmma1}$	m_{mma1}-m_{left1}	81.52 g	±0.02 g
$m_{addedmma2}$	m_{mma2}-m_{left2}	65.48 g	±0.02 g
$m_{addedmma3}$	m_{mma3}-m_{left3}	64.48 g	±0.02 g
$m_{addedmma4}$	m_{mma4}-m_{left4}	54.88 g	±0.02 g
m_{m50}	Direct measurement	140.56 g	±0.03 g [1]
m_{mma}	$m_{addedmma1}+m_{addedmma2}+m_{addedmma3}+m_{addedmma4}$	266.2 g	±0.09 g
% mma	$m_{mma}/m_{up}*100\%$	1.9016 wt%	±0.0008 wt%
% m50	$m_{m50}/(m_{up}+m_{mma})*100\%$	0.9853 wt%	±0.0003 wt%
Dye concentration	$m_{dye}/(m_{up}+m_{mma}+m_{m50})$	11.1067 μg/g	±0.6951 μg/g

[1] 3 measurements were taken due to limited volume in the small container.

From Table 3.2, the percentage of MMA in the UP resin is 1.9016 wt% (±0.0008 wt%), the percentage of Buthanox M-50 in UP resin added with MMA is 0.9853 wt% (±0.0003 wt%), and the dye concentration in the LSC is 11.1067 μg/g (±0.6951 μg/g). Evaporation of the UP resin and MMA during the curing process was ignored in the calculation. Accuracy in the table for direct-measured values were determined by the accuracy of the electronic balance used during the LSC construction, where accuracy for calculated values were determined by first calculating the maximum and minimum possible values and then taking the maximum mismatch from the calculated value as calculated accuracy.

3.3.1 Shrinkage of LSC Sample

Figure 3.3: Separation of LSC edge from the side of mirror mold.

From the actual measurement after the LSC is fully cured, the inner dimension of mold is 98.7cm x 48.6cm x 2.6cm, therefore having the capacity of 12471.73 cm^3. However, the shrinkage which occurred during the LSC curing process reduced the LSC dimension to 95.8cm x 47.9cm x 2.5cm, or volume of 11472.05 cm^3. In other words, the LSC volume was reduced by 8.02% during the curing process of unsaturated polyester resin. The shrinkage is shown in Figure 3.3 where LSC volume was reduced and its edges were eventually separated from the mold surfaces at the edges. The volume shrinkage is affected by the amount of MMA added into the resin. The more MMA is added, the cured sample has higher optical transmission but at the same time also has significantly higher volume shrinkage (Cao and James Lee, 2003).

The volume shrinkage of UP resin in this case cannot be compensated directly by adding low profile additives into the UP resin. This is because the low profile additives compensate the volume shrinkage by micro-void formation in the resin during polymerization in the curing process (Haider *et al.*, 2007), therefore at the same time it also greatly reduce the optical transmission of the end product.

3.3.2 Surface Quality of LSC Sample

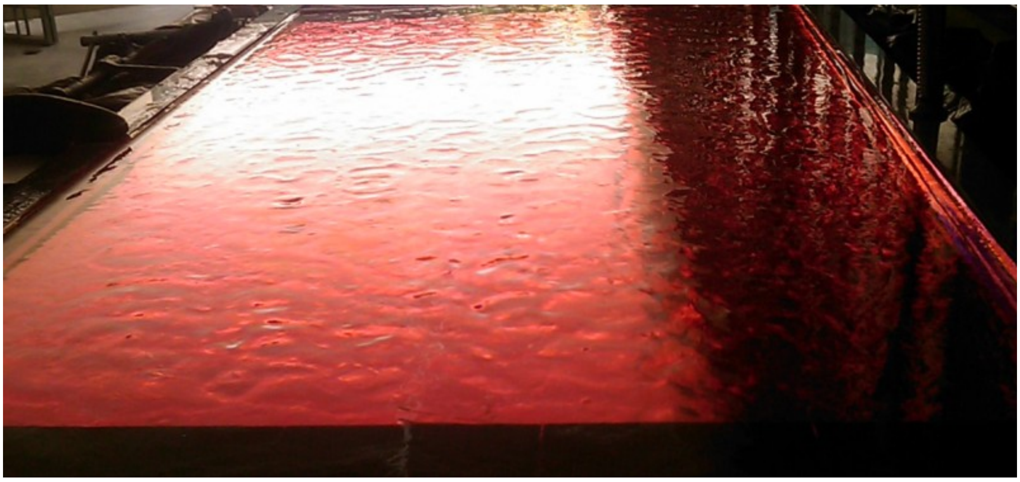

Figure 3.4: Ripple was formed on the top surface of LSC during the curing process at the moment when the resin started to become gel-like, i.e. at its gelation point.

Although the LSC edges are not in contact with the side mirrors anymore after its curing process due to the volume shrinkage, the LSC surfaces at the edges are still specular or mirror-like, having the same shape as the shape of mold (side mirrors) during its curing process. However, the top surface of LSC, which was not in contact with any solid surface, is flat but contains very small ripple on it, as shown in Figure 3.4. This is caused by the small ground vibration during the curing process.

Post-curing treatment of the LSC, such as surface polishing, is difficult to be done immediately after the LSC becomes solid form, due to unsaturated polyester and styrene residual which were still present on the top of the LSC sample even after 1 day. This is because the unsaturated polyester resin residual was not yet fully cured, which caused the uncured residual on the surface to stick on the grinding sand paper or polishing cloth and lowered the efficiency of surface polishing process. A study on the degree of cure of UP resin as described in a publication (Shah and Schubel, 2010) revealed that only 85% of the resin was cured under ambient condition after 1 day, which explains the observation on the LSC sample surface after the curing process.

3.3.3 Air-gap between LSC and Solar Cells

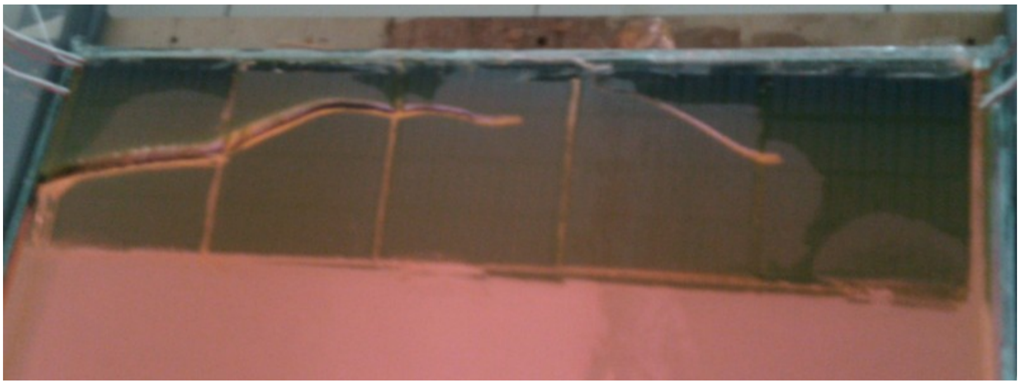

Figure 3.5: Air gap and cracks at the boundary between solar cells and LSC material.

Unwanted air gap and cracks were formed in part of the solar cells surface in contact with the LSC edge surface, as shown in Figure 3.5. This is because the solar cells were fixed on the bottom and edge mirror, where the shrinkage force that pulled the solar cells via the solar cell surface during the curing process eventually caused the separation of LSC material with the solar cell surface, when the force is larger than the adhesion force between the solar cell surface and the LSC molecules. The total internal reflection from the LSC and air-gap boundary significantly reduced the solar cell performance where the air-gap was formed.

3.4 Suggested Improvement on the LSC Construction Procedure

A few improvement can be made on the proposed low-cost LSC construction procedure. First of all, the molding process can be done on an anti-vibration table to improve the LSC top surface quality. A low cost alternative solution can also be used by putting a light weight thin glass sheet on the top of unsaturated polyester resin during the curing process and take it away after the LSC is fully cured. The glass sheet can be hung from a support structure on top of the mold to control it from sinking too much into the liquid form of LSC during the early stage of curing process when the unsaturated polyester resin is still in liquid form.

Besides, the LSC can be put outdoor during the later stage of its curing process, covered with transparent plastic sheet for heat treatment using sunlight. This is because elevated temperature can accelerate the curing process of the LSC, so that any post-curing surface polishing can be done in a shorter period of time after the LSC is fully cured.

On the other hand, solar cell can be put on the bottom mirror instead of stick on it, with the aid of support structure made by plastic sheet of paper to allow certain degree of solar cells movement as the LSC shrink during the curing process so that air gap will not form between the solar cell surface and the LSC.

3.5 Construction of Light Source with Large Illumination Area and Adjustable Intensity

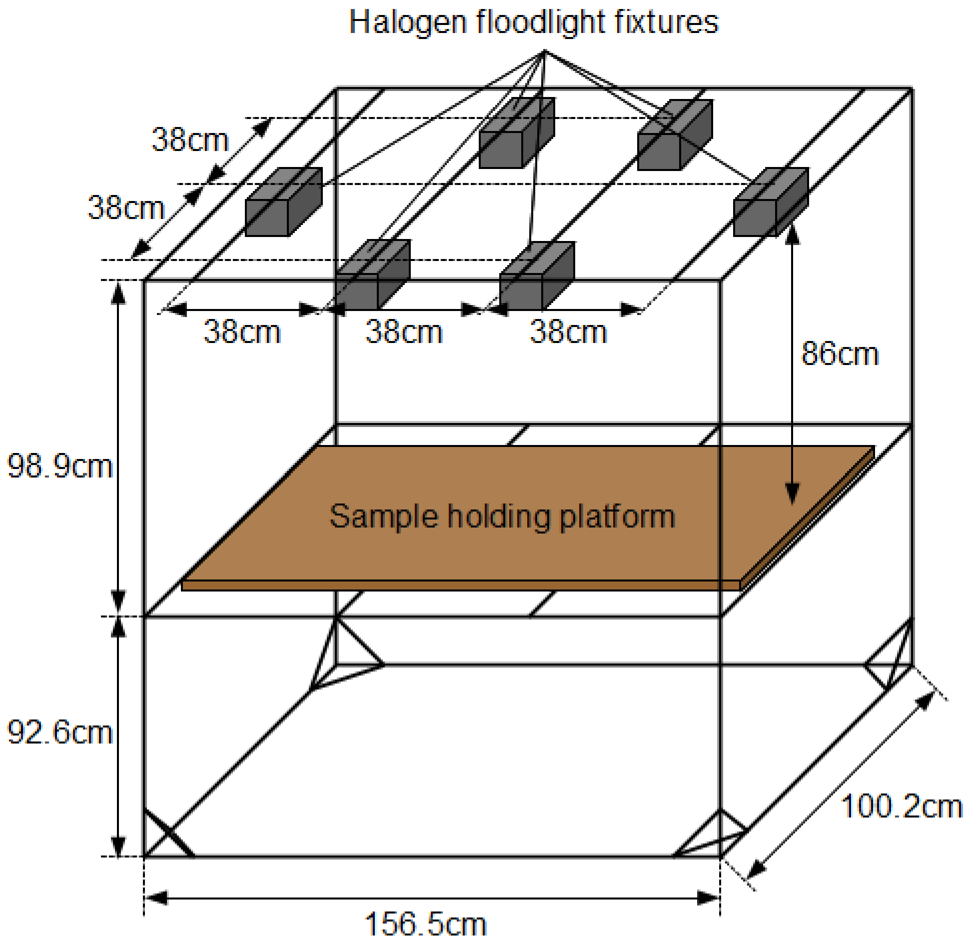

Figure 3.6: Light source with large illumination area constructed using halogen flood lights.

A light source with large illumination area and adjustable light intensity was built for the measurement of a large LSC sample. The lamp support structure, including the sample holding platform was built using slotted angle irons. Design and dimension of the lamp support structure is illustrated in Figure 3.6. Halogen flood lights were used as the light source and arranged as shown in Figure 3.7 to provide a large illumination area.

Figure 3.7: Light source with large illumination area constructed using halogen flood lights.

Figure 3.8: A variable auto-transformer or Variac.

The light intensity were controlled by a variable auto-transformer (commonly known as Variac, as shown in Figure 3.8) which adjust the voltage for the light sources. All the 6 halogen lights are connected in parallel, with input voltage of 240V and total rated operating power of 2400W. Metal casings of all halogen flood light fixtures as well as the casing of the variable auto-transformer was grounded. A 13-Ampere fuse was also included for over-current protection of the lamps.

3.5.1 Relative Irradiance Spectrum of the Light Source

Relative irradiance spectrum of the light source were measured using Ocean Optics USB4000 spectrometer with relative irradiance calibrated using the Mikropack HL-2000-HP-FHSA halogen light source, a blackbody source having a known color temperature of 3000K. Measurements were taken using a cosine corrector connected to the spectrometer using a fiber optic, on the sample holding platform at 6 different points in the middle, as shown in Figure 3.9. The relative irradiance measurement result is shown in Figure 3.10.

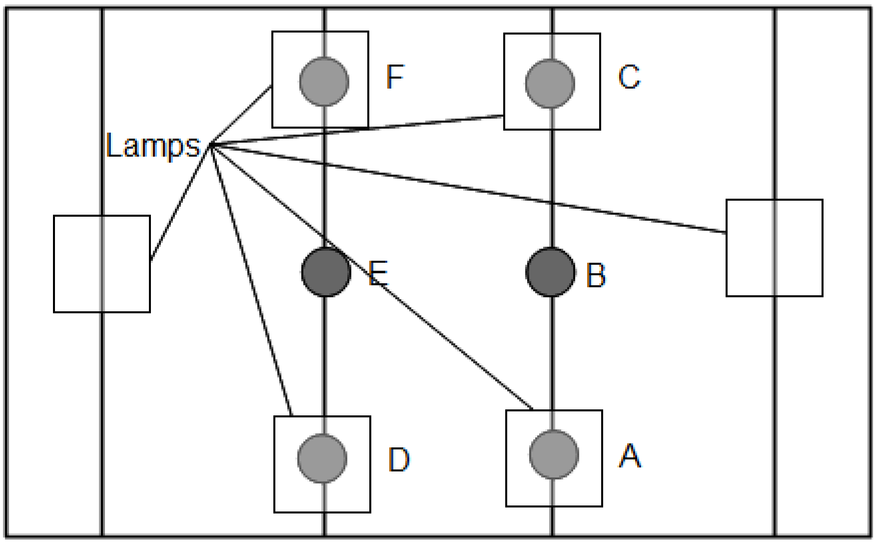

Figure 3.9: Measurement points for relative irradiance measurement of the light source on the sample holding platform.

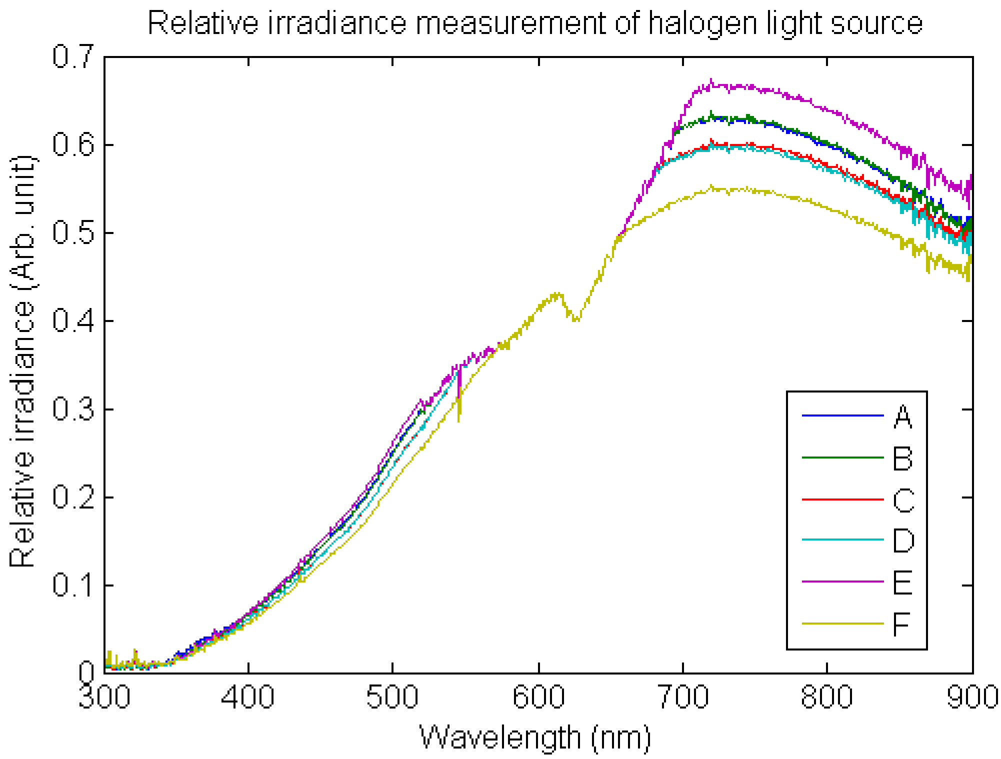

Figure 3.10: Relative irradiance measurement of the light source at different point on the sample holding platform.

The measured relative irradiance spectrum can be modeled by blackbody spectrum since the tungsten halogen light is an incandescent light. The blackbody radiance spectrum is given by,

$$L_B(\lambda) = \frac{2hc^2}{\lambda^5}\left[\exp\left(\frac{hc}{\lambda kT}\right) - 1\right]^{-1} \tag{3.1}$$

The irradiance spectrum of light received by the cosine corrector is calculated by multiplying Eq. 3.1 by the solid angle the light source was subtended by, together with the constant term $2hc^2$ and an arbitrary constant to account for the unknown irradiance magnitude in relative irradiance measurement, they can be lumped into a constant term to be curve-fitted.

However, the constant term did not fit well with the measured spectrum because the reflection from back reflector and transmission at the cover glass on the fixture altered the shape of the light spectrum. Since they are wavelength dependence, the constant term is replaced by a 2 degree polynomial function with 3 coefficients to be determined by curve fitting. The temperature in the blackbody radiance spectrum is another coefficients to be determined by curve fitting. Robust non-linear least square fitting was used for the curve fitting.

The best-fit irradiance function is,

$$E_{fit}(\lambda) = F_1(\lambda)\frac{1}{\lambda^5}\left[\exp\left(\frac{hc}{\lambda kT}\right)-1\right]^{-1} \tag{3.2}$$

Where,

$$F_1(\lambda) = A + B\lambda + C\lambda^2 \tag{3.3}$$

The values of the coefficients from the curve-fitting are A=-5.78e-29, B=2.666e-22, C=-1.916e-16, T=3500. Goodness of fit is r^2=0.9993, SSE=0.143. The irradiance function together with the average irradiance spectrum used for the curve fitting is shown in Figure 3.11.

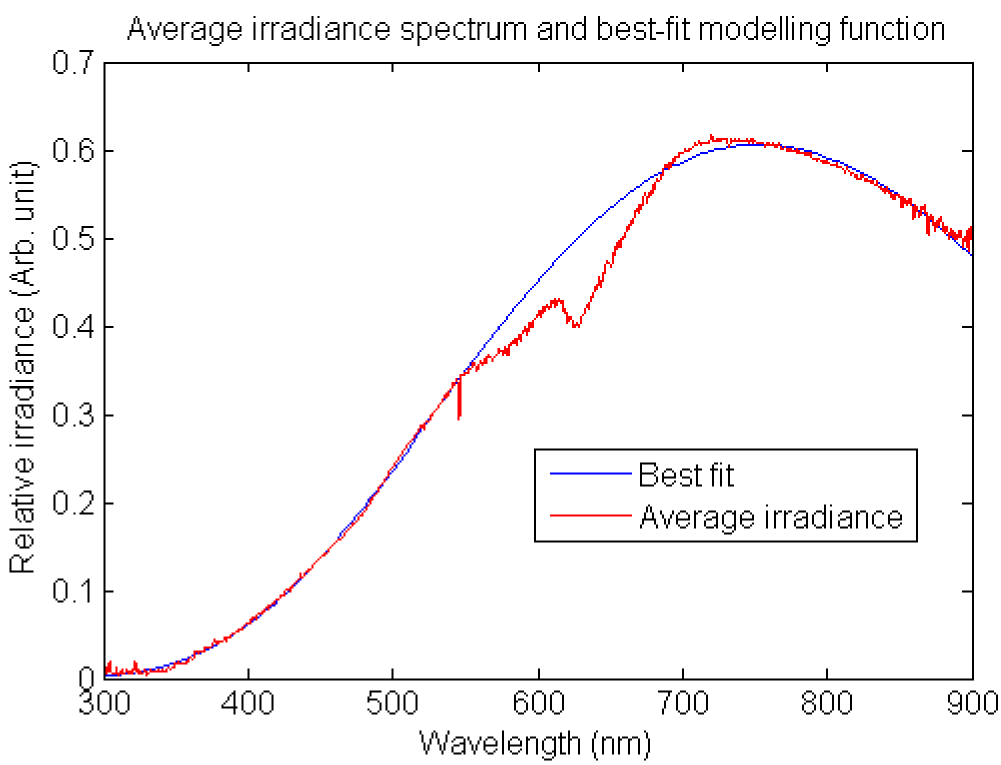

Figure 3.11: Average of the relative irradiance measurement and the best-fit modelling function for the light source.

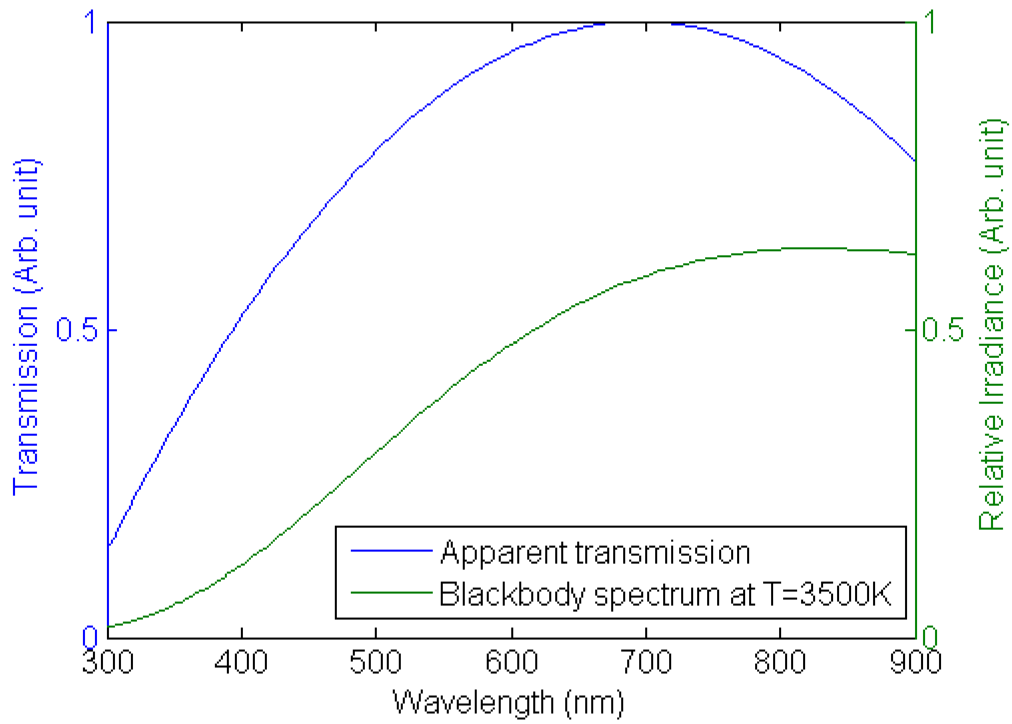

Figure 3.12: The shape of the blackbody radiation at T=3500K and normalized curve-fitted apparent transmission of the floodlight fixture.

The polynomial function $F_1(\lambda)$ represent the apparent transmission from the floodlight fixture, which is a combination effect of the back reflector and its glass transmission. The function normalized to have peak value of 1 and the shape of a blackbody spectrum at T=3500K is shown in Figure 3.12. The drop of apparent transmission in the apparent transmission can be explained by the UV filter effect from the cover glass of the fixture where the drop in the near infrared can be explained by the drop in spectral reflectance of aluminium back reflector in the near infrared region as shown in a publication (Hatch, 1984).

As a conclusion, the constructed light source can be used in simulation by modelling it with good accuracy using the function in Eq. 3.3. However, it was not used in the experiment in subsequent chapters due to its unstable light intensity over a long period of time, where LED light is found to be a better substitute due to its constant light intensity over a long period of time for the experiment on simulation model verification in Chapter 4.3.1.

3.6 Measurement on the LSC Sample

Short circuit current measurement on the solar cells attached to LSC edge was found to be lower than the short circuit current from the solar cells exposed directly under the light source. Light source constructed in the previous chapter was used in both cases. This is mainly because of the air-gap and cracks found in the interface between the solar cells and the LSC material, which causes the light to be reflected back to the LSC by total internal reflection before it reach the solar cells. Therefore full characterization of electrical behaviour (current-voltage curve and power-voltage curve, maximum power point, etc.) of the solar cells attached to LSC edge was not done.

Furthermore, comparison between the measurement of the large LSC sample in this chapter and the simulation result in Chapter 7 is not done because there are too many differences in both cases, especially the air-gap and cracks found in the interface between the solar cells and the LSC material, and uneven top surface for the real sample, in contrast to the ideal flat interface between solar cells and LSC material and mirror-like top surface for the sample in simulation.

CHAPTER 4

NEW HYBRID SIMULATION ALGORITHM FOR LSC

4.1 Mathematical Theory Behind the Hybrid Algorithm

Consider a ray from an arbitrary direction travelling inside the LSC as shown in Figure 4.1, where L_1 represent the incident light. Align the x direction to the direction of ray and set x=0 at the boundary for convenience.

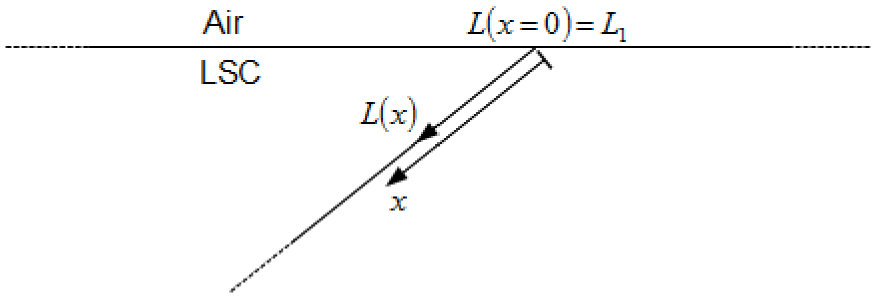

Figure 4.1: A ray travelling inside the LSC.

From the radiative transfer equation introduced in Chapter 2.2.4,

$$\frac{dL(x)}{dx} = -N\sigma L(x) + N\sigma L_s(x) \tag{4.1}$$

Rearrange Eq. 4.1,

$$\frac{d}{dx}L(x) + N\sigma L(x) = N\sigma L_s(x) \tag{4.2}$$

The term at the right hand side of Eq. 4.2 can be found using the thermodynamic two-flux model, which solve the spatially varying photon chemical potential in which the luminescent brightness and hence the source function $L_s(x)$ is dependent on.

Using the technique to solve the differential equation for linear time invariant system equation for continuous time system, where in this case the time is replaced by spatial variable x, input is replaced by $L_s(x)$ and output by

L(x), the output L(x) is the superposition (summation) of two components: trapped incident light (analogy of natural response) and dye emission (analogy of forced response) (Kani, 2010).

4.1.1 Trapped Incident Light

The trapped incident light is an analogy of natural response, which is solved by setting $L_s(x)=0$ (input equals to zero) and apply the initial condition $L(x=0)=L_1$. The differential equation therefore becomes,

$$\frac{dL(x)}{dx} = -N\sigma L(x) \tag{4.3}$$

Together with the incident light at the boundary, this is the case where the dye absorb but never emit light in the LSC. The solution of Eq. 4.3 is simply the incident light which trapped inside the LSC and eventually travel to the edge and received by the solar cell.

Therefore it can be simulated using existing ray-tracing software that include a material to attenuate the ray intensity from an input parameters of absorption coefficient of the material. The LSC absorption coefficient in this case, $\alpha=N\sigma$ is the total absorption of the dye and the host material.

4.1.2 Dye Emission

Dye emission is an analogy of forced response, which is solved by setting the incident light (initial condition) equals to zero, i.e. $L(x=0)=0$. Then the green function (analogy of impulse response) should be found and multiplied to source function $L_s(x)$ (the input function). The green function and hence the solution was found by authors in the publication (Chatten *et al.*, 2004) where the horizontal escape flux in the 3D flux thermodynamic model, contributed purely from dye emission which travel toward the edge and received by the solar cell, is actually the dye emission term in our case.

4.1.3 Total Spectral Irradiance

Spectral radiance of the ray in the LSC, L(x) is an analogy of the total system response, which is simply the superposition or summation of trapped incident light and dye emission calculated from ray-tracing model and thermodynamic model respectively.

The total spectral irradiance at the LSC edge is the integration of spectral radiance with respect to the solid angle of a hemisphere on the LSC edge. For dye emission it is simply the horizontal flux escape from the boundary in thermodynamic model. However, in the case of trapped incident light, the integration should be done by converting it into a summation of discrete values of spectral radiance simulated by the ray-tracing software. Similar to the spectral radiance, the total spectral irradiance at the LSC edge is the summation of the trapped incident light simulated by the ray-tracing model and the dye emission simulated by the thermodynamic model.

4.2 Hybrid Algorithm

In this hybrid simulation approach, the two-flux thermodynamic model as developed by the authors in the publication (Chatten *et al.*, 2006) is modified and used in conjunction with the open source ray-tracing program, namely Radiance (Larson and Shakespeare, 1998). The input parameters required by the modified two-flux thermodynamic model are LSC dimension, reflective index, luminescent dye concentration, absorption cross-section, luminescent quantum efficiency and temperature. Then the input parameters required by the ray-tracing program are light source radiation spectrum and profile, LSC dimension, reflective index and absorption coefficient. The ray-tracing model simulates the average irradiation spectrum received by the photovoltaic cells, without considering the contribution from the dye emission. It also simulates the average irradiation spectrum as seen by the dye particles at the top surface of LSC, which is then passed to the thermodynamic model. The thermodynamic model simulates the average irradiation spectrum contributed by the dye emission. The average irradiation spectra from the two models are then combined to provide the overall irradiation output spectrum. This spectrum is considered as the incident light to the photovoltaic cells at the edge of LSC. Figure 4.2 is the flow chart of the simulation algorithm.

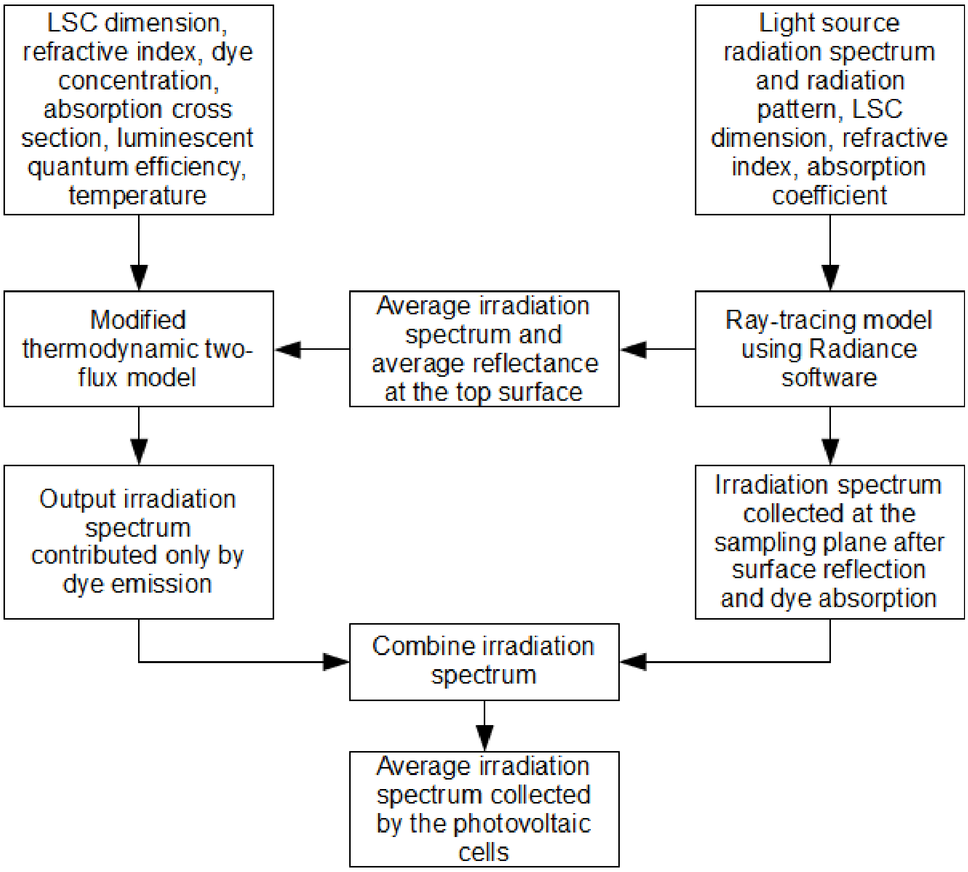

Figure 4.2: Hybrid simulation program flow chart.

4.2.1 Dye Emission from Thermodynamic Model

The two-flux thermodynamic model (Chatten *et al.*, 2004; Chatten *et al.*, 2006) is used here. In this model, the radiation transfer equation is solved for the simplified case of infinite parallel plane. The dye emission is modeled by introducing the photon chemical potential (a function of position in the LSC) into the Planck's distribution function in the radiation transfer equation for an absorbing, emitting, non-scattering medium. Radiative transfer equation is the fundamental description of the variation of radiation intensity in a medium in response to the absorption and emission of the medium (Chandrasekhar, 1950). The solution of radiation transfer equation together with the equation specifying the principle of detailed balance as shown in Eq.

4.4, form a set of simultaneous equations which cannot be solved analytically. However numerical solution can be obtained using Newton's method.

The principle of detailed balance

$$\int \sigma_e(v)[I_E + I_T]dv = \int \frac{\sigma_e(v)}{Q_e} B(v)dv \tag{4.4}$$

Where,

ν = Radiation frequency (Hz),

σ_e = Absorption cross section of dye (m^2),

Q_e = Luminescent quantum efficiency,

B = Luminescent brightness (photons s^{-1} m^{-2} Hz^{-1}),

I_E = Escaped flux (photons s^{-1} m^{-2} Hz^{-1}),

I_T = Trapped flux (photons s^{-1} m^{-2} Hz^{-1}).

The left hand side of eq. 4.4 states that the total number of photons contributes to the net upward transition rate of electrons in the dye particles, which is calculated by multiplying the total photon flux received by the dye particles with the absorption cross section of the dye particles.

The right hand side of eq. 4.4 states that the total number of emitting photons divided by the luminescent quantum efficiency contributes to the net downward transition rate of electrons in the dye particles. The total number of emitting photons is calculated by multiplying the luminescent brightness of the dye particles with the absorption cross section of the dye particles. Eq. 4.4 concludes that the net upward transition rate is equal to the net downward transition rate in the dye particles.

An emitting flux from the dye of LSC can escape to the atmosphere or bounce back from the air to LSC boundary depending on whether the existing flux is within the optical escape cone or not. If the existing flux is within the escape cone, then the flux escapes to the atmosphere. The escaped flux is the average photon flux escaping to the atmosphere. The trapped flux is the average photon flux being trapped inside LSC as illustrated in Figure 4.3.

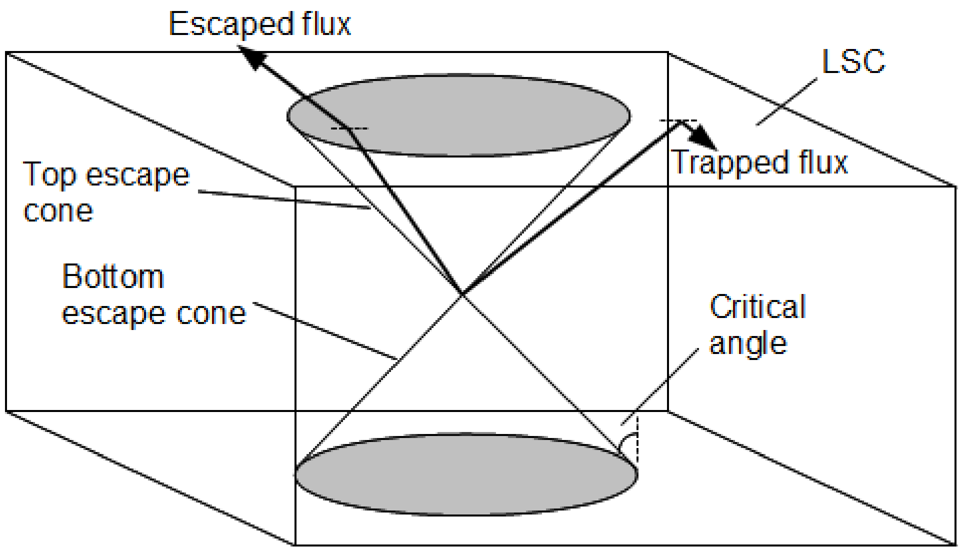

Figure 4.3: Escaped flux and trapped flux.

The dye emission is modeled by introducing photon chemical potential in Eq. 4.5.

$$B(\nu) = \frac{8\pi n^2 \nu^2}{c^2} \frac{1}{e^{[h\nu - \mu]\beta} - 1} \tag{4.5}$$

Where,

μ = Photon chemical potential (J),

β = 1/kT (J^{-1}),

k = Boltzmann constant (J K^{-1}),

T = Temperature (K),

q = Elementary charge constant (C).

The thermodynamic two-flux model introduced by Chatten et al. (Chatten *et al.*, 2006) is used to perform the simulation of dye emission in one dimension. The horizontal flux propagating toward the edge is calculated using the solution of horizontal flux in 3D thermodynamic model (Chatten *et al.*, 2004). In this model, it was assumed that the photon flux escaped from the horizontal surfaces is negligible as compared to the escaped flux from the top and bottom surfaces, so two-flux model was used instead of the complete 3D model to reduce the simulation time.

The two-flux thermodynamic model by Chatten et al. (Chatten *et al.*, 2001) solves the radiative transfer equation (Chandrasekhar, 1950) in one dimensional plane parallel case. The differential equation is split into four coupled equations depending on the polar angle, which are the trapped and escape flux propagating upward, and trapped and escape flux propagating downward. By solving the radiative transfer equation and applying the boundary condition, one would obtain the following solutions.

Solution for the trapped flux

$$\begin{aligned} I_T(z) = {} & \frac{\Omega_2 \lambda_{Te} \cosh(\lambda_{Ta} z)}{4\pi \sinh(\lambda_{Ta} D)} \\ & \times \int_0^D \cosh[\lambda_{Ta}(D - z')] B(z') dz' \\ & - \frac{\Omega_2 \lambda_{Te}}{4\pi} \int_0^z \sinh[\lambda_{Ta}(z - z')] B(z') dz' \end{aligned} \tag{4.6}$$

Solution for the escaped flux

$$I_E(z) = \frac{2I_1 \sinh(\alpha_T/2)\cosh[\lambda_{Ea}(D-z)+\alpha_B/2]}{\sinh(\lambda_{Ea}D+\alpha_{TB})}$$
$$+\frac{\Omega_1\lambda_{Ee}\cosh(\lambda_{Ea}z+\alpha_T/2)}{4\pi\sinh(\lambda_{Ea}D+\alpha_{TB})}$$
$$\times\int_0^D \cosh[\lambda_{Ea}(D-z')+\alpha_B/2]B(z')dz' \tag{4.7}$$
$$-\frac{\Omega_1\lambda_{Ee}}{4\pi}\int_0^z \sinh[\lambda_{Ea}(z-z')]B(z')dz'$$

Where the symbols in Eq. 4.6 and Eq. 4.7 are

$$\lambda_{Te} = \frac{2N\sigma_e}{\cos(\theta_C)} \tag{4.8}$$

$$\lambda_{Ta} = \frac{2N\sigma_a}{\cos(\theta_C)} \tag{4.9}$$

$$\lambda_{Ee} = \frac{N\sigma_e}{\cos^2(\theta_C/2)} \tag{4.10}$$

$$\lambda_{Ea} = \frac{N\sigma_a}{\cos^2(\theta_C/2)} \tag{4.11}$$

$$\Omega_1 = 4\pi(1-\cos\theta_C) \tag{4.12}$$

$$\Omega_2 = 4\pi\cos\theta_C \tag{4.13}$$

$$\alpha_T = -\ln(R_T) \tag{4.14}$$

$$\alpha_B = -\ln(R_B) \tag{4.15}$$

$$\alpha_{TB} = \frac{\alpha_T+\alpha_B}{2} \tag{4.16}$$

Ω_1 is the solid angle extended by two escape cones in steradians and Ω_2 is the solid angle for trapped flux in steradians. σ_e is the absorption cross section of dye in m^2, σ_a is the absorption cross section of sample in m^2.

The value of R_B is the reflection coefficient of unpolarized light averaged over the solid angle of the bottom escape cone, and is calculated by

$$R_B = \frac{1}{\Omega_C}\int_0^{2\pi}\int_0^{\theta_C} R_{bottom}(\theta)\sin\theta d\theta d\varphi \tag{4.17}$$

Where,

$$\Omega_C = 2\pi(1-\cos\theta_C) \tag{4.18}$$

$$R(\theta)=\frac{1}{2}\left[\left(\frac{\sin(\theta-\theta_t)}{\sin(\theta+\theta_t)}\right)^2+\left(\frac{\tan(\theta-\theta_t)}{\tan(\theta+\theta_t)}\right)^2\right] \tag{4.19}$$

$$\theta_t=\sin^{-1}\left[\frac{n}{n_{air}}\sin\theta\right] \tag{4.20}$$

Ω_C is the solid angle extended by one escape cone in steradians, n_{air} is the refractive index of air and n is the refractive index of the LSC. R_T is the reflection coefficient over the top escape cone and is calculated in the same way as R_B. In the case where mirror is attached to the bottom surface of LSC, then $R_B = 1$.

From 3D thermodynamic model (Chatten *et al.*, 2006), the horizontal photon flux escape from the edge surface at x=0 is

$$\begin{aligned}I_{Left}(y,z)=&\frac{\Omega_C\lambda_{Ee}}{2\pi}\frac{\sinh(\alpha_L/2)}{\sinh(\lambda_{Ea}L+\alpha_{LR})}\\&\times\int_0^L\cosh[\lambda_{Ea}(L-x')+\alpha_R/2]B(z)dx'\end{aligned} \tag{4.21}$$

Since we are using two-flux model to calculate the dye emission, B is a function of z only. The equation can be further simplified to

$$\begin{aligned}I_{Left}(y,z)=&\frac{\Omega_C\lambda_{Ee}}{2\pi}\frac{\sinh(\alpha_L/2)}{\sinh(\lambda_{Ea}L+\alpha_{LR})}\\&\times B(z)\int_0^L\cosh[\lambda_{Ea}(L-x')+\alpha_R/2]dx'\end{aligned} \tag{4.22}$$

$$\begin{aligned}I_{Left}(y,z)=&\frac{\Omega_C\lambda_{Ee}}{2\pi\,\lambda_{Ea}}\frac{\sinh(\alpha_L/2)}{\sinh(\lambda_{Ea}L+\alpha_{LR})}\\&\times B(z)[\sinh(\lambda_{Ea}L+\alpha_R/2)-\sinh(\alpha_R/2)]\end{aligned} \tag{4.23}$$

Total optical power received by the surface can be found by integrating over the yz-plane,

$$\begin{aligned}I_{Left}=\int_0^D\int_0^W&\frac{\Omega_C\lambda_{Ee}}{2\pi\,\lambda_{Ea}}\frac{\sinh(\alpha_L/2)}{\sinh(\lambda_{Ea}L+\alpha_{LR})}B(z')\\&\times[\sinh(\lambda_{Ea}L+\alpha_R/2)-\sinh(\alpha_R/2)]dy'dz'\end{aligned} \tag{4.24}$$

$$
\begin{aligned}
I_{Left} = {} & \frac{\Omega_C \lambda_{Ee}}{2\pi\,\lambda_{Ea}} \frac{\sinh(\alpha_L/2)}{\sinh(\lambda_{Ea} L + \alpha_{LR})} \\
& \times [\sinh(\lambda_{Ea} L + \alpha_R/2) - \sinh(\alpha_R/2)] \\
& \times \int_0^W dy' \int_0^D B(z')dz'
\end{aligned}
\tag{4.25}
$$

Therefore, the average irradiation spectrum escape from the left surface is

$$
I_{Left(average)}(\nu) = \frac{I_L}{WD} \tag{4.26}
$$

$$
\begin{aligned}
I_{Left(average)} = {} & \frac{\Omega_C \lambda_{Ee}}{2\pi D\,\lambda_{Ea}} \frac{\sinh(\alpha_L/2)}{\sinh(\lambda_{Ea} L + \alpha_{LR})} \\
& \times [\sinh(\lambda_{Ea} L + \alpha_R/2) - \sinh(\alpha_R/2)] \\
& \times \int_0^D B(\nu, z')dz'
\end{aligned}
\tag{4.27}
$$

Where,

$$
\alpha_L = -\ln(R_L) \tag{4.28}
$$

$$
\alpha_R = -\ln(R_R) \tag{4.29}
$$

$$
\alpha_{LR} = \frac{\alpha_L + \alpha_R}{2} \tag{4.30}
$$

R_L and R_R are calculated in the same way as R_B. For the case where mirror is attached to the opposite edge of the photovoltaic cells, $R_R = 1$.

The escape flux from the output of thermodynamic model is in the domain of frequency, which can be converted to photon flux in the domain of wavelength by

$$
\Phi_{thermo}(\lambda) = -I_{Laverage}(\nu)\frac{c}{\nu^2} \tag{4.31}
$$

The negative sign is not used in the actual calculation, since it merely indicates that the order of integration limit is changed from (ν_1,ν_2) to (λ_2, λ_1), where ν_1=c/λ_1 and ν_2=c/λ_2.

If $\nu_1<\nu_2$ and since c is always positive, it must be the case where $\lambda_1>\lambda_2$, then

$$\int_{\nu_1}^{\nu_2} d\nu = \int_{\lambda_1}^{\lambda_2} d\lambda = -\int_{\lambda_2}^{\lambda_1} d\lambda \tag{4.32}$$

The smaller frequency in thermodynamic model is always used as the lower limit of integration, but in ray tracing and solar cell model the smaller wavelength is always used as the lower limit of integration. Therefore the change in the order of integration limit while changing the domain of integration from frequency to wavelength introduces a negative in the equation, which cancels out the negative sign in Eq. 4.31.

Similarly, the incident spectrum obtained from sampling using ray tracing can be converted to frequency domain by

$$\begin{aligned} I_1(\nu) &= -E_{average}(\lambda)\left(\frac{\lambda}{hc}\right)\left(\frac{c}{\lambda^2}\right) \\ &= -E_{average}(\lambda)\left(\frac{1}{h\lambda}\right) \end{aligned} \tag{4.33}$$

Calculation details of two-flux model for dye emission and that of horizontal flux is outlined in previous paragraphs. Eq. 4.4, Eq. 4.5 together with Eq. 4.6 and Eq. 4.7 are used to solve the photon chemical potential numerically using Newton method. Eq. 4.21 is used to calculate the horizontal escaped flux from the edge as represented by $\Phi_{thermo}(\lambda)$. Figure 4.4 shows the flow chart of the thermodynamic modeling. The material parameters are assumed to be constant along z-direction.

The photon chemical potential is one of the parameters used in the thermodynamic model to determine the dye emission (Chatten *et al.*, 2006). Therefore it is dependent of x, y and z directions. However, due to the uniform incident light distribution across the LSC top surface, the dye emission is constant along x and y directions, and varies only along z direction. Therefore, the photon chemical potential is a function of z direction only.

Up to date, correlation between the photon chemical potential and the material parameters is not apparent in any literature. Therefore, it is assumed that the material parameters are constant, regardless of the chemical potential. The iterative correction of photon chemical potential does not affect the input material parameters in the simulation model.

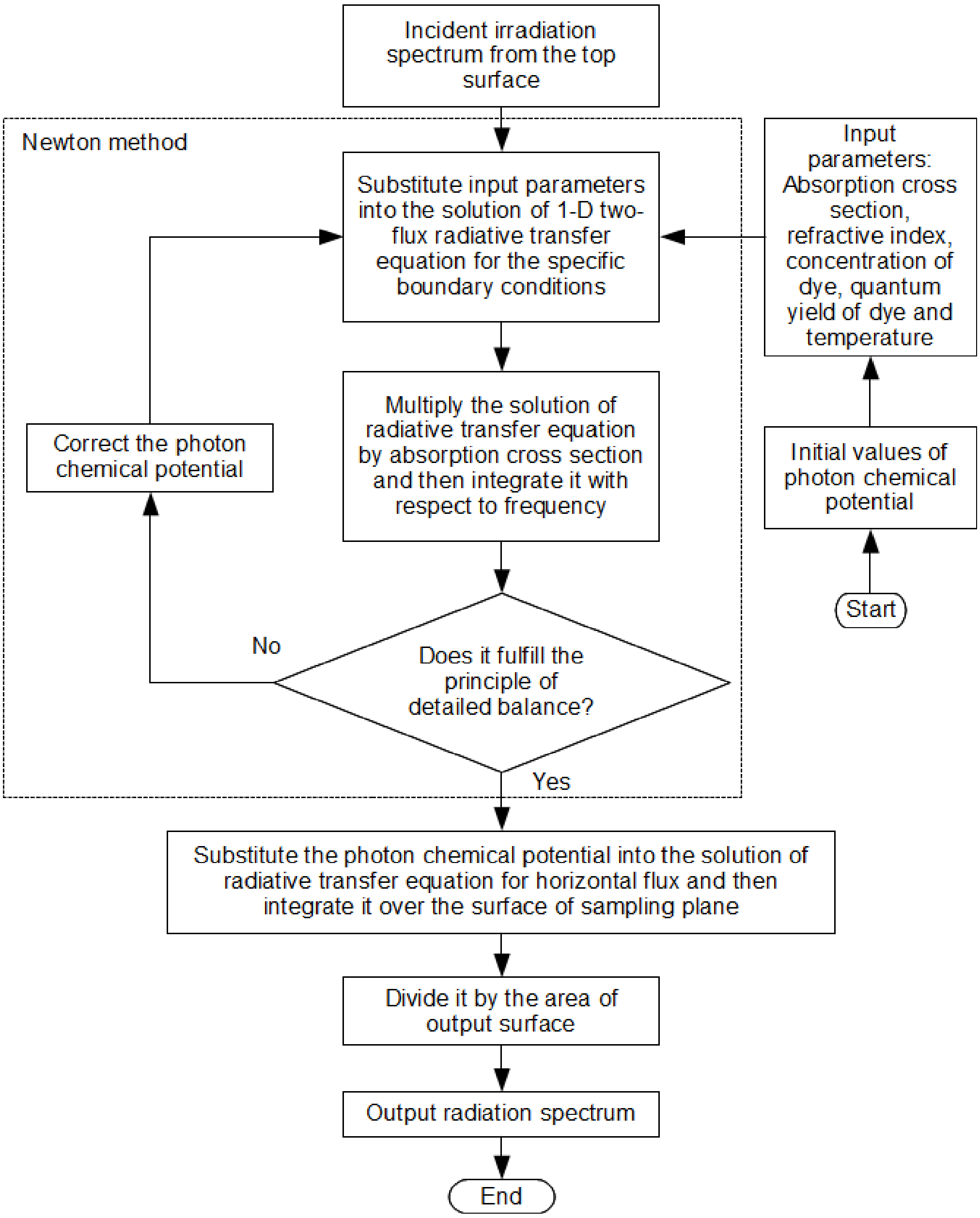

Figure 4.4: Flow chart of thermodynamic model.

4.2.2 Trapped Incident light from Ray-tracing Model

The open source ray-tracing program "Radiance" is used in the ray tracing model of the hybrid algorithm (Larson and Shakespeare, 1998). A ray travels from a light source to its final destination. Forward ray-tracing is a method that traces the ray from the light source to the final destination which is different from backward ray-tracing whereby the ray is traced backwards from the final destination to the light source.

The “Radiance” software uses light-backward ray-tracing method to trace light from a point of interest into the scene and back to the light sources. Its built-in function “rtrace” can trace light from the point along a specific direction and output the radiant intensity for that direction. The unit of the radiant intensity is W m^{-2} sr^{-1}. The total radiant intensity (irradiance) at the point is calculated by integrating all the light intensities arriving at that point from all the directions. The main objective of using Radiance is to determine the average irradiation across the edge of LSC where solar cells are attached to.

A Linux Shell script was written which executes the “rtrace” program in Radiance to perform the ray tracing. The program will then trace lights from a specific direction at a point with a particular wavelength each time when the program is called.

The model of LSC is created in a text file called scene description file where the wavelength dependent variables and the parameters of LSC are defined. Those wavelength dependent variables are incident light intensity, refractive index of LSC and extinction coefficient of LSC. The material properties, such as refractive index and extinction coefficient, are assumed to be constant along x, y and z directions. The scene description file for a simple rectangle structure of LSC as shown in Figure 4.5 is given in Figure 4.6. To include the absorption of the material in LSC, a mist type material is created on the LSC surfaces to model the dye's wavelength dependent absorption.

The software can handle both Lambertian and specular surfaces. All the mirror surfaces were modeled as specular surfaces. The reflections from the LSC surfaces are also specular reflections. All other reflective surfaces in the simulation case studies have the properties between perfect Lambertian and perfect specular. The reflection model used in the software is physically based and the detail of this model can be found in a publication (Ward, 1992).

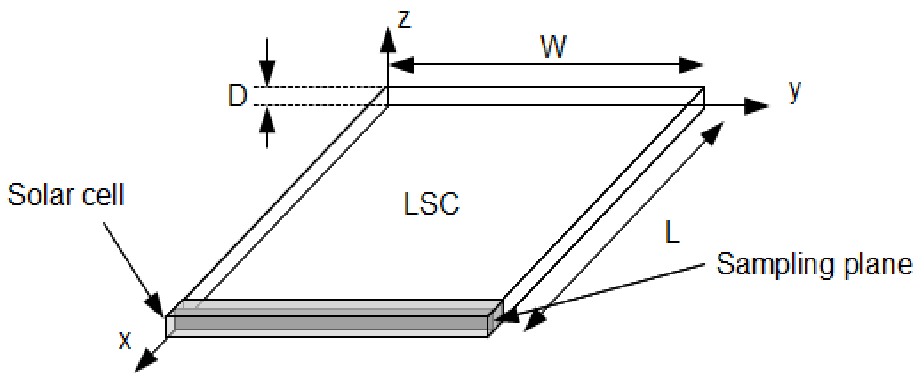

Figure 4.5: Dimension of LSC in ray-tracing model.

Where

L = Length of the LSC (m),

W = Width of the LSC (m),

D = Depth/thickness of the LSC (m).

```
# scene description for LSC with arbitrary parameters.
# the red color ray is treated as monochromatic ray with a specific wavelength,
# therefore only red color parameters are defined.

# define a dielectric type surface with refractive index = 1.58.
void dielectric matrixmat
0
0
5 1 0 0 1.58 0

# create a box extending from the origin to (0.1,0.05,0.005) (in meters).
!genbox matrixmat lsc 0.1 0.05 0.005

# define a mist type material with extinction coefficient = 50, albedo = 0.
void mist lscmat
0
0
6 50 0 0 0 0 0

# create a box extending from the origin to (0.099998,0.049998,0.004998) (in meters).
# transform the box by translating it by 0.000001 to x-direction,
# then 0.000001 to y-direction, and 0.000001 to z-direction.
!genbox lscmat lscabs 0.099998 0.049998 0.004998 | xform -t 0.000001 0.000001 0.000001
```

Figure 4.6: Scene description file for the rectangle structure of LSC.

Then the function "rtrace" is called to perform the ray tracing for each wavelength at a particular point of the sampling plane with all the directions. This is repeated for all the specified locations across the sampling plane and all wavelengths ranging from 300 to 800nm. The irradiance values calculated for the specified locations on the sampling plane are then averaged over the total surface area to give the average irradiance output $E_{average}$. The discrete ordinate method used by Mishra et al. (Mishra *et al.*, 2006) is employed in the algorithm to determine the integration of radiance intensity with respect to solid angle over a hemisphere. The calculation details are shown in following paragraphs. Figure 4.7 shows the algorithm for executing the ray tracing modeling. A maximum of 30 reflections are considered in the simulation case studies.

The radiant power dP_{rad} illuminating an infinitesimal area dA at a position r on the solar cell's surface over an infinitesimal solid angle $d\Omega$, having an angle θ measured from the surface normal is

$$d^2P_{rad}(r) = L(\theta,\phi)\cos\theta d\Omega dA \tag{4.34}$$

Where,

L(θ,ϕ) = Radiance (radiant power per solid angle per unit projected area) ($W\ m^{-2}\ sr^{-1}$),

θ = Polar angle measured from the surface normal (rad),

ϕ = Azimuthal angle measured about the surface normal (rad),

Ω = Solid angle (sr),

r = Position, r(x,y,z) (m).

Therefore the irradiance at r can be found by integrating Eq. 4.34 over a hemisphere

$$E(r) = \frac{dP_{rad}(r)}{dA} = \int_{\Omega=2\pi} L(\theta,\phi)\cos\theta d\Omega \tag{4.35}$$

Where,

E(r) = Irradiance illuminating the solar cell's surface ($W\ m^{-2}$).

The integration in Eq. 4.35 can be approximated by

$$E(r) = \int_{\Omega=2\pi} L(\theta,\phi)\cos\theta d\Omega \approx \sum_{m=1}^{M} W_L^m L^m \tag{4.36}$$

Assuming L^m is centered in a sub-solid angle $\Delta\Omega^m$ and is isotropic over $\Delta\Omega^m$ (Mishra *et al.*, 2006), then

$$\begin{aligned} E(r) &= \int_{\Omega=2\pi} L(\theta,\phi)\cos\theta d\Omega \\ &\approx L^1 \int_{\Omega=\Delta\Omega^1} \cos\theta d\Omega + L^2 \int_{\Omega=\Delta\Omega^2} \cos\theta d\Omega + \dots \\ &\quad + L^m \int_{\Omega=\Delta\Omega^m} \cos\theta d\Omega + \dots + L^M \int_{\Omega=\Delta\Omega^M} \cos\theta d\Omega \end{aligned} \tag{4.37}$$

And the right hand side of Eq. 4.36 is

$$\begin{aligned} \sum_{m=1}^{M} W_L^m L^m &= L^1 W_L^1 + I^2 W_L^2 + \dots \\ &\quad + L^m W_L^m + \dots + I^M W_L^M \end{aligned} \tag{4.38}$$

Comparing Eq. 4.37 and Eq. 4.38, the weight can be found by

$$\begin{aligned} W_L^m &= \int_{\Omega=\Delta\Omega^m} \cos\theta d\Omega = \int_{\phi^l-\frac{\Delta\phi^l}{2}}^{\phi^l+\frac{\Delta\phi^l}{2}} \int_{\theta^k-\frac{\Delta\theta^k}{2}}^{\theta^k+\frac{\Delta\theta^k}{2}} \cos\theta\sin\theta d\theta d\phi \\ &= \frac{1}{4}\left[-\cos\left(2\theta^k+\Delta\theta^k\right)+\cos\left(2\theta^k-\Delta\theta^k\right)\right]\Delta\phi^l \\ &= \left[\sin\theta^k\cos\theta^k\sin\left(\Delta\theta^k\right)\right]\Delta\phi^l \end{aligned} \tag{4.39}$$

The value of each L^m can be found by running the "rtrace" program to trace the ray passing through r(x,y,z) from a direction opposite to (θ^k,ϕ^l), k=1, 2, … , M_θ, l=1, 2, … , M_ϕ.

$$\theta^k = (2k-1)\frac{\pi/2}{2M_\theta}, \quad k = 1,2,\ldots,M_\theta \tag{4.40}$$

$$\Delta\theta^k = \frac{\pi/2}{M_\theta} \tag{4.41}$$

$$\phi^l = (2l-1)\frac{2\pi}{2M_\phi}, \quad l = 1,2,\ldots,M_\phi \tag{4.42}$$

$$\Delta\phi^l = \frac{2\pi}{M_\phi} \tag{4.43}$$

Where,

M_θ = Number of discrete θ,

M_ϕ = Number of discrete ϕ.

Eq. 4.44, Eq. 4.45 and Eq. 4.46 calculate a list of normalized direction vectors in Cartesian coordinate which cover a hemisphere on a plane with normal vector $\mathbf{N}=(0 \quad 0 \quad 1)^T$.

$$\Theta_x^m = \sin\theta^k\cos\varphi^l \tag{4.44}$$

$$\Theta_y^m = \sin\theta^k\sin\varphi^l \tag{4.45}$$

$$\Theta_z^m = \cos\theta^k \tag{4.46}$$

For the particular orientation of solar cell's surface as shown in Figure 4.5, all the direction vectors should be rotated by θ_{rot}=94° around the axis using Eq. 4.47, due to the different normal vector of the sampling plane.

$$\begin{bmatrix} \Theta_x^{m\prime} \\ \Theta_y^{m\prime} \\ \Theta_z^{m\prime} \end{bmatrix} = \begin{bmatrix} M_{11} & M_{12} & M_{13} \\ M_{21} & M_{22} & M_{23} \\ M_{31} & M_{32} & M_{33} \end{bmatrix}^{-1} \begin{bmatrix} N_1 \\ N_2 \\ N_3 \end{bmatrix} + \mathbf{B} \tag{4.47}$$

Where,

$$\mathbf{A} = \begin{bmatrix} 0 & -1 & 0 \end{bmatrix}^T \tag{4.48}$$

$$\theta_{rot} = 94° \tag{4.49}$$

$$\hat{\mathbf{A}} = \frac{\mathbf{A}}{\|\mathbf{A}\|} \tag{4.50}$$

$$\mathbf{B^m} = \left(\hat{\mathbf{A}} \cdot \mathbf{\Theta}^m\right)\hat{\mathbf{A}} \tag{4.51}$$

$$\mathbf{C^m} = \mathbf{\Theta^m} - \mathbf{B^m} \tag{4.52}$$

$$N_1 = 0 \tag{4.53}$$

$$N_2 = \left(\mathbf{C^m} \cdot \mathbf{C^m}\right)\cos(\theta_{rot}) \tag{4.54}$$

$$N_3 = \left(\mathbf{C^m} \cdot \mathbf{C^m}\right)\sin(\theta_{rot}) \tag{4.55}$$

$$\begin{bmatrix} M_{11} & M_{12} & M_{13} \end{bmatrix} = \left(\hat{\mathbf{A}}\right)^T \tag{4.56}$$

$$\begin{bmatrix} M_{21} & M_{22} & M_{23} \end{bmatrix} = \left(\mathbf{C^m}\right)^T \tag{4.57}$$

$$\begin{bmatrix} M_{31} & M_{32} & M_{33} \end{bmatrix} = \left(\hat{\mathbf{A}} \times \mathbf{C^m}\right)^T \tag{4.58}$$

The vector $\mathbf{\Theta}^m = \left(\Theta_x^m \quad \Theta_y^m \quad \Theta_z^m\right)^T$ is the original direction vector, $\mathbf{\Theta^m}' = \left(\Theta_x^{m\prime} \quad \Theta_y^{m\prime} \quad \Theta_z^{m\prime}\right)^T$ is the direction vector after the rotation, θ_{rot} is the rotation angle. Derivation of Eq. 4.47 is shown in Appendix A.

The irradiance at r(x,y,z) is approximated by the weighted sum in Eq. 4.36, where L^m is the radiance value returned by the rtrace program, and the weight W_L^m is calculated using Eq. 4.39.

$$E(r) \approx \sum_{m=1}^{M} W_L^m L^m\left(r, \mathbf{\Theta^m}'\right) \tag{4.59}$$

The total radiant power illuminating the solar cell's surface can be found by integrating the radiance at r over the surface area of the solar cell.

$$P_{rad(total)} = \int_{A_{sc}} E(r)dA \tag{4.60}$$

The integration in Eq. 4.60 can be approximated in a similar way by

$$P_{rad(total)} = \int_{A_{sc}} E(r)dA \approx \sum_{n=1}^{N} W_E^n E^n \tag{4.61}$$

Assuming E^n is centered in a small area ΔA^n and is constant over ΔA^n, then

$$\begin{aligned} P_{rad(total)} = \int_{A_{sc}} E(r)dA \approx E^1 \int_{\Delta A^1} dA + E^2 \int_{\Delta A^2} dA + \ldots \\ + E^n \int_{\Delta A^n} dA + \ldots + E^N \int_{\Delta A^N} dA \end{aligned} \tag{4.62}$$

The right hand side is

$$\begin{aligned} \sum_{n=1}^{N} W_E^n E^n = E^1 W_E^1 + E^2 W_E^2 + \ldots \\ + E^n W_E^n + \ldots + E^N W_E^N \end{aligned} \tag{4.63}$$

And the weights can be found by comparing Eq. 4.62 and Eq. 4.63.

$$W_E^n = \int_{\Delta A^n} dA = \int_{z^j - \frac{\Delta z^j}{2}}^{z^j + \frac{\Delta z^j}{2}} \int_{y^i - \frac{\Delta y^i}{2}}^{y^i + \frac{\Delta y^i}{2}} dydz = \Delta y^i \Delta z^j \tag{4.64}$$

The value of each E^n can be found by repeating the process that approximates E(r) at one point r(x,y,z) until the points covers every combination of (y^i,z^j), i=1, 2, … , M_y, j=1, 2, … , M_z.

$$y^i = (2i-1)\frac{W}{2M_y}, \quad i = 1,2,\ldots,M_y \tag{4.65}$$

$$\Delta y^i = \frac{W}{M_y} \tag{4.66}$$

$$z^j = (2j-1)\frac{D}{2M_z}, \quad j = 1,2,\ldots,M_z \tag{4.67}$$

$$\Delta z^j = \frac{D}{M_z} \tag{4.68}$$

Where,

M_y = Number of discrete points along y direction,

M_z = Number of discrete points along z direction.

The position vector $r^n = \begin{pmatrix} x^n & y^n & z^n \end{pmatrix}^T$ can be calculated from the list of (y^i,z^j) by

$$x^n = L + \delta x + \left(D - z^j\right)\tan\left(\theta_{tilt}\right) \tag{4.69}$$

$$y^n = y^i \tag{4.70}$$

$$z^n = z^j \tag{4.71}$$

Where δx is the small gap from the edge of LSC to the sampling plane. For the simulation in Section 4.0, δx=0.00055m, θ_{tilt}=4°.

The total irradiance is approximated by the weighted sum in Eq. 4.61, where the weight is calculated for the list of (y^i,z^j) using Eq. 4.64.

$$P_{rad(total)} \approx \sum_{n=1}^{N} W_E^n E^n\left(r^n\right) \tag{4.72}$$

The average irradiance collected by the sampling plane is

$$E_{average} = \frac{P_{rad(total)}}{WD} \tag{4.73}$$

The steps above evaluate the output irradiance at a single wavelength. To get the spectrum output they are repeated for all wavelength of interest. It is done by changing the radiance value of the incident light, refractive index of LSC, absorption coefficient of the mist type material (extinction coefficient with albedo equals to zero) and refractive index of solar cell for the particular wavelength and then repeating the steps above. The results in Section 5.0 were obtained using M_θ=630, M_φ=2520, M_y=1, M_z=20.

The output $E_{average}$ will be converted into photo flux by using the following equation.

$$\Phi_{rtrace}(\lambda) = E_{average}(\lambda)\frac{\lambda}{hc} \tag{4.74}$$

Where,

$\Phi_{rtrace}(\lambda)$ = The average spectral photon flux from ray-tracing model (photons s m^{-2} nm^{-1}),

$E_{average}(\lambda)$ = The average spectral irradiance (W m^{-2} nm^{-1}),

λ = Radiation wavelength (nm),

c = Speed of light in free space (m s^{-1}),

h = Planck constant (J s).

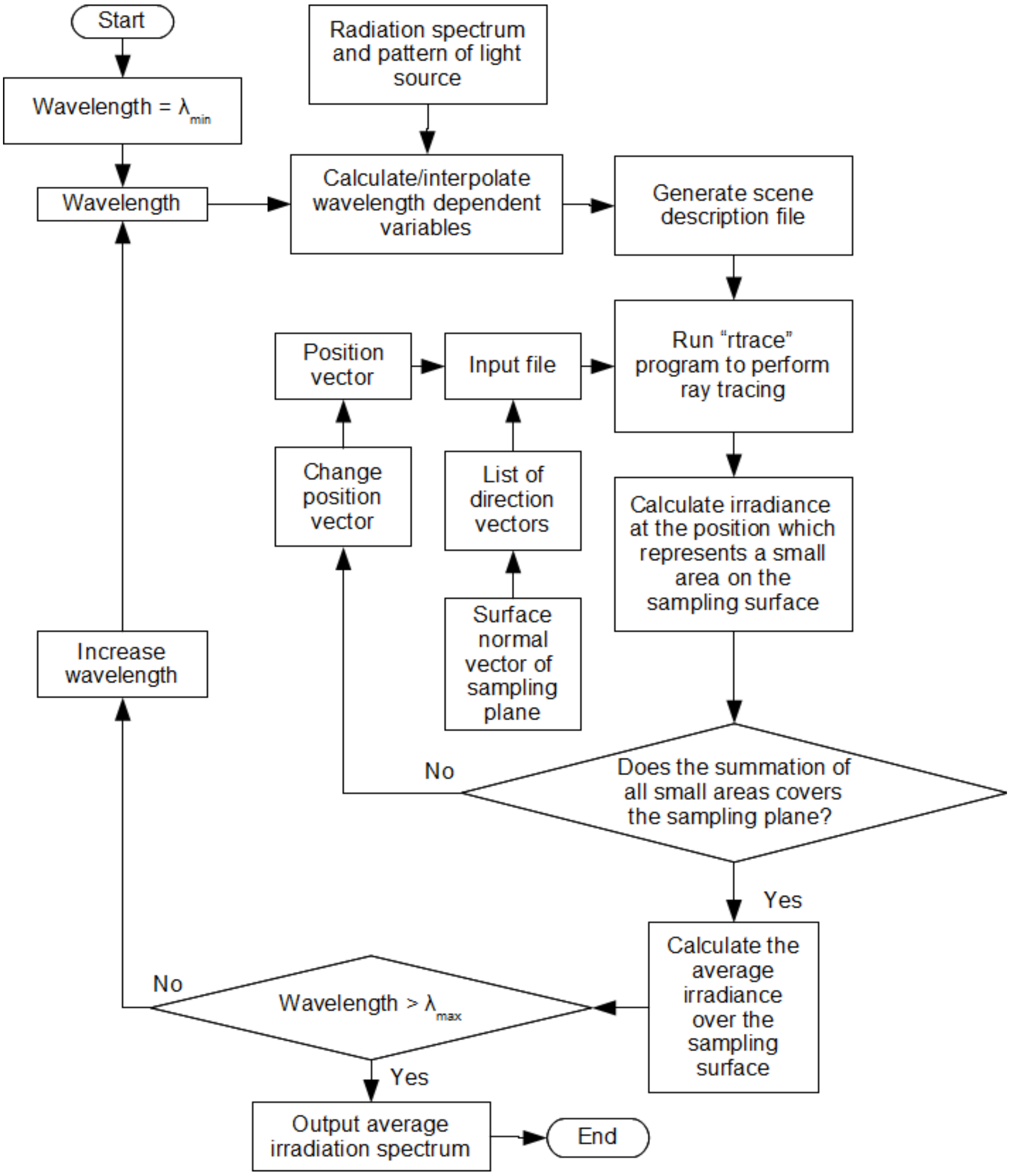

Figure 4.7: Flow chart of ray-tracing model.

The total photon flux is the summation of photon flux from ray tracing model and photon flux from thermodynamic model as given below.

$$\Phi(\lambda) = \Phi_{rtrace}(\lambda) + \Phi_{thermo}(\lambda) \tag{4.75}$$

4.3 Verification of Hybrid Algorithm

Verification of simulation result from the new hybrid algorithm was carried out by performing experimental measurement on a well prepared sample, then create a simulation case study for the experiment using the new algorithm and compare the result between simulation and experimental measurement.

4.3.1 Preparation of Sample

The LSC sample being used in the experiment is a 10cm x 5cm x 0.5cm unsaturated polyester (UP) with 5% methyl methacrylate (MMA) doped with 3.75×10^{-5}M Rhodamine 6G. The preparation steps of the LSC sample are similar to those described in Chapter 3.2.2 with some steps specially modified for constructing small LSC sample, including the use of centrifuge machine for degassing process and replacing the mirror mold by metal mold because mirrors in that small dimension are very hard to be cut into. Full detail of the preparation steps were described in a publication (Tan *et al.*, 2010).

4.3.2 Experimental Measurement

The experiment setup is shown in Figure 4.8. The white light emitting diode (LED) from a torch light was used as the light source, filtered by blue optical filter which consists of 6 layers of blue transparent plastic film. The filtered light source illuminated the LSC sample from a point at 5cm above the center of the LSC sample. Mirrors were put at the bottom and 3 edges except for the edge where the irradiance output was collected by a cosine corrector which was connected to a wavelength-and-radiometry-calibrated Avantes Spectrometer via a fiber optic. The reflective surfaces of the mirrors were covered by black paper except for the part in contact with the LSC sample.

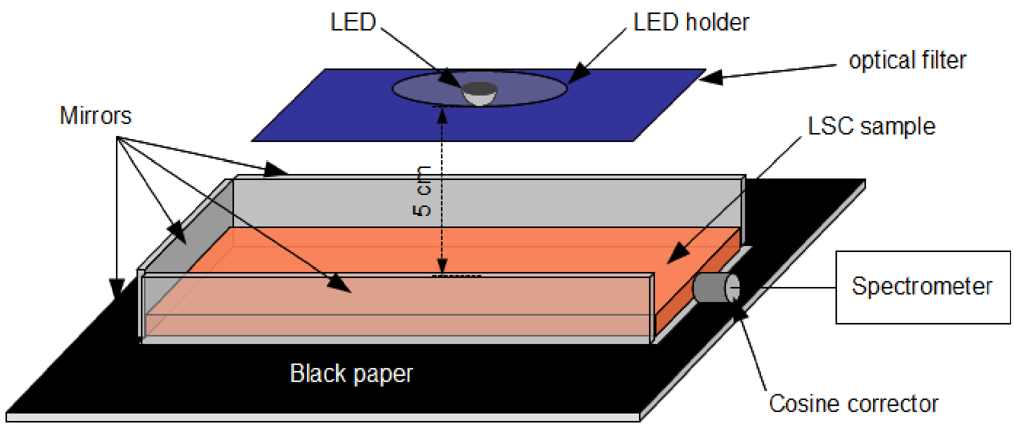

Figure 4.8: Experiment setup.

4.3.3 Simulation Input Parameters

The purpose of the experiment is to verify the solution obtained from the proposed simulation approach. Therefore the program was modified to introduce the effect of cosine corrector and the small air gap between the LSC edge surface and the cosine corrector diffuser surface. The cosine corrector was modeled as a perfect diffuser collecting light from 180 degree field of view. The simulation input parameters are listed in Table 4.1 together with the corresponding measured values.

Table 4.1. Simulation input parameters versus the actual measured values.

Property	Simulation input parameter	Measured value/spectrum
Dimension	10cm x 5cm x 0.5cm	9.8cm x 4.9cm x 0.5cm
Refractive index	1.58	1.57
Luminescent quantum efficiency	0.95 [1]	Not measured.
Concentration	3.75×10^{-5} mol/dm^3	3.75×10^{-5} mol/dm^3
Temperature	25 °C	Not measured.
Absorption cross section (dye)	Refer to Figure 4.9	Refer to Figure 4.9
Absorption cross section (sample)	Refer to Figure 4.10	Refer to Figure 4.10
Incident light	Refer to Figure 4.13	Refer to Figure 4.13

[1] Obtained from (Kubin and Fletcher, 1982).

The absorption cross-section of the dye (Rhodamine 6G) was measured from the mixture of UP resin, Rhodamine 6G and MMA in the same proportion as the one in the hardened LSC sample. The mixture was put inside a 1cm cuvette, with the mixture of UP resin and MMA as the reference solution. The absorbance was measured using a wavelength-calibrated Ocean Optics USB4000 spectrometer connected to the Ocean Optics CUV-ALL-UV cuvette holder, with the Mikropack HL-2000-HP-FHSA halogen light source connected to the cuvette holder at the opposite direction. The absorbance spectrum was then converted to absorption cross section spectrum, as shown in Figure 4.9.

The absorbance of the sample was measured by fixing the solid LSC sample vertically in between two Ocean-Optics-84-UV-25 collimating lens mounted on an optical table. The Mikropack HL-2000-HP-FHSA halogen light source was connected to one of the collimating lens, while another lens was connected to the Ocean Optics USB4000 spectrometer. No reference sample was prepared in this case since there was some difficulty in preparing an ideal well-polished flat plate sample of 5mm thickness for spectroscopic measurement. Therefore the reflection at the air-to-LSC boundary was ignored in the measurement. The absorbance spectrum was then converted to absorption cross section spectrum, as shown in Figure 4.10.

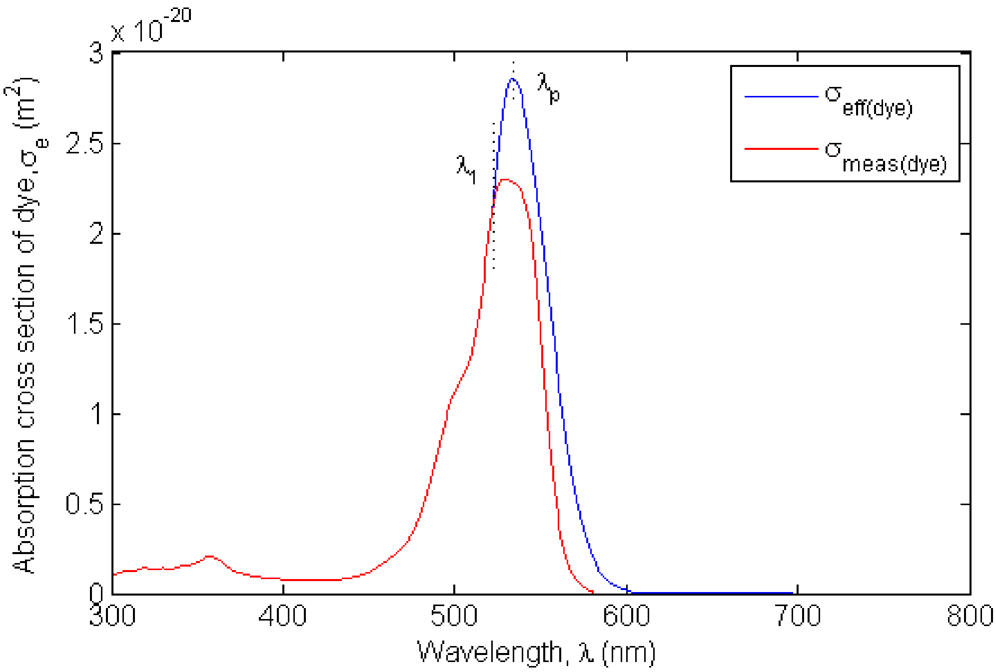

Figure 4.9: Dye absorption cross section.

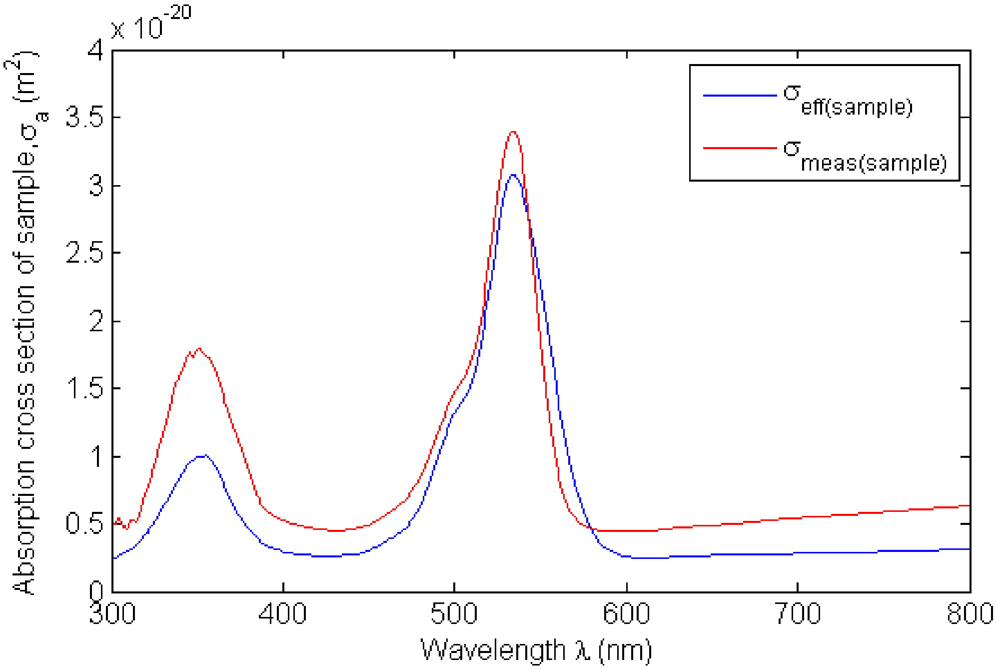

Figure 4.10: Sample absorption cross section.

The red lines in Figure 4.9 and Figure 4.10 represent the experimental data which is not the pure absorption cross sections of the dye and LSC plate because the data contains unwanted effects such as the reflectance and absorption of the cuvette, reflectance of the LSC surfaces and emission of the dye. As a result, the experimental data could not be used directly as the input data to the simulation model. Attempts were carried out to remove all the distortions from the measurement data by using analytical approach. In these attempts, all the distortions were measured and fed into the analytical equations in the hope that the effective absorption cross sections of the dyes and LSC plate could be determined. However, none of the analytical equations took into account all the unwanted effects correctly. In fact, the analytical equations became relatively complicated in the situation where the top and bottom surfaces of LSC were not perfectly uniform and flat. Therefore, it was decided to use empirical approach to determine the effective absorption cross sections of the dye and LSC plate.

Figure 4.11 describes the empirical approach used to find the effective absorption cross section of the dye. This absorption cross section spectrum, $\sigma_{meas(dye)}$, is used as the initial spectrum to be curve fitted. A Gaussian function and a cubic spline function are used to curve fit $\sigma_{meas(dye)}$. The result of the curve fitting $\sigma_{fit\_ini(dye)}$ is fed into the thermodynamic model to generate an emission spectrum with a peak wavelength of $\lambda_{em\_peak(sim)}$. It is noticed that the absorption cross section spectrum of the dye affects predominantly the wavelength of the peak. Therefore, $\lambda_{em\_peak(sim)}$ is used to compare with peak wavelength in measured emission spectrum $\lambda_{em\_peak(meas)}$. The difference between the two is used to adjust a constant, C_1. This new constant value is used in the Gaussian function in $\sigma_{fit(dye)}$ to produce a new absorption cross section spectrum which in turn is fed into the thermodynamic model. This adjustment process is repeated until the difference between $\lambda_{em\_peak(meas)}$ and $\lambda_{em\_peak(sim)}$ is less than a specified tolerance. The effective absorption cross section of the dye, $\sigma_{eff(dye)}$, is then determined.

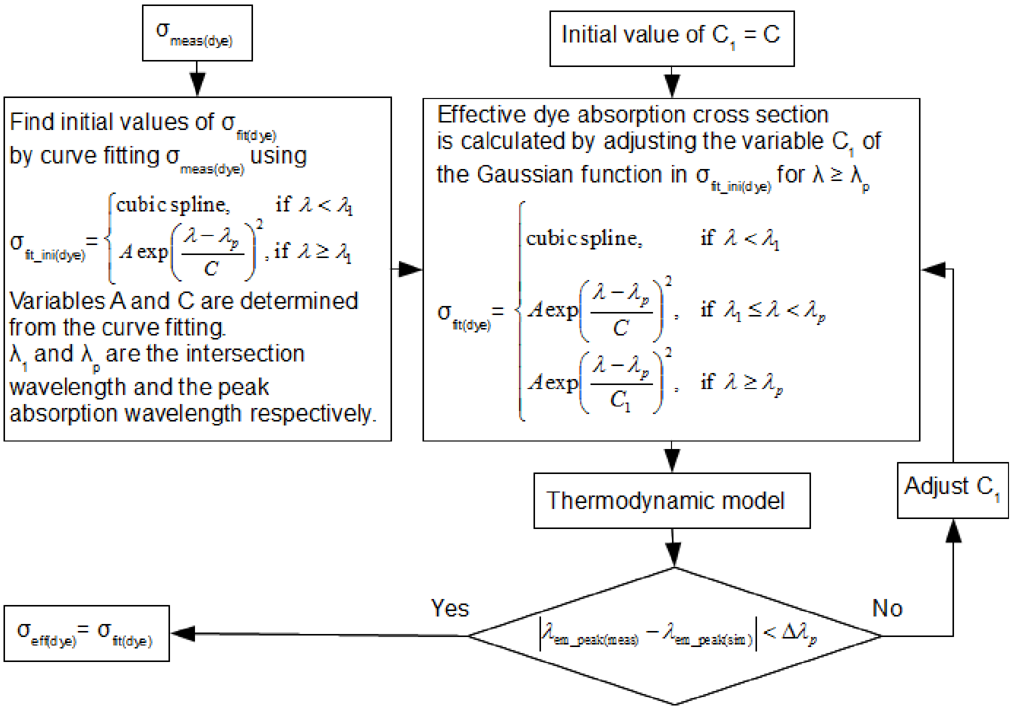

Figure 4.11: Flow chart for calculating the effective absorption cross section of the dye.

Figure 4.12 describes the empirical approach used to find the effective absorption cross section of the LSC sample, $\sigma_{eff(sample)}$. LSC sample means the host material with the dye. Firstly, the absorption cross section of the host material without the dye, $\sigma_{meas(host)}$, is determined by subtracting the measured absorption cross section of the LSC sample, $\sigma_{meas(sample)}$, from that of the dye, $\sigma_{meas(dye)}$. A combination of linear and Gaussian functions was used to curve fit $\sigma_{meas(host)}$ in order to generate a function, $\sigma_{fit\_ini(host)}$. The magnitude of the function, $\sigma_{fit\_ini(host)}$, is then multiplied by a factor, D, in order to correct the effect of the imperfection on the surface of the solid LSC sample. The factor, D, is always less than one. Then the corrected function, $\sigma_{fit(host)}$, and the effective absorption cross section of the dye, $\sigma_{eff(dye)}$, are fed into thermodynamic model to generate the emission spectrum. It is noticed that the absorption cross section spectrum of the host material affects mainly the magnitude of the peak. Therefore, the magnitude of the peak in the emission spectrum, $I_{em\_peak(sim)}$, is used to compare with the measured peak magnitude, $I_{em\_peak(meas)}$. The difference between the two is used to adjust the factor, D, which in turn is used in Gaussian functions to generate new function. The adjustment process is repeated until the difference ($I_{em\_peak(meas)}$ - $I_{em\_peak(sim)}$) is less than a specified tolerance. The effective absorption cross section of LSC sample, $\sigma_{eff(sample)}$, is then determined.

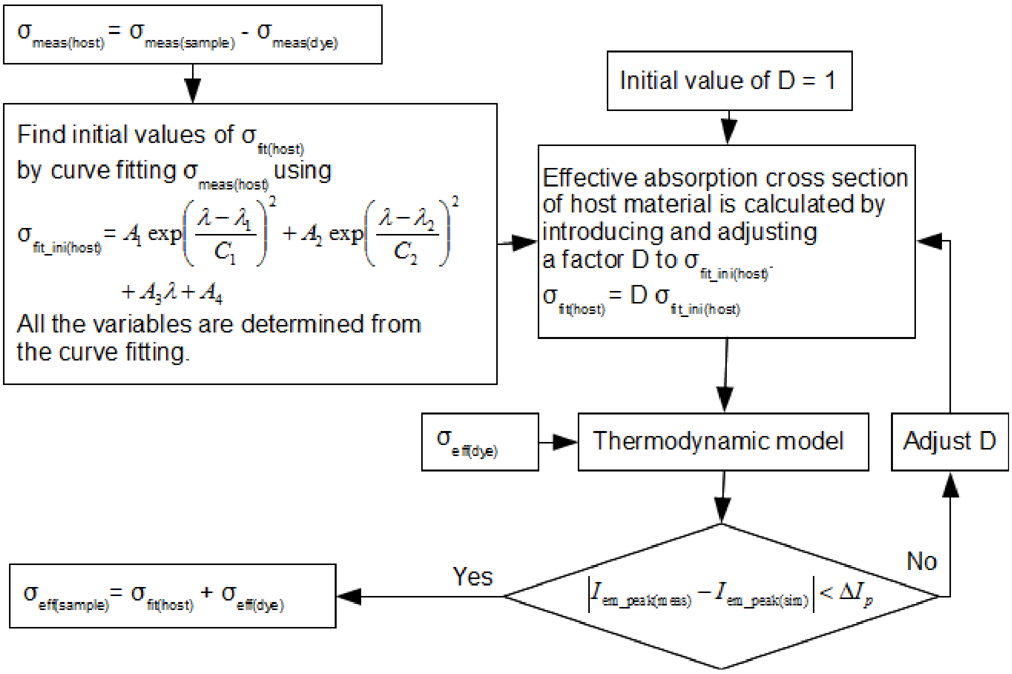

Figure 4.12: Flow chart for calculating the effective absorption cross section of the sample.

The effective absorption cross sections of the dye and the sample are represented by the blue lines in Figure 4.9 and Figure 4.10 These effective absorption cross sections of the dye and the sample were used in various case studies with different settings of LSC. The simulation results generated from one setting were found to match well with the experimental results from the same setting. This is how the effective absorption cross section of the dye and the sample were verified.

There are two peaks in Figure 4.10. The peak at the wavelength of 350 nm is the absorption cross section of the host material or unsaturated polyester without considering the dye. The peak at wavelength of 530 nm is the absorption cross section of the dye. It can be noticed that the peak at wavelength of 530 nm is the same as that in Figure 4.9. The peak at 530 nm is higher than that at 350 nm because the host material itself is more transparent than the dye.

The incident light source irradiance spectrum as shown in Figure 4.13 was measured using Avantes spectrometer connected to a cosine corrector via a fiber optic, by pointing the cosine corrector upward to the center of the LED after the optical filter, at a distance of 5cm from the LED. The LED and the optical filter was lumped together and modeled as a round shape isotropic area source having a diameter of 3mm and radiance value of $L_{FilteredLED}$ calculated using Eq. 4.76 in the Radiance scene description.

$$L_{FilteredLED}(\lambda) = E_{measured}(\lambda) \Big/ \left[\pi \sin^2 \left(\tan^{-1} \frac{d/2}{D} \right) \right] \tag{4.76}$$

Where,

$E_{measured}$ = Measured incident light spectrum,

d = Diameter of the LED (0.3 cm)

D = Distance between the sample and the light source (5 cm).

The term in the denominator at the right hand side of Eq. 4.76 is derived from,

$$E(\lambda) = \int_0^{2\pi} \int_0^{\theta_{LED}} L(\lambda) \cos\theta \sin\theta d\theta d\phi \quad , \theta_{LED} = \tan^{-1} \frac{d/2}{D} \tag{4.77}$$

$$L(\lambda) = E(\lambda) \big/ \left[\pi \sin^2 \theta_{LED}\right] \quad , \theta_{LED} = \tan^{-1} \frac{d/2}{D} \tag{4.78}$$

The incident light spectrum was sampled in Radiance by generating a scene that consists of the light source only, representing the experiment setup which measures the incident light irradiance spectrum. The irradiance collected by the vertically upward sampling plane over a hemisphere at a point 5cm below the light source is obtained using the calculation in Chapter 4.3.2. The minimum values of M_θ and M_φ were determined by increasing their values gradually until the sampled spectrum match reasonably well to the measured incident irradiance spectrum. The sampled spectrum as shown in Figure 4.13 is used as the input parameter in the thermodynamic model. For this experiment, the average reflectance at the top surface of LSC was calculated using Eq. 4.17 from Chapter 4.2.1 since it was assumed that the top surface of the LSC sample in the experiment is a perfectly flat surface where the average reflectance can be easily calculated.

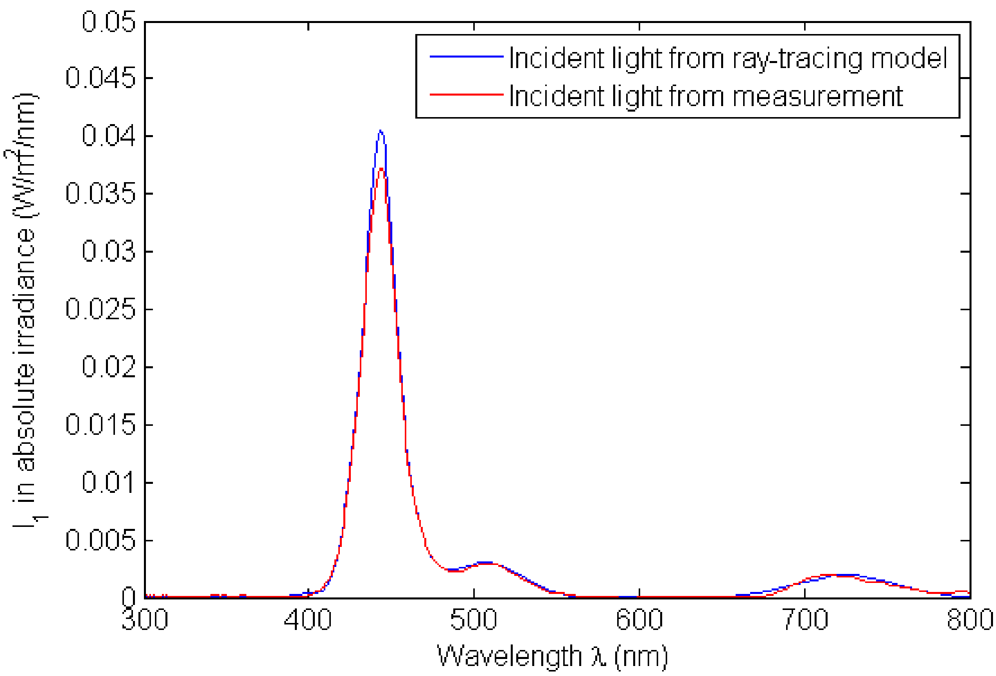

Figure 4.13: Incident light spectrum.

The scene description file used by the ray-tracing model created by the Shell script model the scene set up which is shown in Figure 4.14 and Figure 4.15. The dimension in the scene was determined from the actual experiment setup. The tilt angle of the sampling plane was due to the structure of the connector connecting the fiber optic and the cosine corrector, which has a diameter slightly larger than the diameter of the cosine corrector, and causes a small tilt when the cosine corrector was put on the flat surface.

The filter holder surface was included to account for the small reflection from that surface, which was collected by the cosine corrector directly. The black paper was modeled as a plastic type surface having reflectance of 0.05, specularity fraction of 0.1 and roughness of 0.15. The LSC was modeled by a combination of dielectric surfaces with the specified refractive index and the mist type material to account for the absorption. A 2 mm dielectric with refractive index of 1.52 was included for the bottom mirror to model the thin layer of glass on the mirror used in the experiment. The mirrors at the 3 edges were modeled by metal type surface with reflectance of 1, specularity of 1 and zero roughness.

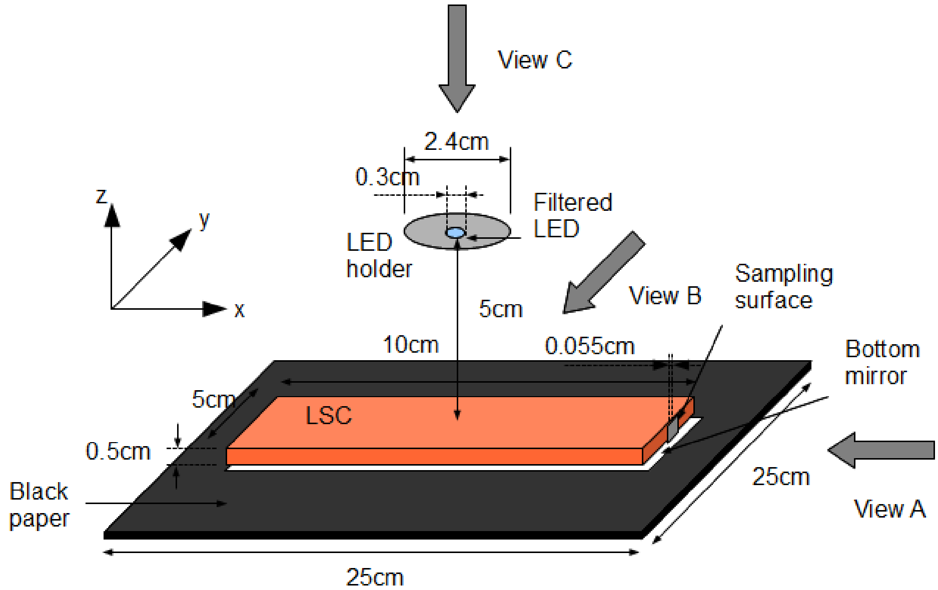

Figure 4.14: Ray-tracing simulation model.

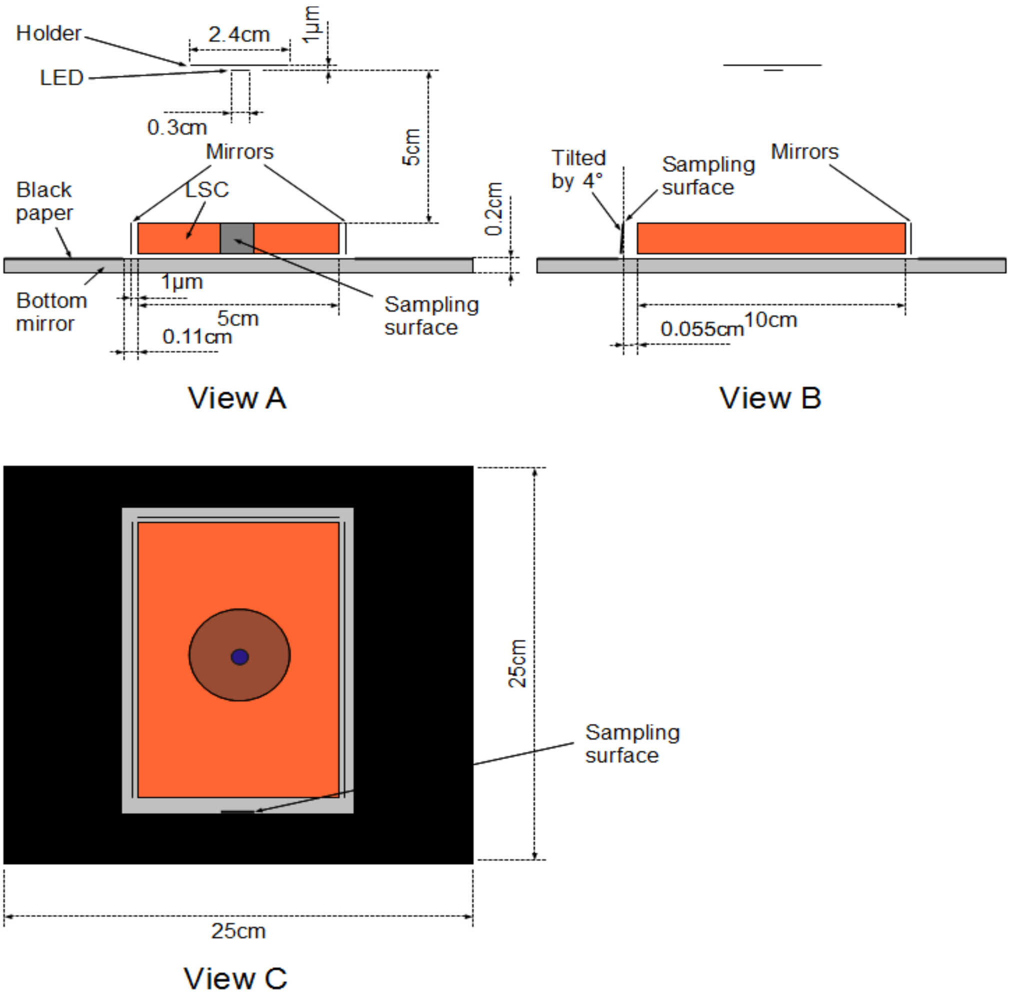

Figure 4.15: Two-dimensional view of the ray-tracing simulation model.

4.3.4 Simulation Result

The measurement result is shown in Figure 4.16, together with its magnified graph in the middle. Incident light was attenuated by the optical filter in the region of wavelength between 550nm to 650nm so that the dye emission can be clearly observed in the measured emission spectrum from the edge.

The emission spectrum in Figure 4.16 represents both luminescent emission plus light confinement. Since theoretically the separate components come from splitting the solution of radiative transfer equation into two parts where one part is affected by the incident light only, and another part affected by the dye emission. Therefore, it is not possible to separate them in real measurement and verify each contribution separately.

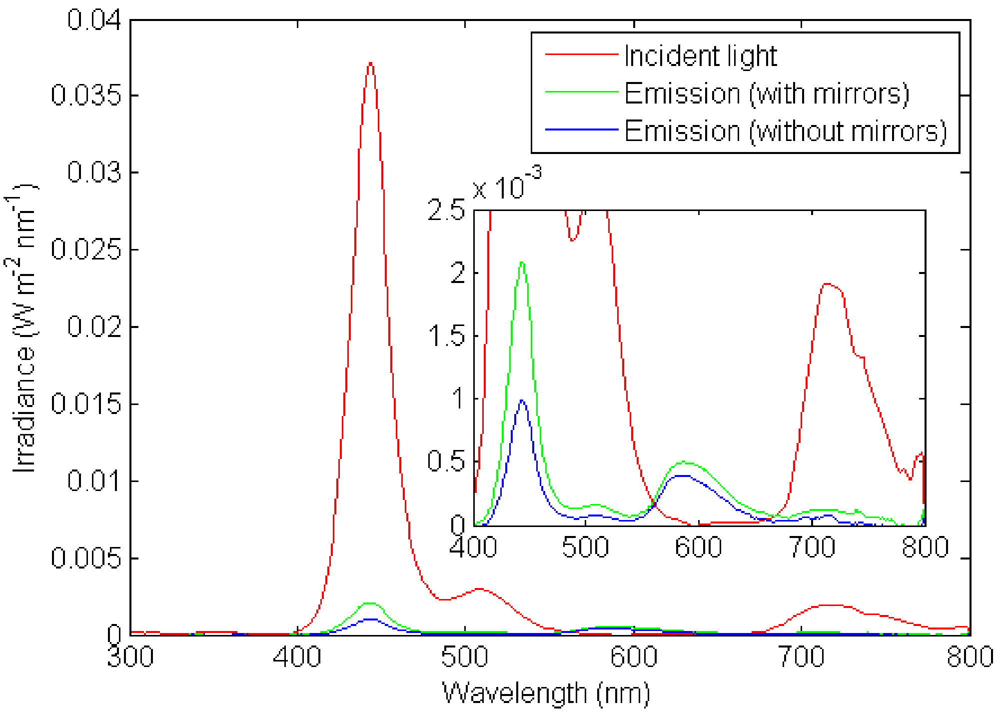

Figure 4.16: Experimental measurement result.

The simulation results for the cases of LSC with mirrors and without any mirror are shown in Figure 4.17 and Figure 4.18 respectively, together with the experimental result for comparison. Two peaks were observed in the experimental result. Separate contribution from each model is shown in Figure 4.19 and Figure 4.20.

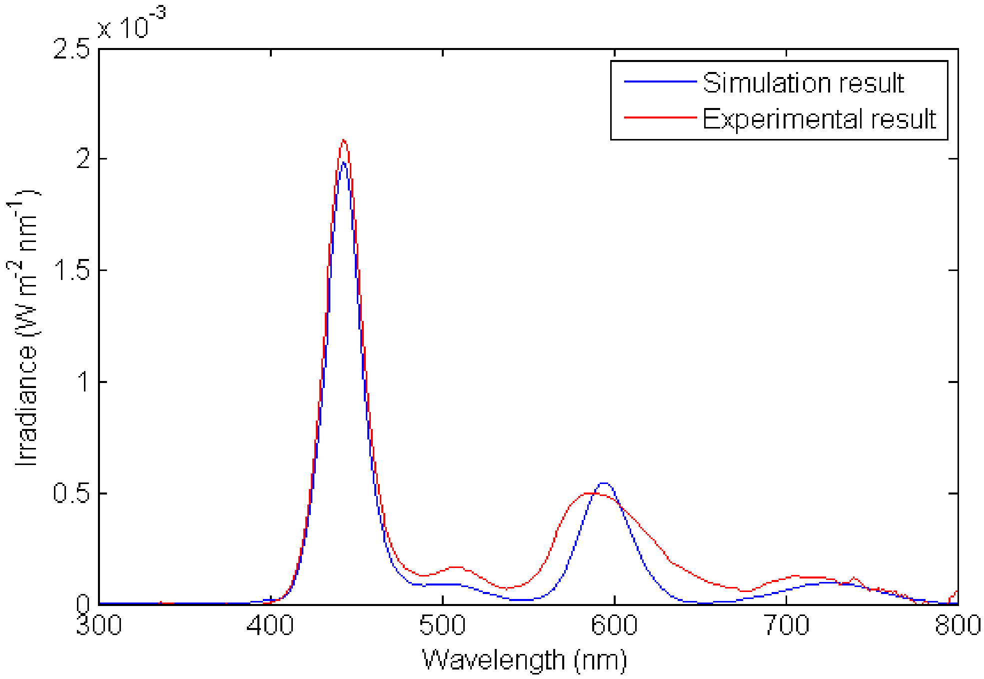

Figure 4.17: Simulation result versus experimental result for the case with mirrors.

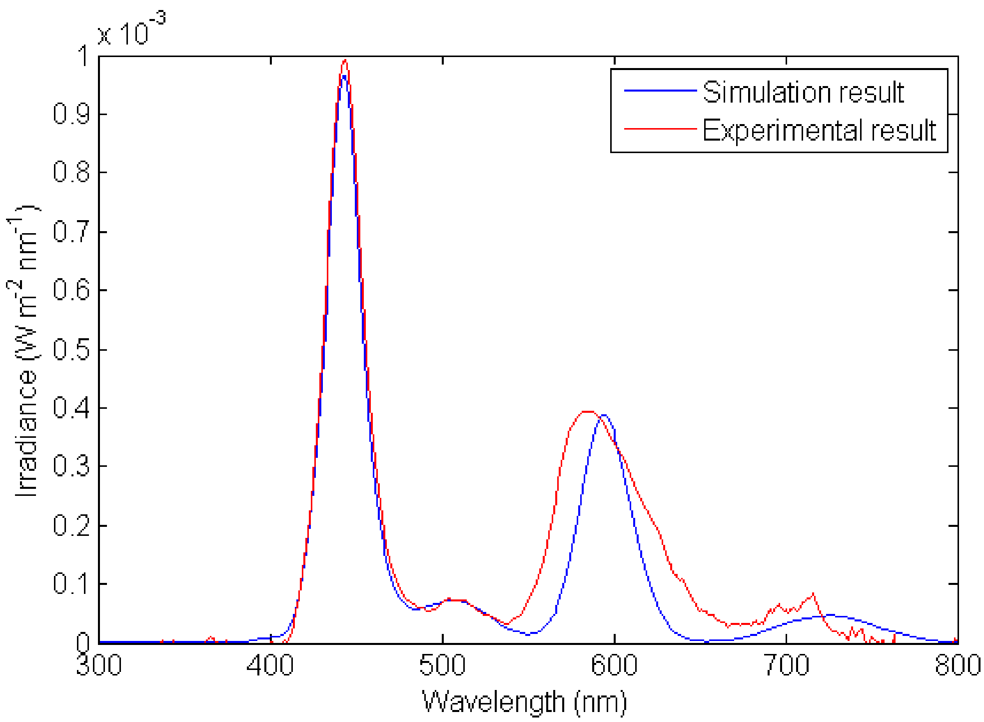

Figure 4.18: Simulation result versus experimental result for the case without any mirror.

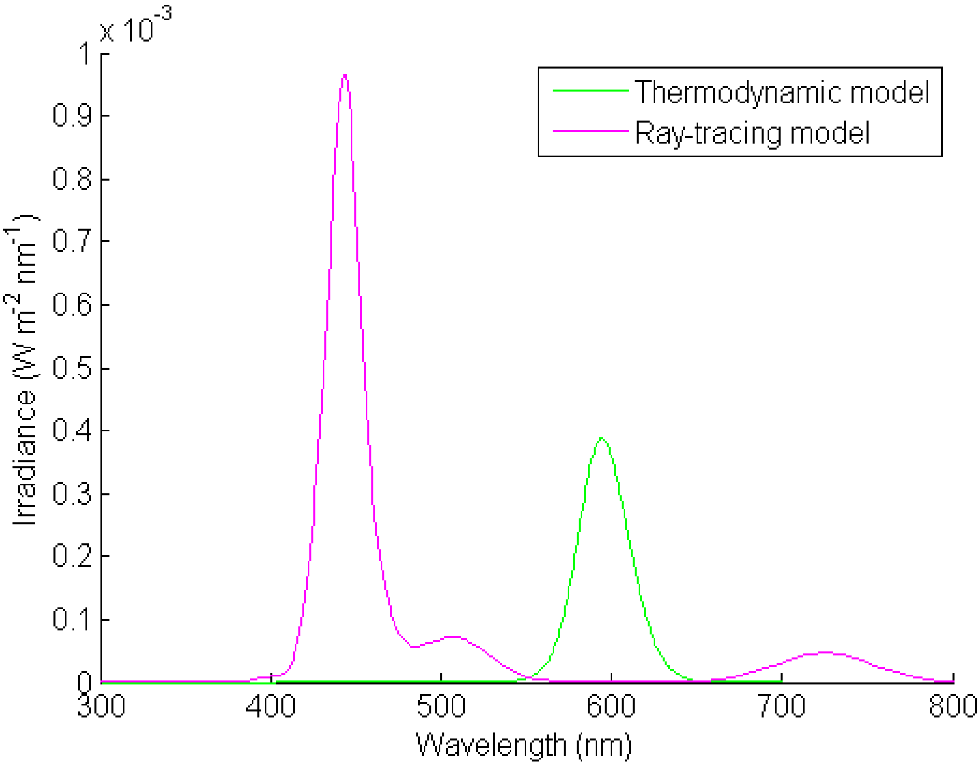

Figure 4.19: Separate contribution from the two models for no-mirror case.

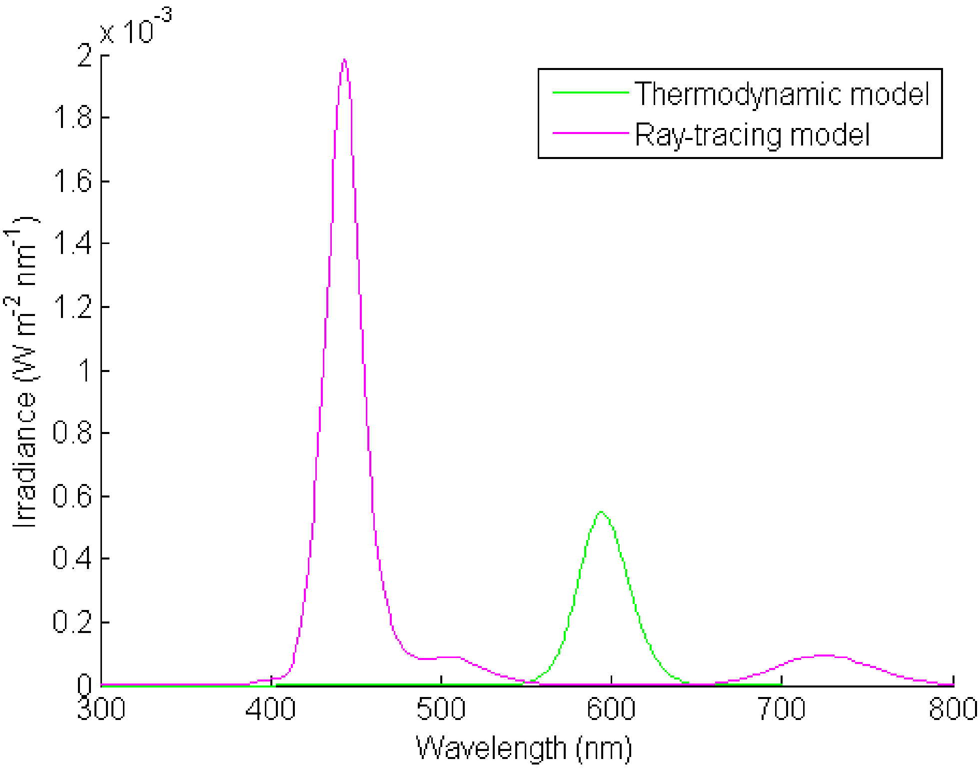

Figure 4.20: Separate contribution from the two models for with-mirror case.

4.3.5 Comparison between Experiment and Simulation Results

The irradiance values of the peaks and the corresponding wavelengths are listed in Table 4.2 together with the calculated values from simulation result. The simulation output can predict the peak irradiance and wavelength in the measurement result for the case without any mirror accurately using the same set of parameters adjusted to match the measurement result for the case with mirrors. Therefore it validates the adjustment of parameters described in Chapter 4.3.3: Simulation Input Parameters.

Two peaks are observed from the output irradiance spectral of LSC. The first peak at 443nm is contributed by the trapped light. The second peak at 594nm is by the luminescence of the dye. The first peak is much higher than the second peak. The surface of LSC is able to capture the incident light and guide the light to the edge. The contribution of the trapped light to the output irradiance of LSC is significant. Therefore, it is important to consider the contribution of the trapped light into the design of LSC.

Table 4.2. Peak irradiance and wavelength in irradiance spectrum.

Peak in irradiance spectrum	Simulation		Experiment	
	Irradiance ($W/m^2/nm$)	Wavelength (nm)	Irradiance ($W/m^2/nm$)	Wavelength (nm)
1st peak, with mirrors	1.99E-03	443	2.09E-03	443
1st peak, without mirrors	9.66E-03	443	9.92E-03	444
2nd peak, with mirror	5.48E-04	594	5.02E-04	586
2nd peak, without mirror	3.89E-04	594	3.89E-04	588

Table 4.3. Comparison of total irradiance from simulation result and experimental result.

Total irradiance	Simulation (W/m^2)	Experiment (W/m^2)	% difference
With mirrors	0.0872	0.1125	22%
Without mirrors	0.0489	0.0579	16%

Total irradiance in Table 4.3 is calculated by integrating the irradiance spectrum with respect to the wavelength. The differences between the predicted total irradiance values from simulation and the measured values are 22% for the case with mirrors, and 16% for the case without any mirror.

The reasons of the mismatch between the simulation output and the experimental measurement include scattering effect which occurs in the transparent host material and the difficulties to model the non-perfectly-flat LSC surfaces correctly.

In the simulation cases studies, the reflectors at the bottom and edges of LSC are specular reflector, however the hybrid model can also be used for diffuse reflectors as long as the effective reflectance of the diffuse reflectors is first modeled using ray-tracing. The thermodynamic and ray-tracing models can handle various values of effective reflectance of the diffuse reflectors.

Besides, a metal mold was used to prepare the small LSC sample in the experiment as described in Chapter 4.3.1. After the small LSC sample was casted, then the metal mold was removed from the LSC sample and mirrors were attached to the sample. As a result, air gaps exist in between the mirrors and the LSC sample. Therefore it is reasonable to observe that the simulation results are lower than the experimental results. This means that the preparation of the small LSC sample in Chapter 4.3.1 was not the same as the one described in Chapter 3.2.2 where a big mirror mold was constructed and used to construct a big LSC sample. The reason why a mirror mold was not used to prepare a small LSC sample is because a small dimension of the mirror mold is very difficult to be constructed since it is difficult to cut the mirrors into small pieces precisely at the required dimensions.

CHAPTER 5

IMPROVEMENTS ON THE HYBRID ALGORITHM FOR PLANAR LSC WITH BOTTOM MIRROR

5.1 Reducing the Simulation Time of Ray-tracing Model

The ray-tracing model from Chapter 4.2.2 has non-uniform ray distribution over the hemisphere of the sampling plane where much more rays are traced in the direction near the sampling surface normal and less rays are traced in the direction further away from the sampling surface normal. It has poor efficiency if the incident light rays reach the sampling surface from directions which make large angles to the surface normal. It also takes long time when it is used in the simulation of LSC placed under the sun because of the small angle (0.5331°) extended by the sun compared to the angle (180°) extended by diffuse part of incident light from the sky. To ensure there are rays coming from direct part of the sun light, $\Delta\theta$ must be reduced to the angle smaller than the angle extended by the sun. However, reducing $\Delta\theta$ to the required angle will make the total number of rays too large until it takes weeks to complete. In short, increasing the total number of rays does not efficiently improve the accuracy in the original model.

Besides, the planar LSC structure has the light trapping property which can trap the dye emission efficiently in the direction outside the escape cones due to its parallel top and bottom surfaces. However, incident light can only enter the LSC from the directions within the escape cones. In other word, from certain sampling directions, the rays that enter the solar cells are entirely contributed by the dye emission, where the trapped incident ray has no way to enter the solar cells from those directions if all the LSC edges are covered by mirrors or solar cells. This property can be used to greatly reduce the total number of rays being traced in the ray-tracing model.

Strategy for a more efficient ray-tracing model is shown in Figure 5.1. Each section in the flow charts is explained in the following subchapters.

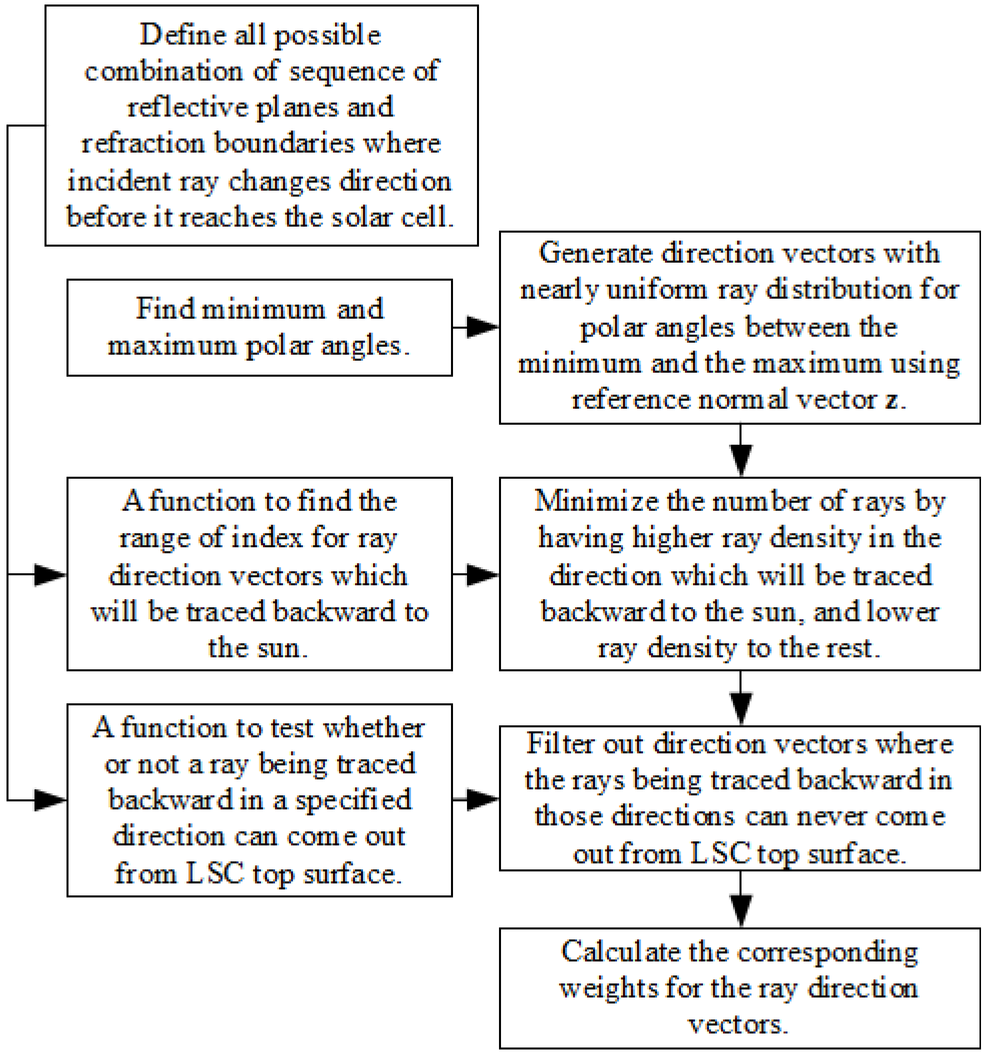

Figure 5.1: Overall strategy to minimize the number of ray directions in ray-tracing model.

5.2 Minimum and Maximum Polar Angles on the Sampling Surface

The total number of ray directions in the ray-tracing model can be reduced greatly while achieving the same accuracy if the minimum and maximum polar angles can be specified for a flat sampling surface. The limit of the polar angles usually comes from the critical angle at the refraction boundaries. The polar angle limit can be specified for the following two flat sampling surfaces: LSC top surface and solar cell surface, as explained in detail in following section.

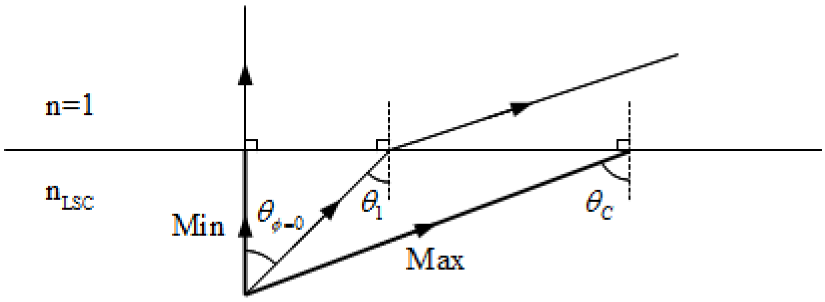

Figure 5.2: 2D view of the ray direction at ϕ=0 for LSC top surface.

Two-dimension view of the ray direction for LSC top surface, when ϕ=0, is shown in Figure 5.2.

From the figure, the minimum and maximum polar angles can be found for ϕ=0,

$$\theta_{\phi=0\,(\min)} = \theta_{1\,(\min)} = 0 \tag{5.1}$$

$$\theta_{\phi=0\,(\max)} = \theta_{1\,(\max)} = \theta_C = \sin^{-1}\left(\frac{1}{n_{LSC}}\right) \tag{5.2}$$

Since the reference normal vector where the ray direction vectors are generated has the same direction as the surface normal of LSC top surface, in general, at any value of ϕ,

$$\theta_{\min} = \theta_{\phi=0\,(\min)} = 0 \tag{5.3}$$

$$\theta_{\max} = \theta_{\phi=0\,(\max)} = \sin^{-1}\left(\frac{1}{n_{LSC}}\right) \tag{5.4}$$

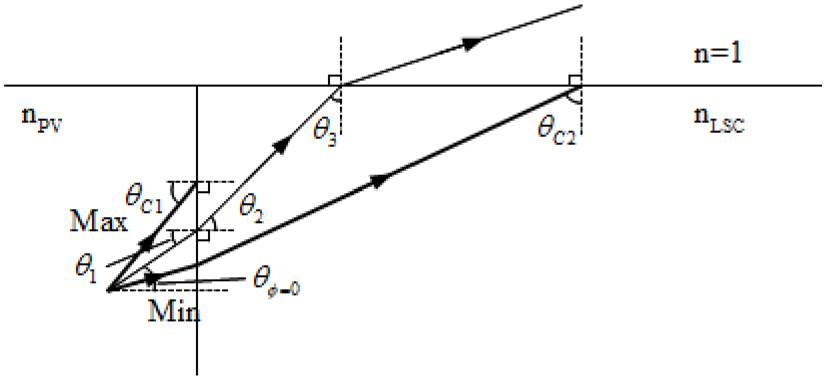

Figure 5.3: 2D view of the ray direction at φ=0 for solar cell surface.

Two dimensional view of the ray direction at φ=0 for solar cell surface is shown in Figure 5.3.

From the figure,

$$\theta_2 = \frac{\pi}{2} - \theta_3 \tag{5.5}$$

$$\sin\theta_1 = \frac{n_{LSC}\sin\theta_2}{n_{PV}} \tag{5.6}$$

Then θ_1 can be expressed in term of θ_3 by

$$\sin\theta_1 = \left(\frac{n_{LSC}}{n_{PV}}\right)\sin\left(\frac{\pi}{2} - \theta_3\right) \tag{5.7}$$

Minimum value of θ_1 can be found when θ_3 is at its maximum,

$$\sin\theta_{1(\min)} = \left(\frac{n_{LSC}}{n_{PV}}\right)\sin\left(\frac{\pi}{2} - \theta_{3(\max)}\right) \tag{5.8}$$

Since the maximum value of θ_3 is θ_{C2},

$$\sin\theta_{3(\max)} = \sin\theta_{C2} = \frac{1}{n_{LSC}} \tag{5.9}$$

$$\sin\left(\frac{\pi}{2} - \theta_{3(\max)}\right) = \frac{\sqrt{n_{LSC}^{\ 2} - 1}}{n_{LSC}} \tag{5.10}$$

Substitute Eq. 5.10 into Eq. 5.8, minimum value of polar angle at φ=0 can be found by,

$$\theta_{\phi=0(\min)} = \theta_{1(\min)} = \sin^{-1}\left(\frac{\sqrt{n_{LSC}^{\ 2} - 1}}{n_{PV}}\right) \tag{5.11}$$

The maximum polar angle is simply θ_{C1},

$$\theta_{\phi=0(\max)} = \theta_{C1} = \sin^{-1}\left(\frac{n_{LSC}}{n_{PV}}\right) \tag{5.12}$$

In general case, at any value of ϕ,

$$\theta_{\max} = \theta_{\phi=0(\max)} = \sin^{-1}\left(\frac{n_{LSC}}{n_{PV}}\right) \tag{5.13}$$

The minimum polar angle is a function of ϕ. However, it can be shown that the minimum polar angle is at its minimum when $\phi=0$ (refer to Appendix B). In other words, at any value of ϕ,

$$\theta_{\min} > \theta_{\phi=0(\min)} \tag{5.14}$$

Set the minimum polar angle as,

$$\theta_{\min} = \theta_{\phi=0(\min)} = \sin^{-1}\left(\frac{\sqrt{n_{LSC}{}^{2}-1}}{n_{PV}}\right) \tag{5.15}$$

All the rays generated using direction vectors at $\theta_{\min}<\theta<\theta_{\min(\text{actual},\phi\text{ dependent})}$, $\phi\neq 0$ and $\theta_{\min(\text{actual},\phi\text{ dependent})}\leq \theta_{\max}$ do not come out from the LSC top surface when they are traced backward. However, they can be filtered out from the list of ray direction vectors using the method described in Chapter 5.6.

5.3 Direction Vectors with Nearly Uniform Ray Distribution

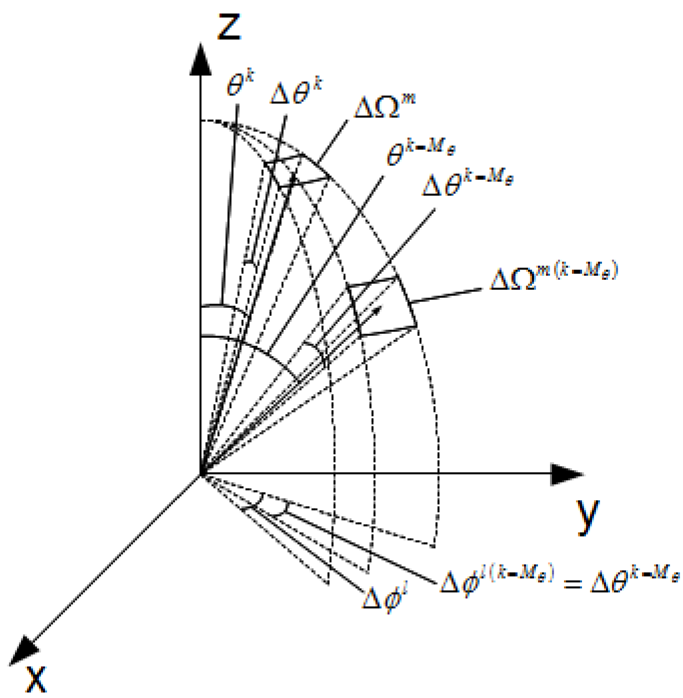

Figure 5.4: New algorithm to generate ray direction vectors to give all rays nearly uniform ray distribution.

The original algorithm in Chapter 4.2.2 generates ray direction vectors back-tracing from different angles over a hemisphere on the sampling plane non-uniformly. There are more rays from smaller polar angle than those from larger polar angle. As a result, even though the same number of rays are traced, the accuracy is higher if the light source is closer to polar axis of the sampling plane, compared to the one with exactly the same light source but at a larger angle from polar axis of the sampling plane. Therefore the algorithm was modified to generate ray direction vectors from different directions almost uniformly over the hemisphere to reduce the computation time, at the same time retain the same accuracy for rays tracing backward to the light source regardless of the light source angle from the polar axis.

Figure 5.4 shows two rays which are traced backward from the point at the origin along the direction of the vectors. To obtain uniform distribution of rays over the hemisphere, the value of M_ϕ is set to be depedent on the value of k for θ^k so that the discretized solid angle $\Delta\Omega^m$ at any θ^k is always less than the discretized solid angle at $k=M_\theta$. The value of discretized azimuthal angle $\Delta\phi^l$ is set to be equal to $\Delta\theta^k$ at $k=M_\theta$. Following paragraphs shows the detail derivation for the formula to calculate M_ϕ for any value of k.

At any (θ^k, ϕ^l), the discretized solid angle can be found by

$$\Delta\Omega^m = \int_{\phi^l-\frac{\Delta\phi^l}{2}}^{\phi^l+\frac{\Delta\phi^l}{2}} \int_{\theta^k-\frac{\Delta\theta^k}{2}}^{\theta^k+\frac{\Delta\theta^k}{2}} \sin\theta \, d\theta \, d\phi = 2\Delta\phi^l \left(\sin\theta^k \sin\frac{\Delta\theta^k}{2} \right) \tag{5.16}$$

At $k=M_\theta$, set $\Delta\phi = \Delta\theta$, the discretized solid angle is

$$\Delta\Omega^{m(k=M_\theta)} = 2\Delta\theta^{k=M_\theta} \left(\sin\theta^{k=M_\theta} \sin\frac{\Delta\theta^{k=M_\theta}}{2} \right) \tag{5.17}$$

Set the discretized solid angle at any k to be less than that at $k=M_\theta$,

$$\Delta\Omega^m \le \Delta\Omega^{m(k=M_\theta)} \tag{5.18}$$

Substitute Eq. 5.16 and Eq. 5.17 into Eq. 5.18,

$$\Delta\phi^l \left(\sin\theta^k \sin\frac{\Delta\theta^k}{2} \right) \le \Delta\theta^{k=M_\theta} \left(\sin\theta^{k=M_\theta} \sin\frac{\Delta\theta^{k=M_\theta}}{2} \right) \tag{5.19}$$

The angle $\Delta\theta^k$ is related to θ_{max} and M_θ by

$$\Delta\theta^{k=M_\theta} = \Delta\theta^k = \frac{\theta_{\max}}{M_\theta} \tag{5.20}$$

Substitute Eq. 5.20 into Eq. 5.19 and simplify,

$$\Delta\phi^l \sin\theta^k \le \frac{\theta_{\max}}{M_\theta} \sin\theta^{k=M_\theta} \tag{5.21}$$

$$\Delta\phi^l \le \frac{\theta_{\max} \sin\theta^{k=M_\theta}}{M_\theta \sin\theta^k} \tag{5.22}$$

The angle $\Delta\phi$ is related to M_ϕ by

$$\Delta\phi^l = \frac{2\pi}{M_\phi} \tag{5.23}$$

Substitute Eq. 5.23 into Eq. 5.22 and rearrange the equation,

$$M_\phi \geq \frac{2\pi}{\theta_{\max}} \frac{\sin\theta^k}{\sin\theta^{k=M_\theta}} M_\theta \tag{5.24}$$

Therefore, the value of M_ϕ is determined by

$$M_\phi = \text{ceil}\left(\frac{2\pi}{\theta_{\max}} \frac{\sin\theta^k}{\sin\theta^{k=M_\theta}} M_\theta\right) \tag{5.25}$$

Where the ceil function rounds the value inside the bracket to the nearest integer greater than or equal to that value.

The angle θ^k at $k=M_\theta$ is

$$\theta^{k=M_\theta} = \theta_{\min} + \frac{2M_\theta - 1}{2M_\theta}(\theta_{\max} - \theta_{\min}) \tag{5.26}$$

Since M_θ is usually a large integer in order to obtain reasonable accuracy in the ray-tracing model,

$$\frac{2M_\theta - 1}{2M_\theta} \approx 1 \tag{5.27}$$

Therefore,

$$\theta^{k=M_\theta} \approx \theta_{\min} + (\theta_{\max} - \theta_{\min}) = \theta_{\max} \tag{5.28}$$

In this way, Eq. 5.25 can be simplified to

$$M_\phi = ceil\left(\frac{2\pi}{\theta_{\max}} \frac{\sin\theta^k}{\sin\theta_{\max}} M_\theta\right) \tag{5.29}$$

Then θ^k, ϕ^l, $\Delta\theta^k$, and $\Delta\phi^l$ can be found by,

$$\theta^k = \theta_{\min} + \frac{2k-1}{2\mathrm{M}_\theta}(\theta_{\max} - \theta_{\min}) \tag{5.30}$$

$$\phi^l = \phi_{\min} + \frac{2l-1}{2\mathrm{M}_\phi}(\phi_{\max} - \phi_{\min}) \tag{5.31}$$

$$\Delta\theta^k = \frac{\theta_{\max} - \theta_{\min}}{M_\theta} \tag{5.32}$$

$$\Delta\phi^l = \frac{\phi_{\max} - \phi_{\min}}{M_\phi} \tag{5.33}$$

The ray direction vectors is then generated using z axis as the polar axis,

$$\mathbf{\Theta^m} = \begin{bmatrix} \sin\theta^k \cos\phi^l \\ \sin\theta^k \sin\phi^l \\ \cos\theta^k \end{bmatrix}^T \tag{5.34}$$

The weight is determined using Eq. 4.39 in page 60. The direction vectors are then rotated using the algorithm in Appendix A. The rotation axis and angle are found by,

$$\mathbf{A} = \hat{\mathbf{z}} \times \mathbf{N_{sampling}} \tag{5.35}$$

$$\theta_{rot} = \cos^{-1}\left(\hat{\mathbf{z}} \cdot \mathbf{N_{sampling}}\right) \tag{5.36}$$

Where $\mathbf{N_{sampling}}$ is the surface normal of the sampling plane.

The algorithm to generate ray direction vectors without modification for more rays back-traced to the sun is shown in Figure 5.5. It will be further modified and the value of M_θ will be determined in Chapter 5.7.

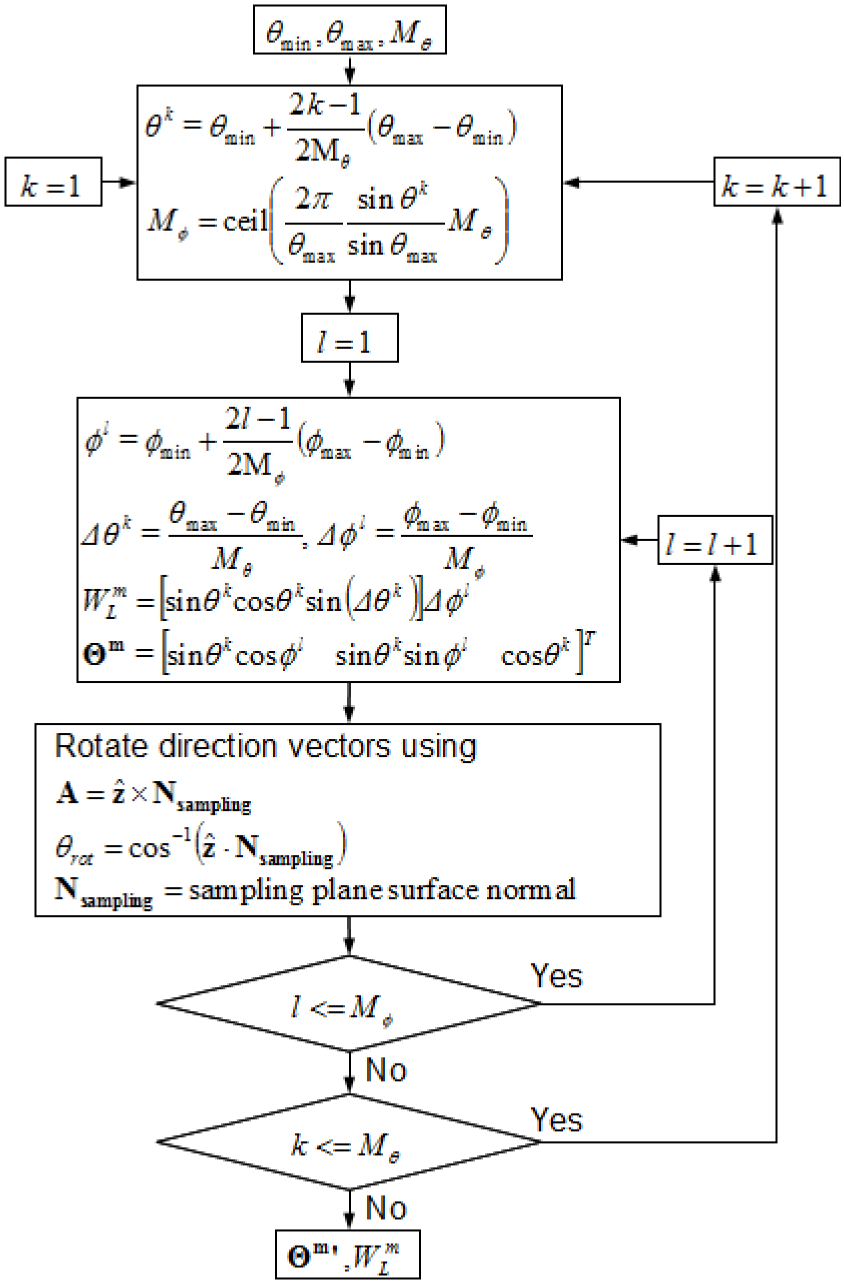

Figure 5.5: Generation of ray direction vectors with nearly uniform ray distribution without altering to focus more rays back-traced to the sun.

5.4 Reflective Planes and Refraction Boundaries

This chapter use a simpler algorithm to trace the ray backward in term of its change in direction, without considering its magnitude and the location of intersection point where the ray direction changes due to reflection or refraction. This algorithm is used in Chapter 5.5 and Chapter 5.6 to find out which back-tracing rays with direction vectors generated using the sampling surface surface normal as the polar axis will eventually back-trace to the sun, and also filter out those directions in which the back-tracing rays which will never contribute to the total irradiance calculation.

5.4.1 Change in Ray Direction at Reflective Plane

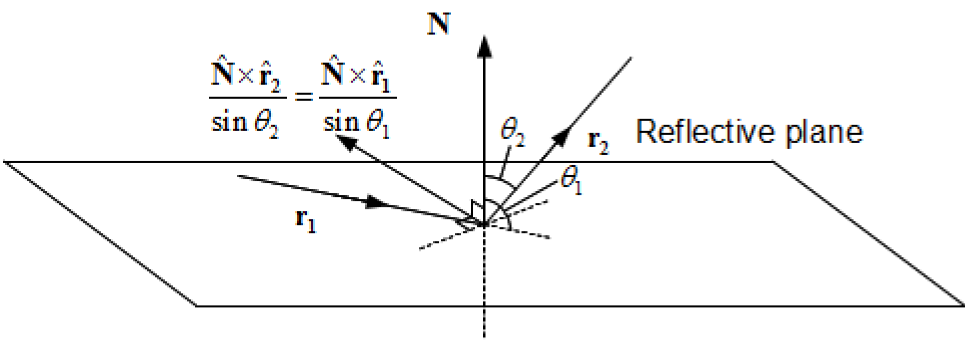

Figure 5.6: Change in ray direction when the ray hit a reflective plane.

Consider a back-tracing ray coming from an arbitrary direction hit a reflective side of a reflective plane, as shown in Figure 5.6, where light ray incident on the surface in a direction opposite to $\mathbf{r}_2$, and reflected from the surface in a direction opposite to $\mathbf{r}_1$. The surface normal of the reflective plane is pointing away from the reflective side of the plane.

Normalize the surface normal and incident ray direction vector,

$$\hat{\mathbf{N}} = \frac{\mathbf{N}}{\|\mathbf{N}\|} \tag{5.37}$$

$$\hat{\mathbf{r}}_1 = \frac{\mathbf{r}_1}{\|\mathbf{r}_1\|} \tag{5.38}$$

The following two vector equations can be deduced from Figure 5.6,

$$\hat{\mathbf{N}}\times\hat{\mathbf{r}}_2 = \left(\hat{\mathbf{N}}\times\hat{\mathbf{r}}_1\right)\frac{\sin\theta_2}{\sin\theta_1} \tag{5.39}$$

$$\hat{\mathbf{N}}\cdot\hat{\mathbf{r}}_2 = \cos\theta_2 \tag{5.40}$$

From Eq. 5.39, 3 equations can be obtained,

$$\hat{N}_y\hat{r}_{2z} - \hat{N}_z\hat{r}_{2y} = \left(\hat{N}_y\hat{r}_{1z} - \hat{N}_z\hat{r}_{1y}\right)\sin\theta_2/\sin\theta_1 \tag{5.41}$$

$$\hat{N}_z\hat{r}_{2x} - \hat{N}_x\hat{r}_{2z} = \left(\hat{N}_z\hat{r}_{1x} - \hat{N}_x\hat{r}_{1z}\right)\sin\theta_2/\sin\theta_1 \tag{5.42}$$

$$\hat{N}_x\hat{r}_{2y} - \hat{N}_y\hat{r}_{2x} = \left(\hat{N}_x\hat{r}_{1y} - \hat{N}_y\hat{r}_{1x}\right)\sin\theta_2/\sin\theta_1 \tag{5.43}$$

Add Eq. 5.41 with Eq. 5.42, and Eq. 5.42 with Eq. 5.43, together with Eq. 5.40, the following simultaneous equations can be found,

$$\hat{N}_z\hat{r}_{2x} - \hat{N}_z\hat{r}_{2y} + \left(\hat{N}_y - \hat{N}_x\right)\hat{r}_{2z} = \left[\hat{N}_z\hat{r}_{1x} - \hat{N}_z\hat{r}_{1y} + \left(\hat{N}_y - \hat{N}_x\right)\hat{r}_{1z}\right]\sin\theta_2/\sin\theta_1 \tag{5.44}$$

$$\left(\hat{N}_z - \hat{N}_y\right)\hat{r}_{2x} + \hat{N}_x\hat{r}_{2y} - \hat{N}_x\hat{r}_{2z} = \left[\left(\hat{N}_z - \hat{N}_y\right)\hat{r}_{1x} + \hat{N}_x\hat{r}_{1y} - \hat{N}_x\hat{r}_{1z}\right]\sin\theta_2/\sin\theta_1 \tag{5.45}$$

$$\hat{N}_x\hat{r}_{2x} + \hat{N}_y\hat{r}_{2y} + \hat{N}_z\hat{r}_{2z} = \cos\theta_2 \tag{5.46}$$

Rewrite Eq. 5.44, Eq. 5.45, and Eq. 5.46 in matrix form,

$$\begin{bmatrix} \hat{r}_{2x} \\ \hat{r}_{2y} \\ \hat{r}_{2z} \end{bmatrix} = \begin{bmatrix} \hat{N}_z & -\hat{N}_z & \hat{N}_y - \hat{N}_x \\ \hat{N}_z - \hat{N}_y & \hat{N}_x & -\hat{N}_x \\ \hat{N}_x & \hat{N}_y & \hat{N}_z \end{bmatrix}^{-1} \begin{bmatrix} A \\ B \\ C \end{bmatrix} \tag{5.47}$$

Where,

$$A = \left[\hat{N}_z\hat{r}_{1x} - \hat{N}_z\hat{r}_{1y} + \left(\hat{N}_y - \hat{N}_x\right)\hat{r}_{1z}\right]\sin\theta_2/\sin\theta_1 \tag{5.48}$$

$$B = \left[\left(\hat{N}_z - \hat{N}_y\right)\hat{r}_{1x} + \hat{N}_x\hat{r}_{1y} - \hat{N}_x\hat{r}_{1z}\right]\sin\theta_2/\sin\theta_1 \tag{5.49}$$

$$C = \cos\theta_2 \tag{5.50}$$

The angles θ_1 can be found from the dot product of the normalized surface normal and normalized incident ray direction vector, θ_2 by appying the laws of reflection,

$$\theta_1 = \cos^{-1}\left(\hat{\mathbf{N}} \cdot \hat{\mathbf{r}}_1\right) \tag{5.51}$$

$$\theta_2 = \pi - \theta_1 \tag{5.52}$$

The reflective plane is defined as having reflective surface at only one side and never reflect any ray at the other side. Therefore, following condition shoud be check before applying the transformation of ray direction vector in Eq. 5.47, which corresponds to $\pi/2<\theta_1\leq\pi$,

$$\hat{\mathbf{N}} \cdot \hat{\mathbf{r}}_1 < 0 \tag{5.53}$$

Ray direction vectors which do not fulfill the condition specified by the inequality 5.53 correspond to rays which will never intersect with the reflective surface, or rays which hit the non-reflective side of the reflective plane, thus reflection will not occur for incident rays with those directions.

If $\mathbf{r}_2$ is given, $\mathbf{r}_1$ can be found by using exactly the same algorithm with $\mathbf{r}_1$ and $\mathbf{r}_2$ replaced by each other. However, the condition for reflection to occur is changed into $0 \leq \theta_2 < \pi/2$, or

$$\hat{\mathbf{N}} \cdot \hat{\mathbf{r}}_2 > 0 \tag{5.54}$$

5.4.2 Change in Ray Direction at Refraction Boundary

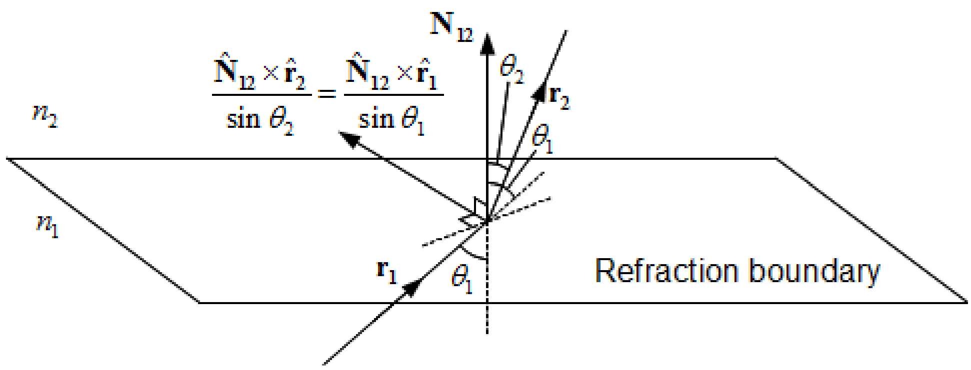

Figure 5.7: Change in ray direction when the ray hit the boundary between two materials with different refractive index.

Figure 5.7 shows the boundary between two materials with different refractive index. Define the surface normal $\mathbf{N}_{12}$ to be the surface normal of the boundary surface and points to the material with refractive index n_2 and light is expected to come from that material to the material with refractive index n_1. Similar to the previous section, the direction shown is back-tracing ray, where light ray follows the direction opposite to the direction vectors $\mathbf{r}_1$ and $\mathbf{r}_2$.

Normalize the surface normal and incident ray direction vector,

$$\hat{\mathbf{N}}_{12} = \frac{\mathbf{N}_{12}}{\|\mathbf{N}_{12}\|} \tag{5.55}$$

$$\hat{\mathbf{r}}_1 = \frac{\mathbf{r}_1}{\|\mathbf{r}_1\|} \tag{5.56}$$

The following two vector equations can be deduced from Figure 5.7,

$$\hat{\mathbf{N}}_{12} \times \hat{\mathbf{r}}_2 = \left(\hat{\mathbf{N}}_{12} \times \hat{\mathbf{r}}_1\right)\frac{\sin\theta_2}{\sin\theta_1} \tag{5.57}$$

$$\hat{\mathbf{N}}_{12} \cdot \hat{\mathbf{r}}_2 = \cos\theta_2 \tag{5.58}$$

Following the same derivation steps as shown in Chapter 5.4.1, the following matrix equation can be obtained,

$$\begin{bmatrix} \hat{r}_{2x} \\ \hat{r}_{2y} \\ \hat{r}_{2z} \end{bmatrix} = \begin{bmatrix} \hat{N}_{12z} & -\hat{N}_{12z} & \hat{N}_{12y} - \hat{N}_{12x} \\ \hat{N}_{12z} - \hat{N}_{12y} & \hat{N}_{12x} & -\hat{N}_{12x} \\ \hat{N}_{12x} & \hat{N}_{12y} & \hat{N}_{12z} \end{bmatrix}^{-1} \begin{bmatrix} A \\ B \\ C \end{bmatrix} \tag{5.59}$$

Where,

$$A = \left[\hat{N}_{12z}\hat{r}_{1x} - \hat{N}_{12z}\hat{r}_{1y} + \left(\hat{N}_{12y} - \hat{N}_{12x}\right)\hat{r}_{1z}\right]\sin\theta_2/\sin\theta_1 \tag{5.60}$$

$$B = \left[\left(\hat{N}_{12z} - \hat{N}_{12y}\right)\hat{r}_{1x} + \hat{N}_{12x}\hat{r}_{1y} - \hat{N}_{12x}\hat{r}_{1z}\right]\sin\theta_2/\sin\theta_1 \tag{5.61}$$

$$C = \cos\theta_2 \tag{5.62}$$

The angles θ_1 can be found from the dot product of the normalized surface normal and normalized incident ray direction vector, θ_2 by appying the Snell's law,

$$\theta_1 = \cos^{-1}\left(\hat{\mathbf{N}}_{12} \cdot \hat{\mathbf{r}}_1\right) \tag{5.63}$$

$$\theta_2 = \sin^{-1}\left(\frac{n_1 \sin\theta_1}{n_2}\right) \tag{5.64}$$

The surface normal $\mathbf{N}_{12}$ is defined to point toward the side where light is expected to come from that side of the boundary, so that only rays coming from that side will intersect with the boundary. However, for back-tracing rays, only those coming from the other side will intersect with the boundary, or $0 \le \theta_1 < \pi/2$,

$$\hat{\mathbf{N}}_{12} \cdot \hat{\mathbf{r}}_1 > 0 \tag{5.65}$$

Only back-tracing rays with direction vectors fulfilling the inequality 5.65 will intersect with the boundary and change direction due to refraction. Similar to the previous subchapter, if $\mathbf{r}_2$ is given, $\mathbf{r}_1$ can be found by using exactly the same algorithm with $\mathbf{r}_1$, n_1 and $\mathbf{r}_2$, n_2 replaced by each other. The condition for refraction in this case is $0 \le \theta_2 < \pi/2$,

$$\hat{\mathbf{N}}_{12} \cdot \hat{\mathbf{r}}_2 > 0 \tag{5.66}$$

5.4.3 Sequences of Reflective Planes and Refraction Boundaries

Every surface comprising the LSC and solar cells, including the LSC top surface, bottom mirror, side mirrors and the boundary between LSC and solar cells, is modeled as perfectly flat surface in the simulation in Chapter 6. This property can be used to limit the number of surfaces in which the backward rays pass or reflected from for the calculation in the next 2 sections.

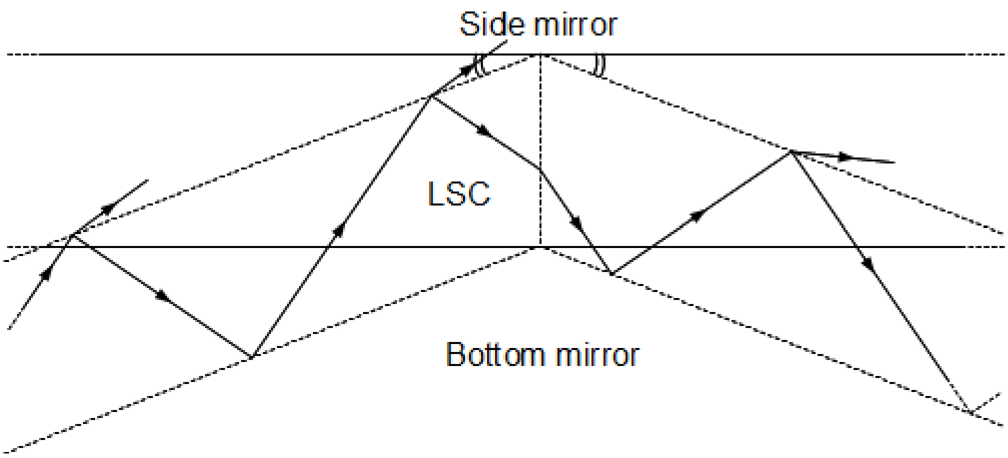

Figure 5.8: Reflection at the side mirror.

The effect of reflection at the side mirror is shown in Figure 5.8. Reflection from the bottom mirror or that from the top surface occurs at a plane for the ray, where the plane is perpendicular to both the top surface and the bottom mirror. It can be shown (refer to Appendix C) that the plane will be “reflected” from the side mirror with "plane reflected angle" the same as "plane incident angle". The angle where the ray makes with the surface normal of bottom mirror or top surface after the "plane reflection" from the side mirror will be the same as the one before the "plane reflection". This is illustrated in Figure 5.8 where the angle in which the reflection/refraction plane makes with the side mirror surface before and after the reflection are the same but opposite in direction if it is measured from the side mirror to the plane.

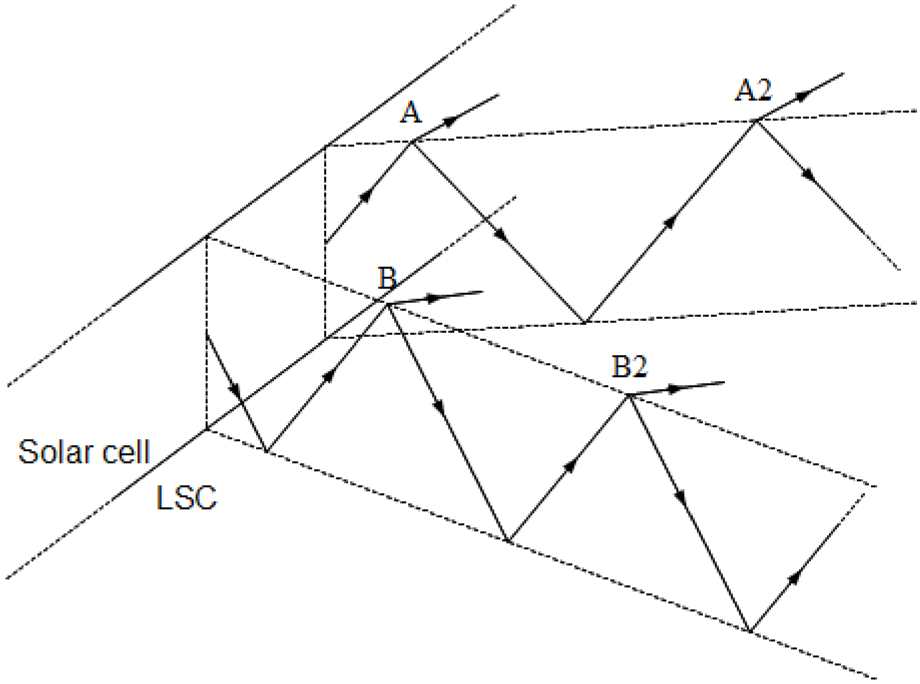

Figure 5.9: Different paths of rays tracing backward for solar cell surface.

There are many combinations of surfaces the ray will pass through or reflected from before it reach the solar cell surface. However, there are only two distinct ways where the backward rays can trace toward the sun, where the rest can be grouped into the two distinct ways.

For example, consider the different paths of rays tracing backward from the solar cell surface as shown in Figure 5.9, ray A2 and A can be grouped together because whatever angle the light source incident on the top surface from A2, the angle the ray eventually make with the solar cell surface normal must be the same as that from A due to the parallel surfaces which never change the angle of reflection from the top surface and the bottom mirror. Similarly, B2 and B can be grouped into B.

Since the incident angle of the ray to the bottom mirror or top surface does not change after the reflection from the side mirror, the side mirror can be excluded from the surface combination for the calculation. The sequence of surfaces which should be taken into account for is listed in Table 5.1.

Table 5.1. Sequence of surfaces that change the ray direction for solar cell surface.

Path	Surface	Type	Surface normal	Additional input
A	1	Refraction	$[0\ 0\ 1]^T$	$n_1=n_{LSC}$, $n_2=1$
	2	Refraction	$[-1\ 0\ 0]^T$	$n_1=n_{PV}$, $n_2=n_{LSC}$
B	1	Refraction	$[0\ 0\ 1]^T$	$n_1=n_{LSC}$, $n_2=1$
	2	Reflection	$[0\ 0\ 1]^T$	-
	3	Refraction	$[-1\ 0\ 0]^T$	$n_1=n_{PV}$, $n_2=n_{LSC}$

For the ray directions calculation at the LSC top surface, ray will only pass through the top surface by refraction. Therefore, only one surface is included in the calculation, as shown in Table 5.2.

Table 5.2. Sequence of surfaces that change the ray direction for LSC top surface.

Path	Surface	Type	Surface normal	Additional input
A	1	Refraction	$[0\ 0\ 1]^T$	$n_1=n_{LSC}$, $n_2=1$

5.5 Ray Direction Tracing Backward to the Sun

In this subchapter, the ranges of polar and azimuthal angles for ray direction vectors generation where the rays generated in those directions trace backward to the sun are found. A function is first developed in Chapter 5.5.1 to output vectors which points toward the sun perimeter as seen from the sampling surface. The function is then used to determine the minimum and maximum of polar and azimuthal angles in Chapter 5.5.2 by using a minimization algorithm without derivatives in MATLAB.

5.5.1 Function to Draw Perimeter of the Sun as Seen from the Sampling Surface

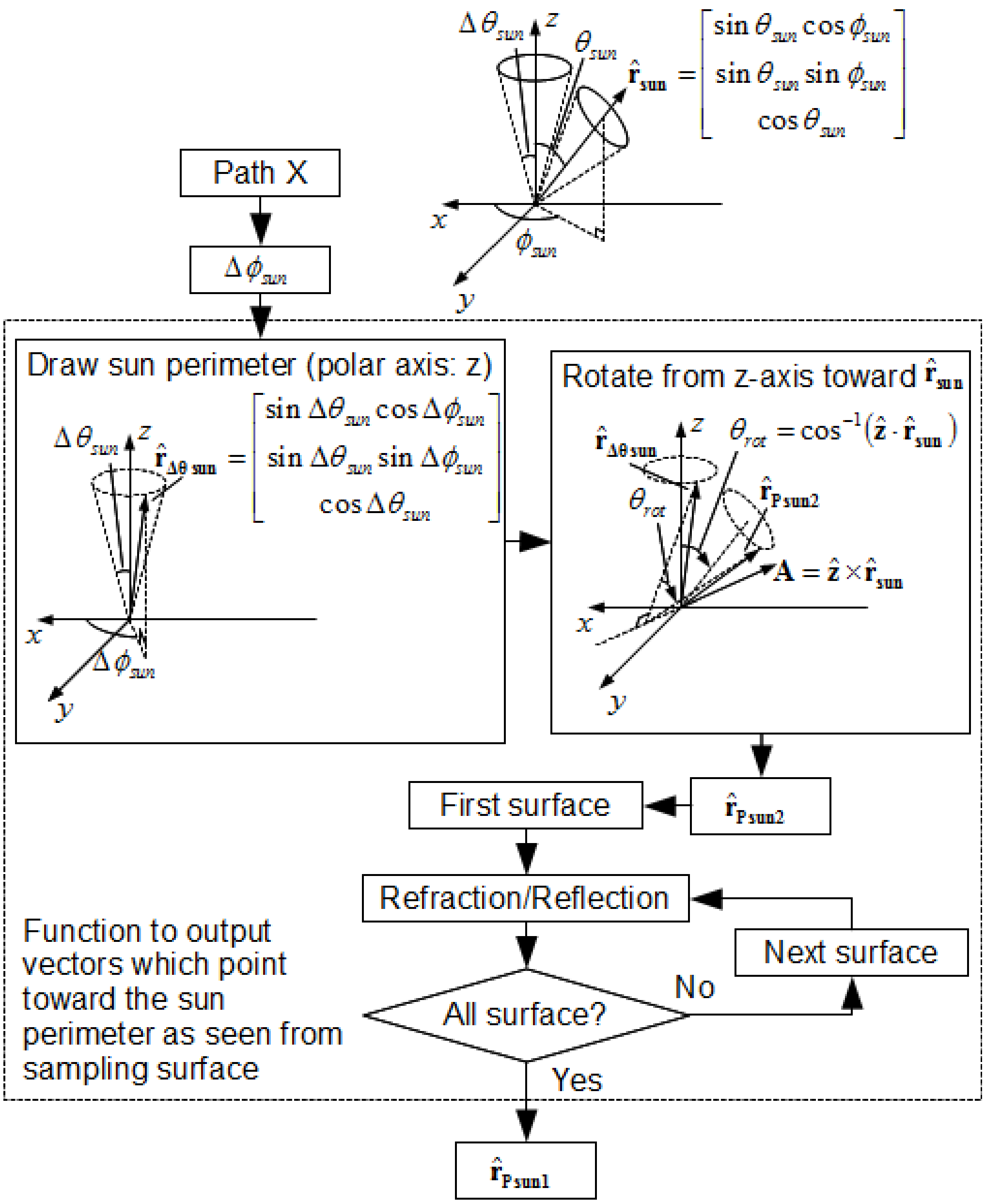

Figure 5.10: Function that gives vectors which point toward the sun perimeter as seen from sampling surface.

The function illustrated by the flow chart in Figure 5.10 is able to draw the perimeter of the sun as seen from the sampling surface, given the input values of $\Delta\phi_{sun}$ range from 0 to 2π. The definition of the solar zenith distance and solar azimuth θ_{sun}, ϕ_{sun}, together with the angle extended by the sun $\Delta\theta_{sun}$ are illustrated at the top of Figure 5.10.

The center of sun is located at a direction given by the normalized vector,

$$\hat{\mathbf{r}}_{\mathbf{sun}} = \begin{bmatrix} \sin\theta_{sun}\cos\phi_{sun} \\ \sin\theta_{sun}\sin\phi_{sun} \\ \cos\theta_{sun} \end{bmatrix} \tag{5.67}$$

Given a value of $\Delta\phi_{sun}$ for $0 \leq \Delta\phi_{sun} < 2\pi$, a normalized vector pointing toward the perimeter of the sun centered at the polar axis is,

$$\hat{\mathbf{r}}_{\mathbf{\Delta\theta\ sun}} = \begin{bmatrix} \sin\Delta\theta_{sun}\cos\Delta\phi_{sun} \\ \sin\Delta\theta_{sun}\sin\Delta\phi_{sun} \\ \cos\Delta\theta_{sun} \end{bmatrix} \tag{5.68}$$

For the actual sun at $\hat{\mathbf{r}}_{\mathbf{sun}}$, the vector is rotated using the algorithm in Appendix A where the rotation axis and angle are,

$$\mathbf{A} = \hat{\mathbf{z}} \times \hat{\mathbf{r}}_{\mathbf{sun}} \tag{5.69}$$

$$\theta_{rot} = \cos^{-1}\left(\hat{\mathbf{z}} \cdot \hat{\mathbf{r}}_{\mathbf{sun}}\right) \tag{5.70}$$

The rotated vector, $\hat{\mathbf{r}}_{\mathbf{Psun2}}$ is transformed via refraction or reflection at every defined surfaces, starting from the LSC top surface to the sampling surface for the specified Path X, using the calculation derived in Chapter 5.4. The output of the function is a vector $\hat{\mathbf{r}}_{\mathbf{Psun1}}$ after all the transformations, which points toward the perimeter of the sun as seen from the sampling surface.

5.5.2 Ranges of Polar and Azimuthal Angle Where the Sun Can Be Found

In this subchapter, the ranges of polar and azimuthal angles for ray direction vectors generation (with z-axis as the polar axis before being rotated toward the surface normal of the sampling plane) where rays generated in these directions can back-trace to the sun are found using the function developed in the previous subchapter. The algorithm is illustrated in the flow chart in Figure 5.11.

The vector from the function in the previous chapter $\hat{\mathbf{r}}_{\mathbf{Psun1}}$ is first rotated with the rotation axis and angle,

$$\mathbf{A} = \hat{\mathbf{N}} \times \hat{\mathbf{z}} \tag{5.71}$$

$$\theta_{rot} = \cos^{-1}\left(\hat{\mathbf{N}} \cdot \hat{\mathbf{z}}\right) \tag{5.72}$$

Where the vector **N** is the surface normal of the sampling plane.

Denote $\hat{\mathbf{r}}_{\mathbf{Psun}}$ as the vector after the rotation. In Cartesian form,

$$\hat{\mathbf{r}}_{\mathbf{Psun}} = \begin{bmatrix} \hat{r}_{Psunx} \\ \hat{r}_{Psuny} \\ \hat{r}_{Psunz} \end{bmatrix} \tag{5.73}$$

It is converted into polar and azimuthal angles by,

$$\theta_s = \cos^{-1} \hat{r}_{Psunz} \tag{5.74}$$

$$\phi_s = \tan^{-1}\left(\frac{\hat{r}_{Psuny}}{\hat{r}_{Psunx}}\right) \tag{5.75}$$

The minimum values of the angles are found by a non-derivatives minimization algorithm using a MATLAB function "fminbnd" for independent variable $0 \leq \Delta\phi_{sun} < 2\pi$. The maximum values can be found by first finding the minimum values of $-\theta_s$ and $-\phi_s$ where θ_s and ϕ_s then become the maximum values.

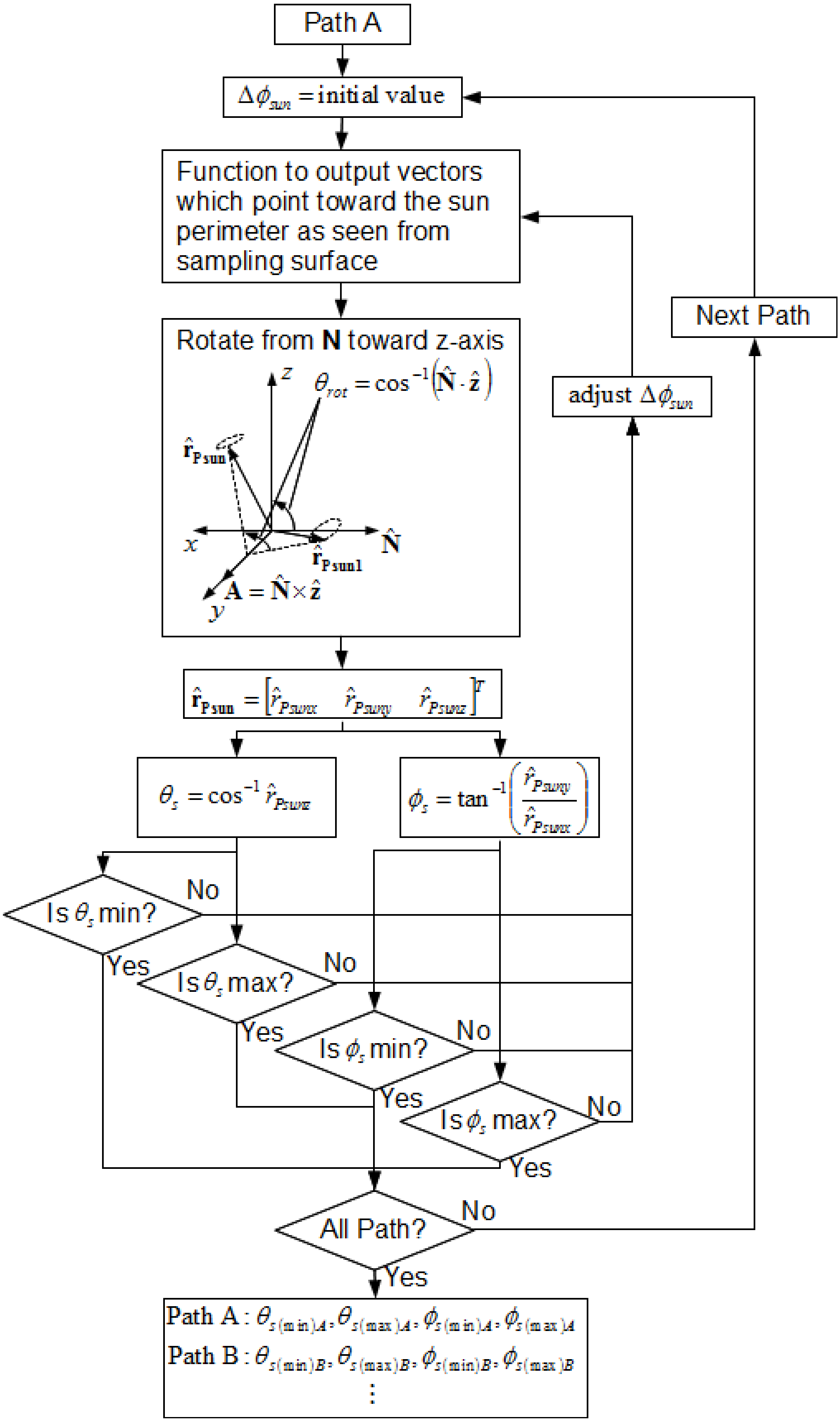

Figure 5.11: Algorithm to calculate the range of polar and azimuthal angles for ray direction vectors where the sun can be traced.

Special care must be taken for the inverse tangent in Figure 5.11 to give the value of ϕ_s in the correct quadrant for $0 \le \phi_s < 2\pi$. If $\phi_{s(min)} < 0$ and $\phi_{s(max)} > 0$, it can be splitted into two: $\phi_{s1(min)} = 0$, $\phi_{s1(max)} = \phi_{s(max)}$ and $\phi_{s2(min)} = 2\pi + \phi_{s(min)}$, $\phi_{s2(max)} = 2\pi$.

For a generalized ray direction vectors generation algorithm as shown in Figure 5.5, the ray direction vectors are generated using polar angle θ^k and azimuthal angle ϕ^l,

$$\theta^k = \theta_{\min} + \frac{2k-1}{2\mathrm{M}_\theta}\left(\theta_{\max} - \theta_{\min}\right) \tag{5.76}$$

$$\phi^l = \phi_{\min} + \frac{2l-1}{2\mathrm{M}_\phi}\left(\phi_{\max} - \phi_{\min}\right) \tag{5.77}$$

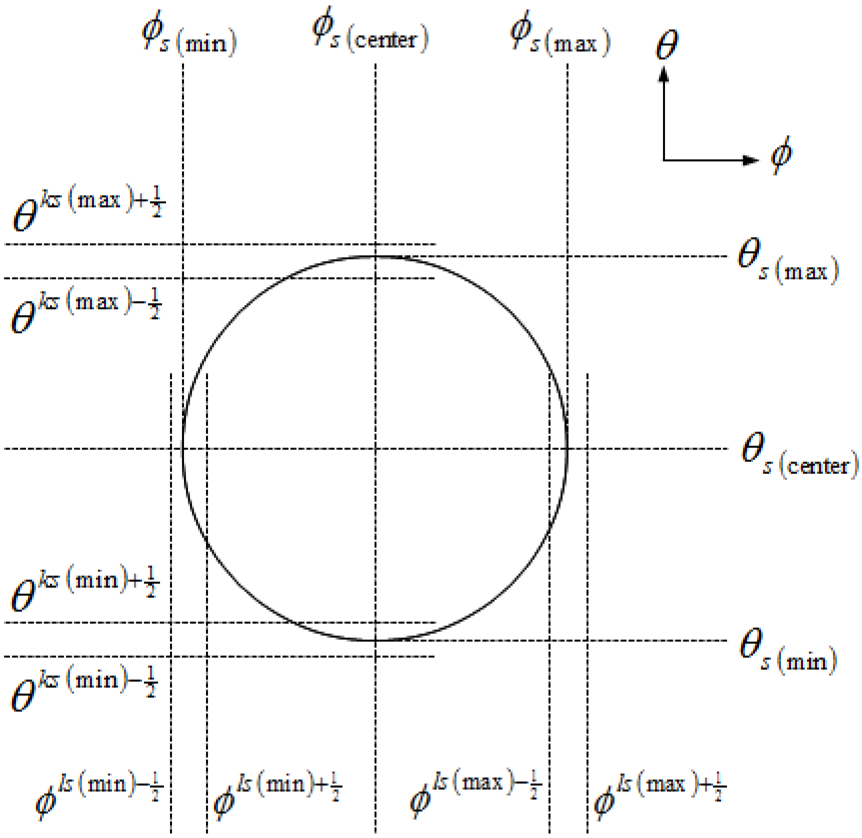

Figure 5.12: Conversion of polar and azimuthal angles ranges into ranges of index k and l in ray direction vector generation.

Ray with direction vector generated using (θ^k,ϕ^l) represent the solid angle in the range of $\theta^{k-\frac{1}{2}} < \theta < \theta^{k+\frac{1}{2}}$ and $\phi^{k-\frac{1}{2}} < \phi < \phi^{k+\frac{1}{2}}$. Where,

$$\theta^{k-\frac{1}{2}} = \theta_{\min} + \frac{2\left(k-\frac{1}{2}\right)-1}{2\mathrm{M}_\theta}\left(\theta_{\max}-\theta_{\min}\right) = \theta_{\min} + \frac{k-1}{\mathrm{M}_\theta}\left(\theta_{\max}-\theta_{\min}\right) \tag{5.78}$$

$$\theta^{k+\frac{1}{2}} = \theta_{\min} + \frac{2\left(k+\frac{1}{2}\right)-1}{2\mathrm{M}_\theta}\left(\theta_{\max}-\theta_{\min}\right) = \theta_{\min} + \frac{k}{\mathrm{M}_\theta}\left(\theta_{\max}-\theta_{\min}\right) \tag{5.79}$$

$$\phi^{l-\frac{1}{2}} = \phi_{\min} + \frac{2\left(l-\frac{1}{2}\right)-1}{2\mathrm{M}_\phi}\left(\phi_{\max}-\phi_{\min}\right) = \phi_{\min} + \frac{l-1}{\mathrm{M}_\phi}\left(\phi_{\max}-\phi_{\min}\right) \tag{5.80}$$

$$\phi^{l+\frac{1}{2}} = \phi_{\min} + \frac{2\left(l+\frac{1}{2}\right)-1}{2\mathrm{M}_\phi}\left(\phi_{\max}-\phi_{\min}\right) = \phi_{\min} + \frac{l}{\mathrm{M}_\phi}\left(\phi_{\max}-\phi_{\min}\right) \tag{5.81}$$

From Figure 5.12,

$$\theta^{ks(\min)-\frac{1}{2}} < \theta_{s(\min)} < \theta^{ks(\min)+\frac{1}{2}} \tag{5.82}$$

Solving the inequality on the left hand side of Eq. 5.82,

$$\begin{gathered} \theta_{\min} + \frac{k_{s(\min)}-1}{\mathrm{M}_\theta}\left(\theta_{\max}-\theta_{\min}\right) < \theta_{s(\min)} \\ k_{s(\min)} < \frac{\mathrm{M}_\theta\left(\theta_{s(\min)}-\theta_{\min}\right)}{\theta_{\max}-\theta_{\min}} + 1 \end{gathered} \tag{5.83}$$

For the inequality on the right hand side of Eq. 5.82,

$$\begin{gathered} \theta_{s(\min)} < \theta_{\min} + \frac{k_{s(\min)}}{\mathrm{M}_\theta}\left(\theta_{\max}-\theta_{\min}\right) \\ k_{s(\min)} > \frac{\mathrm{M}_\theta\left(\theta_{s(\min)}-\theta_{\min}\right)}{\theta_{\max}-\theta_{\min}} \end{gathered} \tag{5.84}$$

Combine inequalities 5.83 and 5.84,

$$\frac{\mathrm{M}_\theta\left(\theta_{s(\min)}-\theta_{\min}\right)}{\theta_{\max}-\theta_{\min}} < k_{s(\min)} < \frac{\mathrm{M}_\theta\left(\theta_{s(\min)}-\theta_{\min}\right)}{\theta_{\max}-\theta_{\min}} + 1 \tag{5.85}$$

Similarly, from Figure 5.12, using the same derivation,

$$\begin{gathered} \theta^{ks(\max)-\frac{1}{2}} < \theta_{s(\max)} < \theta^{ks(\max)+\frac{1}{2}} \\ \frac{\mathrm{M}_\theta\left(\theta_{s(\max)}-\theta_{\min}\right)}{\theta_{\max}-\theta_{\min}} < k_{s(\max)} < \frac{\mathrm{M}_\theta\left(\theta_{s(\max)}-\theta_{\min}\right)}{\theta_{\max}-\theta_{\min}} + 1 \end{gathered} \tag{5.86}$$

Since k must be an integer, it can be set to the nearest integer greater than or equal to the left hand side of the inequality using the ceil function, or the nearest integers smaller than or equal to the right hand side of the inequality using the floor function.

Set $k_{s(min)}$ and $k_{s(max)}$ to be,

$$k_{s\,(\min)} = \text{floor}\left[\frac{\mathrm{M}_\theta\left(\theta_{s\,(\min)} - \theta_{\min}\right)}{\theta_{\max} - \theta_{\min}} + 1\right] \tag{5.87}$$

$$k_{s\,(\max)} = \text{ceil}\left[\frac{\mathrm{M}_\theta\left(\theta_{s\,(\max)} - \theta_{\min}\right)}{\theta_{\max} - \theta_{\min}}\right] \tag{5.88}$$

Also, from Figure 5.12,

$$\phi^{ls(\min)-\frac{1}{2}} < \phi_{s\,(\min)} < \phi^{ls(\min)+\frac{1}{2}} \tag{5.89}$$

$$\phi^{ls(\max)-\frac{1}{2}} < \phi_{s\,(\max)} < \phi^{ls(\max)+\frac{1}{2}} \tag{5.90}$$

Using the same derivation,

$$l_{s\,(\min)} = \text{floor}\left[\frac{\mathrm{M}_\phi\left(\phi_{s\,(\min)} - \phi_{\min}\right)}{\phi_{\max} - \phi_{\min}} + 1\right] \tag{5.91}$$

$$l_{s\,(\max)} = \text{ceil}\left[\frac{\mathrm{M}_\phi\left(\phi_{s\,(\max)} - \phi_{\min}\right)}{\phi_{\max} - \phi_{\min}}\right] \tag{5.92}$$

Substitute $\phi_{min}=0$ and $\phi_{max}=2\pi$ into Eq. 5.91 and Eq. 5.92,

$$l_{s\,(\min)} = \text{floor}\left(\frac{\mathrm{M}_\phi \phi_{s\,(\min)}}{2\pi} + 1\right) \tag{5.93}$$

$$l_{s\,(\max)} = \text{ceil}\left(\frac{\mathrm{M}_\phi \phi_{s\,(\max)}}{2\pi}\right) \tag{5.94}$$

The range of k_s and l_s are used to check if the generated ray in that direction will back-traced to the sun or not. Denote subscript n for different possible paths as described in Chapter 5.4.3, if $k_{sn(min)} \le k \le k_{sn(max)}$ and $l_{sn(min)} \le l \le l_{sn(max)}$, for any path, the ray direction vectors will be generated using smaller $\Delta\theta$ and $\Delta\phi$ (larger M_θ and M_ϕ).

5.6 Condition for Rays Tracing Backward Which Eventually Come Out from LSC Top Surface

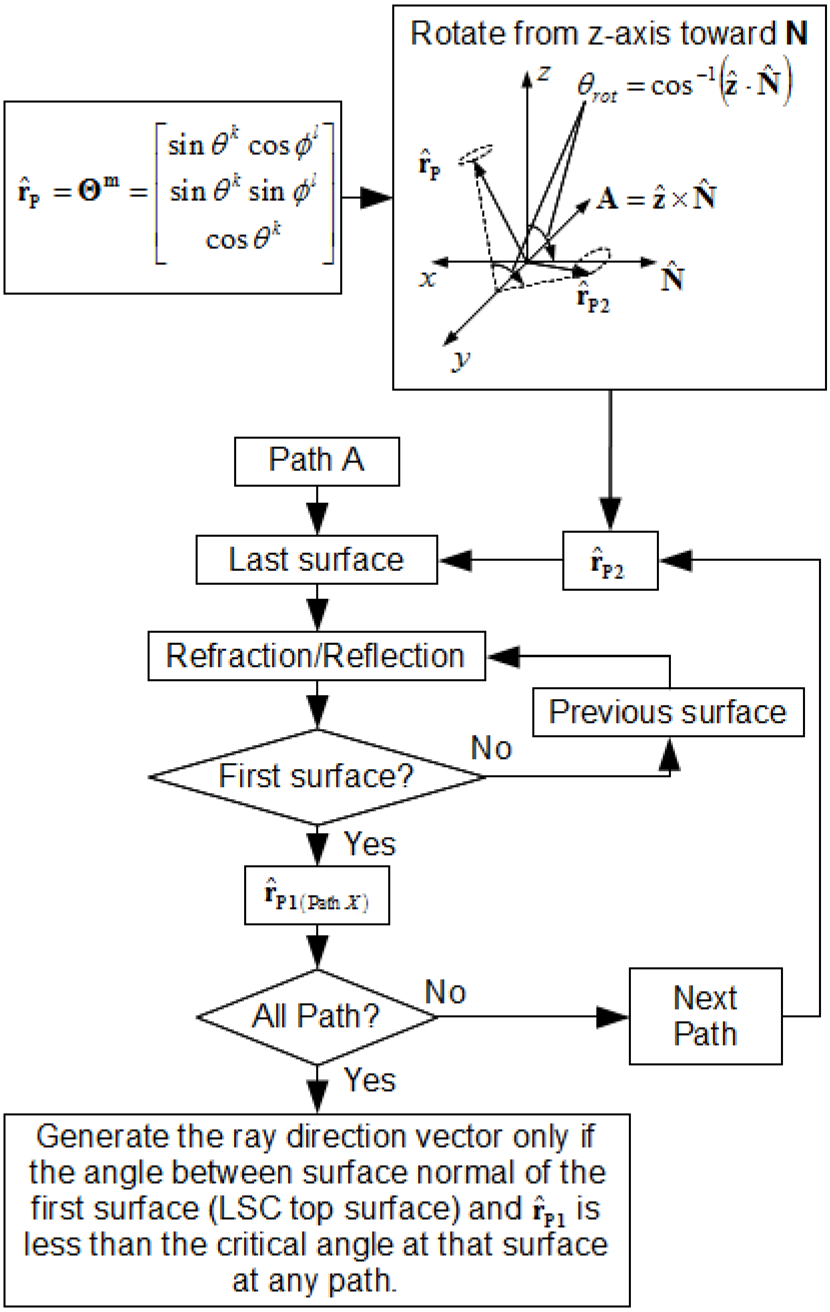

Figure 5.13: Algorithm to check if the ray traced backward in a particular direction will eventually come out from the LSC top surface or not.

To filter out unnecessary ray direction vectors in which the generated back-tracing ray will never come out from the LSC top surface, the angle in which the generated back-tracing ray will make with the surface normal of the LSC top surface when it hit the surface is checked so that any ray with that angle larger than the critical angle on the LSC top surface will be filtered out. The algorithm to check for this condition is illustrated in the flow chart in Figure 5.13.

The ray direction vector generated using z-axis as the polar axis is first rotated via the following rotation axis and angle,

$$\mathbf{A} = \hat{\mathbf{z}} \times \hat{\mathbf{N}} \tag{5.95}$$

$$\theta_{rot} = \cos^{-1}\left(\hat{\mathbf{z}} \cdot \hat{\mathbf{N}}\right) \tag{5.96}$$

Where vector **N** is the surface normal of the sampling surface.

The rotated vector $\hat{\mathbf{r}}_{\mathbf{P2}}$ is then transformed via refraction or reflection at all surfaces except the LSC top surface, starting from the sampling surface and stop at the LSC top surface using the calculation derived in Chapter 5.4. The output of the function is a vector $\hat{\mathbf{r}}_{\mathbf{P1}}$ after the transformations, where the angle it makes with the surface normal of the LSC top surface is checked against the critical angle at that suface, i.e.

$$\theta_C = \cos^{-1}\left(\frac{1}{n_{LSC}}\right) \tag{5.97}$$

$$\theta_{rN} = \cos^{-1}\left(\hat{\mathbf{r}}_{\mathbf{P1}} \cdot \hat{\mathbf{N}}_{(LSC\,top)}\right) \tag{5.98}$$

Where n_{LSC} is the reflective index of LSC and $N_{(LSC\ top)}$ is the surface normal of LSC top surface.

The check is then repeated for every path as illustrated in Figure 5.13. If θ_{rN} at any path is less than θ_C, then only the ray direction vectors will be generated.

5.6.1 Simpler and Faster Calculation for Special Case of Planar LSC

If the LSC is planar structure with the solar cell's surface normal perpendicular to the LSC top and bottom surface normal, a much more effective algorithm can be used to replace the algorithm discussed in the previous section, which consist of only 1 equation derived in Appendix B.

$$\left|\cos\phi^l\right| > \frac{\sqrt{{n_{LSC}}^2 - 1}}{n_{PV}\sin\theta^k} \tag{5.99}$$

Where the angles θ^k and ϕ^l are the polar and azimuthal angles for ray direction vectors generation, n_{LSC} and n_{PV} are the reflective index of LSC and solar cell respectively. Only ray direction vectors with the values of (θ^k,ϕ^l) fulfilling the inequality in Eq. 5.99 at any path will be generated for the ray-tracing program.

5.7 Overall ray direction vectors generation algorithm

The flow chart of overall ray direction vectors generation algorithm is shown in Figure 5.14.

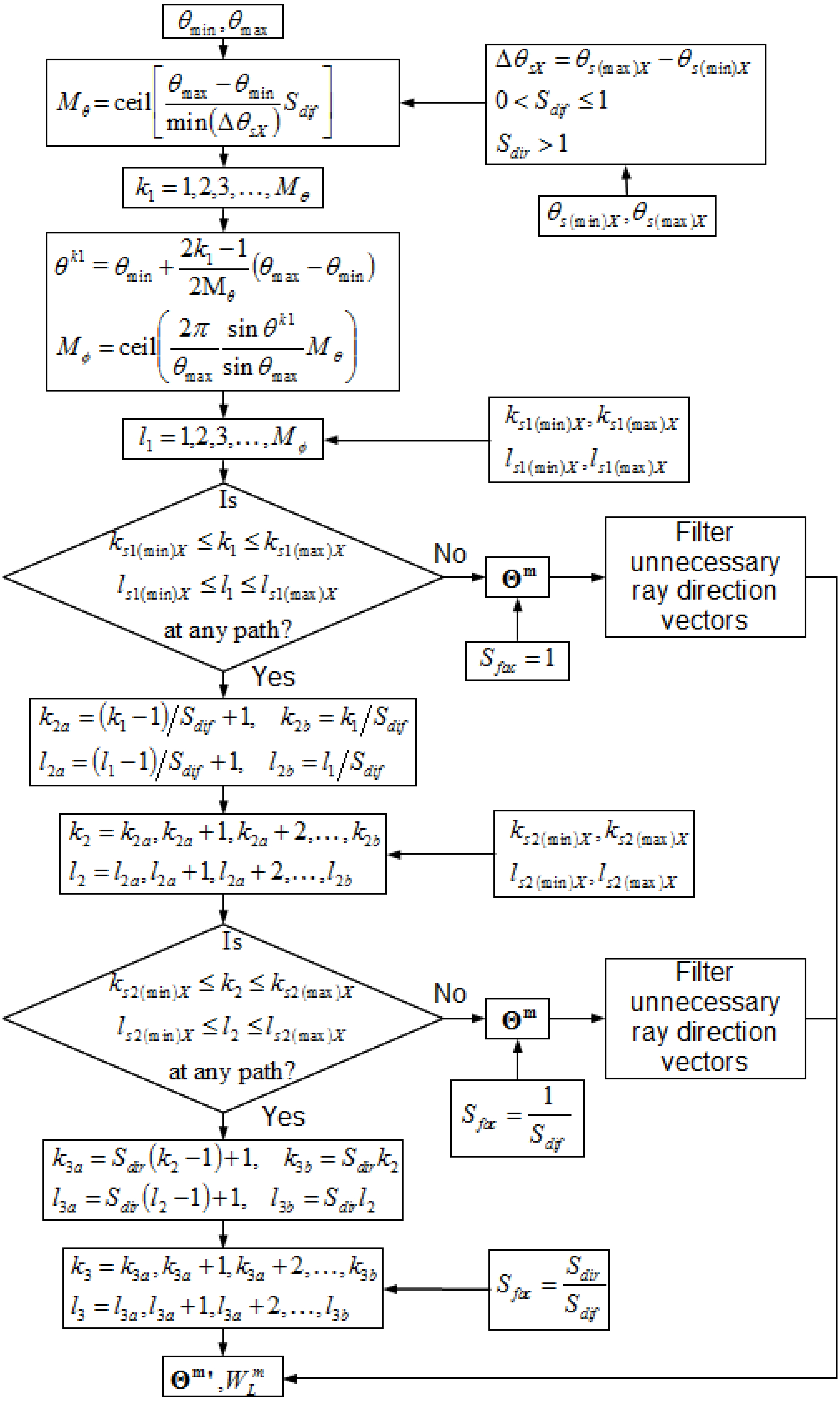

Figure 5.14: Overall algorithm to generate ray direction vectors optimized for planar LSC simulation.

To fit the overall flow chart in one page, some of the algorithms derived in Chapter 5.2-5.6 are denoted by just the output of the algorithm or their functions in simple words. The algorithm to determine the minimum and maximum polar angles in Chapter 5.2 is denoted by $\theta_{min},\theta_{max}$ in the flow chart, the algorithm to find out the range of polar angle for rays back-traced to the sun in Chapter 5.5.1 is denoted by $\theta_{s(min)X},\theta_{s(max)X}$, where the formulas for corresponding index for ray direction vector generation derived in Chapter 5.5.2 is denoted by $k_{s(min)X},k_{s(max)X},l_{s(min)X},l_{s(max)X}$ with the subscript X denotes the different path described in Chapter 5.4.3, while the process box labeled as "Filter unnecessary ray direction vectors" represents the method to remove direction vectors in which generated back-tracing rays will never come out from the LSC top surface described in Chapter 5.6.

The sub-algorithms as shown in Figure 5.15 are denoted by their corresponding output only in the overall flow chart (Figure 5.14).

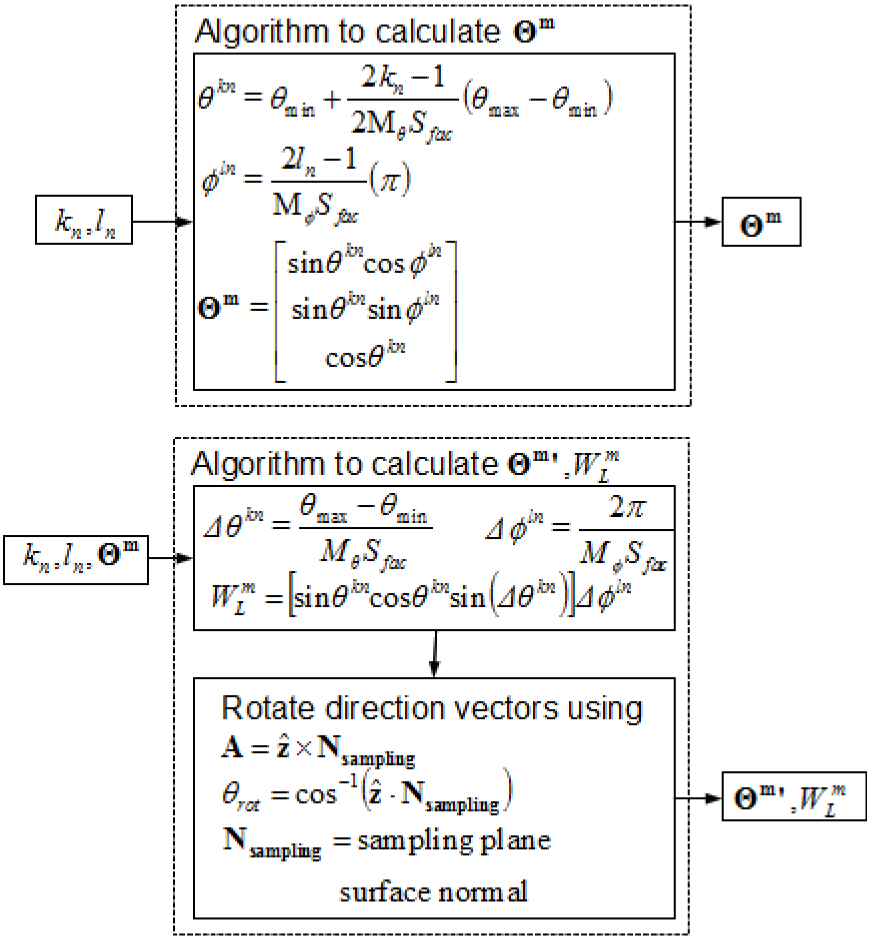

Figure 5.15: Sub-algorithm in the overall algorithm flow chart to generate ray direction vectors and their corresponding weights.

In short, the overall algorithm in Figure 5.14 can generate ray direction vectors where there are higher ray density on the directions where the rays are expected to back-traced to the sun, and lower ray density on tracing the diffuse part of the sunlight, as illustrated in Figure 5.16.

Refer to Figure 5.14, the minimum and maximum polar angle is first determined using the calculation in Chapter 5.2. Then the range of polar angle, $\theta_{s(min)X}$,$\theta_{s(max)X}$, where the sun can be back-traced by rays in the directions in the range is calculated using the algorithm in Chapter 5.5.1.

The factors S_{dif} and S_{dir} are then defined, where the factors will determine the total number of rays back-traced over a hemisphere and affect the accuracy of the simulation. Refer to Figure 5.16, S_{dif} is the ratio of $\Delta\theta^{k2}$ to $\Delta\theta^{k1}$, while S_{dir} is the ratio of $\Delta\theta^{k2}$ to $\Delta\theta^{k3}$, where $\Delta\theta^{k2}$ is approximately equal to the minimum of $\theta_{s(max)X}$-$\theta_{s(min)X}$ among all path X. So by definition, $0<S_{dif}\leq 1$ and $S_{dir}>1$. For example, $S_{dif}=1/6$ and $S_{dir}=4$ in Figure 5.16.

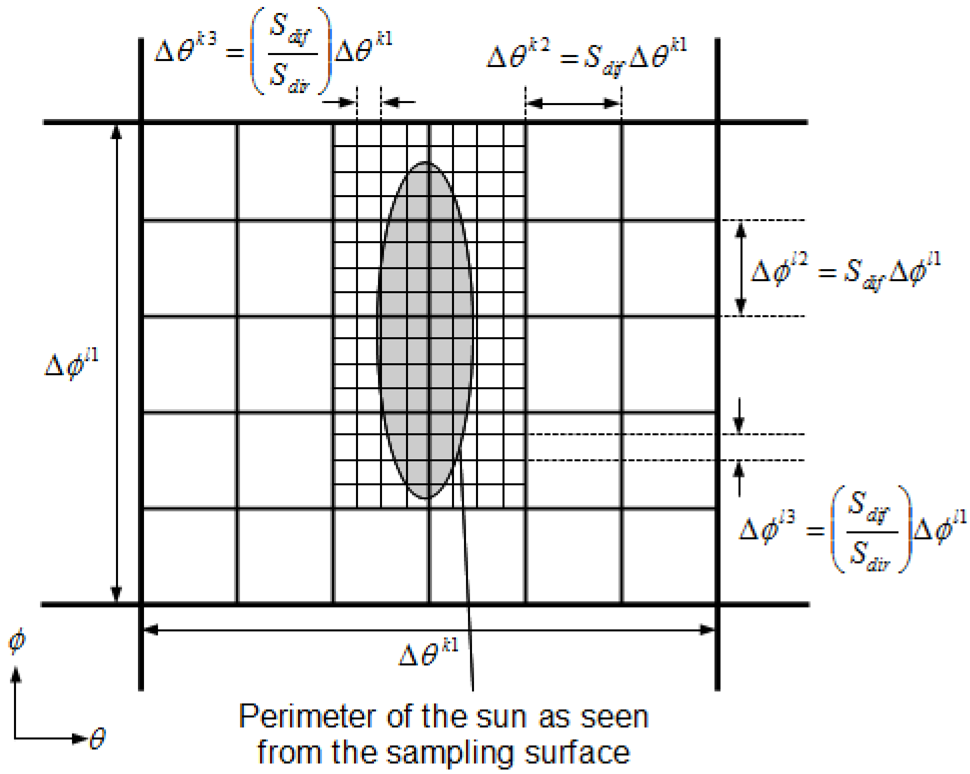

Figure 5.16: Effect of the improved overall algorithm to generate ray direction vectors for the ray-tracing program.

The value of M_θ is calculated by,

$$M_\theta = \text{ceil}\left[\frac{\theta_{\max} - \theta_{\min}}{\min(\Delta\theta_{sX})} S_{dif}\right] \tag{5.100}$$

Where the min function determine the minimum among all $\Delta\theta_{sX}$.

Then, M_ϕ is found using the algorithm in Chapter 5.3,

$$\theta^{k1} = \theta_{\min} + \frac{2k_1 - 1}{2\text{M}_\theta}(\theta_{\max} - \theta_{\min}) \tag{5.101}$$

$$M_\phi = \text{ceil}\left(\frac{2\pi}{\theta_{\max}} \frac{\sin\theta^{k1}}{\sin\theta_{\max}} M_\theta\right) \tag{5.102}$$

After that, the ray direction vector generation algorithm as shown in the top flow chart of Figure 5.15 is iterated with k_1=1,2,3,...,M_θ, l_1=1,2,3,...,M_ϕ with the substitution $\phi_{min}=0$, $\phi_{max}=2\pi$. The value of θ^{k1} is found from Eq. 5.101, while ϕ^{l1} and $\mathbf{\Theta^m}$ is

$$\phi^{l1} = \frac{2l_1 - 1}{\mathrm{M}_\phi}(\pi) \tag{5.103}$$

$$\mathbf{\Theta^m} = \begin{bmatrix} \sin\theta^{k1}\cos\phi^{l1} \\ \sin\theta^{k1}\sin\phi^{l1} \\ \cos\theta^{k1} \end{bmatrix} \tag{5.104}$$

Unnecessary ray direction vectors are filtered using the algorithm in Chapter 5.6. The ray direction vectors passing the filter algorithm is rotated as shown in the bottom flow chart of Figure 5.15 and their corresponding weights are calculated by

$$\varDelta\theta^{k1} = \frac{\theta_{\max} - \theta_{\min}}{M_\theta} \tag{5.105}$$

$$\varDelta\phi^{l1} = \frac{2\pi}{M_\phi} \tag{5.106}$$

$$W_L^m = \left[\sin\theta^{k1}\cos\theta^{k1}\sin\left(\varDelta\theta^{k1}\right)\right]\varDelta\phi^{l1} \tag{5.107}$$

The range of k_{s1} and l_{s1} are calculated using the algorithm in Chapter 5.5,

$$\text{Path X} : k_{s1(\min)X} = \text{floor}\left[\frac{\mathrm{M}_\theta\left(\theta_{s(\min)} - \theta_{\min}\right)}{\theta_{\max} - \theta_{\min}} + 1\right] \tag{5.108}$$

$$\text{Path X} : k_{s1(\max)X} = \text{ceil}\left[\frac{\mathrm{M}_\theta\left(\theta_{s(\max)} - \theta_{\min}\right)}{\theta_{\max} - \theta_{\min}}\right] \tag{5.109}$$

$$\text{Path X} : l_{s1(\min)X} = \text{floor}\left(\frac{\mathrm{M}_\phi\phi_{s(\min)}}{2\pi} + 1\right) \tag{5.110}$$

$$\text{Path X} : l_{s1(\max)X} = \text{ceil}\left(\frac{\mathrm{M}_\phi\phi_{s(\max)}}{2\pi}\right) \tag{5.111}$$

For every combination of k_1,l_1 which satisfies both $k_{s1(\min)X} \le k_1 \le k_{s1(\max)X}$ and $l_{s1(\min)X} \le l_1 \le l_{s1(\max)X}$ for any path X, the ray direction vectors are generated using smaller $\Delta\theta^k$ and $\Delta\phi^l$. The new index for the iterations is named k_2,l_2, where,

$$k_2 = k_{2a}, k_{2a}+1, k_{2a}+2, \ldots, k_{2b} \quad k_{2a} = (k_1 - 1)/S_{dif} + 1, k_{2b} = k_1/S_{dif} \tag{5.112}$$

$$l_2 = l_{2a}, l_{2a}+1, l_{2a}+2, \ldots, l_{2b} \quad l_{2a} = (l_1 - 1)/S_{dif} + 1, l_{2b} = l_1/S_{dif} \tag{5.113}$$

The ray direction vectors are then generated using,

$$\theta^{k2} = \theta_{\min} + \frac{2k_2 - 1}{2\mathrm{M}_\theta/S_{dif}}(\theta_{\max} - \theta_{\min}) \tag{5.114}$$

$$\phi^{l2} = \frac{2l_2 - 1}{\mathrm{M}_\phi/S_{dif}}(\pi) \tag{5.115}$$

$$\mathbf{\Theta^m} = \begin{bmatrix} \sin\theta^{k2}\cos\phi^{l2} \\ \sin\theta^{k2}\sin\phi^{l2} \\ \cos\theta^{k2} \end{bmatrix} \tag{5.116}$$

Unnecessary ray direction vectors are filtered out and the rotated ray direction vectors are calculated and their corresponding weights are,

$$\Delta\theta^{k2} = \frac{\theta_{\max} - \theta_{\min}}{M_\theta/S_{dif}} \tag{5.117}$$

$$\Delta\phi^{l2} = \frac{2\pi}{M_\phi/S_{dif}} \tag{5.118}$$

$$W_L^m = \left[\sin\theta^{k2}\cos\theta^{k2}\sin\left(\Delta\theta^{k2}\right)\right]\Delta\phi^{l2} \tag{5.119}$$

The range of k_{s2} and l_{s2} are calculated by,

$$\text{Path X}: k_{s2(\min)X} = \text{floor}\left[\frac{(\mathrm{M}_\theta/S_{dif})(\theta_{s(\min)} - \theta_{\min})}{\theta_{\max} - \theta_{\min}} + 1\right] \tag{5.120}$$

$$\text{Path X}: k_{s2(\max)X} = \text{ceil}\left[\frac{(\mathrm{M}_\theta/S_{dif})(\theta_{s(\max)} - \theta_{\min})}{\theta_{\max} - \theta_{\min}}\right] \tag{5.121}$$

$$\text{Path X}: l_{s2(\min)X} = \text{floor}\left[\frac{(\mathrm{M}_\phi/S_{dif})\phi_{s(\min)}}{2\pi} + 1\right] \tag{5.122}$$

$$\text{Path X}: l_{s2(\max)X} = \text{ceil}\left[\frac{(\mathrm{M}_\phi/S_{dif})\phi_{s(\max)}}{2\pi}\right] \tag{5.123}$$

Similarly, for all combination of k_2,l_2 that satisfy both $k_{s2(\min)X} \le k_2 \le k_{s2(\max)X}$ and $l_{s2(\min)X} \le l_2 \le l_{s2(\max)X}$ for any path X, the ray direction vectors are generated using even smaller $\Delta\theta^k$ and $\Delta\phi^l$. The new index for the iterations is named k_3,l_3, where,

$$k_3 = k_{3a}, k_{3a}+1, k_{3a}+2, \ldots, k_{3b} \quad k_{3a} = S_{dir}(k_2 - 1) + 1,\, k_{3b} = S_{dir}k_2 \tag{5.124}$$

$$l_3 = l_{3a}, l_{3a}+1, l_{3a}+2, \ldots, l_{3b} \quad l_{3a} = S_{dir}(l_2 - 1) + 1,\, l_{3b} = S_{dir}l_2 \tag{5.125}$$

The ray direction vectors are then generated using,

$$\theta^{k3} = \theta_{\min} + \frac{2k_3 - 1}{2\mathrm{M}_\theta S_{dir} / S_{dif}}(\theta_{\max} - \theta_{\min}) \tag{5.126}$$

$$\phi^{l3} = \frac{2l_3 - 1}{\mathrm{M}_\phi S_{dir} / S_{dif}}(\pi) \tag{5.127}$$

$$\mathbf{\Theta^m} = \begin{bmatrix} \sin\theta^{k3}\cos\phi^{l3} \\ \sin\theta^{k3}\sin\phi^{l3} \\ \cos\theta^{k3} \end{bmatrix} \tag{5.128}$$

Unnecessary ray direction vectors are then filtered out and the ray direction vectors are rotated. Their corresponding weights are,

$$\Delta\theta^{k3} = \frac{\theta_{\max} - \theta_{\min}}{M_\theta S_{dir} / S_{dif}} \tag{5.129}$$

$$\Delta\phi^{l3} = \frac{2\pi}{M_\phi S_{dir} / S_{dif}} \tag{5.130}$$

$$W_L^m = \left[\sin\theta^{k3}\cos\theta^{k3}\sin\left(\Delta\theta^{k3}\right)\right]\Delta\phi^{l3} \tag{5.131}$$

5.8 Separate Contribution from Direct and Diffuse Sunlight to Trapped Incident Light

When the incident light is sunlight, the trapped incident light discussed in Chapter 4.2.2 can be further divided into contribution from trapped direct sunlight and trapped diffuse sunlight.

5.8.1 Contribution from Direct Sunlight

The contribution from direct sunlight to the trapped incident light is named as trapped direct sunlight in the following chapters. It can be simulated by simply taking away the diffuse sunlight from the ray-tracing input file. It is expected to be dependent on the tilt angle of the LSC.

5.8.2 Contribution from Diffuse Sunlight

Trapped diffuse sunlight is used as the name of the contribution from diffuse sunlight to the trapped incident light for the subsequent chapters. Similar to the trapped direct sunlight, it can be simulated by simply removing the direct sunlight from the simulation input to the ray-tracing program. However, it is expected to be less dependent on the LSC tilt angle.

CHAPTER 6

INSTALLATION ORIENTATION STUDY OF LSC AT A SPECIFIC LOCATION BASED ON THE HYBRID ALGORITHM

6.1 Installation Environment and LSC Design

The overall flow chart of the simulation of electrical power and energy output from solar cells attached to the edge of a luminescent solar concentrator is shown in Figure 6.1. Simulation programs or models are represented process boxes in thick border, the rest are simulation input and output variables.

Simulation in this chapter can be separated into 3 parts: direct and diffuse solar irradiance spectrum simulation, irradiance spectrum received by the solar cells at the edge of LSC using the hybrid algorithm developed in Chapter 4, and solar cells electrical power output simulation using single diode model where photo-generated current is calculated by integrating the multiplication of solar cells internal quantum efficiency spectrum and irradiance spectrum from LSC. A brief introduction to the programs or algorithms involved in the simulation is given in the following paragraphs, and the detailed input to the programs or algorithms is outlined in the following sub-chapters.

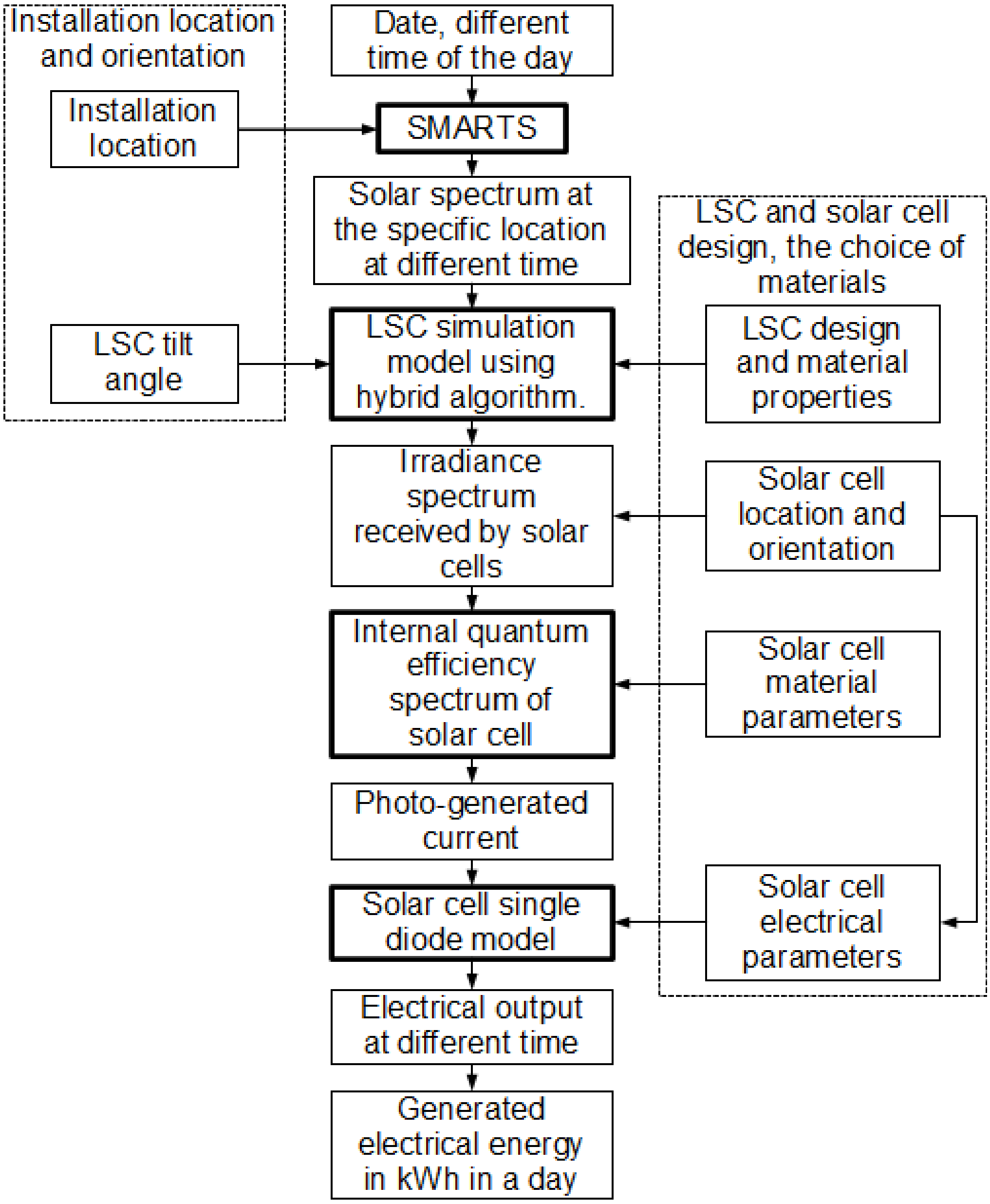

Figure 6.1: Overall flow chart of the electrical energy output simulation of solar cells attached to the LSC.

Solar irradiance spectrum simulation is done by an atmospheric radiadive transfer program called Simple Model of the Atmospheric Radiative Transfer of Sunshine (SMARTS) version 2.9.5. The program is able to simulate direct, diffuse and global irradiance spectrum incident on the earth surface at a user specified date/time. Its version 2.9.2 has been chosen to define the standard air mass 1.5 direct and global irradiance spectra (Gueymard *et al.*, 2002).

LSC simulation is done by the hybrid algorithm described in Chapter 4 taking the direct and diffuse solar irradiance spectra output from SMARTS as the input incident light spectra. The direction of the sun as seen from the specific location on the earth surface at different time is calculated using PSA Algorithm (Blanco-Muriel *et al.*, 2001), translated from a subroutine in the Fortran source code of SMARTS to MATLAB script. The sun direction together with its corresponding irradiance spectrum at differen time in a specific day then become the incident light input to the hybrid algorithm.

Once the irradiance spectrum received by the solar cells from the LSC is obtained from the hybrid algorithm, it is multiplied with solar cells internal quantum efficiency calculated from the solar cells material parameters using the algorithm described in a publication (Yang *et al.*, 2008). The integration of the multiplication of the two spectra with respect to wavelength gives the photo-generated current which is then the input to the single diode model for solar cells.

Electrical power output at different time is calculated from the single diode model which takes the solar cells electrical parameters as its input. Finally, generated electricity or electric energy (kWh) in that day can be calculated by integrating the electrical power output with respect to the time of the day.

6.2 Simulation of Solar Spectrum and Sun Direction

6.2.1 Simple Model of the Atmospheric Radiative Transfer of Sunshine

The location for the simulation is chosen as Kuala Lumpur, Malaysia with latitude and longitude of 3.133N, 101.683E, altitude of 21.95m. A particular date 1 March 2011 is set in the simulation. The atmosphere is assumed to be a clear sky throughout that day. Typical values for tropical zone and urban area or otherwise default values are used in the input parameters. Besides, it is set to generate spectra from 280nm to 4000nm in wavelength. All the input parameter values to SMARTS program, with brief description for each of them are shown in Table 6.1.

Table 6.1. Input parameters to SMARTS program.

Constant input values	
Input values	Description of the input values
KL MSIA on 1 MARCH 2011'	Card 1 Comment
1	Card 2 ISPR
1013.25 0.02195 0.	Card 2a Pressure, altitude, height
1	Card 3 IATMOS
TRL'	Card 3a Atmos
1	Card 4 IH2O
1	Card 5 IO3
1	Card 6 IGAS
391.48	Card 7 CO2 amount (ppm)
0	Card 7a ISPCTR
S&F_URBAN'	Card 8 Aeros (aerosol model)
0	Card 9 ITURB
0.084	Card 9a Turbidity coeff. (TAU5)
-1	Card 10 IALBDX
0	Card 10a RHOX
1	Card 10b ITILT

38 -999 -999		Card 10c IALBDG, TILT, WAZIM
280 4000 1.0 1367.0		Card 11 Min & max wavelengths; sun-earth distance correction; solar constant
2		Card 12 IPRT
280 4000 .5		Card12a Min & max wavelengths to be printed; ideal printing step size
3		Card12b Number of Variables to Print
3 5 6		Card12c Variable codes
0		Card 13 ICIRC
0		Card 14 ISCAN
0		Card 15 ILLUM
0		Card 16 IUV
3		Card 17 IMASS
Input values that change with time of the day		
Time	Input values	Description of the input values
0800	2011 3 1 8 3.133 101.683 8	Card 17a YEAR, MONTH, DAY, HOUR, LATIT, LONGIT,ZONE
1000	2011 3 1 10 3.133 101.683 8	
1200	2011 3 1 12 3.133 101.683 8	
1326	2011 3 1 13.433 3.133 101.683 8	
1400	2011 3 1 14 3.133 101.683 8	
1600	2011 3 1 16 3.133 101.683 8	
1800	2011 3 1 18 3.133 101.683 8	

The time listed in Table 6.1 is the local time at the installed location of LSC. It starts from 08:00 until 18:00 with a step of 2 hours. A particular time at 13:26 is also included where the sun makes the smallest angle to surface normal of the ground, or in other words, it is 12:00 in term of apparent time at the installation location.

Input parameters in Table 6.1 is supplied to the SMARTS program as input in the form of text document file, where the parameter values are listed in the sequence as shown in the table with the corresponding Card 17a input taken from one of the input values for the particular time. The SMARTS program output 3 spectra: diffuse horizontal irradiance, direct horizontal irradiance and direct tilted irradiance. Direct tilted irradiance spectrum, as shown in Figure 6.2, is the direct sunlight received by the surface facing to the sun on the ground. Diffuse horizontal irradiance, as shown in Figure 6.3, is the diffuse sunlight received by the horizontal ground surface. Only these 2 spectra are used to define the incident light for the hybrid algorithm. The SMARTS program was run for every time of the day to generate the corresponding direct and diffuse solar spectra for the corresponding time.

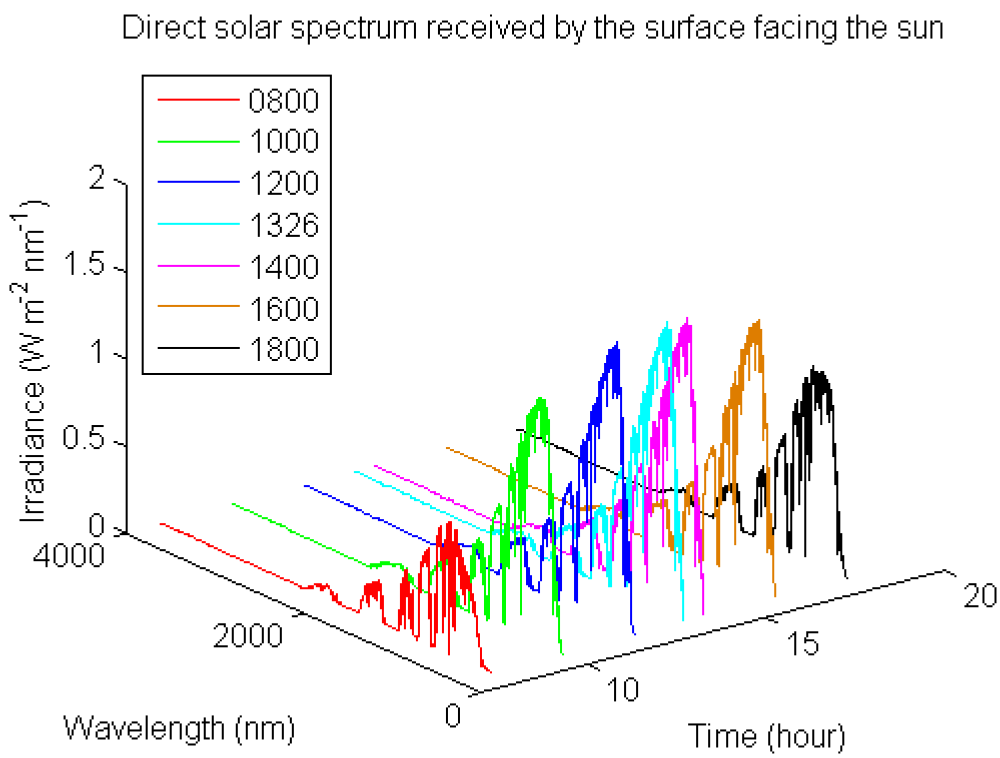

Figure 6.2: Direct solar spectra received by the surface on the ground facing the sun.

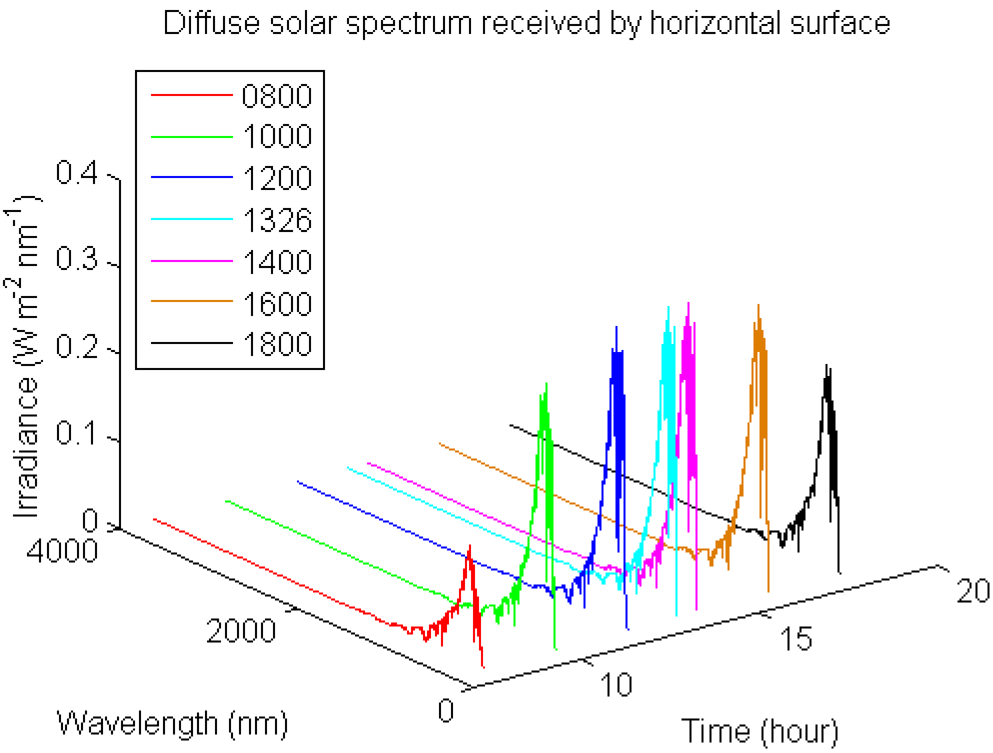

Figure 6.3: Diffuse solar spectra received by horizontal surface on the ground.

Radiance (in W m^{-2} sr^{-1} nm^{-1}) input of the direct and diffuse sunlight model is required for the hybrid algorithm, which is calculated from Eq. 4.78 in Chapter 4.3.3 with θ_{LED} replaced by half of the angle extended by the direct or diffuse sunlight, $\Delta\theta_{solar}/2$, i.e.,

$$L_{solar}(\lambda) = E_{solar}(\lambda) / \left[\pi \sin^2(\Delta\theta_{solar}/2)\right] \tag{6.1}$$

To get a smoother curve for faster simulation, the calculated radiance spectra are then curve fitted using an empirical formula which consists of a general blackbody radiation formula subtracted by a number of Gaussian functions. Finally, the curve-fitted radiance spectra are used as the incident light spectra input in the hybrid algorithm.

Instead of using the original wavelength limit 280nm-4000nm, the wavelength limit of all radiance spectra to be curve fitted is set to the range where all other input spectra are known. In other words, it was assumed that sunlight outside that wavelength limit does not contribute to electricity generation. Direct and diffuse solar radiance spectra, after the curve fitting are shown in Figure 6.4 and Figure 6.5 respectively.

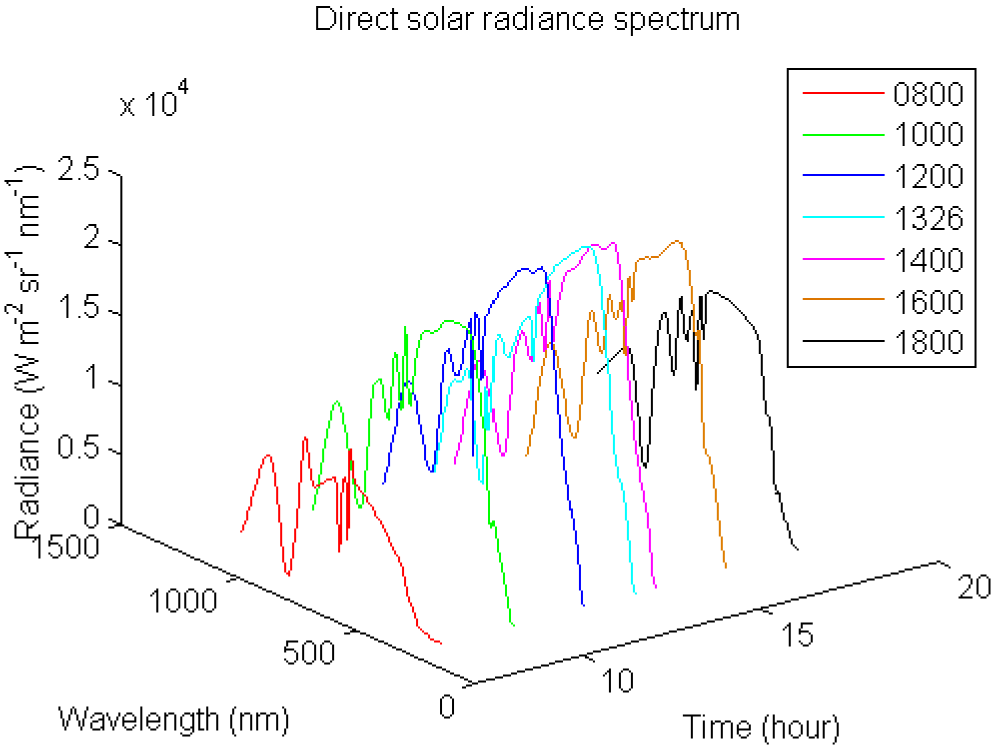

Figure 6.4: Direct solar radiance spectra.

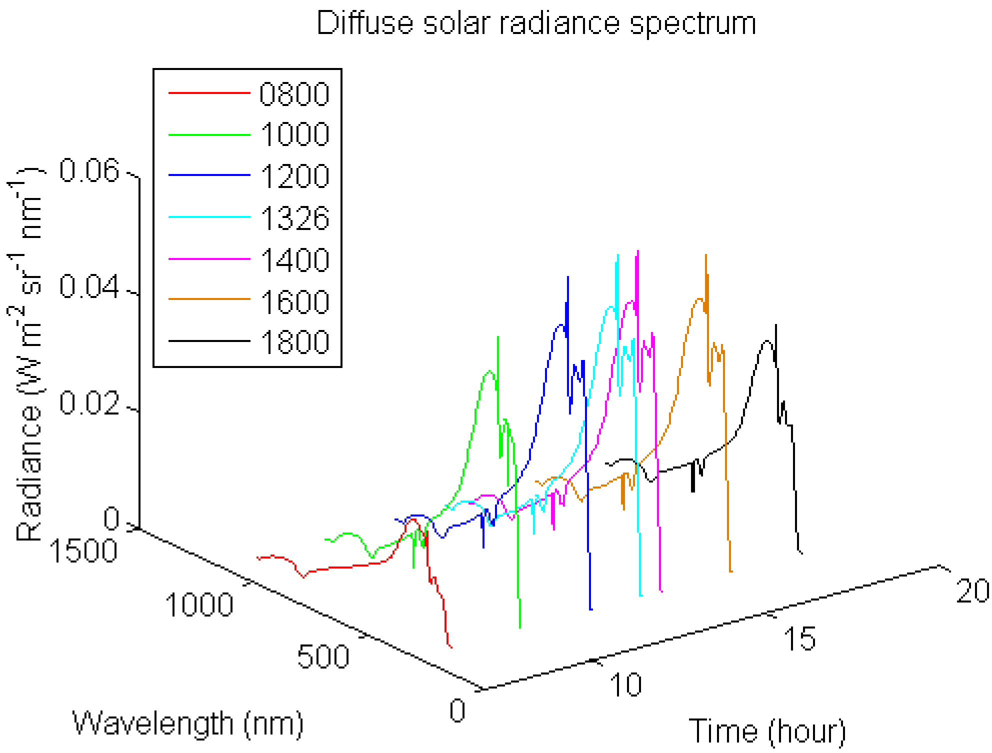

Figure 6.5: Diffuse solar radiance spectra.

6.2.2 Direction of the Sun as Seen from the Earth Surface

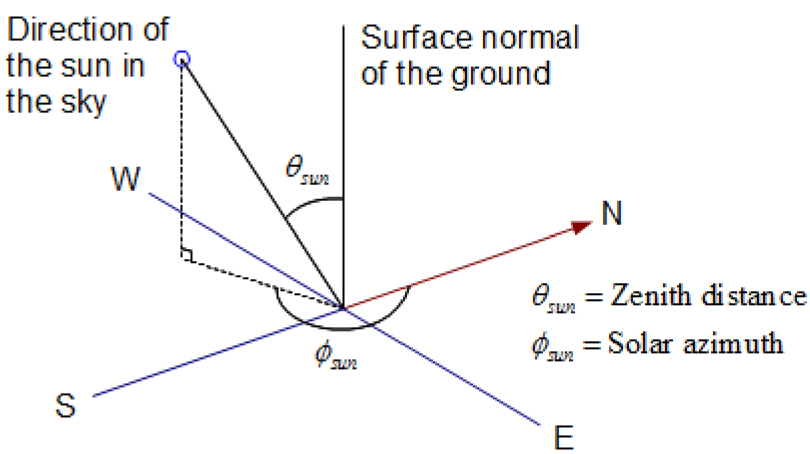

Figure 6.6: Solar azimuth and zenith distance.

The direction of the sun relative to the Earth surface is represented in horizontal coordinate system, i.e. by two angular variables: solar azimuth and zenith distance. The meaning of the two angles are illustrated in Figure 6.6, where the cross represent a compass on the ground or local horizon, with red arrow pointing to the north direction, labeled as "N", and directions to the east, south and west are represented by blue lines, labeled as "E", "S" and "W" respectively. The surface normal of the ground is called zenith, where zenith distance is angle of the sun direction relative to the zenith. Solar azimuth is the angle of the sun measured from the north, increasing toward the east around the horizon.

Solar azimuth and zenith distance of the sun at the installation location in the particular day are calculated using PSA algorithm (Blanco-Muriel *et al.*, 2001). Following paragraphs show the formulae in the algorithm for the ease of reference, while the detailed description of the algorithm and the meaning of all intermediate variables can be found in the cited reference.

The Julian Day, jd is calculated by

$$\begin{aligned} jd = &(1426\times(y+4800+(m-14)/12))/4 \\ &+(367\times(m-2-12\times((m-14)/12)))/12 \\ &-(3\times((y+4900+(m-14)/12)/100))/4 \\ &+d-32075-0.5+hour/24.0 \end{aligned} \tag{6.2}$$

Where y=year, m=month, d=day, and hour=hour of the day in Universal Time in decimal format. In the case of this simulation, y=2011, m=3, d=1, hour=0,2,4,5.433,6,8,10 which correspond to the local time of 08:00, 10:00, 12:00, 13:26, 14:00, 16:00, and 18:00 at Kuala Lumpur, Malaysia with time zone of UTC+8.

The ecliptic coordinates of the sun are,

$$\begin{aligned} l = &L+0.03341607\times\sin(g)+0.00034894\times\sin(2g) \\ &-0.0001134-0.0000203\times\sin(\Omega) \end{aligned} \tag{6.3}$$

$$ep = 0.4090928-6.2140\times10^{-9}\times n+0.0000203\times\cos(\Omega) \tag{6.4}$$

Where,

$$n = jd-2451545.0 \tag{6.5}$$

$$\Omega = 2.1429 - 0.0010394594 \times n \tag{6.6}$$
$$L = 4.8950630 + 0.017202791698 \times n \tag{6.7}$$
$$g = 6.2400600 + 0.0172019699 \times n \tag{6.8}$$

Convert to celestial coordinates,

$$ra = \tan^{-1}\left[\frac{\cos(ep) \times \sin(l)}{\cos(l)}\right] \tag{6.9}$$
$$\delta = \sin^{-1}[\sin(ep) \times \sin(l)] \tag{6.10}$$

Convert to horizontal coordinates,

$$\theta_{sun} = \theta_z + parallax \tag{6.11}$$
$$\phi_{sun} = \tan^{-1}\left[\frac{-\sin(\omega)}{\tan(\delta)\cos(latitude) - \sin(latitude)\cos(\omega)}\right] \tag{6.12}$$

Where θ_{sun} is the zenith distance, ϕ_{sun} is the solar azimuth, and the intermediate variables θ_z and *parallax* and ω are,

$$\theta_z = \cos^{-1}[\cos(latitude)\cos(\omega)\cos(\delta) + \sin(\delta)\sin(latitude)] \tag{6.13}$$
$$Parallax = \frac{EarthMeanRadius}{AstronomicalUnit} \times \sin(\theta_z) \tag{6.14}$$
$$EarthMeanRadius = 6371.01 \tag{6.15}$$
$$AstronomicalUnit = 149597890 \tag{6.16}$$
$$\omega = lmst - ra \tag{6.17}$$
$$lmst = (gmst \times 15 + longitude) \times (\pi/180) \tag{6.18}$$
$$gmst = 6.6974243242 + 0.0657098283 \times n + hour \tag{6.19}$$

The variables *longitude*=101.683° and *latitude*=3.133° are geographical longitude and latitude for Kuala Lumpur, Malaysia.

Table 6.2. Solar azimuth and zenith distance of the sun at different time.

Time	08:00	10:00	12:00	13:26	14:00	16:00	18:00
Solar azimuth	97.54°	101.31°	115.35°	180.97°	220.78°	255.39°	261.48°
Zenith distance	81.70°	52.20°	23.54°	10.04°	13.25°	39.87°	69.24°

Figure 6.7 shows the position of the sun on the sky as seen from the earth surface, using the values of solar azimuth and zenith distance in Table 6.2 calculated using the PSA algorithm. In the figure, the blue circles represent the positions of the sun at different time, together with a corresponding time label

next to each of them. A compass is shown on the ground with the direction of the north in red color. The smaller figure in the lower left corner is the two-dimensional view as seen from the east. Another two-dimensional view of Figure 6.7 as seen from the south is shown in Figure 6.8.

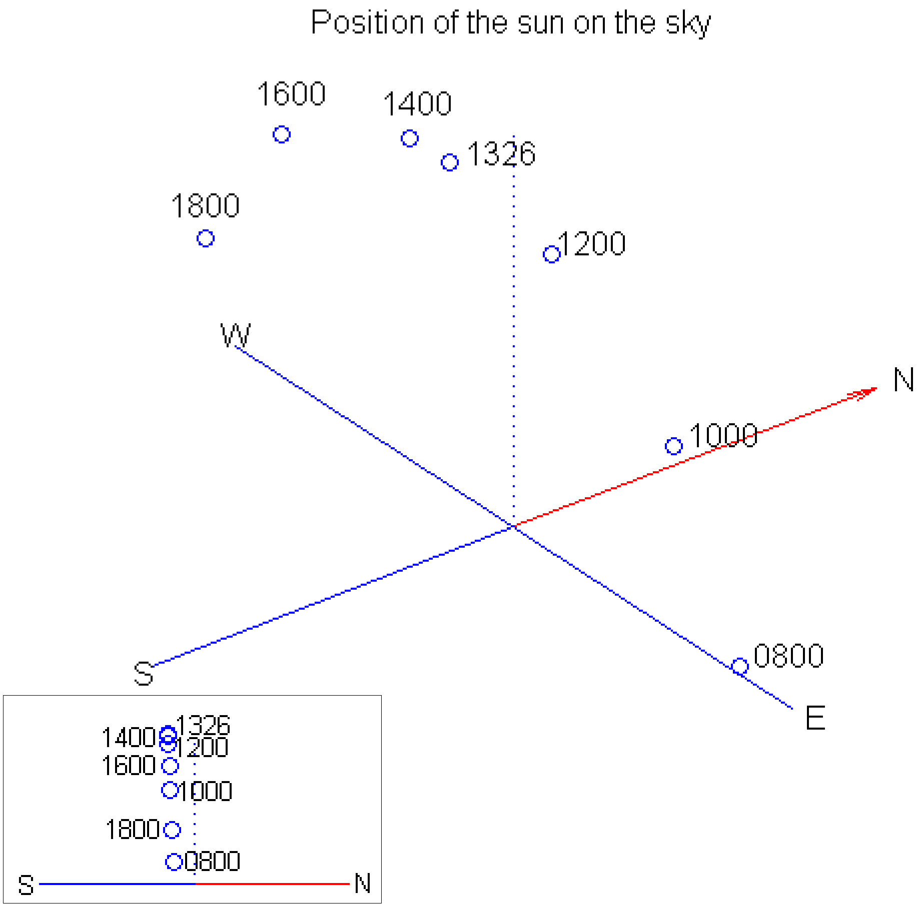

Figure 6.7: Directions of the sun at different time.

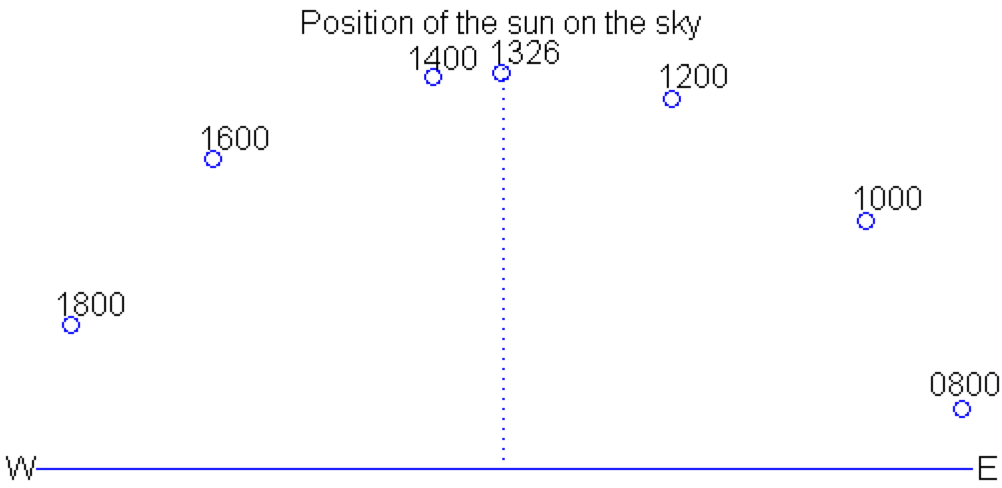

Figure 6.8: Directions of the sun at different time (viewed from the South).

6.3 Simulation of LSC Output

6.3.1 LSC Materials and Geometry

The LSC for the simulation in this chapter is made of Poly-methyl-methacrylate (PMMA) with Rhodamine 6G (Rh6G) as luminescent dye. Mirrors at the edge are assumed to be air-gap mirrors. Silicon solar cells are attached to the edge of the LSC which is facing the north. LSC design described in this paragraph is shown in Figure 6.9 with exaggerated air gap size for illustration purpose.

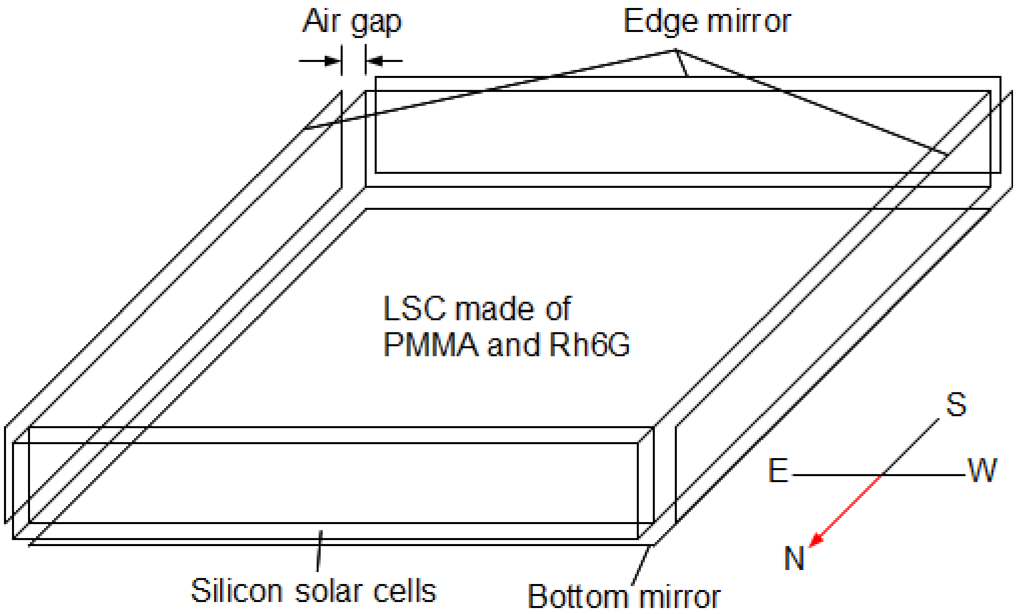

Figure 6.9: LSC in horizontal orientation with air-gap mirrors and silicon solar cells attached to the LSC edge facing north.

The sizes of each component in Figure 6.9 is shown in Figure 6.10. Thickness of the LSC is 2cm and its top surface area is 50cm x 50cm. The air gap between the mirrors and the LSC surface is 1 µm. Size of the bottom mirror is 50cm x 50cm where the size of mirror at the edge is 50cm x 2cm. Total surface area of the solar cells is 50cm x 2cm, with thickness of 1mm.

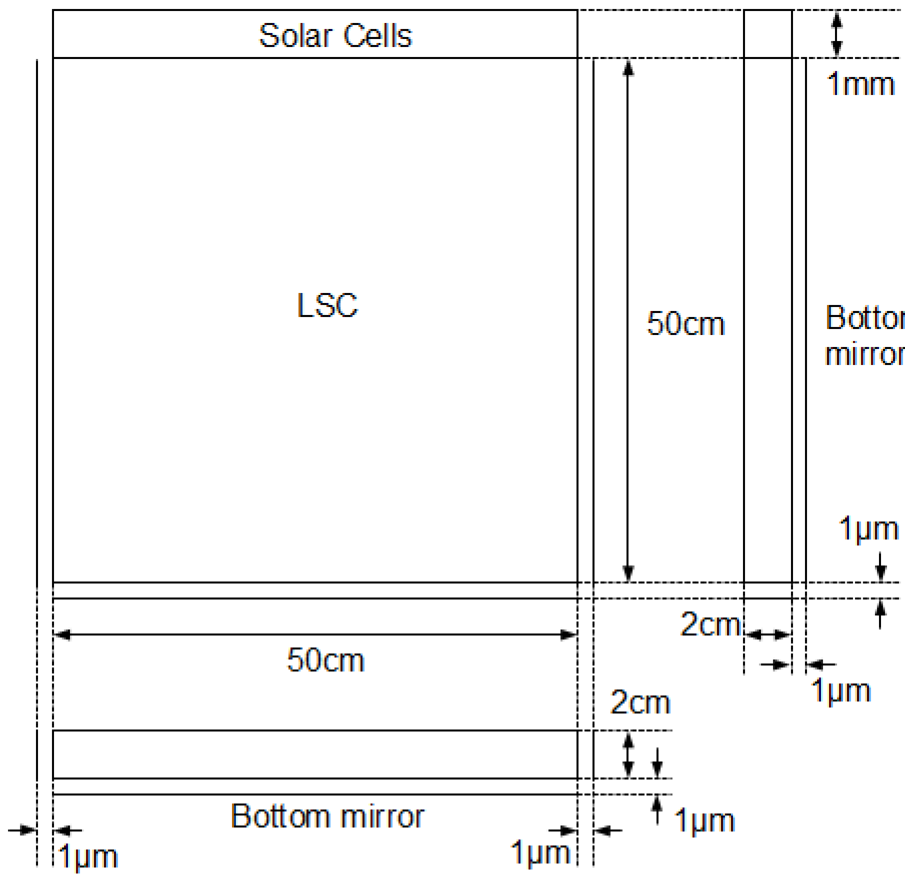

Figure 6.10: LSC geometry in the simulation (drawing not to scale).

The concentration of the dye, Rhodamine 6G is the same as the one used in Chapter 4.3 (3.75×10^{-5}M). Absorption cross section of Rhodamine 6G is shown in Figure 6.11. The absorption coefficient of the LSC host material, PMMA is $4m^{-1}$ (independent on wavelength, taken from (Burgers *et al.*, 2005)). Therefore the absorption coefficient of the LSC, as shown in Figure 6.12, is the summation from that of PMMA and absorption cross section of Rhodamine 6G multiplied by its concentration in number of dye particles per unit volume.

Refractive index of the LSC is 1.492 (independent on wavelength, assuming it is the same as the refractive index of the PMMA without any luminescent dye), and the solar cell refractive index is shown in Figure 6.21 from Chapter 6.4.1.

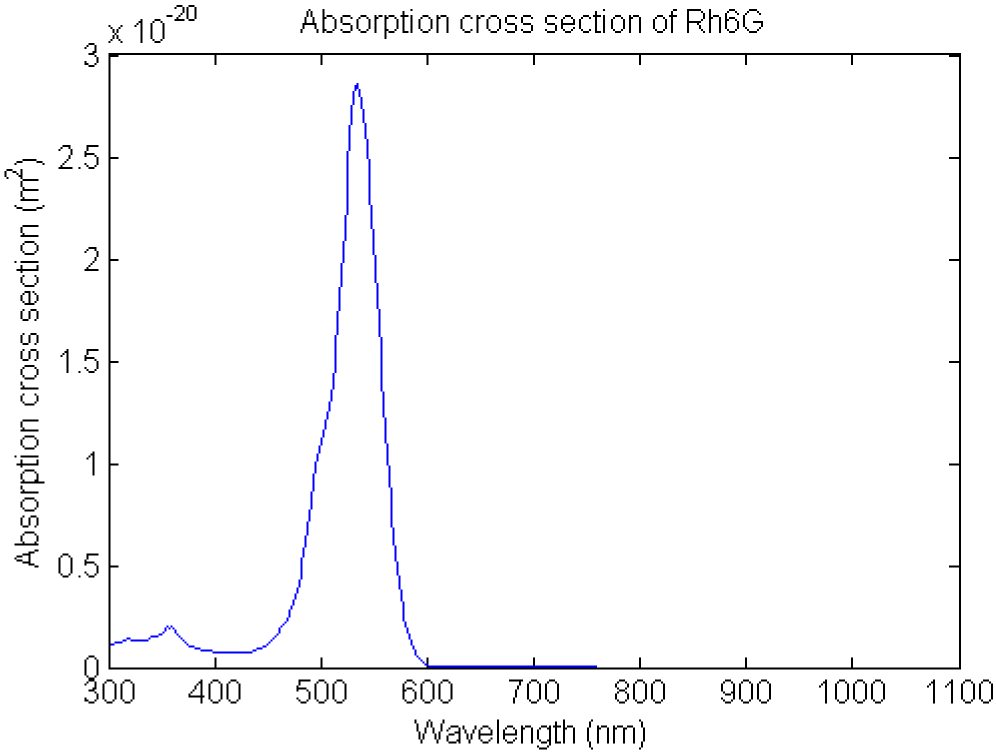

Figure 6.11: Absorption cross section of Rhodamine 6G.

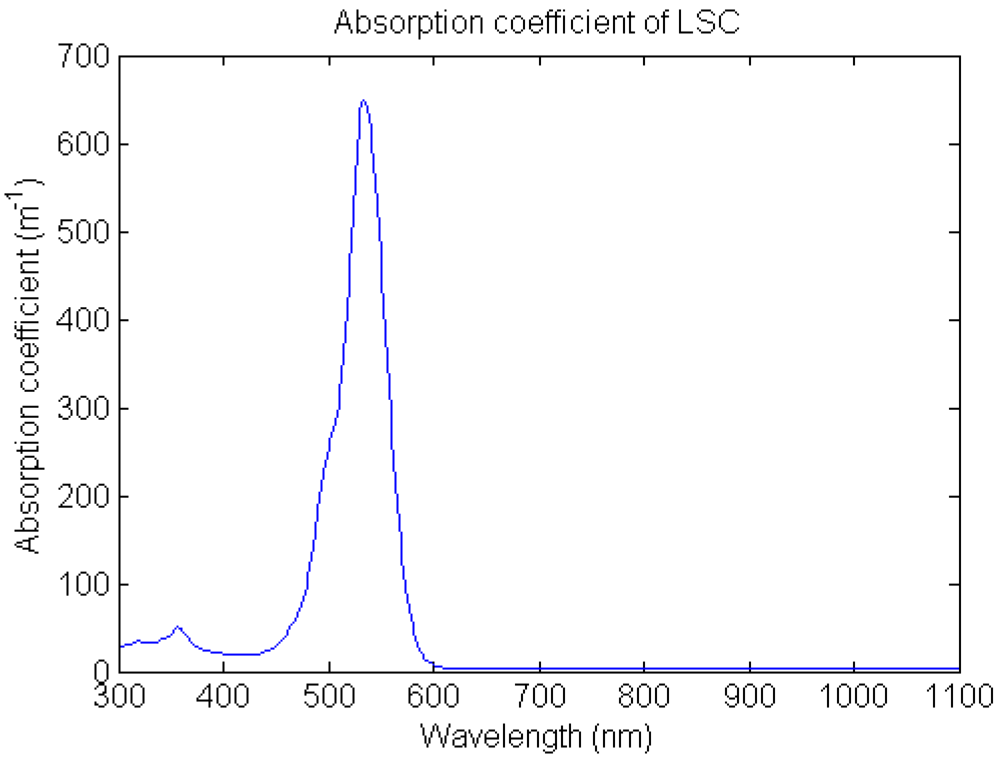

Figure 6.12: Absorption coefficient of the LSC.

6.3.2 Orientation of LSC

The LSC in horizontal orientation on the ground is shown in Figure 6.13. LSC in other orientation where it forms a non-zero tilt angle to the ground surface is shown in Figure 6.14 to Figure 6.17. In all cases, the LSC is placed in the orientation such that the edge where the solar cells are attached to is always facing the north, so that the solar cells can always receive more from the trapped direct incident sunlight.

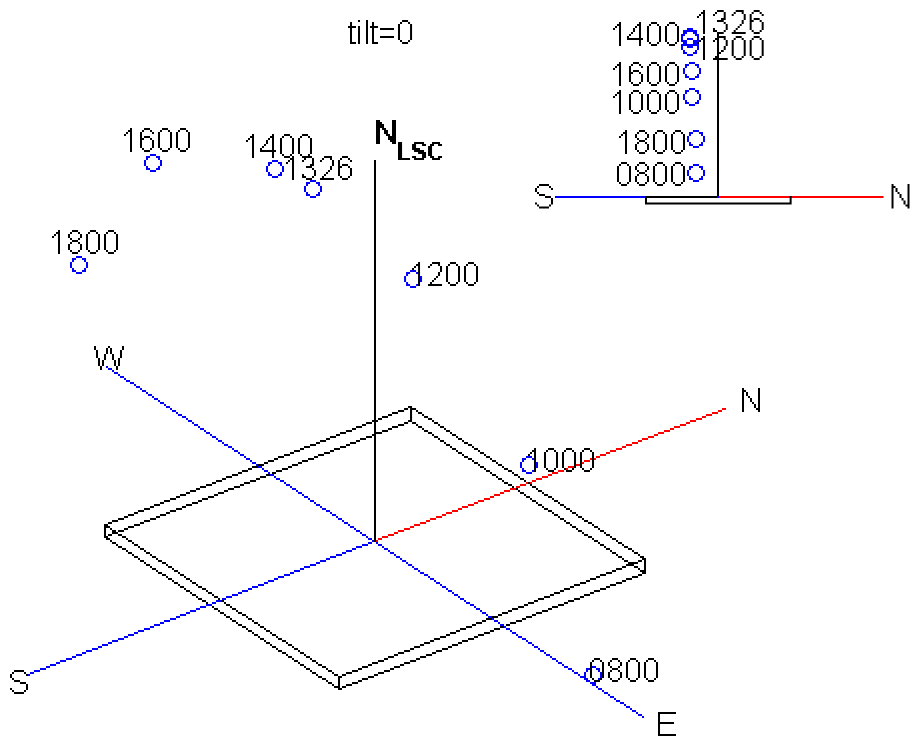

Figure 6.13: Horizontal installation of LSC.

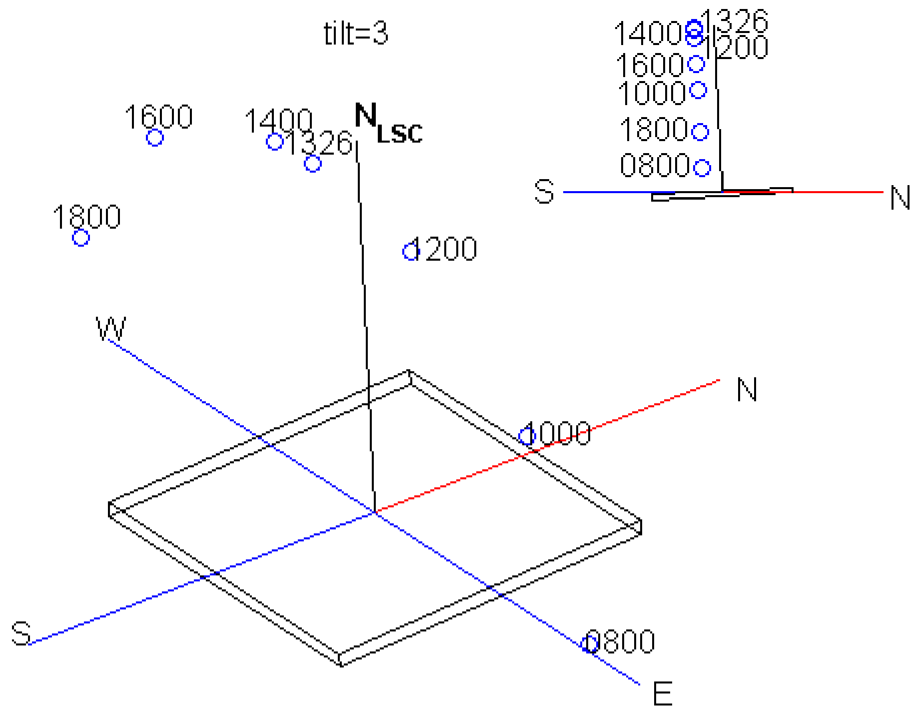

Figure 6.14: LSC tilted by 3 degree toward south.

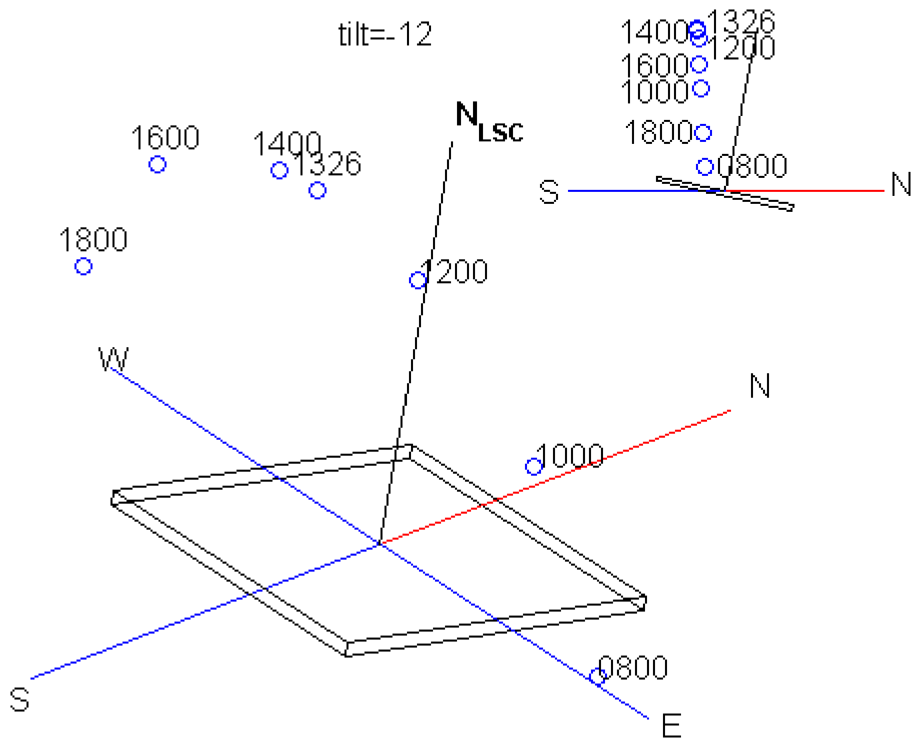

Figure 6.15: LSC tilted by 12 degree toward north.

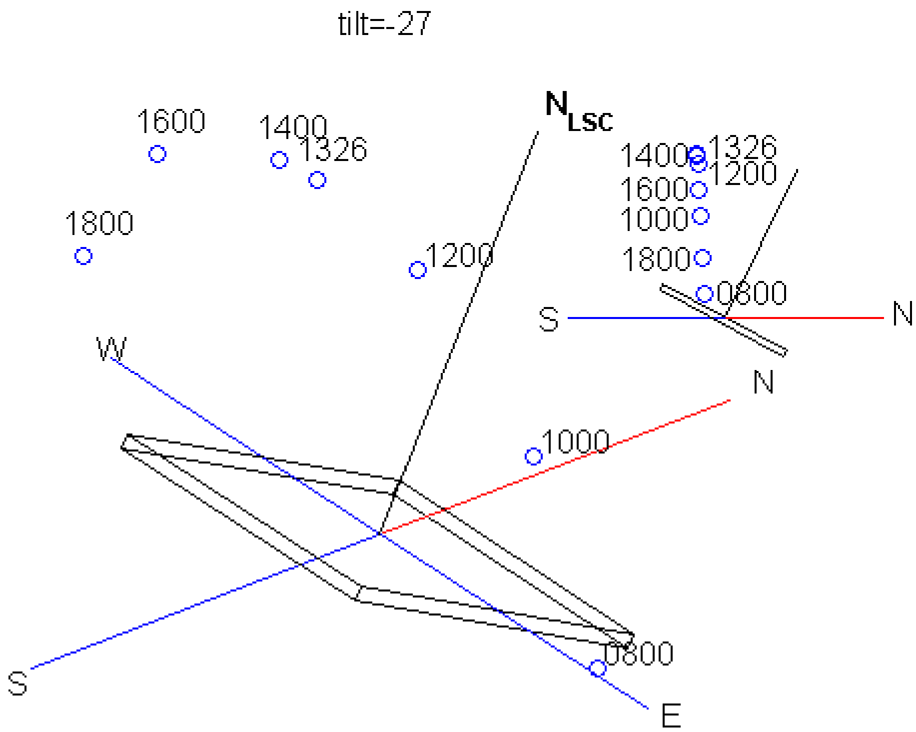

Figure 6.16: LSC tilted by 27 degree toward north.

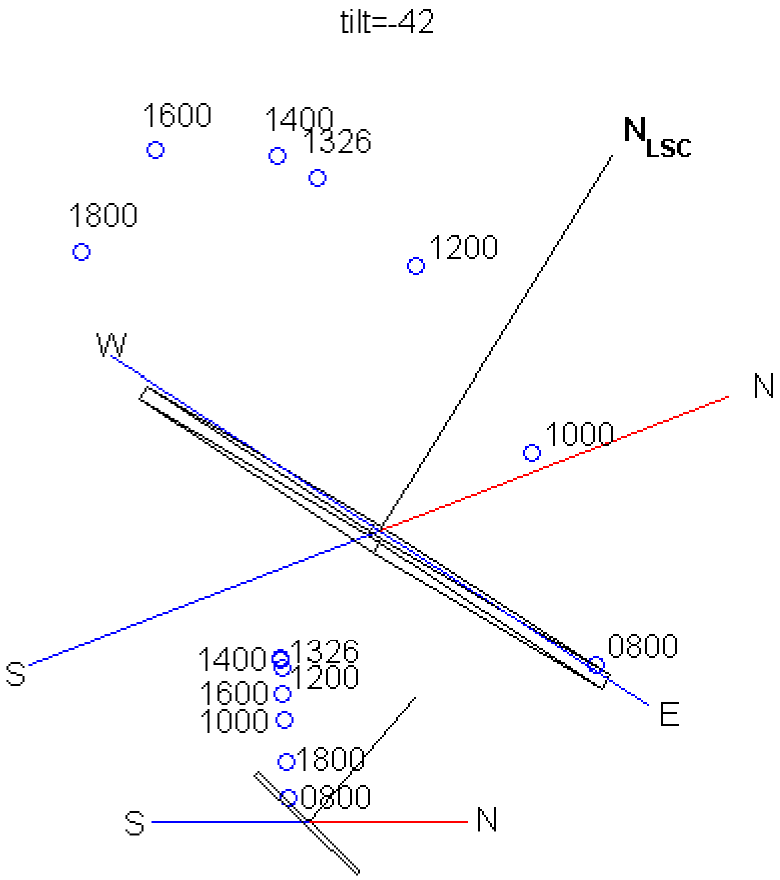

Figure 6.17: LSC tilted by 42 degree toward north.

6.3.3 Simulation Using Hybrid Algorithm

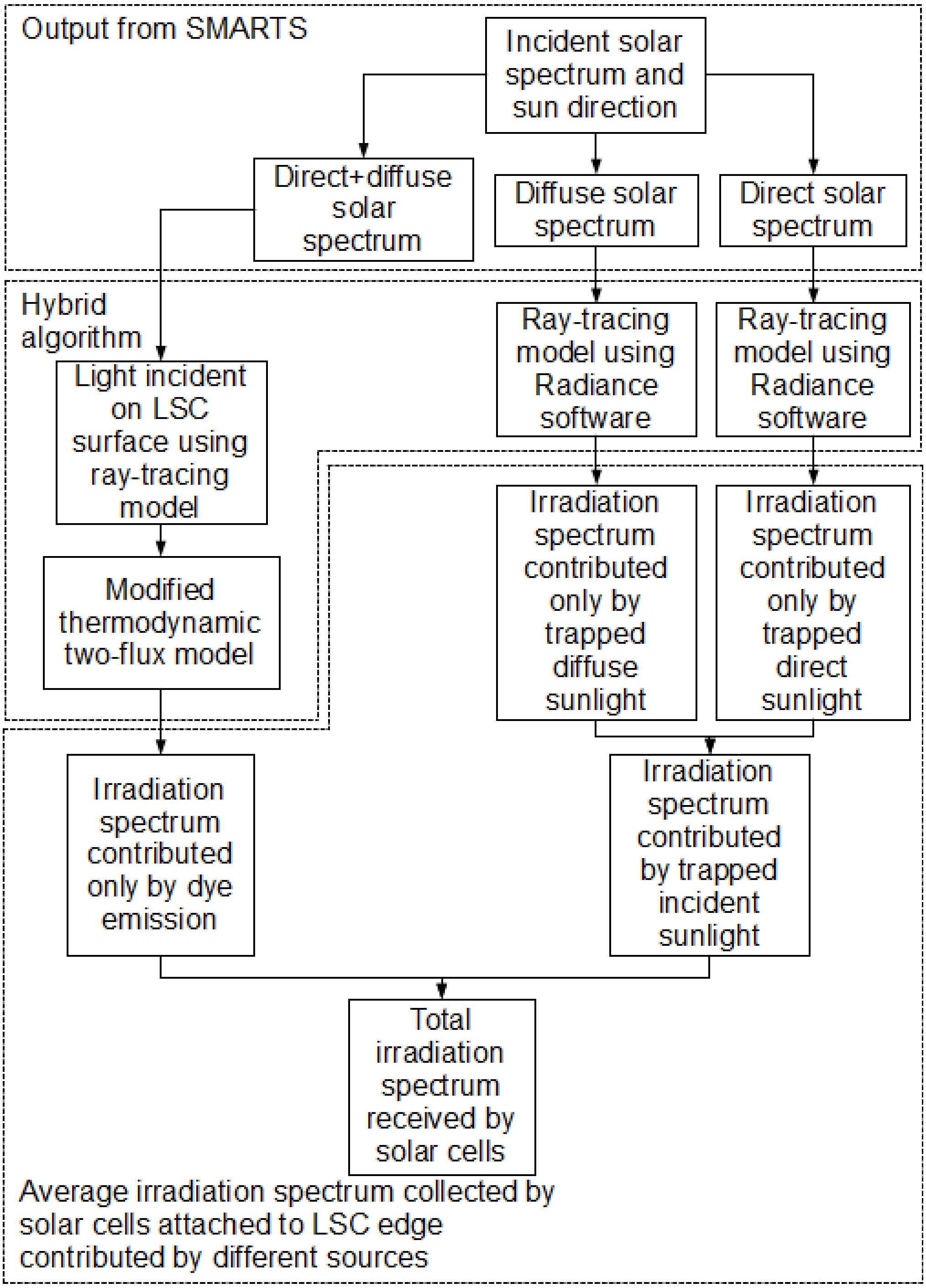

Figure 6.18: Flow chart for the simulation of irradiance spectrum received by the solar cells using hybrid algorithm.

The hybrid algorithm described in Chapter 4 was used here to determine the incident irradiance spectrum on the solar cells attached to one of the LSC edges. Flow charts for the overall algorithm, thermodynamic model, and ray-tracing model are shown in Figure 6.18, Figure 4.4, and Figure 4.7 respectively. Following modifications were made on the hybrid algorithm developed in Chapter 4 for the simulation cases in this chapter.

The list of direction vectors in Figure 4.7 were generated using the algorithm described in Chapter 5 with the factors S_{dif}=0.5 and S_{dir}=50. Light source in the simulation was modeled by direction of the light source center and angle extended by the light source. Two light sources were defined in Radiance scene file to model the contribution to trapped incident light from direct and diffuse sunlight separately, and also combined contribution from both of them.

To simplify the simulation, for different cases of LSC tilt, the sunlight light sources were tilted instead of tilting the LSC. In other words, the z-axis of coordinate system in the simulation was set to always align with the surface normal of the LSC, while the atmosphere was rotated in the opposite direction of the LSC tilt. Rotation of the light sources was done by converting the solar azimuth and zenith distance at different time into vectors, rotating the vectors using the algorithm in Appendix A, and finally converting back to solar azimuth and zenith distance. Since it is the direction of the atmosphere as seen by the tilted LSC surface, the new solar angles are named the apparent solar azimuth and apparent zenith distance. The apparent solar angles after the rotation is shown in Table 6.3. LSC tilt toward north by 12, 27, 42 degree are labeled as -12, -27, -42 degree tilt toward south respectively in the table.

In the simulation, direct sunlight is modeled as a light source subtended by 0.5331 degree, centered at direction listed in Table 6.3. Diffuse sunlight is modeled as a light source subtended by 180 degree, centered at direction of the z-axis tilted at an angle opposite to the LSC tilt angle.

Table 6.3. Apparent solar azimuth and zenith distance of the sun for different LSC tilt angles.

LSC tilt toward south	Time	08:00	10:00	12:00	13:26	14:00	16:00	18:00
3	Solar azimuth (°)	97.96	103.56	121.22	180.75	213.72	251.99	260.37
	Zenith distance (°)	82.10	52.85	24.96	13.04	15.64	40.71	69.71
0	Solar azimuth (°)	97.54	101.31	115.35	180.97	220.78	255.39	261.48
	Zenith distance (°)	81.70	52.20	23.54	10.04	13.25	39.87	69.24
-12	Solar azimuth (°)	95.65	91.79	86.30	355.07	282.29	270.13	266.18
	Zenith distance (°)	80.32	50.82	21.20	1.97	8.81	38.34	67.94
-27	Solar azimuth (°)	92.93	79.74	53.83	359.42	332.47	288.23	272.32
	Zenith distance (°)	79.19	51.94	26.56	16.96	18.90	40.78	67.75
-42	Solar azimuth (°)	89.99	69.16	36.58	359.68	344.01	302.38	278.26
	Zenith distance (°)	78.80	56.00	37.28	31.96	32.91	47.27	69.14

The average total irradiance received by LSC top surface is simulated by ray-tracing model, with only the LSC top surface, direct sunlight and diffuse sunlight included in the Radiance scene file for different cases of sun incident directions with their respective spectra and LSC tilt angles. Together with the calculated reflectance on the LSC top surface, they form two of the input parameters to the thermodynamic model.

Besides, for all simulation cases in this chapter, the solar cells are attached to the LSC edge perfectly without any airgap or intermediate material. This is possible if the solar cells are attached to the LSC during the molding process of LSC, where the top surface coating from ordinary solar cell is replaced directly by the LSC edge. Therefore, there will be no critical angle for the light travelling from the LSC to the solar cell, incident on the boundary between the two materials. The solid angle of the escape cones for the horizontal photon flux calculation using Eq. 4.27 in page 52 should be modified to account for the larger solid angle, which is the solid angle of a hemisphere excluding the solid angles of top and bottom escape cones as shown in the left hand side of Figure 6.19. Calculation detail of the horizontal photon flux for the simulation in this chapter is given in the following paragraphs.

The solid angle for horizontal escape flux at the boundary between LSC and solar cell is modeled using solid angle of effective escape cone as illustrated in Figure 6.19. The effective critical angle which is used in calculation of effective escape cone can be found by equating the solid angles at the two sides in Figure 6.19.

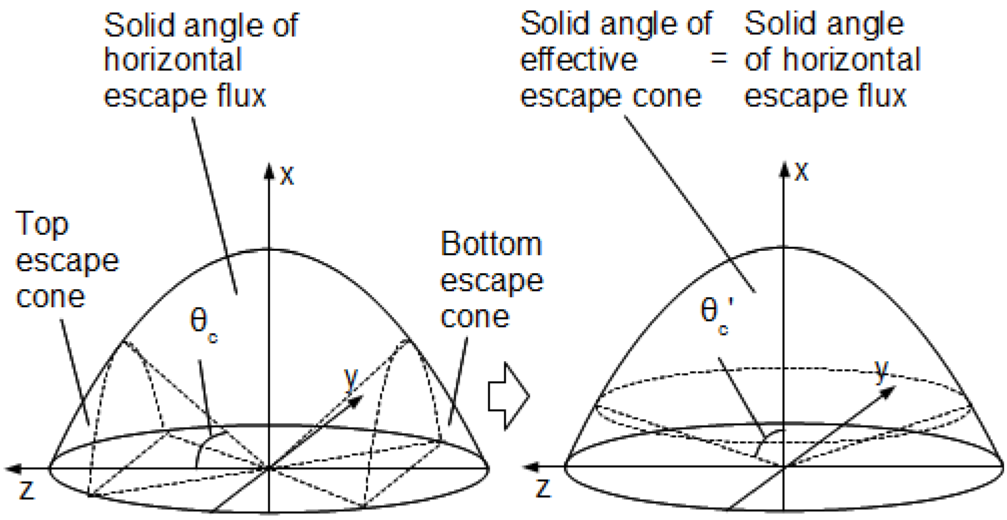

Figure 6.19: Modelling of solid angle for horizontal escape flux using effective escape cone in the calculation of horizontal escape flux.

Effective critical angle θ_C' can be calculated by,

$$\int_0^{2\pi}\int_0^{\theta_C}\sin\theta d\theta d\phi = \int_0^{2\pi}\int_{\theta_C'}^{\pi/2}\sin\theta d\theta d\phi \tag{6.20}$$

$$2\pi\left(1-\cos\theta_C\right) = 2\pi\left[\cos\theta_C' - \cos\frac{\pi}{2}\right] \tag{6.21}$$

$$\theta_C' = \cos^{-1}\left[1-\cos\theta_C\right] \tag{6.22}$$

Solid angle of effective escape cone can be calculated by,

$$\Omega_C' = \int_0^{2\pi}\int_0^{\theta_C'}\sin\theta d\theta d\phi = 2\pi\left(1-\cos\theta_C'\right) = 2\pi\cos\theta_C \tag{6.23}$$

To calculate the reflectance averaged over the solid angle at the boundary between LSC and solar cell, reflectance is integrated with respect to solid angle over the solid angle of horizontal escape flux as shown in left side of Figure 6.19, and then divided by the solid angle of horizontal escape flux.

$$R_L' = \frac{1}{\Omega_C'}\int_0^{2\pi}\int_0^{F(\phi)} R_{left}(\theta)\sin\theta d\theta d\phi \tag{6.24}$$

Where,

$$R_{left}(\theta) = \frac{1}{2}\left[\left(\frac{\sin(\theta-\theta_t)}{\sin(\theta+\theta_t)}\right)^2 + \left(\frac{\tan(\theta-\theta_t)}{\tan(\theta+\theta_t)}\right)^2\right] \tag{6.25}$$

$$\theta_t = \sin^{-1}\left[\frac{n_{LSC}}{n_{PV}}\sin\theta\right] \tag{6.26}$$

The function F in the inner integration upper limit describes the contour of the boundary for solid angle of horizontal escape flux in the left side of Figure 6.19, which is the hemisphere excluding top and bottom escape cones.

$$F(\phi)=\begin{cases} \dfrac{\pi}{2} & ,0 \le \phi < \dfrac{\pi}{2}-\theta_C \\ \cos^{-1}\left[\cos\theta_C\sqrt{\tan^2\theta_C\cot^2\phi}\right] & ,\dfrac{\pi}{2}-\theta_C \le \phi < \dfrac{\pi}{2}+\theta_C \\ \dfrac{\pi}{2} & ,\dfrac{\pi}{2}+\theta_C \le \phi < \dfrac{3\pi}{2}-\theta_C \\ \cos^{-1}\left[\cos\theta_C\sqrt{\tan^2\theta_C\cot^2\phi}\right] & ,\dfrac{3\pi}{2}-\theta_C \le \phi < \dfrac{3\pi}{2}+\theta_C \\ \dfrac{\pi}{2} & ,\dfrac{3\pi}{2}+\theta_C \le \phi < 2\pi \end{cases} \tag{6.27}$$

The function F(ϕ) is found by comparing the spherical coordinate unit vector representation of top escape cone with z-axis as polar axis to that with x-axis as polar axis as shown in Figure 6.20.

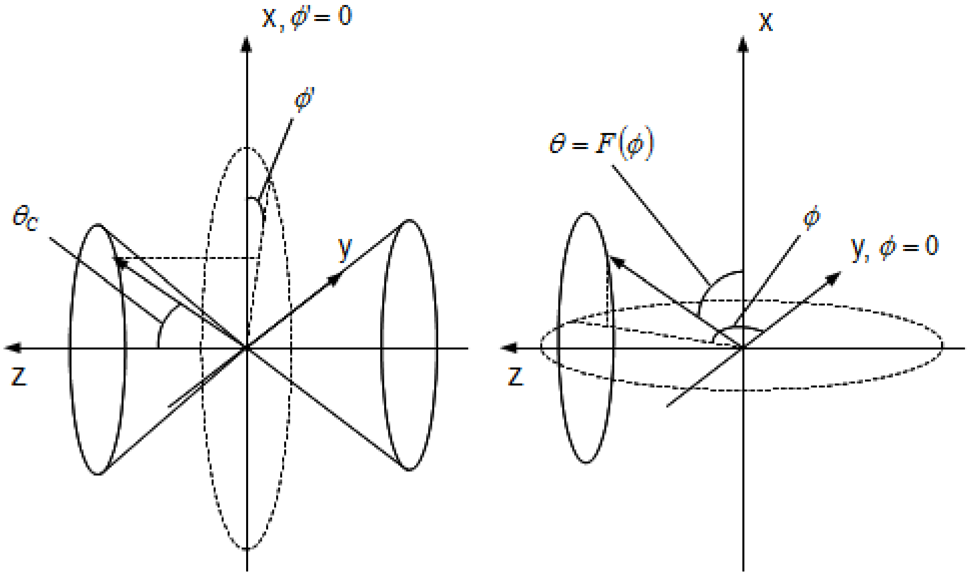

Figure 6.20: Representing top and bottom escape cones boundary using unit vector in spherical coordinate with z-axis as polar axis on the left and x-axis as polar axis on the right.

Using z-axis as polar axis, half of top escape cone in the left side of Figure 6.20 can be represented by,

$$\mathbf{V}_{\mathbf{z(top)}} = \begin{bmatrix} \sin\theta_C \cos\phi' \\ \sin\theta_C \sin\phi' \\ \cos\theta_C \end{bmatrix} \quad , -\frac{\pi}{2} \le \phi' \le \frac{\pi}{2} \tag{6.28}$$

It can also be represeted using x-axis as polar axis by,

$$\mathbf{V}_{\mathbf{x(top)}} = \begin{bmatrix} \cos\theta \\ \sin\theta\cos\phi \\ \sin\theta\sin\phi \end{bmatrix} \quad , \frac{\pi}{2} - \theta_C \le \phi < \frac{\pi}{2} + \theta_C \tag{6.29}$$

Compare Eq. 6.28 and Eq. 6.29,

$$\cos\theta = \sin\theta_C \cos\phi' \tag{6.30}$$

$$\sin\theta\cos\phi = \sin\theta_C \sin\phi' \tag{6.31}$$

$$\sin\theta\sin\phi = \cos\theta_C \tag{6.32}$$

Dividing Eq. 6.32 by Eq. 6.31,

$$\tan\phi = \cot\theta_C \csc\phi' \tag{6.33}$$

$$\sin\phi' = \cot\theta_C \cot\phi \tag{6.34}$$

$$\cos\phi' = \sqrt{1 - \cot^2\theta_C \cot^2\phi} \tag{6.35}$$

Substitute Eq. 6.35 into Eq. 6.30,

$$\cos\theta = \sin\theta_C \sqrt{1 - \cot^2\theta_C \cot^2\phi} \tag{6.36}$$

Rearrange Eq. 6.36 and simplify,

$$F(\phi) = \theta = \cos^{-1}\left[\cos\theta_C \sqrt{\tan^2\theta_C - \cot^2\phi}\right] \quad , \frac{\pi}{2} - \theta_C \le \phi < \frac{\pi}{2} + \theta_C \tag{6.37}$$

The function for bottom escape cone can be found by using symmetry. The azimutal angle in Eq. 6.37 is replaced by 2π-ϕ for bottom escape cone,

$$F(\phi) = \cos^{-1}\left[\cos\theta_C \sqrt{\tan^2\theta_C - \cot^2(2\pi - \phi)}\right] \quad , \frac{3\pi}{2} - \theta_C \le \phi < \frac{3\pi}{2} + \theta_C \tag{6.38}$$

$$F(\phi) = \cos^{-1}\left[\cos\theta_C \sqrt{\tan^2\theta_C - \cot^2\phi}\right] \quad , \frac{3\pi}{2} - \theta_C \le \phi < \frac{3\pi}{2} + \theta_C \tag{6.39}$$

Finally, the photon flux can be calculated by,

$$
\begin{aligned}
I_{Left(average)} = \frac{\Omega_C' \lambda_{Ee}}{2\pi D \lambda_{Ea}} \frac{\sinh(\alpha_L/2)}{\sinh(\lambda_{Ea} L + \alpha_{LR}')} \\
\times \left[\sinh(\lambda_{Ea} L + \alpha_R/2) - \sinh(\alpha_R/2)\right] \\
\times \int_0^D B(v, z')dz'
\end{aligned}
\tag{6.40}
$$

Where,

$$\alpha_{LR}' = \frac{\alpha_L' + \alpha_R}{2} \tag{6.41}$$

$$\alpha_L' = -\ln(R_L') \tag{6.42}$$

$$\alpha_R = -\ln(R_R) \tag{6.43}$$

The new variables, R_L' is found using Eq. 6.24 and Ω_C' is found using Eq. 6.23.

Other than the calculation of horizontal photon flux incident on the solar cells surface in thermodynamic model and the ray direction vectors generation algorithm in ray-tracing model, the simulation algorithms and formula used for thermodynamic model and ray-tracing model are the same as those described in Chapter 4.

6.4 Simulation of Solar Cell Output

It was assumed that the solar cell output becomes zero at sunrise and sunset, which are at time of 07:24 and 19:27 respectively. Both the zero output points at the two time are therefore included in the graphs of all solar cell output results for illustration purpose, but excluded from the tables. Calculation of generated electrical energy involves integration of the power at maximum power point with respect to time of the day where the integration limit is from 07:24 to 19:27.

Solar cells maximum output power (power at maximum power point) can be obtained from its power-voltage characteristic curve calculated using single diode model in this thesis. Two parameters in the single diode model, the photo-generated current and diode saturated current are dependent on and thus derived from the solar cell's carrier transport equations, which consists of a set of differential equations governing the carrier concentration in the solar cell.

For a flat-band p-n homojunction solar cell, after appropriate simplification under steady-state condition and several other assumptions, analytical solution for the carrier concentration can be derived from the differential equations, then the spectral photo-generated current density which depends on derivative of the carrier concentration can be calculated. The solution is then separated into multiplication of light spectrum received by the solar cell with its internal quantum efficiency (IQE), using the definition of IQE in Eq. 6.53. Only important formulas required to calculate the IQE from the publication (Yang *et al.*, 2008) is presented in this thesis. Detailed derivation can be found in the publication (Yang *et al.*, 2008) and citations therein.

Internal quantum efficiency is calculated instead of a direct calculation of photo-generated current because it can be used to show and evaluate how well is the spectral matching between solar cell and the light spectrum received by it, as discussed in detail in Chapter 7.2.3. Besides, external quantum efficiency (EQE) which takes into account of the surface reflection on the solar cell surface is not use in this thesis because the surface reflection depends on the boundary between the solar cell and LSC, which can be included in the simulation model of LSC. Moreover, surface reflection is different in the case where the solar cell is attached to the LSC without air-gap from the case where the solar cell is exposed directly to the sunlight, making it difficult to compare between the EQE for the two cases. Therefore calculating IQE is preferable in this thesis.

For the diode saturated current in this simulation, however, is not derived from the carrier transport equations as described in a publication (Castañer and Silvestre, 2002) because it is a constant term which is independent on the incident light spectrum. Therefore, to simplify the simulation, it was assumed to be the same as that calculated from the experiment measurement of a real silicon solar cell, together with other constant electrical parameters.

6.4.1 Solar Cell's Characteristics

Flat-band p-n homojunction silicon solar cell is used in the simulation. It is charaterized by its material parameters (Yang *et al.*, 2008), electrical parameters (Phang *et al.*, 1984), silicon absorption spectrum (Sze and Ng, 1981), and silicon refractive index (Philipp and Taft, 1960). Material parameters and electrical parameters of the solar cell are shown in Table 6.4 and Table 6.5 respectively, where the graph of silicon refractive index versus wavelength and graph of silicon absorption coefficient versus wavelength are shown in Figure 6.21 and Figure 6.22 respectively.

Table 6.4. Material parameters of silicon solar cell in the simulation.

Symbol	Name	Value

W_e	Width of emitter layer	0.5e-6 m
W_b	Width of base layer	298e-6 m
W_{scr}	Width of space charge region	1e-6 m
D_b	Electron diffusion constant in the base layer	3e-3 m^2 s^{-1}
D_e	Hole diffusion constant in the emitter layer	5e-4 m^2 s^{-1}
L_b	Electron diffusion length in the base layer	1e-4 m
L_e	Hole diffusion length in the emitter layer	1.5e-5 m
S_e	Emitter surface recombination velocity	100 m s^{-1}
S_b	Base surface recombination velocity	100000 m s^{-1}

Table 6.5. Electrical parameters of silicon solar cell in the simulation for single diode model.

Symbol	Name	Value
I_0	Diode saturated current	0.1034e-6 A
A	Diode quality factor	1.5017
R_s	Lumped series resistance	68.51e-3 Ω
R_{sh}	Lumped shunt resistance	1003.1 Ω
T_s	Temperature of solar cells	300 K

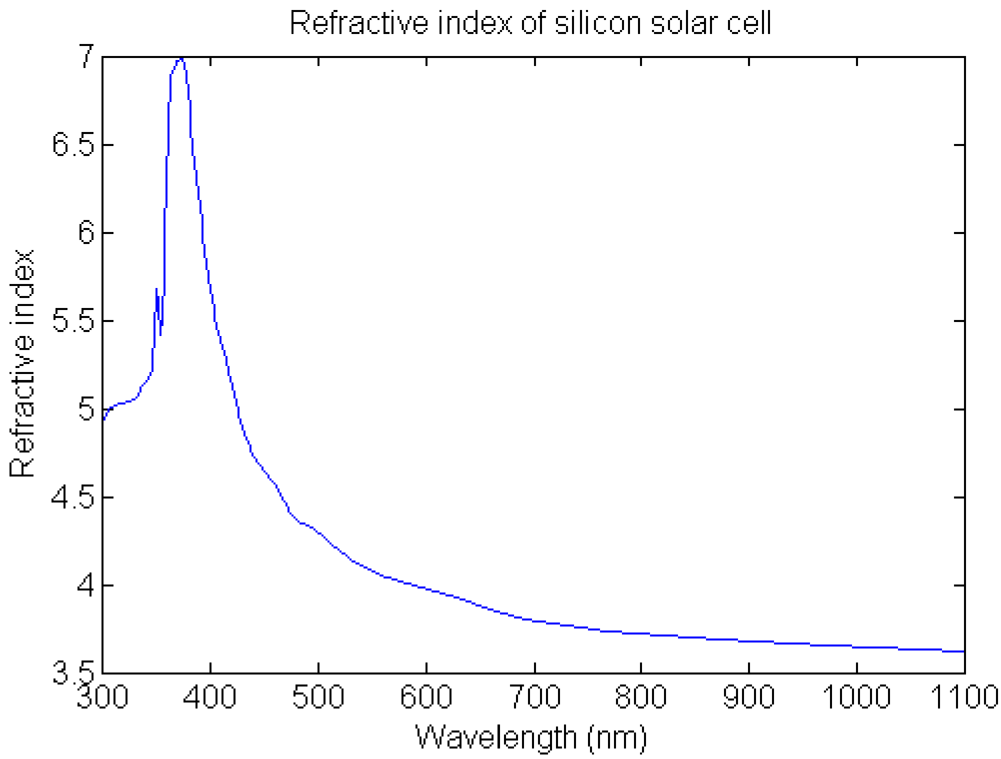

Figure 6.21: Refractive index of a silicon solar cell.

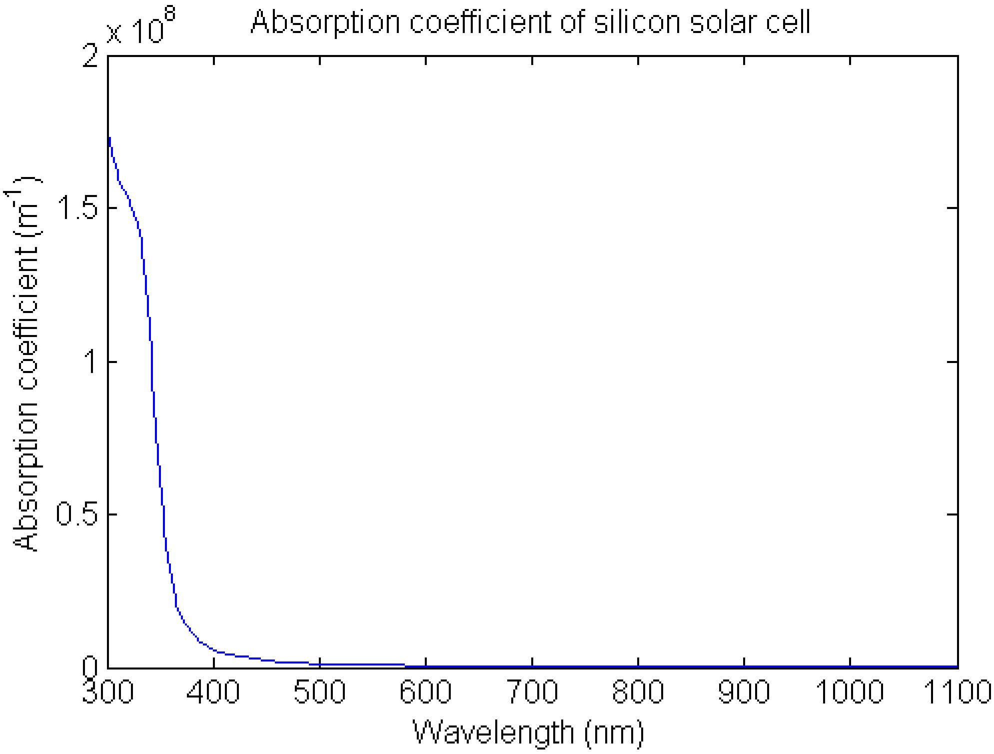

Figure 6.22: Absorption coefficient of a silicon solar cell.

6.4.2 Internal Quantum Efficiency of a Solar Cell

Given the light spectrum received by the solar cell, the solar cell photo-generated current can be calculated by integrating the spectral photo-generated current with respect to wavelength, where the spectral photo-generated current can be calculated by multiplying the received light spectrum with internal quantum efficiency of the solar cell.

The internal quantum efficiency of a solar cell (Yang *et al.*, 2008) is calculated by,

$$IQE(\alpha) = IQE_e(\alpha) + IQE_{scr}(\alpha) + IQE_b(\alpha) \tag{6.44}$$

Where,

IQE = Total internal quantum efficiency,

IQE_e = Internal quantum efficiency contributed by the emitter region,

IQE_{scr} = Internal quantum efficiency contributed by the space charge region,

IQE_b = Internal quantum efficiency contributed by the base region.

They are calculated by

$$\begin{aligned} IQE_b\left(\alpha \neq \frac{1}{L_b}\right) &= \frac{\alpha L_b}{(\alpha L_b)^2 - 1} e^{-\alpha \cdot w} \\ &\times \left[\alpha L_b - \frac{\zeta_b \cosh \frac{w_b}{L_b} + \sinh \frac{w_b}{L_b} + (\alpha L_b - \zeta_b) e^{-\alpha \cdot w_b}}{\zeta_b \sinh \frac{w_b}{L_b} + \cosh \frac{w_b}{L_b}} \right] \end{aligned} \tag{6.45}$$

$$\begin{aligned} IQE_e\left(\alpha \neq \frac{1}{L_e}\right) &= \frac{\alpha L_e}{(\alpha L_e)^2 - 1} \\ &\times \left[\frac{\zeta_e + \alpha L_e - \left(\zeta_e \cosh \frac{w_e}{L_e} + \sinh \frac{w_e}{L_e}\right) e^{-\alpha \cdot w_e}}{\zeta_e \sinh \frac{w_e}{L_e} + \cosh \frac{w_e}{L_e}} - \alpha L_e e^{-\alpha \cdot w_e} \right] \end{aligned} \tag{6.46}$$

$$IQE_{scr}(\alpha) = e^{-\alpha \cdot w_e}\left(1 - e^{-\alpha \cdot w_{scr}}\right) \tag{6.47}$$

$$\zeta_b = \frac{S_b \cdot L_b}{D_b} \tag{6.48}$$

$$\zeta_e = \frac{S_e \cdot L_e}{D_e} \tag{6.49}$$

$$w = w_e + w_{scr} \tag{6.50}$$

The IQE at the singularity points for Eq. 6.45 and Eq. 6.46 can be found by,

$$\lim_{\alpha \to 1/L_b} IQE_b(\alpha) = \frac{1}{2} e^{-w/L_b} \left[1 - \frac{1 - \frac{w_b}{L_b}\left(1 - \zeta_b\right)}{\zeta_b \sinh \frac{w_b}{L_b} + \cosh \frac{w_b}{L_b}} e^{-w_b/L_b} \right] \tag{6.51}$$

$$\lim_{\alpha \to 1/L_e} IQE_e(\alpha) = \frac{1}{2} \left[\frac{1 + \frac{w_e}{L_e}\left(\zeta_e + 1\right)}{\zeta_e \sinh \frac{w_e}{L_e} + \cosh \frac{w_e}{L_e}} - e^{w_e/L_e} \right] \tag{6.52}$$

A minor correction has been made on the formula from (Yang *et al.*, 2008) to calculate IQE_e at the limit $\alpha = 1/L_e$, hence detailed derivation of IQE_b at $\alpha = 1/L_b$ and IQE_e at $\alpha = 1/L_e$ are given in Appendix D.

Total internal quantum efficiency calculated using Eq. 6.44, together with its components, IQE_b from Eq. 6.45 (with Eq. 6.51 for $\alpha = 1/L_b$), IQE_e from Eq. 6.46 (with Eq. 6.52 for $\alpha = 1/L_e$), and IQE_{scr} from Eq. 6.47, are shown in Figure 6.23. The values of silicon solar cell's material parameters are taken from Table 6.4 and Figure 6.22.

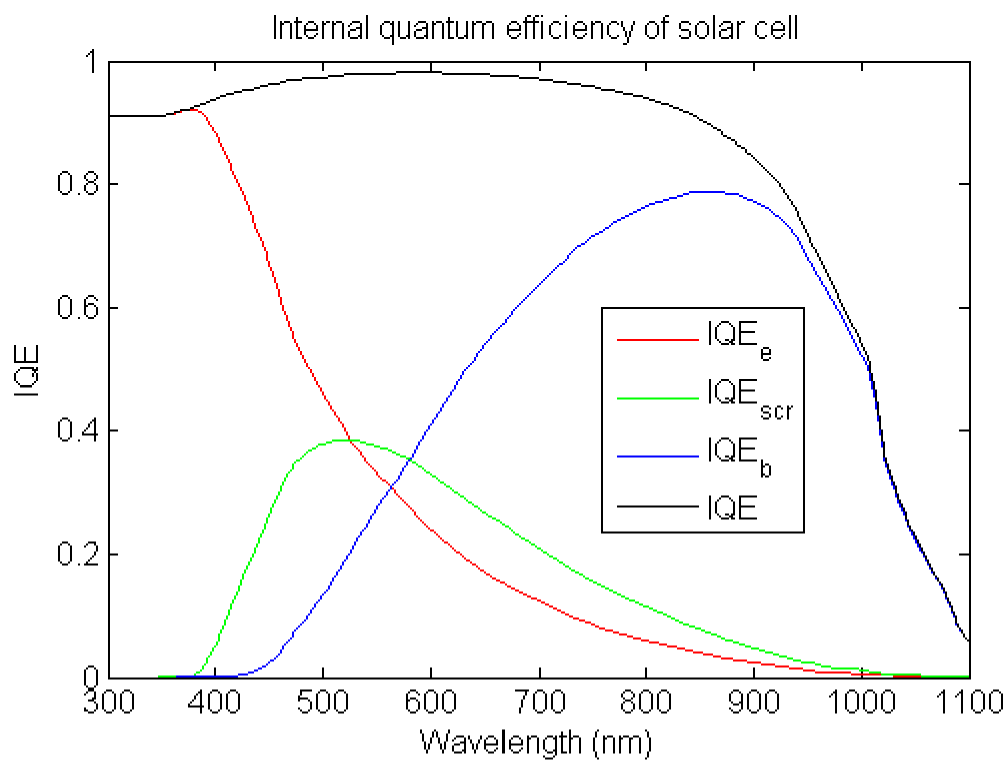

Figure 6.23: Internal quantum efficiency of solar cell in the simulation.

Internal quantum efficiency is related to the photogenerated current density by,

$$IQE(\lambda) = \frac{J_{ph}(\lambda)/e}{E_{pv}(\lambda)/(hc/\lambda)} \tag{6.53}$$

Where,

IQE(λ) = Internal quantum efficiency,

$J_{ph}(\lambda)$ = Spectral photogenerated current density (A m^{-2}),

$E_{pv}(\lambda)$ = Irradiance spectrum received by the solar cell after transmitted through its surface, obtained from the hybrid algorithm output (W m^{-2} nm^{-1}),

e = Elementary charge constant (C),

h = Planck constant (J s),

c = Speed of light in vacuum (m s^{-1}),

λ = Wavelength of light (nm).

The authors in the publication (Yang *et al.*, 2008) who derived the internal quantum efficiency equations used in this subchapter label the photogenerated current as short circuit current. However, the short circuit current defined in the form in Eq. 6.53 is actually the short circuit current measured at the internal solar cell terminals (Castañer and Silvestre, 2002), where the short circuit current defined in the next subchapter, which is calculated using the single diode model is the one measured at the external solar cell terminals. To avoid any disambiguition, it was renamed as photogenerated current here.

Rearrange Eq. 6.53,

$$J_{ph}(\lambda) = \frac{e\lambda}{hc} IQE(\lambda) E_{pv}(\lambda) \tag{6.54}$$

The photogenerated current can be found by integrating the spectral photo-generated current density in Eq. 6.54 with respect to wavelength then multiplied by a solar cell's area,

$$I_{ph} = A_{pv} \times \int J_{ph}(\lambda)\, d\lambda = A_{pv} \times \int \frac{e\lambda}{hc} IQE(\lambda) E_{pv}(\lambda)\, d\lambda \tag{6.55}$$

Where A_{pv} is a solar cell's area.

6.4.3 Single Diode Model for Solar Cells

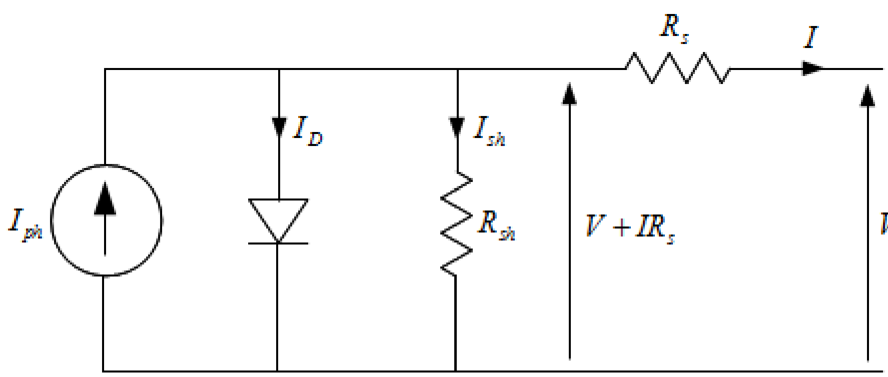

Figure 6.24: Equivalent circuit of a solar cell in single diode model.

The equivalent circuit as shown in Figure 6.24 represents a solar cell in single diode model. From the circuit,

$$I_D = I_0\left[\exp\left(\frac{V+IR_s}{AV_T}\right)-1\right] \tag{6.56}$$

$$I_{sh} = \frac{V+IR_s}{R_{sh}} \tag{6.57}$$

$$I_D + I_{sh} + I = I_{ph} \tag{6.58}$$

Substitute Eq. 6.56 and Eq. 6.57 into Eq. 6.58,

$$I = I_{ph} - I_0\left[\exp\left(\frac{V+IR_s}{AV_T}\right)-1\right]-\frac{V+IR_s}{R_{sh}} \tag{6.59}$$

Where,

$$V_T = \frac{kT_s}{e} \tag{6.60}$$

I = Solar cell output current (A),

V = Solar cell output voltage (V),

k = Boltzmann constant (J K^{-1}),

e = Elementary charge constant (C).

The meaning of other symbols in Eq. 6.59 and Eq. 6.60 together with their corresponding values used in the simulation are shown in Table 6.5.

In the simulation, a total of 23 solar cells are attached to the LSC edge (50cm x 2cm) where each of them having the size of 2.17cm x 2cm (total solar cell area of 49.91cm x 2cm) . All the solar cells are connected in series.

For n_s number of identical solar cells connected in series, denote V_1 and I_1 to be the voltage and current output from a single solar cell,

$$I = I_1 \tag{6.61}$$

$$V = n_s V_1 \tag{6.62}$$

Replace I and V by I_1 and V_1 in Eq 6.59,

$$I_1 = I_{ph} - I_0\left[\exp\left(\frac{V_1 + I_1R_s}{AV_T}\right) - 1\right] - \frac{V_1 + I_1R_s}{R_{sh}} \tag{6.63}$$

Substitute Eq. 6.61 and Eq. 6.62 into Eq. 6.63,

$$I = I_{ph} - I_0\left[\exp\left(\frac{\frac{V}{n_s} + IR_s}{AV_T}\right) - 1\right] - \frac{\frac{V}{n_s} + IR_s}{R_{sh}} \tag{6.64}$$

$$I = I_{ph} - I_0\left\{\exp\left[\frac{V + I(n_sR_s)}{(n_sA)V_T}\right] - 1\right\} - \frac{V + I(n_sR_s)}{(n_sR_{sh})} \tag{6.65}$$

Therefore series connection of the solar cell can be calculated using the same equation in Eq. 6.59 by replacing R_s by n_sR_s, R_{sh} by n_sR_{sh}, and A by n_sA.

The single diode model equation as shown in Eq. 6.59 is solved numerically using Newton's method. The algorithm as shown in Figure 6.25 is used to draw the IV characteristic curve, PV curve, and solve for the short circuit current, where the values of V are given and the values of corresponding I are solved using the algorithm. The value of open circuit voltage is solved using the algorithm described in Figure 6.26, given the value of I=0.

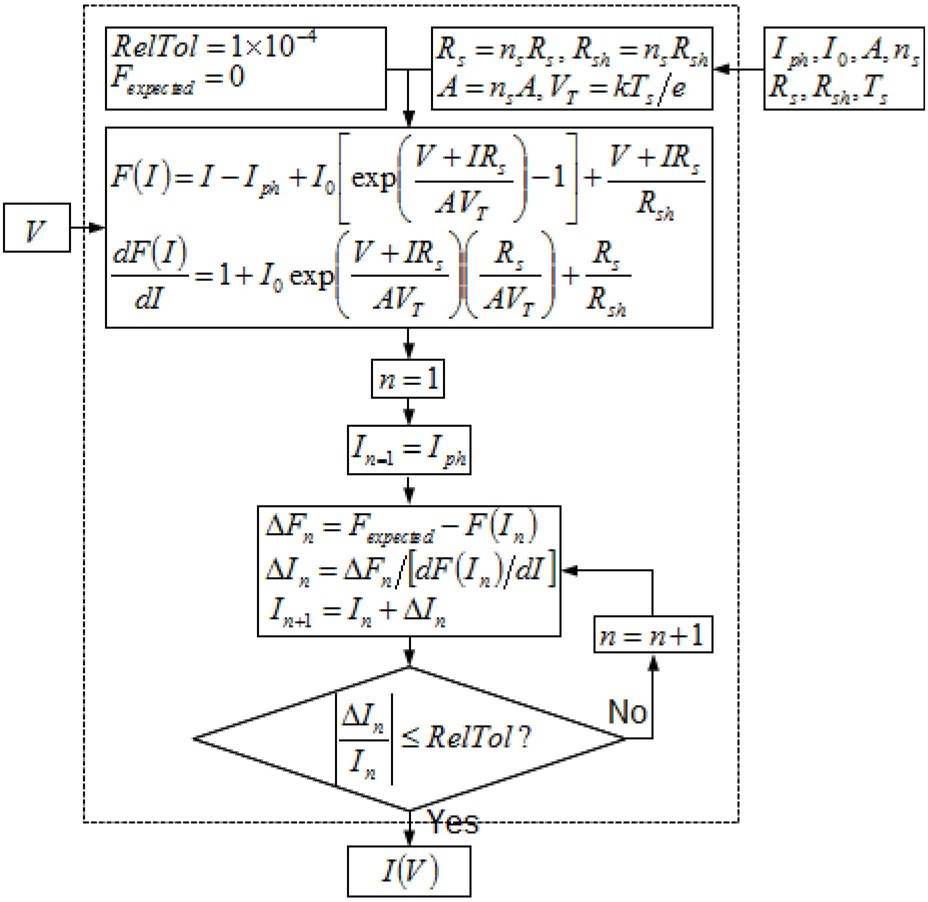

Figure 6.25: Newton's method to find I given the value of V using single diode model equation.

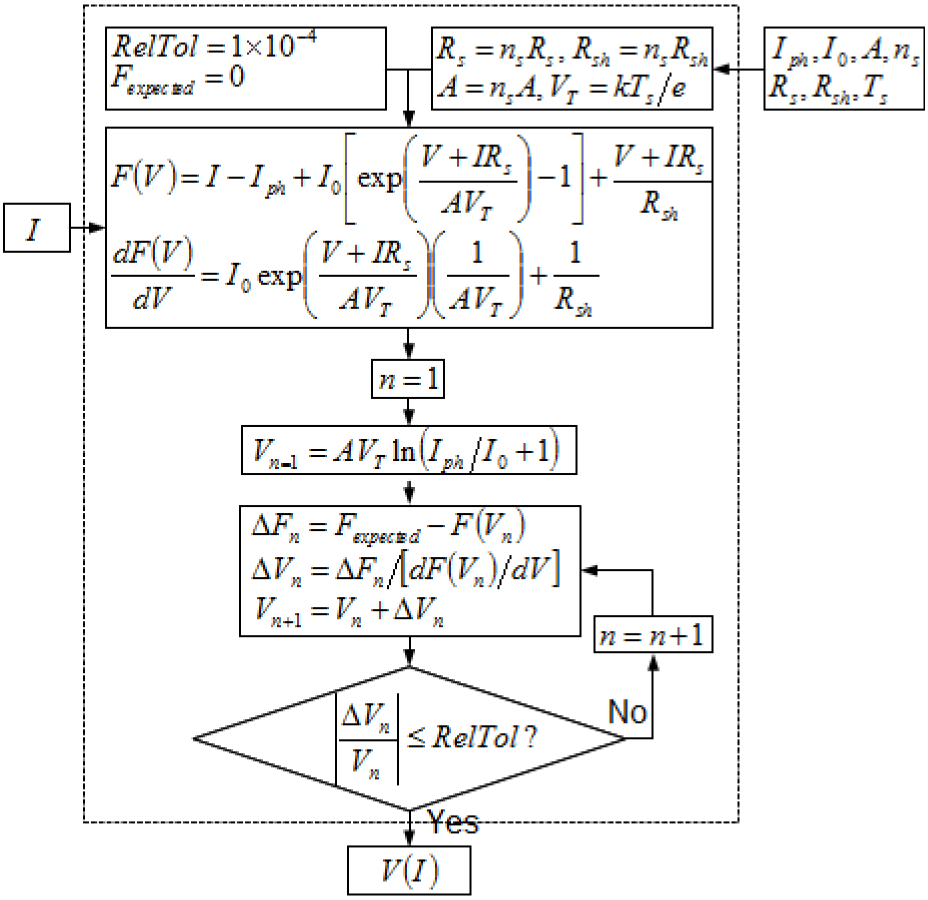

Figure 6.26: Newton's method to find V given the value of I using single diode model equation.

Maximum power point can be found by,

$$\frac{dP}{dV} = I + \frac{dI}{dV}V = 0 \tag{6.66}$$

$$\frac{dI}{dV} = -\frac{I}{V} \tag{6.67}$$

Differentiate both sides of Eq. 6.59,

$$\frac{dI}{dV} = -I_0 \exp\left(\frac{V+IR_s}{AV_T}\right)\left(\frac{1}{AV_T} + \frac{R_s}{AV_T}\frac{dI}{dV}\right) - \frac{1}{R_{sh}} - \frac{R_s}{R_{sh}}\frac{dI}{dV} \tag{6.68}$$

Substitute Eq. 6.67 into Eq. 6.68,

$$-\frac{I}{V} = -I_0 \exp\left(\frac{V+IR_s}{AV_T}\right)\left(\frac{1}{AV_T} - \frac{R_s}{AV_T}\frac{I}{V}\right) - \frac{1}{R_{sh}} + \frac{R_s}{R_{sh}}\frac{I}{V} \tag{6.69}$$

Rearrange and simplify Eq. 6.69,

$$0 = -\frac{I_0(V - IR_s)}{AV_T}\exp\left(\frac{V+IR_s}{AV_T}\right) - \frac{V - IR_s}{R_{sh}} + I \tag{6.70}$$

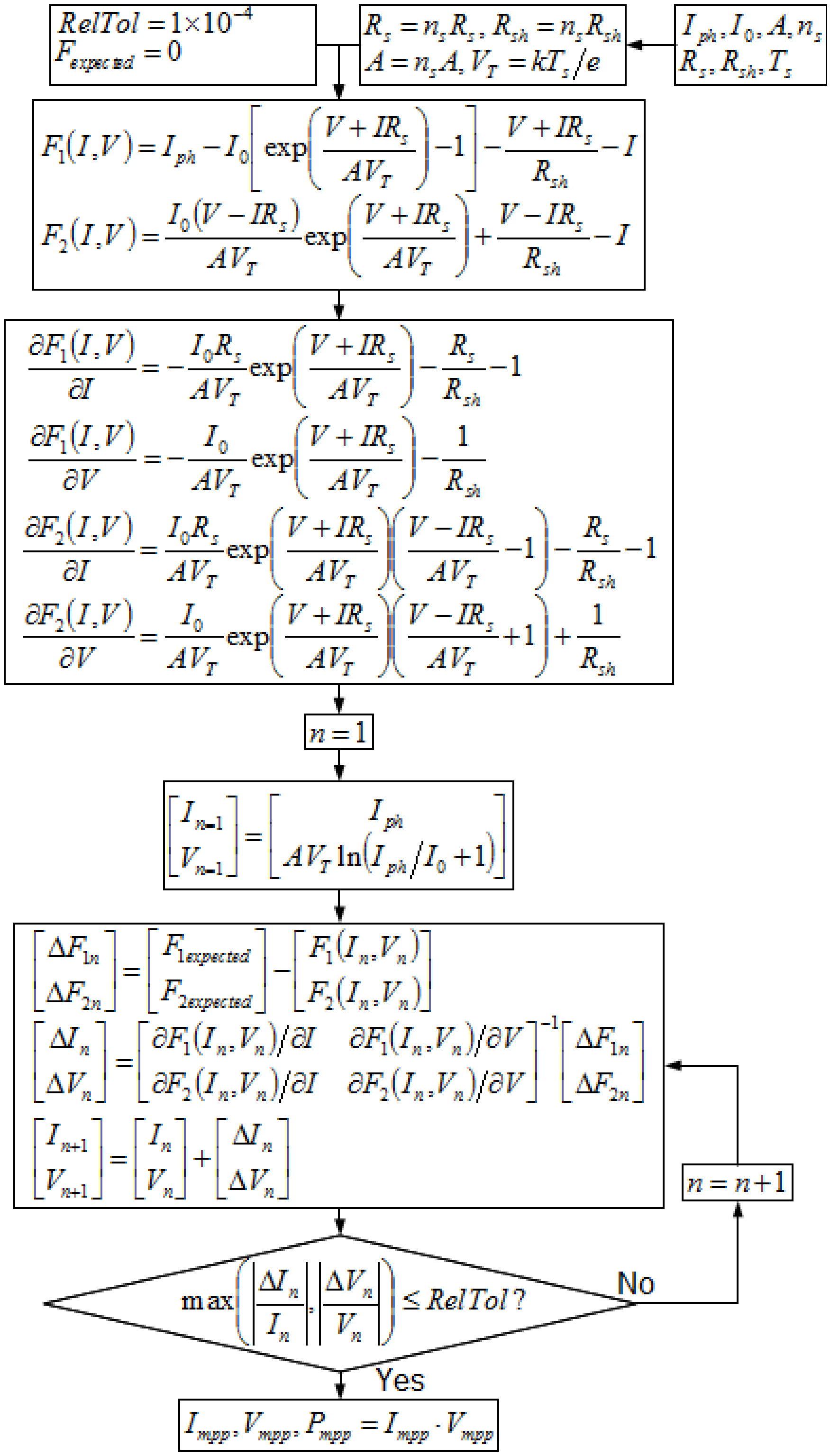

Figure 6.27: Newton's method to find voltage, current and power at the maximum power point.

V and I which fulfill both Eq. 6.70 and Eq. 6.59 are the voltage and current at maximum power point, where the power at the maximum power point can be obtained by multiplying the voltage and current at that point. Newton's method is used to solve the two equations numerically, where detailed algorithm and formula to find the Jacobian matrix is shown in the flow chart in Figure 6.27.

Relative tolerance in Figure 6.25, Figure 6.26, and Figure 6.27 has the default values of 1e-4, 1e-4 and 1e-6. The values of relative tolerance for the first and second algorithms were set to the defaut values where relative tolerance for the algorithm to find maximum power point was set to 1e-9 in the simulation.

6.5 Solar Cells Without LSC

Simulation of solar cells without LSC can be done by using the solar cell single diode model, taking the direct and diffuse incident sunlight spectrum as input from the output of SMARTS software. Let $L_{dir}(\lambda)$ and $L_{dif}(\lambda)$ as the direct and diffuse radiance spectrums respectively. Irradiance spectrum of the light received by the solar cell is,

$$E_{pv}(\lambda) = E_{pvdir}(\lambda) + E_{pvdif}(\lambda) \tag{6.71}$$

Where contribution by direct sunlight and diffuse sunlight are,

$$E_{pvdir}(\lambda) = \int_{\Omega_{dir}} [1 - R(\lambda,\theta)] L_{dir}(\lambda) \cos\theta \, d\Omega \tag{6.72}$$

$$E_{pvdif}(\lambda) = \int_{\Omega_{dif}} [1 - R(\lambda,\theta)] L_{dif}(\lambda) \cos\theta \, d\Omega \tag{6.73}$$

Where,

$E_{pvdir}(\lambda)$ = irradiance spectrum contributed by direct sunlight (W m^{-2}),

$E_{pvdif}(\lambda)$ = irradiance spectrum contributed by diffuse sunlight (W m^{-2}),

$L_{dir}(\lambda)$ = radiance spectrum of direct sunlight (W m^{-2} sr^{-1}),

$L_{dif}(\lambda)$ = radiance spectrum of diffuse sunlight (W m^{-2} sr^{-1}),

Ω_{dir} = range of angles where the direct sunlight is subtended (sr),

Ω_{dif} = range of solid angles where the diffuse sunlight is subtended (sr),

$R(\lambda,\theta)$ is the reflectance calculated by,

$$R(\lambda,\theta)=\frac{1}{2}\left[\left(\frac{\sin[\theta-\theta_t(\lambda,\theta)]}{\sin[\theta+\theta_t(\lambda,\theta)]}\right)^2+\left(\frac{\tan[\theta-\theta_t(\lambda,\theta)]}{\tan[\theta+\theta_t(\lambda,\theta)]}\right)^2\right] \tag{6.74}$$

$$\theta_t(\lambda,\theta)=\sin^{-1}\left[\frac{n_{LSC}(\lambda)}{n_{PV}(\lambda)}\sin\theta\right] \tag{6.75}$$

It is complicated to evaluate the integration in Eq. 6.73 directly because after converting dΩ into sinθdϕdθ, the inner integration limit is a function of the outer intergration variable, where the outer integration limit is not a constant either, but dependent on direction of the direct sunlight and the LSC tilt angle. However, a much simpler method can be used to evaluate it numerically without the need to derive the proper functions for the integration limit, by introducing a new function to multiply with the radiance spectrum. The extra function output the value 1 only for the angles where the sunlight can be found, or otherwise, output the value 0.

Contribution from direct sunlight is calculated by,

$$\begin{aligned}E_{pvdir}(\lambda)&=\int_{\Omega_{dir}}[1-R(\lambda,\theta)]L_{dir}(\lambda)\cos\theta\, d\Omega\\&=\int_{\theta_1}^{\theta_2}\int_{\phi_1}^{\phi_2}[1-R(\lambda,\theta)]L_{dir}(\lambda)F_{dirsa}(\theta,\phi)\cos\theta\sin\theta\, d\phi\, d\theta\\&=L_{dir}(\lambda)\times\int_{\theta_1}^{\theta_2}\int_{\phi_1}^{\phi_2}[1-R(\lambda,\theta)]F_{dirsa}(\theta,\phi)\cos\theta\sin\theta\, d\phi\, d\theta\end{aligned} \tag{6.76}$$

Where,

$$F_{dirsa}(\theta,\phi)=\begin{cases}0 & ,\Delta\theta_{rs1}>\Delta\theta_{sun}\\1 & ,\Delta\theta_{rs1}\le\Delta\theta_{sun}\end{cases} \tag{6.77}$$

$$\Delta\theta_{rs1} = \cos^{-1}\begin{bmatrix}(\sin\theta\cos\phi)(\sin\theta_{sun}\cos\phi_{sun}) \\ +(\sin\theta\sin\phi)(\sin\theta_{sun}\sin\phi_{sun}) \\ +\cos\theta\cos\theta_{sun}\end{bmatrix} \tag{6.78}$$

$$\theta_1 = \begin{cases} 0 & ,\theta_{sun} \le 5\cdot\Delta\theta_{sun} \\ \theta_{sun} - 5\cdot\Delta\theta_{sun} & ,\theta_{sun} > 5\cdot\Delta\theta_{sun} \end{cases} \tag{6.79}$$

$$\theta_2 = \theta_{sun} + 5\cdot\Delta\theta_{sun} \tag{6.80}$$

$$\phi_1 = \begin{cases} 0 & ,\theta_{sun} \le 5\cdot\Delta\theta_{sun} \\ \phi_{sun} - 10\cdot\Delta\theta_{sun} & ,\theta_{sun} > 5\cdot\Delta\theta_{sun} \end{cases} \tag{6.81}$$

$$\phi_2 = \begin{cases} 2\pi & ,\theta_{sun} \le 5\cdot\Delta\theta_{sun} \\ \phi_{sun} + 10\cdot\Delta\theta_{sun} & ,\theta_{sun} > 5\cdot\Delta\theta_{sun} \end{cases} \tag{6.82}$$

Eq. 6.79-6.82 are constant integration limit, which are limited in values near the direction of direct sunlight to make the numerical integration converge properly.

Similarly, contribution from diffuse sunlight is calculated by,

$$\begin{aligned} E_{pvdif}(\lambda) &= \int_{\Omega_{dif}} [1 - R(\lambda,\theta)] L_{dif}(\lambda)\cos\theta \, d\Omega \\ &= \int_0^{\pi/2}\int_0^{2\pi} [1 - R(\lambda,\theta)] L_{dif}(\lambda) F_{difsa}(\theta,\phi)\cos\theta\sin\theta \, d\phi \, d\theta \\ &= L_{dif}(\lambda)\times\int_0^{\pi/2}\int_0^{2\pi} [1 - R(\lambda,\theta)] F_{difsa}(\theta,\phi)\cos\theta\sin\theta \, d\phi \, d\theta \end{aligned} \tag{6.83}$$

$$F_{difsa}(\theta,\phi) = \begin{cases} 0 & ,\Delta\theta_{rs2} > \dfrac{\pi}{2} \\ 1 & ,\Delta\theta_{rs2} \le \dfrac{\pi}{2} \end{cases} \tag{6.84}$$

$$\Delta\theta_{rs2} = \cos^{-1}\begin{bmatrix}(\sin\theta\cos\phi)(\sin\theta_{sctilt}\cos\pi) \\ +(\sin\theta\sin\phi)(\sin\theta_{sctilt}\sin\pi) \\ +\cos\theta\cos\theta_{sun}\end{bmatrix} \tag{6.85}$$

Where θ_{sctilt} is the angle of solar cell tilt toward south.

After calculating irradiance spectrum of light received by the solar cell, Eq. 6.55 can be used to calculate the photo-generated current. However, together with Eq. 6.55, it becomes a 3-dimensional integration with respect to ϕ, θ and λ, which is very slow when evaluated numerically to converge to an adequate accuracy. The convergence speed can be improved by first evaluate the double integration in Eq. 6.76 and Eq. 6.83 for every discrete wavelength where the refractive indices n_{LSC} and n_{PV} are known. Cubic interpolation is then used to estimate the rest of the values for other wavelengths at which the double integration is not evaluated. This turns the triple integration into a single integration in Eq. 6.55 and reduces the overall calculation time.

6.6 Programming code verification

Extensive programming code verification was performed before running the simulation, as described in the following paragraphs. However details of the programming code verification are not documented in the thesis.

Thermodynamic model which simulates dye emission was developed based on a developed simulation model which was verified by comparing with actual measurement in the cited paper (Chatten *et al.*, 2001). The corresponding programming code for the thermodynamic model had been verified by comparing the result with that from the cited reference using the same set of input parameters.

On the other hand, Ray-tracing model which simulates trapped incident light uses part of the Radiance software without any further modification. The Radiance software has been used by many other researchers in various types of simulation. Therefore, only simple and easily calculated examples were simulated and compared with the calculated values using their corresponding formulas. For example, the reflectivity at a boundary between two dielectric materials with different refractive indices at an arbitrary incident angle was first calculated using Fresnel equation, then a simple simulation which consists of only the same dielectric materials was run and the details of a ray being traced from the same incident angle was examined, and the simulation result was found to be exactly the same with the one calculated using the reflectivity from Fresnel equation.

Proceed to the subsequent simulation, the SMARTS program for incident solar irradiance spectrum simulation at different time has also been used by many others in simulation. It was used without any further modification too. Hence, only a simulation from provided example input parameters was run and its result was compared to the provided result to verify that its Fortran source code had been compiled without any error.

Besides, the programming code that calculates internal quantum efficiency of a solar cell was also verified by comparing the spectrum result to the cited paper.

Similarly, codes for the calculation using the solar cell single diode model were verified by running the simulation using the input parameters for a real solar cell taken from the cited paper (Phang *et al.*, 1984) and then comparing the result.

CHAPTER 7

SIMULATION RESULT AND ANALYSIS

7.1 Simulation Result

All simulation results from the simulation model described in Chapter 6 are given in this chapter in the form of tables and graphs. It should be noted that all numbers in the tables in this chapter are rounded to 2 decimal places, therefore a slight mismatch may occur in some cases due to rounding error from the original result data. For example, adding the photo-generated current from the dye emission and that from the trapped incident light does not exactly equal to the total photo-generated current in some cases because of this reason.

7.1.1 Irradiance Spectra Output from LSC Hybrid Algorithm Simulation Model

Simulation output from the hybrid algorithm are shown in Figure 7.1-Figure 7.5. Figure 7.1 are the irradiance spectra output from the LSC to the solar cells at different LSC tilt angles and time of the day. Figure 7.2, Figure 7.3, Figure 7.4, and Figure 7.5 show the separate contribution from dye emission, trapped incident sunlight (trapped direct incident sunlight + trapped diffuse incident sunlight), trapped direct part of incident sunlight, and trapped diffuse part of incident sunlight to the irradiance spectra received by the solar cells respectively.

For all graphs in Figure 7.1-Figure 7.5, irradiance is labeled as E in W m^{-2} nm^{-1}, wavelength as λ in μm, where time of the day is in hour. Titles of the graphs are labeled in the form of "contribution source, tilt angle toward the south". Besides, the axis limit of all graphs with the same contribution source are set to be the same for the ease of comparison.

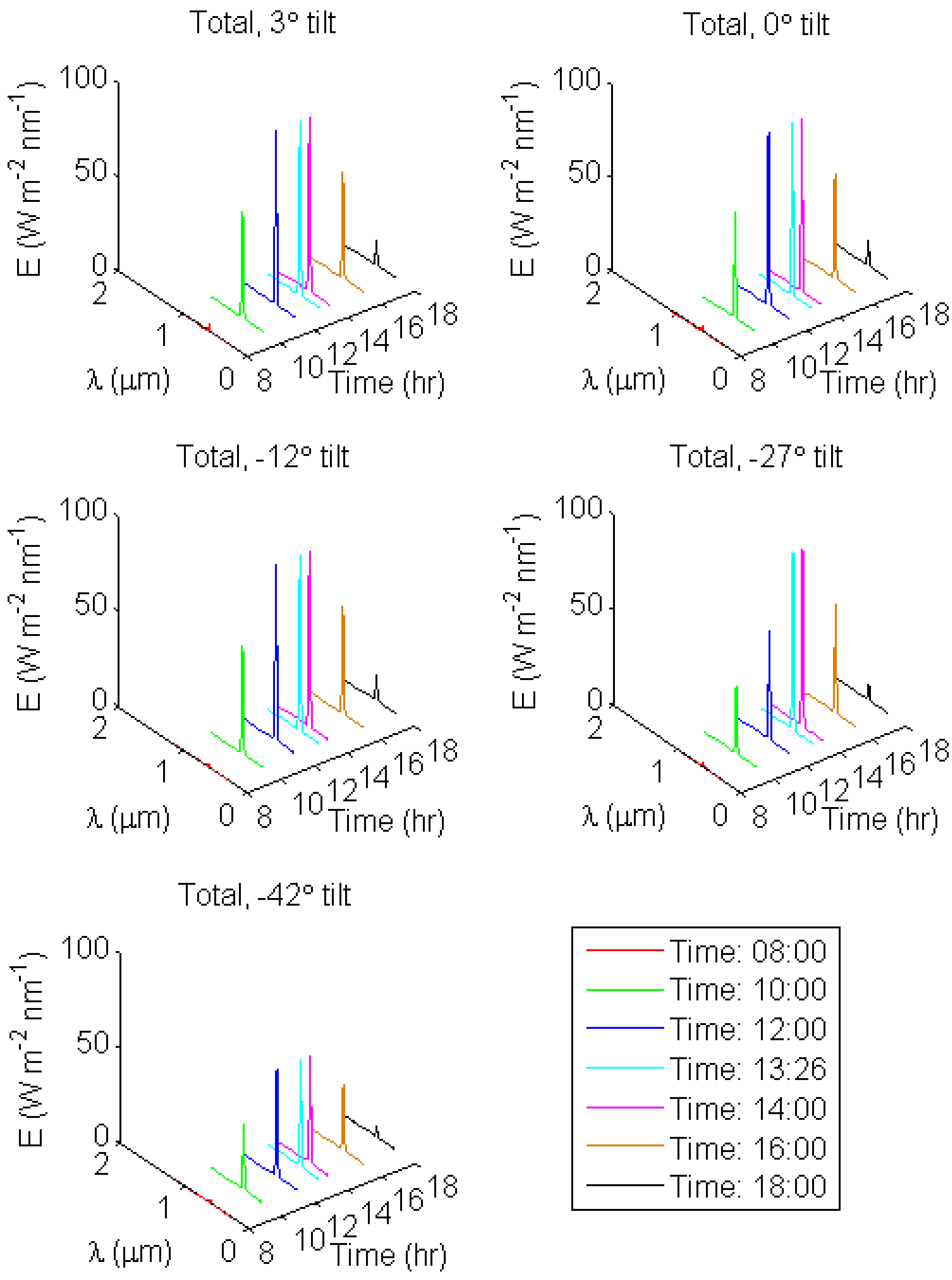

Figure 7.1: Irradiance spectra received by the solar cells.

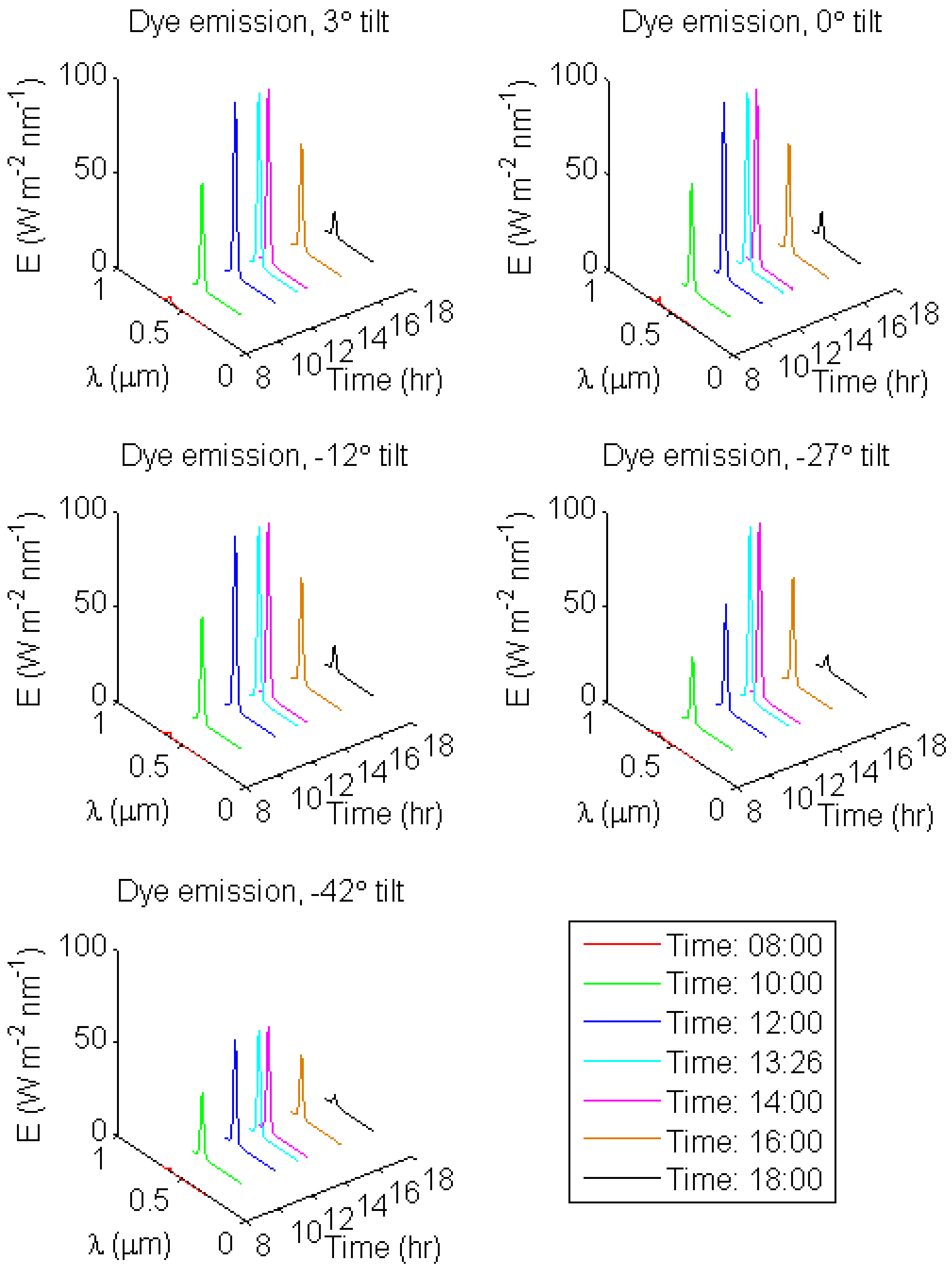

Figure 7.2: Irradiance spectra contributed by dye emission received by the solar cells.

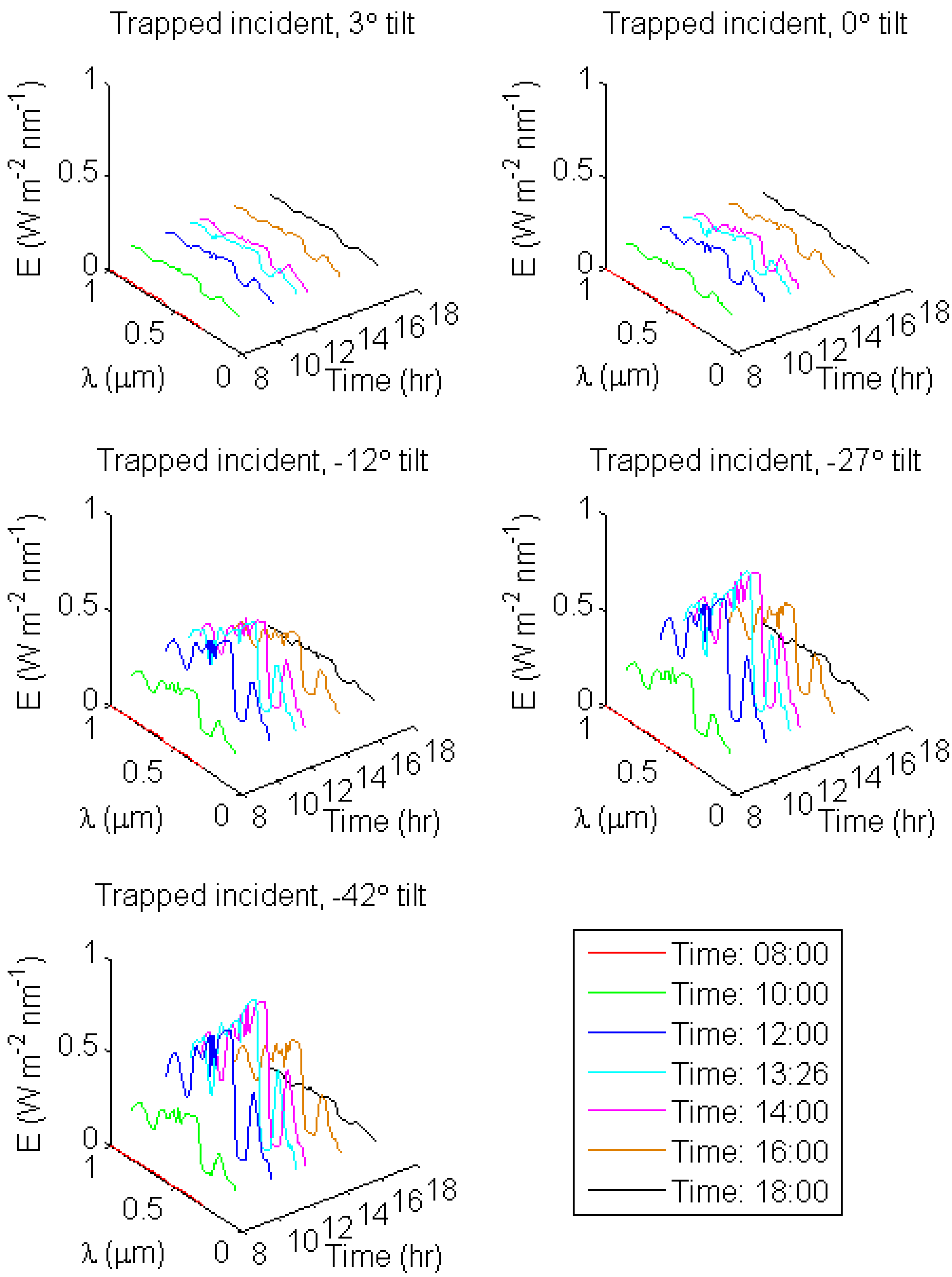

Figure 7.3: Irradiance spectra contributed by trapped incident sunlight (trapped direct incident sunlight + trapped diffuse incident sunlight) received by the solar cells.

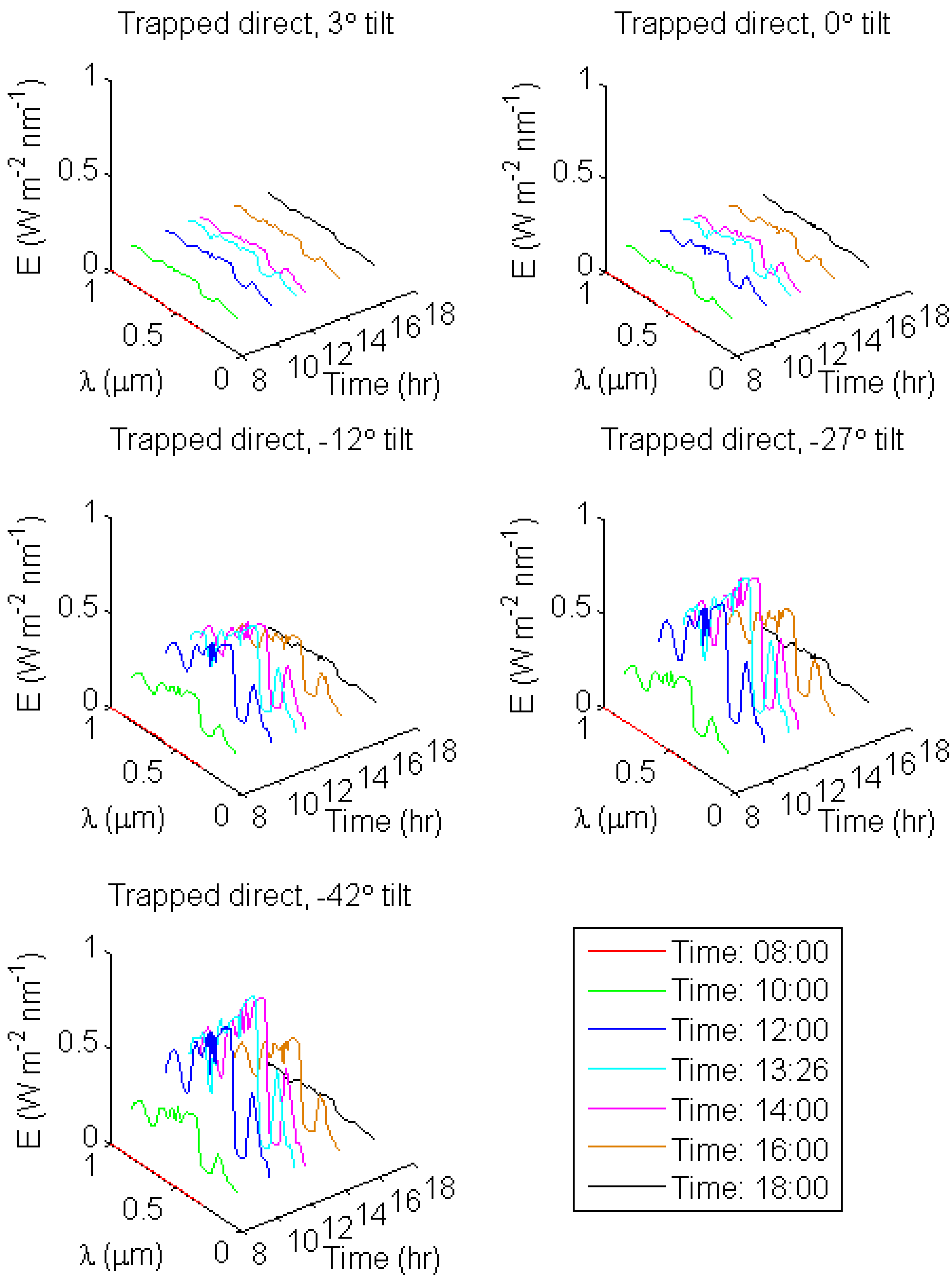

Figure 7.4: Irradiance spectra contributed by trapped direct part of sunlight received by the solar cells.

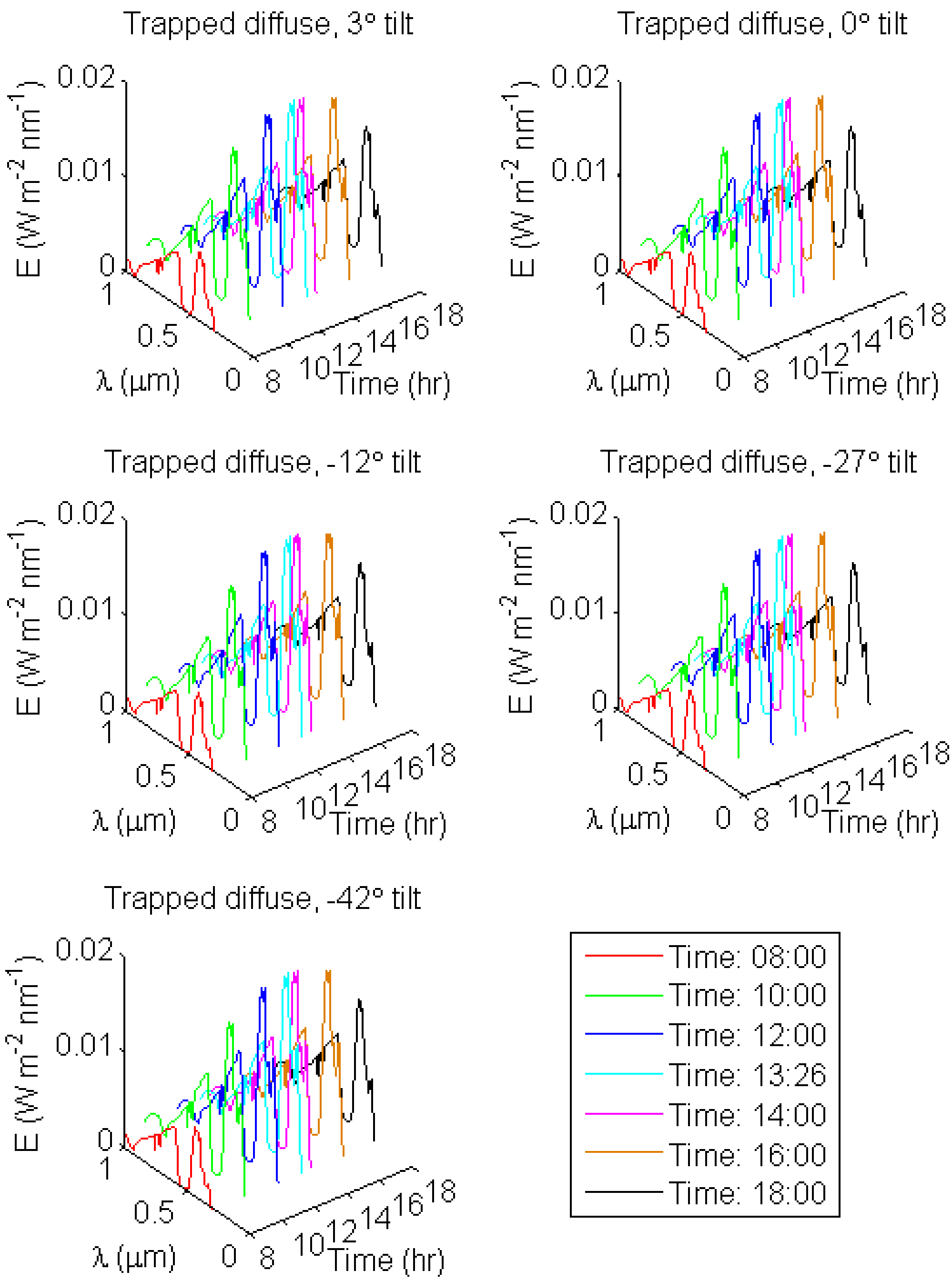

Figure 7.5: Irradiance spectra contributed by trapped diffuse part of sunlight received by the solar cells.

7.1.2 Photo-generated Current from a Solar Cell

Simulation result of the photo-generated current from a solar cell attached to LSC edge is listed in Table 7.1, together with the individual contribution from dye emission, trapped incident sunlight (trapped direct incident sunlight + trapped diffuse incident sunlight), trapped direct incident sunlight, and trapped diffuse incident sunlight to the photo generated current. In the case of horizontal solar cell without the LSC, total photo-generated current received by the solar cell together with individual contribution from direct and diffuse incident sunlight are shown in Table 7.2.

Table 7.1. Photo-generated current from a solar cell attached to LSC edge at different LSC tilt angles toward south and time of the day.

Tilt angle	Time	$I_{ph(total)}$ (mA) $= I_{ph(dye)} + I_{ph(incident)}$	$I_{ph(dye)}$ (mA)	$I_{ph(incident)}$ (mA) $= I_{ph(direct)} + I_{ph(diffuse)}$	$I_{ph(direct)}$ (mA)	$I_{ph(diffuse)}$ (mA)
3°	0800	22.67	21.81	0.87	0.47	0.40
	1000	375.52	370.70	4.82	4.10	0.73
	1200	615.63	608.76	6.88	6.09	0.79
	1326	615.99	608.76	7.24	6.44	0.80
	1400	615.92	608.76	7.16	6.36	0.80
	1600	376.51	370.70	5.82	5.06	0.76
	1800	89.87	87.27	2.60	1.99	0.61
0°	0800	22.70	21.81	0.89	0.49	0.40
	1000	377.38	370.70	6.68	5.96	0.73
	1200	619.93	608.76	11.18	10.39	0.79
	1326	620.93	608.76	12.17	11.37	0.80
	1400	620.74	608.76	11.98	11.18	0.80
	1600	379.50	370.70	8.80	8.04	0.76
	1800	90.37	87.27	3.10	2.48	0.61
-12°	0800	14.80	13.91	0.89	0.49	0.40
	1000	385.09	370.70	14.40	13.67	0.73
	1200	638.97	608.76	30.21	29.42	0.79
	1326	642.98	608.76	34.22	33.42	0.80
	1400	642.27	608.76	33.51	32.71	0.80
	1600	392.45	370.70	21.75	20.98	0.76
	1800	92.16	87.27	4.89	4.27	0.61

-27°	0800	14.62	13.91	0.71	0.31	0.40
	1000	248.27	227.33	20.93	20.21	0.73
	1200	419.10	370.70	48.40	47.61	0.79
	1326	664.25	608.76	55.50	54.70	0.80
	1400	662.97	608.76	54.22	53.42	0.80
	1600	404.29	370.70	33.60	32.83	0.77
	1800	60.49	54.62	5.87	5.25	0.61
-42°	0800	9.38	8.93	0.45	0.05	0.40
	1000	248.32	227.33	20.99	20.26	0.73
	1200	423.73	370.70	53.04	52.25	0.79
	1326	432.45	370.70	61.75	60.95	0.80
	1400	430.90	370.70	60.20	59.40	0.80
	1600	262.93	227.33	35.60	34.83	0.77
	1800	39.29	34.40	4.89	4.27	0.61

Table 7.2. Photo-generated current from a solar cell without LSC at optimum tilt angle and horizontal orientation.

Tilt angle	Time	$I_{ph(total)}$ (mA) $=I_{ph(direct)}+I_{ph(diffuse)}$	$I_{ph(direct)}$ (mA)	$I_{ph(diffuse)}$ (mA)
10°	0800	24.57	22.63	1.95
	1000	223.92	220.18	3.74
	1200	364.30	360.18	4.12
	1326	396.45	392.27	4.18
	1400	390.87	386.70	4.17
	1600	293.84	289.88	3.96
	1800	108.41	105.31	3.10
0°	0800	20.93	18.98	1.96
	1000	217.82	214.06	3.76
	1200	358.25	354.11	4.14
	1326	390.47	386.27	4.20
	1400	384.90	380.71	4.19
	1600	287.83	283.85	3.99
	1800	102.84	99.73	3.11

Percentage of contribution to the total photo-generated current generated by solar cell attached to LSC edge from dye emission, trapped direct incident sunlight and traped diffuse incident sunlight are listed in Table 7.3. In the case of horizontal solar cell without LSC, the percentage of contribution to the total photo-generated current from incident direct sunlight and incident diffuse sunlight are shown in Table 7.4.

Table 7.3. Percentage of contribution to photo-generated current from different sources with LSC.

Tilt angle	Time	Dye emission (%)	Trapped direct incident sunlight (%)	Trapped diffuse incident sunlight (%)
3°	0800	96.17	2.06	1.77
	1000	98.72	1.09	0.19
	1200	98.88	0.99	0.13
	1326	98.82	1.05	0.13
	1400	98.84	1.03	0.13
	1600	98.45	1.34	0.20
	1800	97.11	2.21	0.68
0°	0800	96.08	2.15	1.77
	1000	98.23	1.58	0.19
	1200	98.20	1.68	0.13
	1326	98.04	1.83	0.13
	1400	98.07	1.80	0.13
	1600	97.68	2.12	0.20
	1800	96.57	2.75	0.68
-12°	0800	93.96	3.33	2.72
	1000	96.26	3.55	0.19
	1200	95.27	4.60	0.12
	1326	94.68	5.20	0.12
	1400	94.78	5.09	0.12
	1600	94.46	5.35	0.19
	1800	94.70	4.64	0.67

-27°	0800	95.13	2.12	2.75
	1000	91.57	8.14	0.29
	1200	88.45	11.36	0.19
	1326	91.64	8.23	0.12
	1400	91.82	8.06	0.12
	1600	91.69	8.12	0.19
	1800	90.30	8.69	1.01
-42°	0800	95.20	0.51	4.29
	1000	91.55	8.16	0.29
	1200	87.48	12.33	0.19
	1326	85.72	14.09	0.19
	1400	86.03	13.79	0.19
	1600	86.46	13.25	0.29
	1800	87.57	10.87	1.56

Table 7.4. Percentage of contribution to photo-generated current from direct and diffuse sunlight for a horizontal solar cell without LSC at optimum tilt and horizontal orientation.

Tilt angle	Time	Direct sunlight (%)	Diffuse sunlight (%)
10°	0800	92.08	7.92
	1000	98.33	1.67
	1200	98.87	1.13
	1326	98.95	1.05
	1400	98.93	1.07
	1600	98.65	1.35
	1800	97.14	2.86
0°	0800	90.65	9.35
	1000	98.28	1.72
	1200	98.84	1.16
	1326	98.92	1.08
	1400	98.91	1.09
	1600	98.62	1.38
	1800	96.97	3.03

The total photo-generated current from the solar cell attached to LSC edge versus time of the day for each tilted angle is shown in Figure 7.6. Individual contributions from dye emission, trapped direct incident light, and trapped diffuse incident light to the total photo-generated current are as shown in Figure 7.7, Figure 7.8, and Figure 7.9 respectively.

In the case of horizontal solar cell without LSC at its optimum tilt, the graph of total photo-generated current versus time of the day is shown in Figure 7.10, where similar graphs for separate contribution from direct incident sunlight and diffuse incident sunlight are shown in Figure 7.11 and Figure 7.12 respectively.

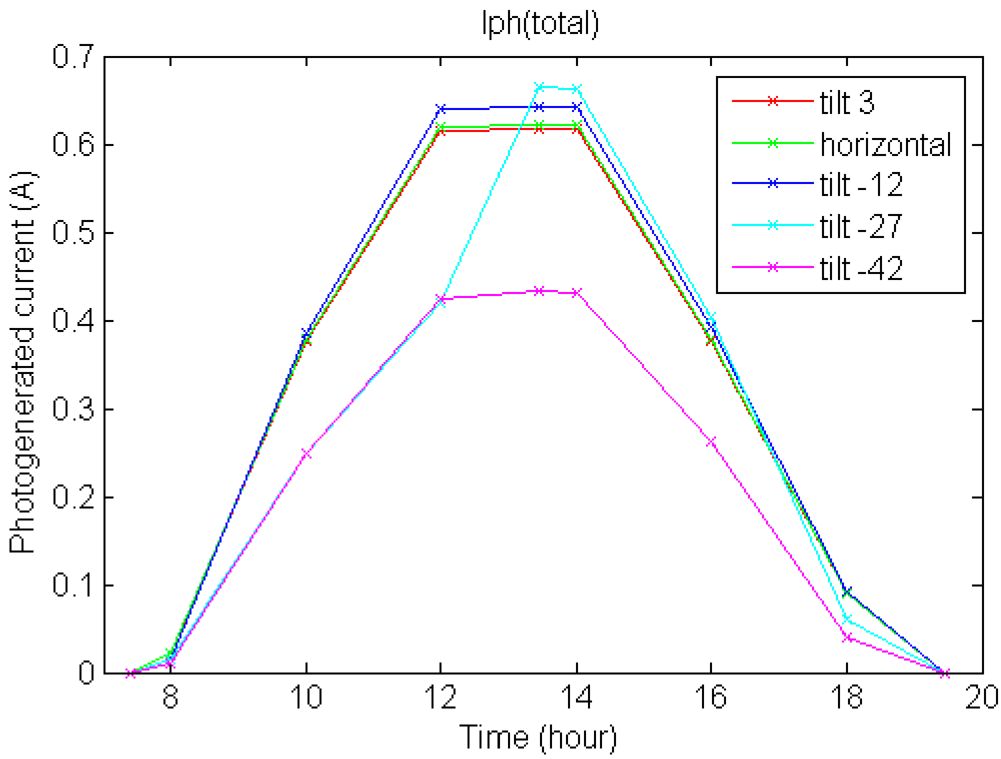

Figure 7.6: Total photo-generated current for different LSC tilt.

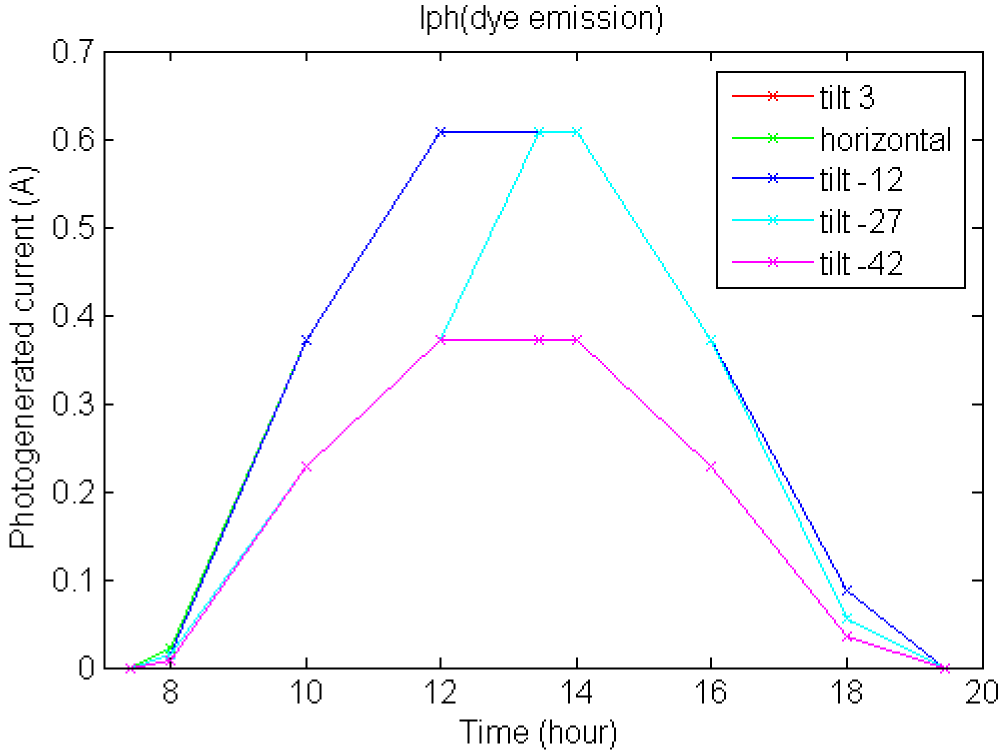

Figure 7.7: Photo-generated current contributed by dye emission for different LSC tilt.

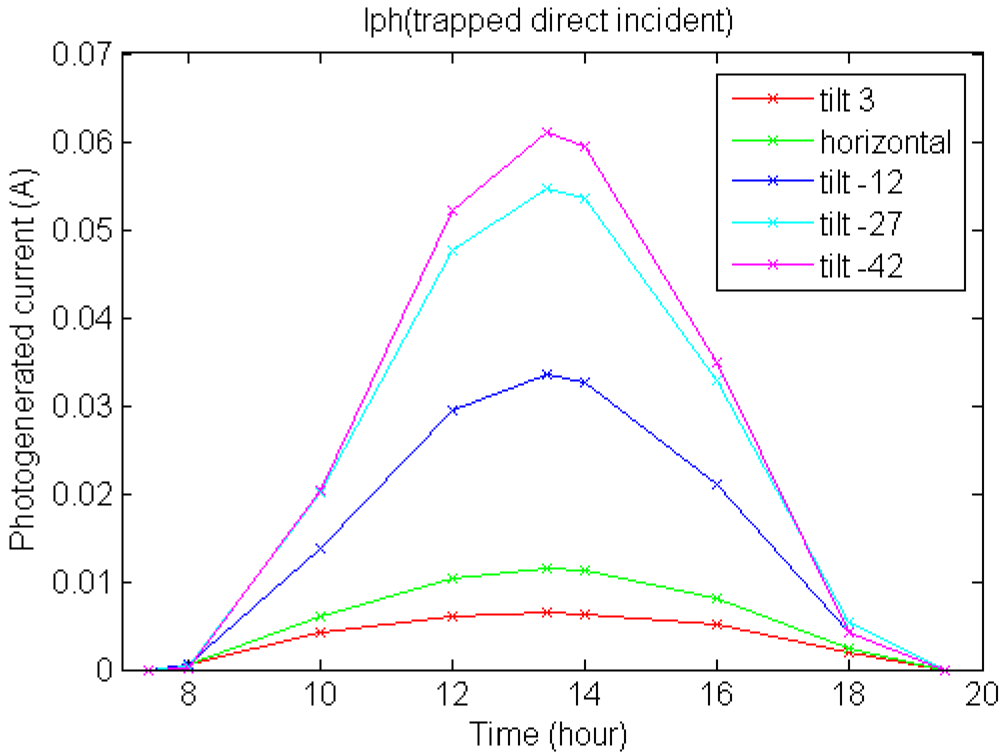

Figure 7.8: Photo-generated current contributed by trapped direct part of sunlight for different LSC tilt.

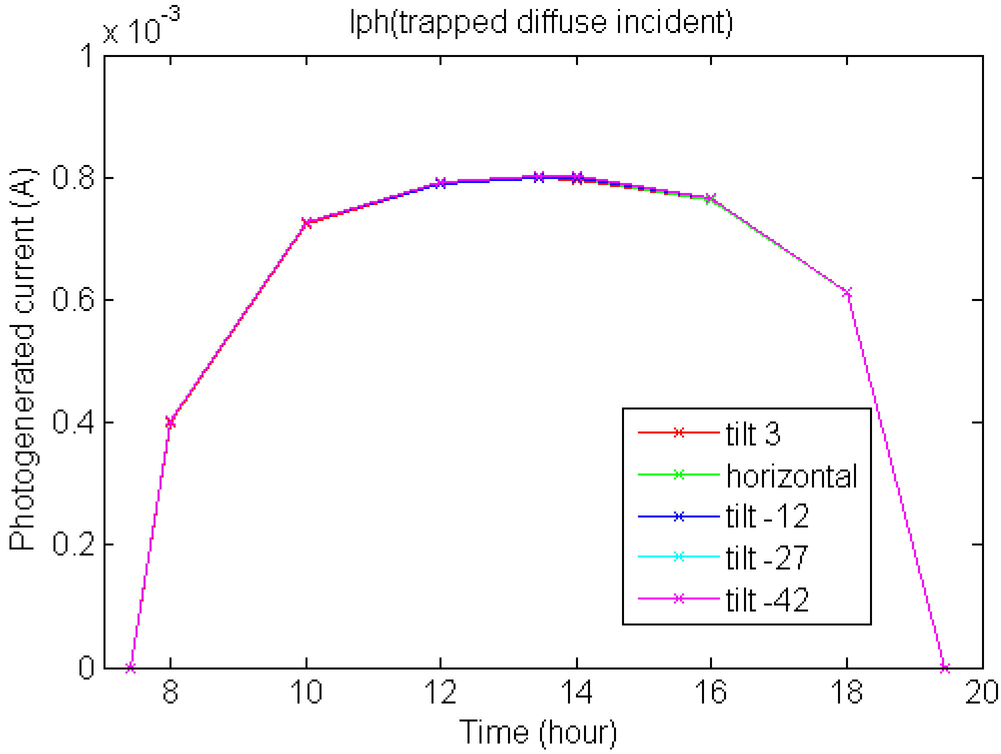

Figure 7.9: Photo-generated current contributed by trapped diffuse part of sunlight for different LSC tilt.

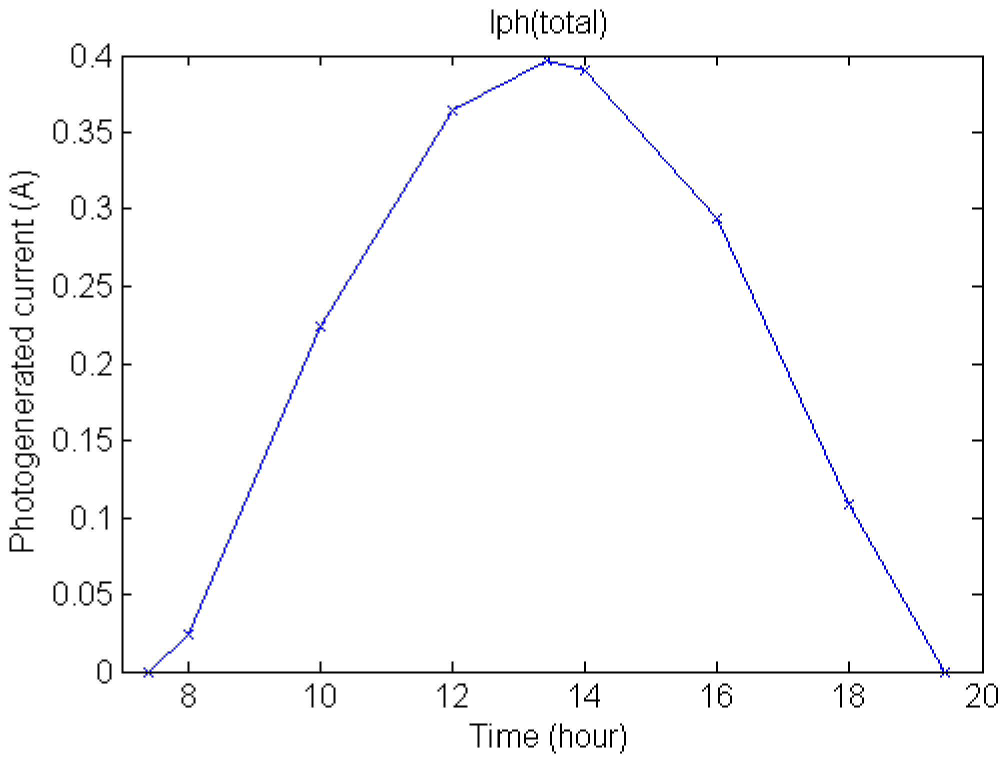

Figure 7.10: Total photo-generated current for solar cell without LSC at optimum tilt angle.

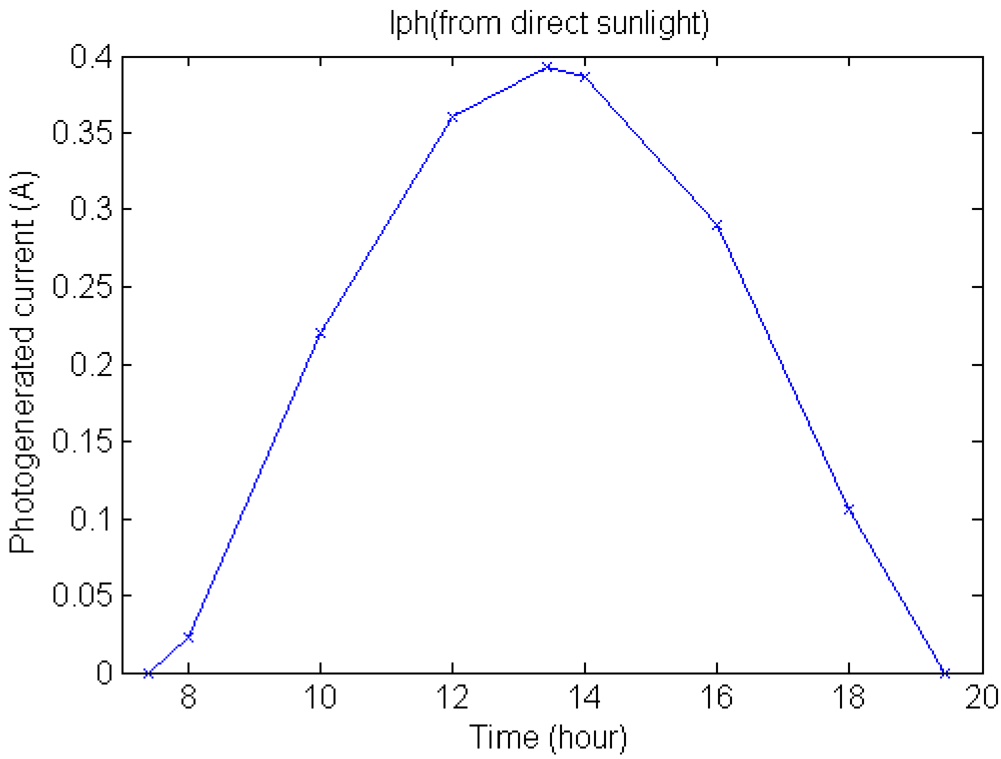

Figure 7.11: Photo-generated current contributed by direct sunlight for solar cell without LSC at optimum tilt angle.

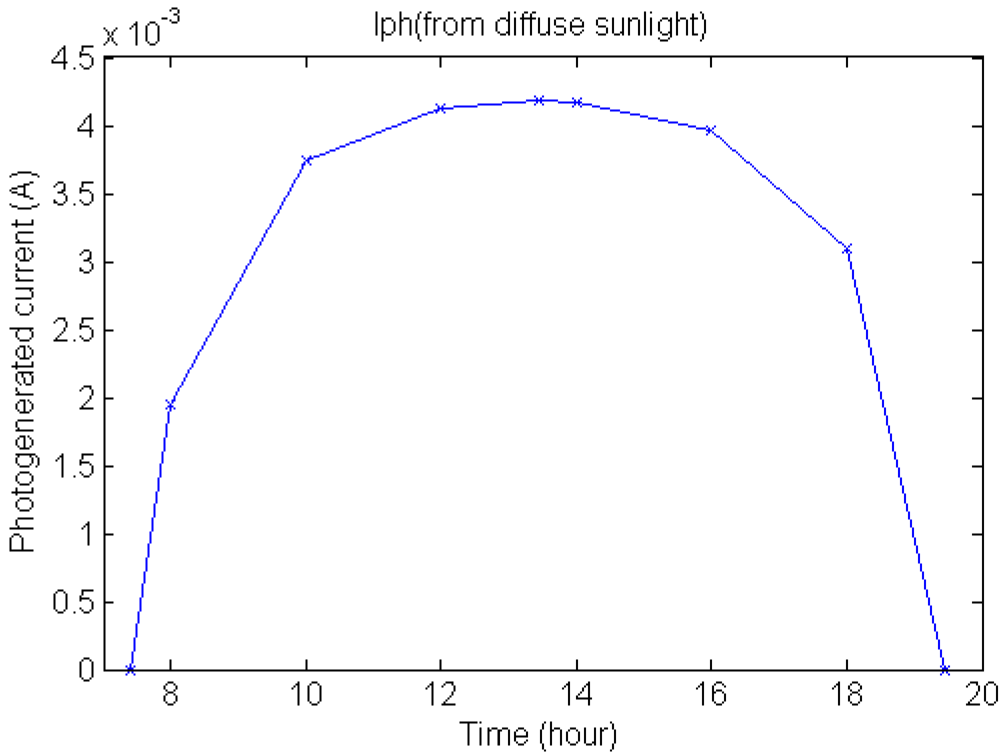

Figure 7.12: Photo-generated current contributed by diffuse sunlight for solar cell without LSC at optimum tilt angle.

7.1.3 Maximum Power Point of Solar Cells

Calculated power, current and voltage at the maximum power point from solar cells are listed in Table 7.5 for the case where solar cells attached to LSC edge at different LSC tilt angles and time of the day. In the case of horizontal solar cells with the same size without LSC, power, current and voltage at the maximum power point are shown in Table 7.6.

Table 7.5. Power at the maximum power point and its corresponding voltage and current from solar cells attached to LSC edge at different LSC tilt angles and time of the day.

Tilt angle	Time	P_{mpp} (W)	I_{mpp} (A)	V_{mpp} (V)
3°	0800	0.18	0.02	8.79
	1000	3.69	0.34	10.70
	1200	6.10	0.56	10.81
	1326	6.11	0.56	10.81
	1400	6.10	0.56	10.81
	1600	3.70	0.35	10.70
	1800	0.81	0.08	9.86
0°	0800	0.18	0.02	8.79
	1000	3.71	0.35	10.70
	1200	6.14	0.57	10.81
	1326	6.15	0.57	10.81
	1400	6.15	0.57	10.81
	1600	3.73	0.35	10.70
	1800	0.81	0.08	9.87
-12°	0800	0.11	0.01	8.44
	1000	3.78	0.35	10.71
	1200	6.33	0.59	10.81
	1326	6.37	0.59	10.81
	1400	6.37	0.59	10.81
	1600	3.86	0.36	10.71
	1800	0.83	0.08	9.88

-27°	0800	0.11	0.01	8.43
	1000	2.39	0.23	10.51
	1200	4.13	0.38	10.73
	1326	6.58	0.61	10.81
	1400	6.57	0.61	10.81
	1600	3.98	0.37	10.72
	1800	0.53	0.05	9.57
-42°	0800	0.07	0.01	8.05
	1000	2.39	0.23	10.51
	1200	4.18	0.39	10.74
	1326	4.26	0.40	10.74
	1400	4.25	0.40	10.74
	1600	2.54	0.24	10.54
	1800	0.33	0.04	9.23

Table 7.6. Power at the maximum power point and its corresponding voltage and current for solar cells without LSC at optimum tilt and horizontal orientation.

Tilt angle	Time	P_{mpp} (W)	I_{mpp} (A)	V_{mpp} (V)
10°	0800	0.19	0.02	8.86
	1000	2.15	0.21	10.45
	1200	3.57	0.33	10.68
	1326	3.90	0.36	10.72
	1400	3.84	0.36	10.71
	1600	2.86	0.27	10.59
	1800	0.99	0.10	9.99
0°	0800	0.16	0.02	8.73
	1000	2.09	0.20	10.44
	1200	3.51	0.33	10.68
	1326	3.84	0.36	10.71
	1400	3.78	0.35	10.71
	1600	2.80	0.26	10.58
	1800	0.94	0.09	9.96

Graph of power at maximum power point versus time of the day is shown in Figure 7.13 for different LSC tilt angles. In the case of solar cells without LSC at its optimum tilt, the graph of power at maximum power point versus time of the day is shown in dashed line in the same figure.

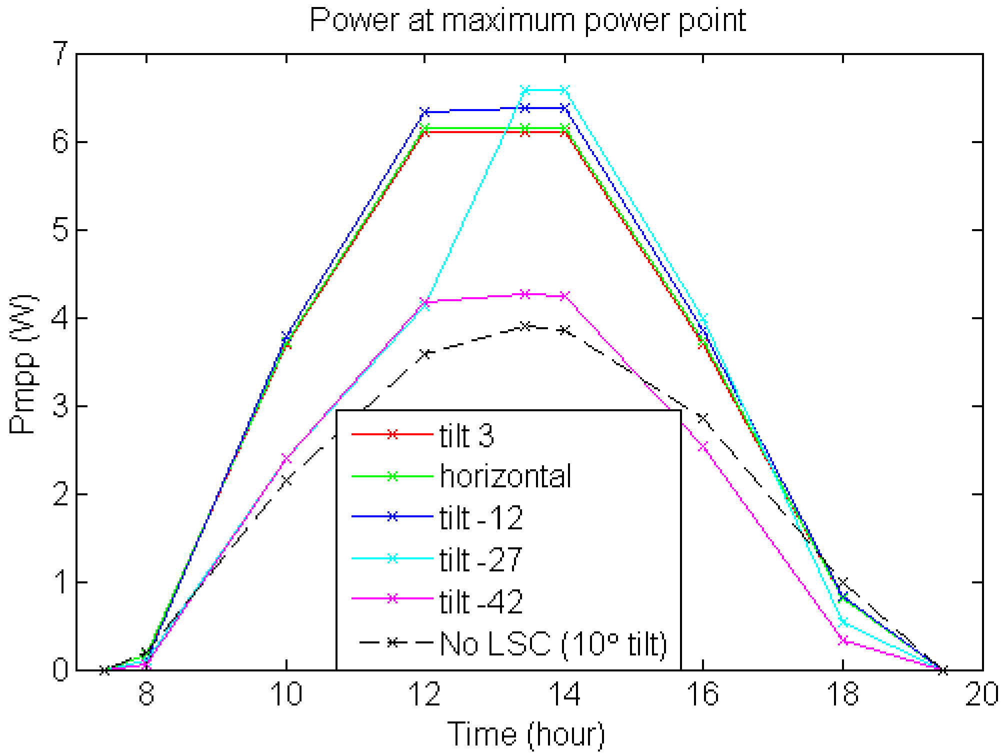

Figure 7.13: Maximum power points at different time for different LSC tilt, together with that for solar cells without LSC at optimum tilt angle in dashed line.

7.1.4 Electrical Energy Generated by the Solar Cells in a Day

Electrical energy generated by the solar cells attached to the LSC edge and that by the same solar cells placed horizontally without LSC in the particular day is listed in Table 7.7. Graph of the generated electrical energy versus LSC tilt angles is shown in Figure 7.14, together with that generated by the same solar cells without LSC at optitmum tilt in dashed line for reference.

Table 7.7. Total generated electrical energy (in kWh) in a day at different LSC tilt angles, together with kWh generated by solar cells without LSC at its optimum tilt.

Tilt angle	3°	0°	-12°	-27°	-42°	10° (no LSC)
Total generated electrical energy in a day (kWh)	40.81	41.10	42.28	35.90	27.41	26.94

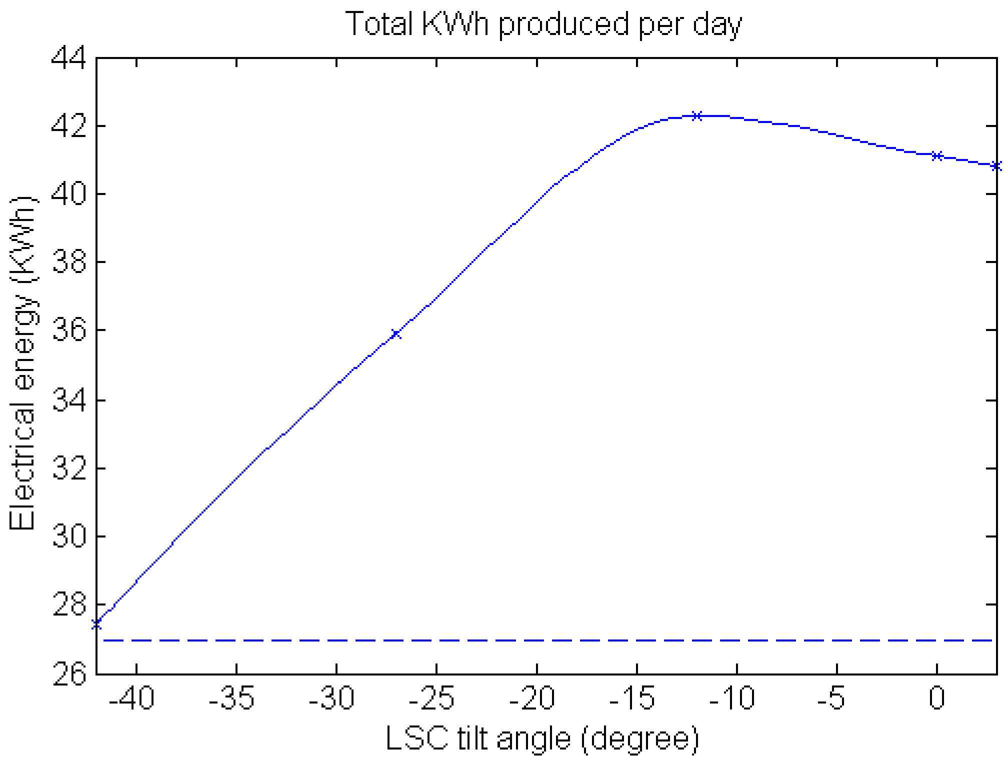

Figure 7.14: Total kWh generated by the solar cells with LSC in a day for different LSC tilt, with that by solar cells without LSC at optimum tilt in dashed line.

7.1.5 Short Circuit Current, Open Circuit Voltage and Fill Factor

The fill factor, FF is calculated by,

$$FF = \frac{I_{sc}V_{oc}}{I_{mpp}V_{mpp}} \tag{7.1}$$

Where I_{sc} is the short circuit current, V_{oc} is the open circuit voltage, I_{mpp} and V_{mpp} are current and voltage at the maximum power point respectively.

The calculated fill factors, short circuit currents, open circuit voltages, together with currents and voltages at the maximum power points are listed in Table 7.8. In the case of solar cells without LSC, they are listed in Table 7.9.

Table 7.8. Short circuit currents, open circuit voltages, and fill factors for different LSC tilt and time of the day.

Tilt angle	Time	I_{sc} (A)	V_{oc} (V)	I_{mpp} (A)	V_{mpp} (V)	FF
3°	0800	0.02	10.96	0.02	8.79	0.72
	1000	0.38	13.49	0.34	10.70	0.73
	1200	0.62	13.93	0.56	10.81	0.71
	1326	0.62	13.93	0.56	10.81	0.71
	1400	0.62	13.93	0.56	10.81	0.71
	1600	0.38	13.49	0.35	10.70	0.73
	1800	0.09	12.21	0.08	9.86	0.74
0°	0800	0.02	10.96	0.02	8.79	0.72
	1000	0.38	13.49	0.35	10.70	0.73
	1200	0.62	13.93	0.57	10.81	0.71
	1326	0.62	13.94	0.57	10.81	0.71
	1400	0.62	13.94	0.57	10.81	0.71
	1600	0.38	13.50	0.35	10.70	0.73
	1800	0.09	12.21	0.08	9.87	0.74
-12°	0800	0.01	10.57	0.01	8.44	0.71
	1000	0.39	13.51	0.35	10.71	0.73
	1200	0.64	13.96	0.59	10.81	0.71
	1326	0.64	13.97	0.59	10.81	0.71
	1400	0.64	13.97	0.59	10.81	0.71
	1600	0.39	13.53	0.36	10.71	0.73
	1800	0.09	12.23	0.08	9.88	0.74
-27°	0800	0.01	10.56	0.01	8.43	0.71
	1000	0.25	13.12	0.23	10.51	0.74
	1200	0.42	13.58	0.38	10.73	0.73
	1326	0.66	14.00	0.61	10.81	0.71

	1400	0.66	13.99	0.61	10.81	0.71
	1600	0.40	13.55	0.37	10.72	0.73
	1800	0.06	11.85	0.05	9.57	0.73
-42°	0800	0.01	10.15	0.01	8.05	0.69
	1000	0.25	13.12	0.23	10.51	0.74
	1200	0.42	13.59	0.39	10.74	0.73
	1326	0.43	13.61	0.40	10.74	0.72
	1400	0.43	13.61	0.40	10.74	0.72
	1600	0.26	13.17	0.24	10.54	0.73
	1800	0.04	11.46	0.04	9.23	0.73

Table 7.9. Short circuit currents, open circuit voltages, and fill factors for solar cells without LSC at optimum tilt and horizontal orientation .

Tilt angle	Time	I_{sc} (A)	V_{oc} (V)	I_{mpp} (A)	V_{mpp} (V)	FF
10°	0800	0.02	11.04	0.02	8.86	0.72
	1000	0.22	13.02	0.21	10.45	0.74
	1200	0.36	13.46	0.33	10.68	0.73
	1326	0.40	13.53	0.36	10.72	0.73
	1400	0.39	13.52	0.36	10.71	0.73
	1600	0.29	13.27	0.27	10.59	0.73
	1800	0.11	12.37	0.10	9.99	0.74
0°	0800	0.02	10.89	0.02	8.73	0.72
	1000	0.22	13.00	0.20	10.44	0.74
	1200	0.36	13.44	0.33	10.68	0.73
	1326	0.39	13.52	0.36	10.71	0.73
	1400	0.38	13.51	0.35	10.71	0.73
	1600	0.29	13.25	0.26	10.58	0.73
	1800	0.10	12.33	0.09	9.96	0.74

7.2 Analysis on the Simulation Result

Several apparent outcomes can be observed from tables and graphs in the previos section. In the case of solar cells with LSC at any tilt angle, the power output first increases from the morning until noon, then starts to decrease in the afternoon and evening until sunset. This is the same in the case for incident irradiance spectrum received by the attached solar cell and photo-generated current from solar cell attached to the LSC, as the power output is dependent on the photo-generated current, and the later depends on incident irradiance spectrum received by attached solar cell from the LSC. Fill factor of the solar cell attached to the LSC has an average value of 0.72, where the average fill factor of solar cell without LSC is 0.73.

Besides, the simulation shows that power output from the solar cells with LSC increase slightly as the LSC is tilted toward north, then decrease when it is tilted further. Therefore its optimum output appears at 12 degree LSC tilt toward north, where in contrast, solar cells without LSC has the optimum tilt of 10 degree toward south. The daily electrical energy output or the daily yield is also higher in the case of solar cells with LSC, as compared to that without using LSC.

Following are some analysis on the simulation result which is non-apparent in the tabulated data and graphs presented in the previous section, together with the assumptions made in the simulation model and a simple cost analysis on the LSC design specified in this simulation.

7.2.1 Assumptions Made in the Simulation

Several assumptions were made in the simulation model described in Chapter 6:

1. Clear sky was assumed throughout the day.

2. Ground reflection was not included in the simulation.
3. Reflection from the solar cell bottom surface back to the LSC was neglected.
4. Reflection from the LSC back to the external environment was neglected.

The first assumption means the calculated electrical output energy is the simulated practical maximum output from the solar cells in a day. The actual output will be limited by the actual cloudy atmosphere, therefore always smaller than the calculated one from the simulation.

Ground reflection is not included in the simulation here because it has no direct effect on horizontal LSC, limited direct effect on LSC with small tilt angle due to large incident angle of ground reflected light on the LSC top surface, and insignificant contribution on the incident diffuse solar spectrum from atmosphere backscattering of reflected light from the ground. Therefore it does not affect much in the LSC installation orientation study and was excluded from the simulation to simplify the study. However, it is possible to include it in the simulation model by first specify the ground reflectance model and generate upward hemispheric ground-reflected irradiance from SMARTS software, then model it as a secondary light source on the ground in the ray-tracing model.

Reflection from the solar cell bottom surface back to the LSC can be safely neglected because of high solar cell absorption that absorb most of the reflected light before it escape from the solar cell surface.

Reflection from the LSC back to the external environment can also be neglected because contribution to the diffuse solar spectrum from backscattering of the reflected light would be insignificant due to limited size of the LSC.

7.2.2 Breakdown of Contribution to Photogenerated Current from Different Sources

The percentage of contribution from dye emission, trapped direct and diffuse incident sunlight as shown in Table 7.3 shows an increase in the percentage of contribution from trapped direct incident sunlight as the LSC tilt toward north. Pie charts in Figure 7.15 and Figure 7.16 illustrate the relative contribution to photo-generated current by the different sources at time 1326 for LSC tilt angles of 3 degree toward south and 42 degree toward north respectively.

Taking values from Table 7.3, when the LSC is rotated by 45 degree from 3 degree tilt toward south to 42 degree tilt toward north, the dye emission contribution drops from 98.82% to 85.72%, the contribution from trapped direct incident sunlight increases from 1.05% to 14.09%, and trapped diffuse incident sunlight has an slight increase in its contribution from 0.13% to 0.19%. This is clearly illustrated in Figure 7.15 and Figure 7.16. However, from Table 7.1, total photo-generated current drops from 615.99mA to 432.45mA from one case to another. Apparently, as shown in Table 7.1, this is because the decrease in dye emission is faster than the increase in trapped direct incident sunlight as the LSC is tilted toward north.

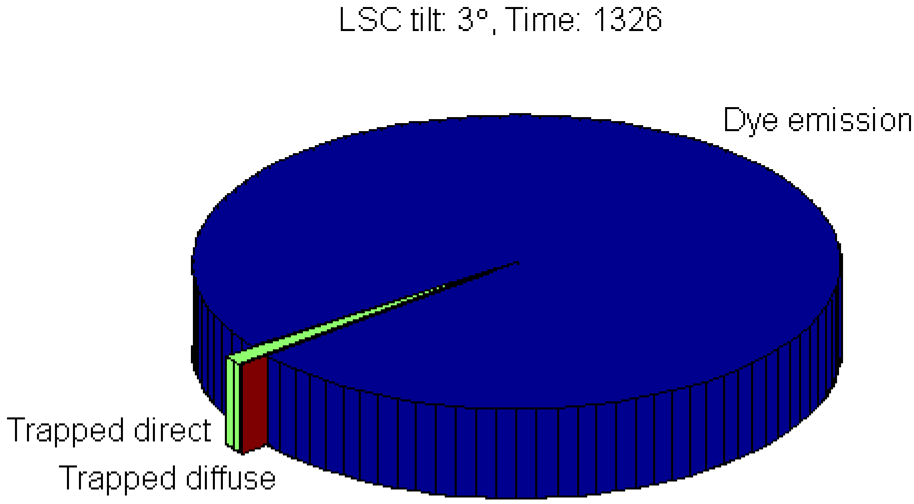

Figure 7.15: Pie chart of the contribution to photo-generated current from solar cell attached to LSC with 3 degree tilt toward south at time 1326.

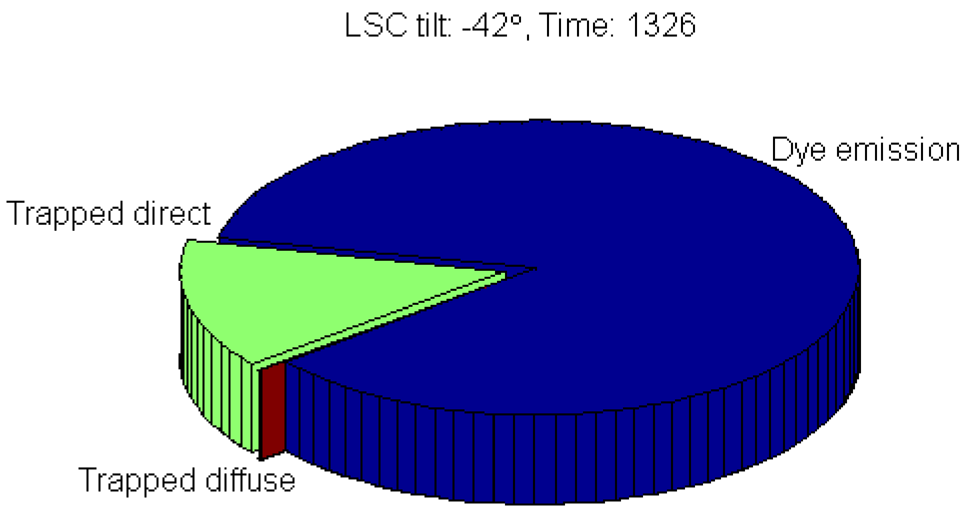

Figure 7.16: Pie chart of the contribution to photo-generated current from solar cell attached to LSC with 42 degree tilt toward north at time 1326.

In the case of solar cell without LSC at its optimum tilt, the percentage of contribution from direct and diffuse sunlight at time 1326 is illustrated by the pie chart in Figure 7.17. From Table 7.4, the direct sunlight contributes 98.95% to the total photo-generated current, where diffuse sunlight contributes 1.05%.

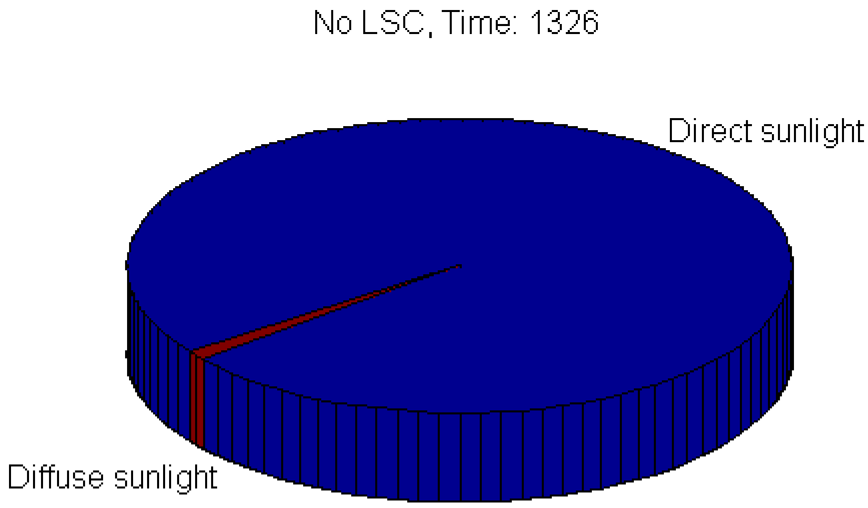

Figure 7.17: Pie chart of the contribution to photo-generated current from solar cell without LSC at its optimum tilt at time 1326.

As a conclusion, photo-generated current is contributed mainly by dye emission for the case of solar cell with LSC, and by direct sunlight for the case of solar cell without LSC. The former case is as expected since the planar LSC is designed to trap the dye emission via total internal reflection inside the LSC, where the later case is also as expected because direct sunlight has much higher total irradiance than diffuse sunlight. Besides, trapped direct incident sunlight contributes more when the LSC is tilted at a larger angle toward north.

7.2.3 Spectral Matching Between Dye Emission and Solar Cell IQE

The question of how well a solar cell match with the dye emission could be answered quantitatively by the ratio of number of generated electrons to number of photons received by the solar cell, since the solar cell behaves like a current source. The worst match produce no current and hence turns 0% of received photons into electrons, where the ideal match convert all photons into electrons and hence turns 100% of all received photons into electrons.

The total number of generated electrons per unit time per unit solar cell area can be derived from Eq. 6.55,

$$N_{el} = \frac{I_{ph}}{A_{pv} \cdot e} = \int \frac{\lambda}{hc} IQE(\lambda) E_{pv}(\lambda)\, d\lambda \tag{7.2}$$

Total number of photons received by the solar cell per unit time per unit solar cell area can be found by,

$$N_{ph} = \int \frac{\lambda}{hc} E_{pv}(\lambda)\, d\lambda \tag{7.3}$$

Therefore the ratio of total number of generated electrons to total number of received photons is,

$$N_{el} : N_{ph} = \frac{\int \frac{\lambda}{hc} IQE(\lambda) E_{pv}(\lambda)\, d\lambda}{\int \frac{\lambda}{hc} E_{pv}(\lambda)\, d\lambda} = \int IQE(\lambda) \frac{E_{pv}(\lambda) \cdot \lambda}{\int E_{pv}(\lambda) \cdot \lambda \, d\lambda}\, d\lambda \tag{7.4}$$

The normalized photon flux in wavelength domain is,

$$\Phi_{ph}(\lambda) = \frac{\frac{\lambda}{hc} E_{pv}(\lambda)}{\int \frac{\lambda}{hc} E_{pv}(\lambda)\, d\lambda} = \frac{E_{pv}(\lambda) \cdot \lambda}{\int E_{pv}(\lambda) \cdot \lambda \, d\lambda} \tag{7.5}$$

Therefore, the ratio is equal to the integration of the multiplication of IQE and normalized photon flux in wavelength domain with respect to wavelength, as shown in Eq. 7.6.

$$\text{Ratio of conversion} = N_{el} : N_{ph} = \int IQE(\lambda) \cdot \Phi_{ph}(\lambda)\, d\lambda \tag{7.6}$$

Define Φ_{el} as the number of electrons generated by photon flux Φ_{ph} from wavelength λ to $\lambda + d\lambda$,

$$\Phi_{el}(\lambda) = IQE(\lambda) \cdot \Phi_{ph}(\lambda) \tag{7.7}$$

The graphs of $\Phi_{el}(\lambda)$, $\Phi_{ph}(\lambda)$,and IQE(λ) in the case of horizontal LSC at time 1326 for dye emission, trapped direct incident sunlight and trapped diffuse incident sunlight are shown in Figure 7.18, Figure 7.19 and Figure 7.20 respectively. In the case of solar cell without LSC at horizontal orientation, the graphs of $\Phi_{el}(\lambda)$, $\Phi_{ph}(\lambda)$,and IQE(λ) for direct and diffuse sunlight are shown in Figure 7.21 and Figure 7.22 respectively. As shown in Eq. 7.5 and Eq. 7.6, the area under $\Phi_{ph}(\lambda)$ is normalized to 1 and the ratio of conversion is numerically equal to the area under the curve $\Phi_{el}(\lambda)$.

In simple words, the gap between $\Phi_{el}(\lambda)$, $\Phi_{ph}(\lambda)$ at the wavelength λ is proportional to the actual loss due to non-unity IQE at λ in the conversion process from photon flux into electrical current. Larger gap contributes higher loss due to non-unity IQE. Therefore, the graphs could qualitatively show the range of incident light wavelength the solar cell output is limited by its IQE.

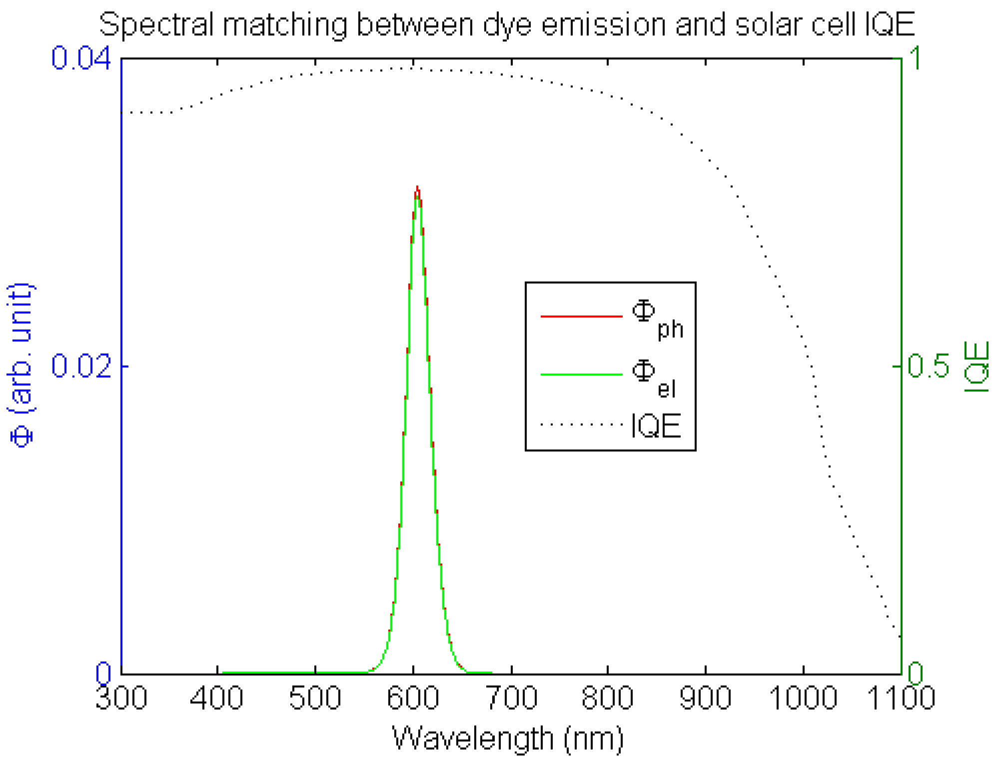

Figure 7.18: Spectral matching between dye emission and solar cell IQE for horizontal LSC at time 1326.

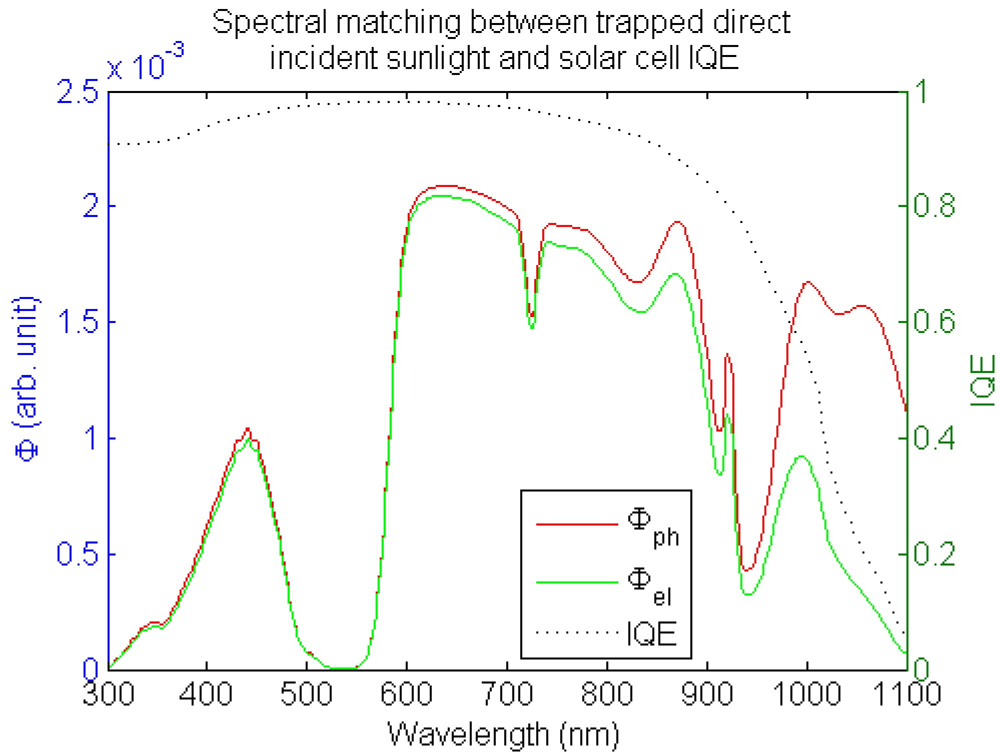

Figure 7.19: Spectral matching between trapped direct incident sunlight and solar cell IQE for horizontal LSC at time 1326.

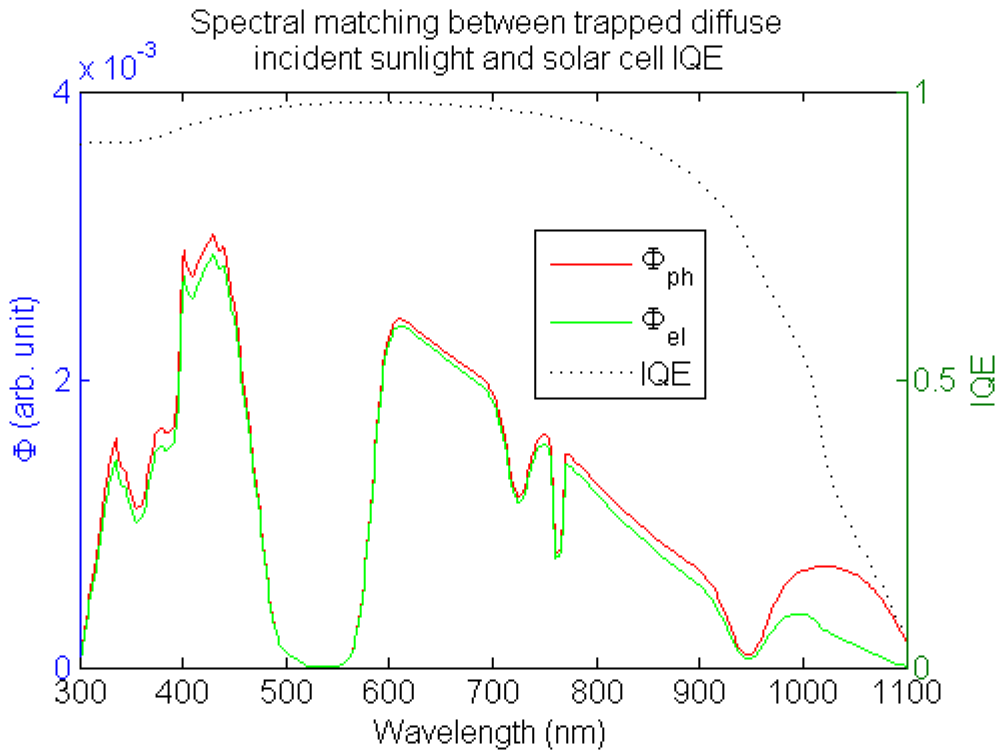

Figure 7.20: Spectral matching between trapped diffuse incident sunlight and solar cell IQE for horizontal LSC at time 1326.

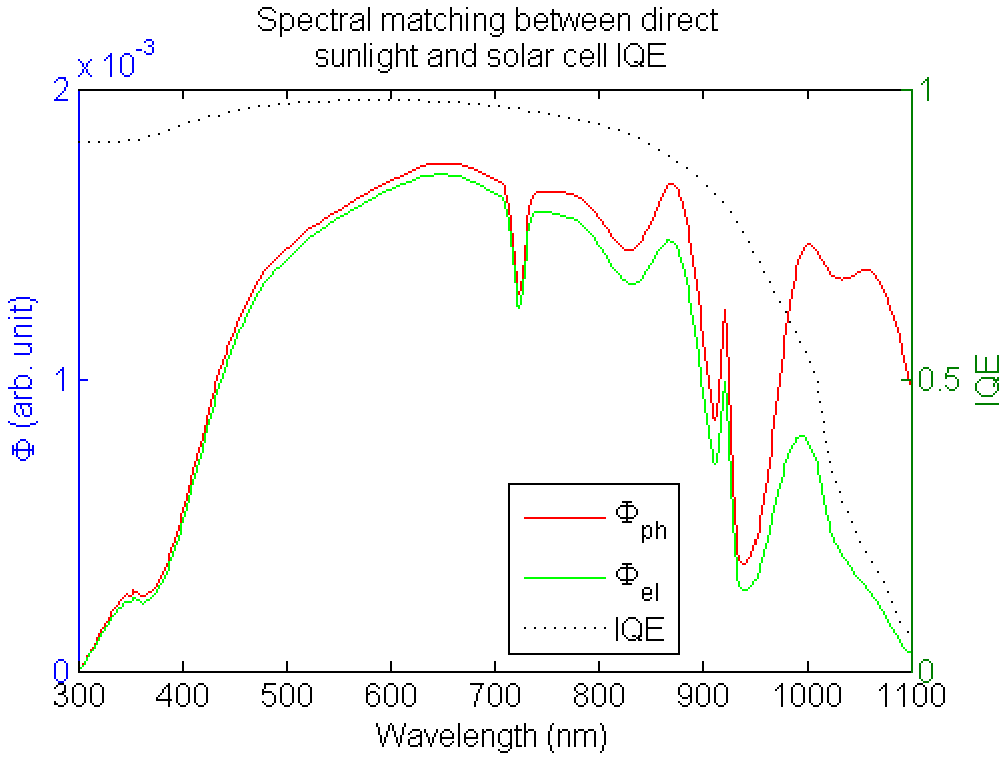

Figure 7.21: Spectral matching between incident direct sunlight and solar cell IQE for horizontal solar cell without LSC at time 1326.

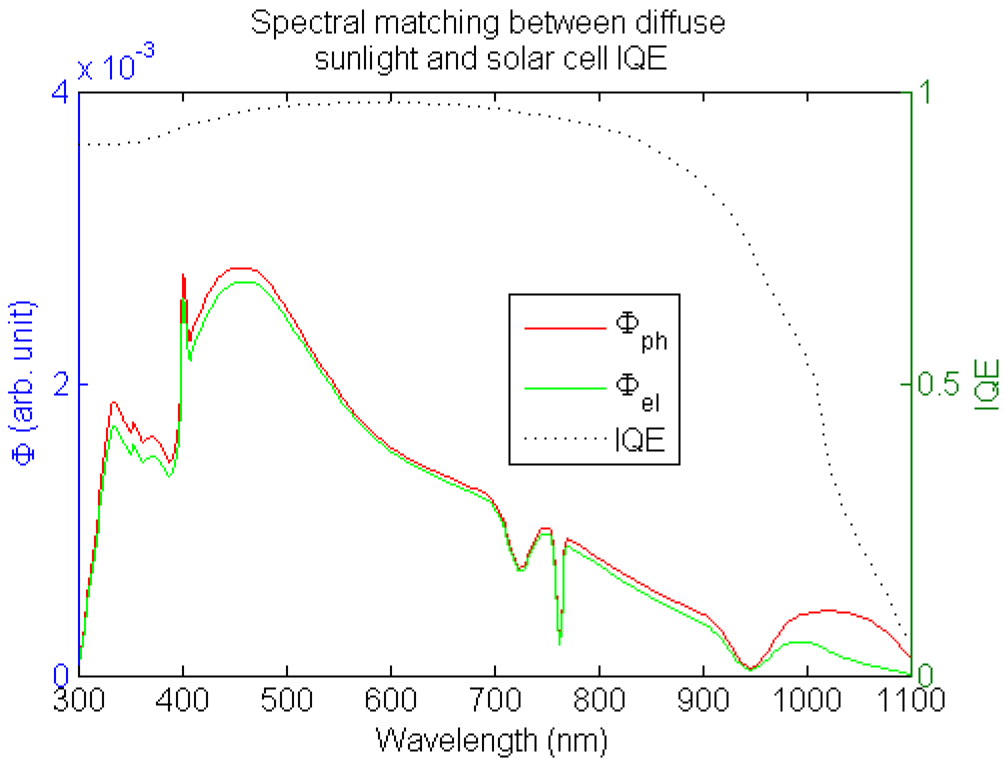

Figure 7.22: Spectral matching between incident diffuse sunlight and solar cell IQE for horizontal solar cell without LSC at time 1326.

From Figure 7.18, the dye emission has nearly perfect match with the solar cell IQE, which is one of the reasons of using LSC with the solar cells: to improve the solar cell efficiency and hence its cost effectiveness.

For trapped direct incident light in the case of solar cell with LSC (Figure 7.19), most of the losses caused by non-unity solar cell IQE come from the wavelength 600nm-1100nm, roughly corresponds to the visible red light to near infrared radiation.

It is similar in the case of trapped diffuse incident light as shown in Figure 7.20, where the losses caused by non-unity solar cell IQE come from the wavelength 800nm-1100nm, corresponds to near infrared radiation.

In other words, the silicon solar cell does not convert the light into electrical current efficiently at that range of wavelength. This factor must be taken into account in the effort to increase the contribution from trapped incident light by changing the LSC design, because higher contribution from the trapped incident light reduces the overall conversion efficiency due to limitation imposed by the solar cell IQE. The overall conversion is determined by that for the dye emission in Figure 7.18 since it contributes the most to the photo-generated current in the case of solar cell attached to LSC.

In contrast, for direct and diffuse sunlight in the case of horizontal solar cell without LSC as shown in Figure 7.21 and Figure 7.22 respectively, the major losses caused by non-unity solar cell IQE come from the wavelength 600nm-1100nm for direct sunlight, 325nm-475nm and 800nm-1100nm for diffuse sunlight. Wavelength of 325nm-475nm corresponds to ultraviolet radiation to visible violet and blue light. In this case, direct sunlight contributes the most to the photo-generated current and therefore the overall conversion is determined by that for the direct sunlight in Figure 7.21.

The ratio of conversion calculated using Eq. 7.6 is listed in Table 7.10 and Table 7.11 for the cases of solar cell with and without LSC respectively.

Table 7.10. Ratio of conversion from photons to electrons in the case of solar cell attached to LSC edge for different contribution sources.

Tilt angle	Time	Ratio of conversion from dye emission	Ratio of conversion from trapped direct incident sunlight	Ratio of conversion from trapped diffuse incident sunlight
3°	0800	0.963	0.726	0.801
	1000	0.980	0.728	0.818
	1200	0.980	0.749	0.827
	1326	0.980	0.774	0.829
	1400	0.980	0.744	0.829
	1600	0.980	0.732	0.825
	1800	0.963	0.714	0.816
0°	0800	0.963	0.725	0.801
	1000	0.980	0.727	0.818
	1200	0.980	0.747	0.827
	1326	0.980	0.773	0.829
	1400	0.980	0.743	0.829
	1600	0.980	0.731	0.824
	1800	0.963	0.715	0.816
-12°	0800	0.998	0.725	0.801
	1000	0.980	0.724	0.818
	1200	0.980	0.744	0.827
	1326	0.980	0.770	0.829
	1400	0.980	0.740	0.829
	1600	0.980	0.729	0.825
	1800	0.963	0.714	0.816
-27°	0800	0.998	0.725	0.801
	1000	0.977	0.725	0.818

	1200	0.980	0.743	0.827
	1326	0.980	0.752	0.829
	1400	0.980	0.794	0.829
	1600	0.980	0.727	0.824
	1800	0.963	0.709	0.816
-42°	0800	0.998	0.719	0.801
	1000	0.977	0.723	0.818
	1200	0.980	0.741	0.828
	1326	0.980	0.749	0.829
	1400	0.980	0.793	0.828
	1600	0.977	0.725	0.824
	1800	0.963	0.708	0.816

Table 7.11. Ratio of conversion from photons to electrons in the case of solar cell without LSC at optimum tilt and horizontal orientation for different contribution sources.

Tilt angle	Time	Ratio of conversion from direct sunlight	Ratio of conversion from diffuse sunlight
10°	0800	0.823	0.898
	1000	0.817	0.891
	1200	0.820	0.882
	1326	0.838	0.882
	1400	0.820	0.882
	1600	0.840	0.884
	1800	0.825	0.892
0°	0800	0.823	0.898
	1000	0.817	0.891
	1200	0.820	0.883
	1326	0.838	0.882
	1400	0.820	0.882
	1600	0.840	0.884
	1800	0.825	0.892

In conclusion, from Table 7.10 and Table 7.11, the average ratio of conversion for dye emission, trapped direct incident sunlight and trapped diffuse incident sunlight are 0.98, 0.74 and 0.82 respectively. Where those for direct sunlight and diffuse sunlight in the case of solar cell without LSC are 0.83 and 0.89 respectively.

Ratios of conversion for trapped direct sunlight and trapped diffuse sunlight in the case of solar cell with LSC are lower than those for direct sunlight and diffuse sunlight in the case of solar cell without LSC. This is because the dye absorbs most of the trapped sunlight in the LSC at the wavelength 500nm-550nm where the IQE is almost at its maximum (refer to Figure 7.19 and Figure 7.20).

The overall ratio of conversion is 0.98 and 0.83 for the cases of solar cell with and without LSC respectively, since the photogenerated current are mostly contributed by dye emission and direct sunlight respectively as shown in Table 7.3 and Table 7.4. Therefore, solar cell with LSC will still perform better than the same solar cell operating alone without LSC even if the total incident photon flux (area under the photon flux spectrum) received by the solar cell is the same in both cases. In other words, even if the gain from dye emission trapping capability of the LSC exactly equals to the losses contributed by its escape cone loss, non-unity dye luminescent quantum efficiency, re-absorption loss, etc., the LSC can still increase the solar cell output.

7.2.4 Electrical Energy Generated by Solar Cells in a Day

Solar cell's performance is commonly evaluated by its nominal power output under AM1.5G spectrum. However, the actual solar irradiance and hence the actual solar cell power ouput varies from place to place. Therefore, simulation study based on the installation location is required to know the actual solar cell performance. Simulation model developed to study the case of solar cells operating without LSC cannot be used directly in the case of solar cells attached to the LSC edge. The simulation model in this thesis is therefore required for this purpose.

Besides, from Figure 7.14, the optimum LSC tilt is apparently different from the optimum solar cell tilt without LSC. From Table 7.7, taking 12 degree LSC tilt toward north as the optimum LSC tilt angle, together with the optimum solar cell tilt angle of 10 degree toward south, the daily yield increases from 26.94kWh to 42.28kWh when LSC (at optimum tilt) is used. Therefore, the use of LSC increases the daily yield of solar cell by (42.28-26.94)/26.94=56.94%.

Evaluation of total electrical energy output in kWh is important because commonly, customer who installs the solar panel is interested only on the cost of generated electricity (cost per kWh), not the cost per nominal output power (cost per kWp). The conversion from the later to the former can be done for the case of the LSC design specified in Chapter 6, with a few assumptions, as discussed in Chapter 7.2.6.

7.2.5 Area occupied by the LSC

Total solar cells area in the simulation is 49.91cm x 2cm, where the LSC has surface area of 50cm x 50cm. Therefore, the installation area is increased from 99.82 cm^2 to 2500 cm^2. In other words, the use of LSC in the simulation case increases the total installation area by 25 times, or 2505%.

7.2.6 Cost Analysis

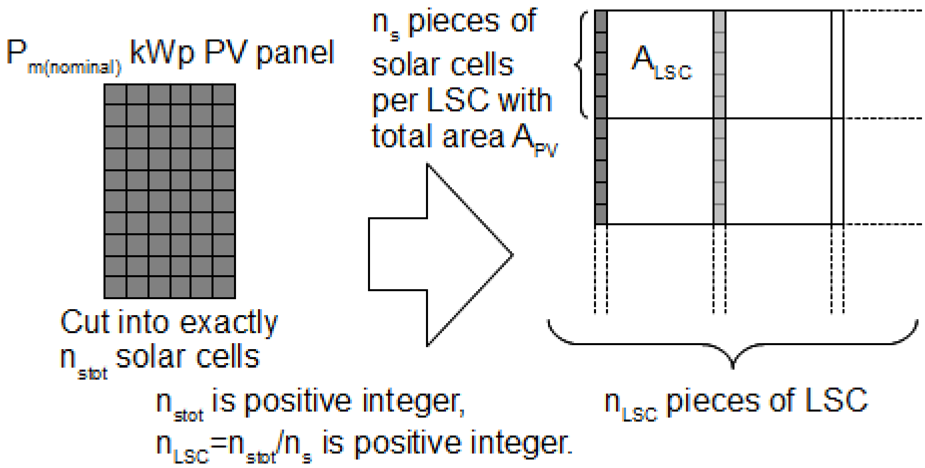

Figure 7.23: Separate a PV panel into solar cells attached to LSCs.

The LSC can be considered as a replacement of coating on the solar cells surface. In other words, the LSC can be cured directly on the solar cells surface during the solar cells manufacturing process and replaces the solar cells surface coating.

Assume that a large piece of solar panel with nominal output power of Pm kWp (power at the maximum power point tested under illumination from AM1.5G standard solar spectrum) can be cut into exactly n_{stot} smaller pieces of solar cell as illustrated in Figure 7.23, where n_{stot} is a positive integer. In the case of LSC in this simulation, each of the smaller pieces has a surface area of 2.17cm x 2cm.

A number of n_s solar cells are connected together and attached to a LSC with surface area of 50cm x 50cm. Therefore, there are a total number of $n_{LSC}=n_{stot}/n_s$ pieces of similar LSC connected together, generating electricity from the attached solar cells, where n_{LSC} is assumed to be a positive integer too.

In the case of solar cells and LSC in this simulation, surface area of the solar panel in cm^2 per kWp nominal power output is,

$$A_{PV} = \left(\frac{99.82\ cm^2}{n_s} \times n_{stot} \right) \Big/ P_{m(nominal)} = \frac{99.82 \times n_{LSC}}{P_{m(nominal)}}\ \text{cm}^2/\text{kWp} \tag{7.8}$$

Total LSC surface area in cm^2 per kWp nominal power output is,

$$A_{LSC} = \frac{2500 \times n_{LSC}}{P_{m(nominal)}}\ \text{cm}^2/\text{kWp} \tag{7.9}$$

Therefore the ratio of their area is,

$$\frac{A_{LSC}}{A_{PV}} = \frac{2500}{99.82} = 25.0451 \tag{7.10}$$

Similarly, the daily PV panel electrical energy output per nominal output power in kWh/kWp is,

$$E_{dailygenPV} = \left(\frac{26.94}{n_s} \times n_{stot} \right) \Big/ P_{m(nominal)} = \frac{26.94 \times n_{LSC}}{P_{m(nominal)}}\ \text{kWh/kWp} \tag{7.11}$$

Total kWh/kWp output from the solar cells with LSC is,

$$E_{dailygenPVLSC} = \frac{42.28 \times n_{LSC}}{P_{m(nominal)}}\ \text{kWh/kWp} \tag{7.12}$$

Therefore the ratio of optimum daily yield of solar cells with LSC to that without LSC is,

$$\frac{E_{dailygenPVLSC}}{E_{dailygenPV}} = \frac{42.28}{26.94} \tag{7.13}$$

The solar panel operating alone without LSC has optimum annual yield of E_{genPV}=1180 kWh/kWp at Kuala Lumpur, Malaysia (Lim *et al.*, 2008). It was calculated based on a simulation of in-plane solar irradiance at 10 degree tilt toward south (optimum tilt of solar panel at Kuala Lumpur, Malaysia), which is then multiplied by performance ratio of a 1kWp solar panel (Jensen *et al.*, 2006).

Optimum annual yield of solar cells with LSC can be estimated by assuming that the ratio of optimum annual yield of solar cells with LSC to the that without LSC is the same as the optimum daily yield ratio of the two. Therefore, the optimum annual yield with LSC, $E_{genPVLSC}$=1180*42.28/26.94=1852 kWh/kWp. Therefore, their ratio is,

$$\frac{E_{genPVLSC}}{E_{genPV}} = \frac{E_{dailygenPVLSC}}{E_{dailygenPV}} = \frac{42.28}{26.94} = 1.5694 \tag{7.14}$$

In general, material cost and installation cost of the solar cells and LSC fluctuate from time to time. Therefore, instead of using the exact cost in the calculation, ratio between costs is used here to find a general relationship between the costs of generated electricty with and without the use of LSC.

Denote the following ratios,

$$r_E = \frac{E_{genPVLSC}}{E_{genPV}} \tag{7.15}$$

$$r_A = \frac{A_{LSC}}{A_{PV}} \tag{7.16}$$

$$r_{C1} = \frac{C_{LSC}}{C_{PV}} \tag{7.17}$$

$$r_{C2} = \frac{C_{PVtotal}}{C_{PVsystem}} \tag{7.18}$$

Where,

$E_{genPVLSC}$ = Annual yield of solar cells with LSC (kWh/kWp),

E_{genPV} = Annual yield of solar cells without LSC (kWh/kWp),

A_{LSC} = Surface area of LSC per kWp nominal power output (m^2/kWp),

A_{PV} = Total surface area of solar cells per kWp nominal power output (m^2/kWp),

C_{LSC} = Cost per unit area of solar cell (cost m^{-2}),

C_{PV} = Cost per unit area of LSC (cost m^{-2}),

$C_{PVtotal}$ = Total cost of a PV panel per kWp nominal power output (cost/kWp),

$C_{PVsystem}$ = Overall installation cost per kWp nominal power output, including the cost of PV panel, cost of inverter with transformer, array support structures and electrical cabling, transportation cost, annual overhead expense (operation cost, maintenance cost and insurance during its lifetime), labor cost, and equipment cost. (cost/kWp).

Total cost of PV panel without using LSC is,

$$C_{PVtotal} = C_{PV} \cdot A_{PV} \tag{7.19}$$

Total cost of PV cells with LSC is,

$$\begin{aligned} C_{PVLSCtotal} &= C_{PV} \cdot A_{PV} + C_{LSC} \cdot A_{LSC} \\ &= C_{PV} \cdot A_{PV} + r_{C1} \cdot C_{PV} \times r_A \cdot A_{PV} \\ &= C_{PV} \cdot A_{PV} \cdot \left(1 + r_{C1} r_A\right) \\ &= C_{PVtotal} \cdot \left(1 + r_{C1} r_A\right) \end{aligned} \tag{7.20}$$

The overall PV system cost without LSC is,

$$
\begin{aligned}
C_{PVsystem} &= C_{PVtotal} \cdot \frac{1}{r_{C2}} \\
&= C_{PVtotal} \cdot \left[1 + \left(\frac{1}{r_{C2}} - 1\right)\right] \qquad (7.21) \\
&= C_{PVtotal} + C_{PVtotal} \cdot \left(\frac{1}{r_{C2}} - 1\right)
\end{aligned}
$$

From Eq. 7.21, the overall PV system cost = total cost of PV panel + additional cost for the rest. Assume that adding the LSC only increases the the additional cost as shown in Eq. 7.21 stays the same for the case with LSC, the overall PV system cost with the use of LSC can be calculated by,

$$
\begin{aligned}
C_{PVLSCsystem} &= C_{PVLSCtotal} + C_{PVtotal} \cdot \left(\frac{1}{r_{C2}} - 1\right) \\
&= C_{PVtotal} \cdot \left(1 + r_{C1} r_A\right) + C_{PVtotal} \cdot \left(\frac{1}{r_{C2}} - 1\right) \qquad (7.22) \\
&= C_{PVtotal} \cdot \frac{1}{r_{C2}} \cdot \left(r_{C2} r_{C1} r_A + 1\right) \\
&= C_{PVsystem} \cdot \left(r_{C2} r_{C1} r_A + 1\right)
\end{aligned}
$$

The cost of generated electricity in term of cost/kWh for the case without LSC is,

$$
C_{PVsystem\,(per\ kWh)} = \frac{C_{PVsystem}}{E_{genPV}} \qquad (7.23)
$$

In the case of solar cells with LSC, the cost of generated electricity is,

$$
\begin{aligned}
C_{PVLSCsystem\,(per\ kWh)} &= \frac{C_{PVLSCsystem}}{E_{genPVLSC}} \\
&= C_{PVsystem} \cdot \left(r_{C2} r_{C1} r_A + 1\right) \cdot \frac{1}{r_E \cdot E_{genPV}} \\
&= C_{PVsystem} \cdot \frac{1}{E_{genPV}} \cdot \left(\frac{r_{C2} r_{C1} r_A + 1}{r_E}\right) \qquad (7.24) \\
&= C_{PVsystem\,(per\ kWh)} \cdot \left(\frac{r_{C2} r_{C1} r_A + 1}{r_E}\right)
\end{aligned}
$$

For the LSC in this simulation, substitute the value of r_E from Eq. 7.14, r_A from Eq. 7.10, and use $r_{C1}=C_{LSC}/C_{PV}=1:15$ from (Bende *et al.*, 2008). Assume that the PV panel cost is 30% of the overall PV system cost, i.e. $r_{C2}=0.3$,

$$\begin{aligned} C_{PVLSCsystem\,(per\,kWh)} &= C_{PVsystem\,(per\,kWh)} \cdot \left(0.3\times\frac{1}{15}\times\frac{2500}{99.82}+1\right)\cdot\left(\frac{26.94}{42.28}\right) \\ &= 0.9230\times C_{PVsystem\,(per\,kWh)} \\ &= C_{PVsystem\,(per\,kWh)} - 0.0770\times C_{PVsystem\,(per\,kWh)} \end{aligned} \tag{7.25}$$

In this case, the LSC can reduce the cost of generated electrical energy by 7.7%.

7.2.7 Criterion for Cost Reduction

From Eq. 7.24,

$$\frac{r_{C2}r_{C1}r_A+1}{r_E}=\frac{C_{PVLSCsystem\,(per\,kWh)}}{C_{PVsystem\,(per\,kWh)}} \tag{7.26}$$

The term at the left hand side of Eq. 7.26 must be less than one to have a reduction in the cost of generated electricity.

$$\begin{gathered} \frac{r_{C2}r_{C1}r_A+1}{r_E}<1 \\ r_{C2}r_{C1}r_A+1<r_E \\ \frac{C_{PVtotal}}{C_{PVsystem}}\frac{C_{LSC}}{C_{PV}}\frac{A_{LSC}}{A_{PV}}+1<\frac{E_{genPVLSC}}{E_{genPV}} \\ \frac{C_{PVtotal}}{C_{PVsystem}}\frac{C_{LSC}}{C_{PV}}\frac{A_{LSC}}{A_{PV}}<\frac{E_{genPVLSC}-E_{genPV}}{E_{genPV}} \\ \left(\frac{C_{PVtotal}}{C_{PVsystem}}\times 100\%\right)\frac{C_{LSC}}{C_{PV}}\frac{A_{LSC}}{A_{PV}}<\frac{E_{genPVLSC}-E_{genPV}}{E_{genPV}}\times 100\% \end{gathered} \tag{7.27}$$

Inequality 7.27 is the criterion which must be met to have a reduction in the cost of generated electricity. Put it in words, multiplication of the percentage of all solar cells cost in the PV system, ratio of LSC cost to solar cell cost (per unit area) and ratio of LSC surface area to solar cell surface area must be less than the percentage of increment in annual yield after using the LSC.

It allows us to perform a quick check on the PV system with LSC to see whether a cost reduction per unit generated electricity is possible or not before doing a detailed cost analysis on it.

For example, in the case of the LSC in this simulation, the increment in annual yield is 56.94% (same as the increment in daily yield as calculated in Chapter 7.2.4). If it is found that PV panel cost is 30% of the total PV system cost, and the solar cell cost per unit area is 15 times higher than the LSC cost per unit area, the multiplication on the left hand side of Eq. 7.27 gives 50.09%, which is smaller than the increment in annual yield, and therefore cost reduction is possible.

When the PV panel cost is 50% of the total PV system cost, even if the solar cell cost per unit area is 20 times higher than the LSC cost per unit area, the multiplication gives 62.95%, which is larger than the increment in annual yield, and therefore cost reduction is not possible in this case.

7.3 Conclusion from the Simulation Result

The overall simulation model in Chapter 6 assumes a clear sky throughout the day, therefore calculates the solar cells (attached to LSC) daily yield as the maximum practical output at the particular location and orientation.

This simulation shows that solar cells attached to the LSC edge have a better electrical output if the LSC is tilted instead of installed horizontally, where the best tilt angle of the LSC is different from the optimum tilt angle of the solar cells without LSC. In the case of the location specified in this simulation (Kuala Lumpur, Malaysia), optimum LSC tilt angle is 12 degree facing north, where the solar cells without have an optimum tilt angle of 10 degree facing south.

Simulation result also confirms that the contribution from trapped direct sunlight will increase as the LSC is tilted toward north, but the contribution from dye emission will decrease at the same time. However, dye emission has the highest contribution to photo-generated current among contribution from dye emission, trapped direct incident sunlight and trapped diffuse incident sunlight.

Besides, a ratio of conversion from photons to electrons was defined to describe quantitatively the spectral matching between solar cell and the light spectrum it receive, including the dye emission spectrum. It was then verified that the silicon solar cell specified in the simulation has very good spectral match with the dye emission spectrum from Rhodamine 6G, converting 98% of the collected photon flux from the dye emission into photo-generated current. In contrast, the silicon solar cell can only convert 83% of the photon flux it received from direct sunlight into photo-generated current.

In addition, a simple cost analysis was done on the solar cells with LSC in this simulation. From the simulation result, the solar cells generate 1.5694 times more electricity when LSC is used, but the LSC surface area is 25.0451 times larger than the area of solar cells attached to its edge. Assume that the LSC cost per unit area is cheaper than that of solar cell by a factor of 15, and the cost of PV panel without LSC is only 30% of the total PV system cost. The cost per generated electricity (cost/kWh) can be reduced by 7.7% using the LSC.

7.4 Suggested Improvement on the LSC Based on the Conclusion

Simulation result presented in this chapter shows that LSC performance can be improved by changing its geometric design, even as simple as tilting it thus changing its installation orientation. This shed new light on optimizing the LSC performance beside looking for better materials to construct it: luminescent dye with higher Stokes shift and luminescent quantum efficiency, transparent host material with lower absorption, and also solar cells with better spectral match with the dye and higher efficiency.

Increasing trapped direct incident sunlight could possibly be another new way to break the limitation on the LSC performance imposed by the properties of materials where the LSC is constructed by, such as low luminescent quantum efficiency or small Stoke shift that causes higher self-absorption loss. These material properties cannot be changed easily unless new materials or method to synthesize them are found to replace the existing ones.

The state-of-the-art LSC at the time of writing has 7.1% power conversion efficiency geometrical concentration (ratio of LSC surface area to total solar cells surface area) of 2.5 (Slooff *et al.*, 2008) where Gallium Arsenide (GaAs) solar cells are attached to all its 4 edges. In contrast, the state-of-the-art quantum dot luminescent solar concentrator with geometrical concentration of 12.38 has 2.8% power conversion efficiency using silicon solar cells (Bomm *et al.*, 2011). It would be interesting to compare the cost of generated electricity two LSC above with different design and materials using the simulation model developed in this thesis. It is reasonable to assume that the optimum design for the lowest electricity cost is different from the optimum design for highest power conversion efficiency tested under the standard AM1.5G solar spectrum. However the later can be used as the first guess to find out the design which gives the lowest generated electricity cost using the simulation model in this thesis.

7.5 Some Notes on the Tilt Angles in the Simulation

Beside 0°, ideally the rest of the tilt angles should be: “without LSC”: 10°; “with LSC”: 10°, -5°, -20°, and -35°, where 10° was used as the optimum tilt angle for Malaysia in another study and it had to be avoided in “with LSC” case, as explained in the following paragraphs. Hence 7° was deducted from every tilt angles for the case “with LSC” and it becomes 3°, -12°, -27°, and -42°.

For the case “without LSC”, the 10° tilt angle in Malaysia will provide close to optimum generation for Malaysia, as quoted from a report of research findings prepared by Jensen, 2006, retrieved from Malaysia Building Integrated Photovoltaic (BIPV) Technology Application Project, or MBIPV Project website. It was found from the simulation that the direction of the sun at time 13:26 is almost parallel to the vertical top direction of the solar cells surface. Therefore the actual optimum tilt angle in this case should be close to, but not exactly 10°. However, 10° tilt angle was still used in the thesis so that it was possible to estimate the annual yield for the case “with LSC”, from the reported annual yield of 1180 kWh/kWp for solar cells with 10° tilt angle (Jensen, 2006). Furthermore, the daily yields for 0° tilt and 10° tilt in this case were found to be 26.31 kWh and 26.94 kWh respectively, with a small different of 0.63 kWh. Therefore it can be safely assumed that in the case of real optimum tilt angle, the calculated difference in generated kWh will not alter the rest of the result significantly.

On the other hand, for the case "with LSC", simulation with tilt angle of 10° was avoided because the direction of the sun at time 13:26 was found to be very close to the vertical top direction from LSC top surface (0.17° relative to the LSC surface normal), which then makes the simulation of trapped direct incident sunlight impractical to perform, since the angle subtended by the sun as seen from the solar cells in this case is extremely small, and thus requiring enormous number of rays to be traced. More specifically, the angle subtended is in the order of $10^{-3\circ}$ while the number of rays is in the order of 10^9 (not including additional rays which are created when a ray hit an interface or surface).

CHAPTER 8

CONCLUSION

In conclusion, the luminescent solar concentrator (LSC) was studied in term of the effect of its installation orientation on its performance using a simulation model developed in this thesis and besides, a low-cost construction procedure for LSC with large surface area of 100cm x 50cm has been proposed.

A LSC sample with dimension of 100cm x 50cm x 2.5cm was constructed using the proposed procedure. However, the LSC sample has a bad top surface quality and air-gap between its edge and the solar cells due to high volume shrinkage during its curing process, which greatly reduce its performance although the sample quality is good, having no bubble and undissolved dye particles. Besides, a light source having large illumination area and adjustable light intensity was built for the LSC measurement.

The subsequent chapter described the newly developed hybrid algorithm for LSC simulation in detail. A technique to solve differential equation in continuous linear time invariant system was used to separate the solution of radiative transfer equation into two parts: trapped incident light and dye emission, where the actual solution is the summation of the two. Simulation code for trapped incident light was named ray-tracing model which was assisted by a ray-tracing software called Radiance, where the code for dye emission was named thermodynamic model since it was in fact a modified version of the existing thermodynamic model. The overall algorithm was named hybrid algorithm since two different algorithms were used.

Spectral irradiance of the light output from the LSC edge can be calculated from the solution of the radiative transfer equation at the edge, together with the fulfillment of detailed balance condition using the thermodynamic two-flux model. Verification of the hybrid algorithm was carried out by first building a small LSC and tested it under filtered LED light, and finally compared the simulated spectrum to the measured spectrum from the LSC edge. From the result, the simulation and measurement was found to be in good agreement.

The simulation code for ray-tracing model was then improved for simulation of LSC under sunlight, which could not be done before the improvement due to the extremely small angle subtended by the sun. Using the original simulation code will either wrongly output the contribution from direct sunlight to be zero or take an unacceptably long time to finish, depends on the number of rays being traced. The improvement find the direction of the sun as seen from the solar cell and then trace more rays toward the direction of the sun, or in other words, different accuracy for direct sunlight and diffuse sunlight.

Finally, the effect of LSC installation orientation to its performance was studied using the improved simulation code. The actual sun irradiance and direction were simulation using a software called Simple Model of the Atmospheric Radiative Transfer of Sunshine (SMARTS). The light received by the solar cells from the LSC was simulated by the hybrid algorithm, taking the input from the output of SMARTS program. The electrical output from the solar cells attached to LSC edge was then simulated using solar cell simulation model.

The outcomes from the simulation study are interesting. First of all, it was found that the contribution from trapped direct sunlight increases as the LSC is tilted, in which the tilt is in opposite direction to the optimum solar cell tilt operating alone without LSC under sunlight. Besides, the LSC performance evaluated by its daily electricity generation in term of kWh from the solar cells using the simulation model in this thesis makes it possible to evaluate the cost of its generated electricity, which can only be roughly estimated before this. Lastly, a simple cost analysis was done and it was found that a reduction of 7.7% in generated electricity cost can be achieved for the LSC materials and design specified in the simulation study under the following assumption: the LSC is 15 times cheaper than the solar cell, and the PV panel costs 30% of the total PV system. The small reduction in electricity generation cost was expected since it was not the optimized design.

Upon further improvement in the simulation code, two possible simulation can be done using the simulation model developed in this thesis: optimization of the LSC design and installation orientation, and practical performance simulation taking into account of the real external environment at the installation location.

8.1 Future Works

The abilities of this simulation model is currently limited by its long computation time. Theoretically, it is possible to use derivative-free optimization algorithm to find out the optimimum LSC design having lowest electricity cost specifically for the installation location, with the aid from the simulation model in Chapter 6 by optimizing multiple design varibles such as LSC dimension, tilt angle, dye concentration etc. However, the algorithm involves evaluation of the solar cells output many times using the computationally extensive simulation model. This is infeasible in term of investment in time without extensive improvement on its simuation efficiency, as determining the optimized design empirically using experiments could be achieved faster than the simulation method.

Therefore improvement in its simulation efficiency should be done in the first place, using some assumptions or simplifications which do not affect the output significantly. Besides, it can also be done by incorporating Monte Carlo methods, i.e. by replacing the multi-dimensional numerical integration in the thermodynamic model with Monte Carlo integration algorithm, for example.

Besides, experimental verification of the overall simulation result should be carried out at the same time. Following are the proposed verification process:

1. Construct a LSC prototype with the same dimension and quality.
2. Install next to the LSC a reference solar panel with known electrical performance to study the accuracy of SMARTS program in solar

irradiance spectrum simulation, and adjust some input parameters from typical values which cannot be measured by available equipment.

3. Install a weather station at an unsheltered location nearby to get some of the input parameters for SMARTS program.
4. Actual measurements can be made in real time by an IV tester for current-voltage curve and power-voltage curve, in both the LSC sample and the reference solar panel.
5. A few simulations on the LSC will be done for the time where the sun is not blocked by clouds, and comparison will be made between the simulations and actual measurements.

Since it is unlikely to have no cloud on the sky throughout a day in Malaysia, only the time where no cloud is blocking the sun is used in the verification, instead of comparing the simulation with the measurement throughout the day. If the mismatch between both results is acceptable, it would be enough to verify the simulation accuracy since the simulation was done by assuming clear sky throughout the day.

8.1.1 Practical Performance Evaluation of Solar Cells Attached to LSC

The significance of this simulation model is its great potential in expansibility to simulate the LSC performance based on its actual installation environment. It can be incorporated into the Radiance simulation software as a new material definition which can calculate the dye emission and bottom mirror reflected light escaped from the LSC top surface, then convert it into a secondary light source to model the LSC appearance for design verification purpose, on the other hand it also simulates the solar cells maximum generated power for the specific location and time, where the SMARTS software is used to generate the neccessary solar irradiance and direct sunlight direction.

In this way, the simulation can include as many objects as possible outside the LSC top surface. For example, the windows of other buildings which reflect light to the LSC during certain time of the day, and diffuse reflection from walls, especially those being painted in white color. It therefore allows us to obtain a more realistic simulated LSC performance based on its actual installation environment, instead of simulation under standard test environment which could be significantly different from the actual installation environment.

This method can avoid extra investment of time and resources in developing a new LSC simulation that simulate its performance under the actual external environment where the LSC is installed because it could be done using the existing Radiance software, which is a well developed ray-tracing software and includes models for various kind of reflective surfaces: specular surface, Lambertian surface or surface having the reflection property in between the two.

Besides, it also allows architects and engineers to study the impact of integrating the LSC into building to its external environment. For example, the intensity of undesired glare caused by the LSC can be studied and its negative impact to the environment could be minimized at the planning stage. Unwanted glare in high intensity might occurs when sunlight is reflected by the tilted LSC installed on a large surface because the LSC bottom mirror reflects a large portion of sunlight unabsorbed by the dye, where its intensity is significantly higher than that caused by diffuse reflection from building walls or partial reflection from windows.

Simulation on the LSC appearance based on its installation location provides a tool to design aesthetically pleasing building with LSC integrated as part of it, making use of the luminescence from LSC and possibly a combination of LSCs in different colors. On the other hand, simulation on the solar cells daily yield with LSC allows one to determine which LSC plates should be attached with solar cells and the rest of inexpensive LSC plates which are not or seldom exposed to sunlight in the day could be merely decorations for the building. This can minimize the cost of electricity generation and thus maximize the return of investment.

REFERENCES

Barnham, K., Marques, J. L., Hassard, J. and O'Brien, P. (2000). Quantum-dot concentrator and thermodynamic model for the global redshift. *Appl. Phys. Lett.*, *76*(9), 1197-1199.

Bende, E. E., Slooff, L. H., Burgers, A. R., Van Sark, W. G. J. H. M. and Kennedy, M. (2008). *Cost & efficiency optimisation of the fluorescent solar concentrator.* In Proc. 23rd Eur. Photovolt. Solar Energy Conf., Valencia, Spain.

Blanco-Muriel, M., Alarcon-Padilla, D. C., Lopez-Moratalla, T. and Lara-Coira, M. (2001). Computing the solar vector. *Solar Energy*, *70*(5), 431-441.

Bomm, J., Büchtemann, A., Chatten, A. J., Bose, R., Farrell, D. J., Chan, N. L. A., Xiao, Y., Slooff, L. H., Meyer, T., Meyer, A., van Sark, W. G. J. H. M. and Koole, R. (2011). Fabrication and full characterization of state-of-the-art quantum dot luminescent solar concentrators. *Solar Energy Materials and Solar Cells*, *95*(8), 2087-2094.

Bose, R., Farrell, D. J., Pardo-Sanchez, C., Pravettoni, M., Mazzer, M., Chatten, A. J. and Barnham, K. W. J. (2009). *Luminescent solar concentrators: cylindrical design*. In Proc. 24th Eur. Photovolt. Solar Energy Conf., Hamburg, Germany.

Burgers, A. R., Slooff, L. H., Kinderman, R. and van Roosmalen, J. A. M. (2005). *Modelling of luminescent concentrators by ray-tracing*. Presented at the 20th European Photovoltaic Solar Energy Conference and Exhibition, Barcelona, Spain.

Cao, X. and James Lee, L. (2003). Control of volume shrinkage and residual styrene of unsaturated polyester resins cured at low temperatures. II. Effect of comonomer. *Polymer*, *44*(5), 1507-1516.

Castañer, L. and Silvestre, S. (2002). *Modelling Photovoltaic Systems using PSpice*. Chichester: Wiley.

Chandrasekhar, S. (1950). *Radiative Transfer.* New York: Dover Publications.

Chatten, A. J., Barnham, K. W. J., Buxton, B. F., Ekins-Daukes, N. J. and Malik, M. A. (2001). *Novel quantum dot concentrators*. In Proc. 17th European Photovoltaic Solar Energy Conference, Munich, Germany.

Chatten, A. J., Barnham, K. W. J., Buxton, B. F., Ekins-Daukes, N. J. and Malik, M. A. (2004). Quantum dot solar concentrators. *Semiconductors*, *38*(8), 909-917.

Chatten, A. J., Farrell, D. J., Buxton, B. F., Büchtemann, A. and Barnham, K. W. J. (2006). *Thermodynamic modelling of luminescent solar concentrators and modules*. In Proc. 21st Eur. Photovolt. Solar Energy Conf., Dresden, Germany.

Currie, M. J., Mapel, J. K., Heidel, T. D., Goffri, S. and Baldo, M. A. (2008). High-efficiency organic solar concentrators for photovoltaics. *Science*, *321*(5886), 226-228.

Debije, M. G., Broer, D. J. and Bastiaansen, C. W. M. (2007). *Effect of dye alignment on the output of a luminescent solar concentrator.* In Proc. 22nd Eur. Photovolt. Solar Energy Conf. Exhib., Milan, Italy.

Debije, M. G., Van, M. P., Verbunt, P. P. C., Broer, D. J. and Bastiaansen, C. W. M. (2009). *The effect of an organic selectively-reflecting mirror on the performance of a luminescent solar concentrator.* In Proc. 24th Eur. Photovolt. Solar Energy Conf., Hamburg, Germany.

Gallagher, S. J., Eames, P. C. and Norton, B. (2004). Quantum dot solar concentrator behaviour, predicted using a ray trace approach. *International Journal of Ambient Energy*, *25*(1), 47-56.

Goldschmidt, J. C., Peters, M., Dimroth, F., Bett, A. W., Steidl, L., Zentel, R., Hermle, M., Glunz, S. W. and Willeke, G. (2009). *Developing large and efficient fluorescent concentrator systems*. In Proc. 24th Eur. Photovolt. Solar Energy Conf., Hamburg, Germany.

Gueymard, C. A., Myers, D. and Emery, K. (2002). Proposed reference irradiance spectra for solar energy systems testing. *Solar Energy*, *73*(6), 443-467.

Haider, M., Hubert, P. and Lessard, L. (2007). Cure shrinkage characterization and modeling of a polyester resin containing low profile additives. *Composites Part A: Applied Science and Manufacturing*, *38*(3), 994 - 1009.

Hatch, J. E. (1984). *Aluminum: properties and physical metallurgy*. Metals Park, Ohio: American Society for Metals.

Jensen, H., Lalchand, G. and Mak, G. (2006). *Compared assessment of selected environmental indicators of photovoltaic electricity in selected OECD cities and Malaysia cities* . Retrieved from http://www.mbipv.net.my/content.asp?zoneid=9&categoryid=49

Kani, A. N. (2010). *Signals & Systems*. New Delhi: McGraw-Hill Education.

Kanschat, G., Meinköhn, E., Rannacher, R. and Wehrse, R. (2009). *Numerical Methods in Multidimensional Radiative Transfer.* Berlin: Springer-Verlag.

Kubin, R. F. and Fletcher, A. N. (1982). Fluorescence quantum yields of some rhodamine dyes. *J. Lumin.*, *27*(4), 455-462.

Larson, G. W. and Shakespeare, R. A. (1998). *Rendering with Radiance*. San Francisco, Calif: Morgan Kaufmann.

Lim, Y. S., Lalchand, G. and Gladys Mak, S. L. (2008). Economical, environmental and technical analysis of building integrated photovoltaic systems in Malaysia. *Energy Policy*, *36*(6), 2130-2142.

Meador, W. E. and Weaver, W. R. (1980). Two-stream approximations to radiative transfer in planetary atmospheres - A unified description of existing methods and a new improvement. *Journal of the Atmospheric Sciences*, *37*(3), 630-643.

Mishra, S. C., Roy, H. K. and Misra, N. (2006). Discrete ordinate method with a new and a simple quadrature scheme. *J. Quant. Spectrosc. Radiat. Transfer*, *101*(2), 249-262.

Phang, J. C. H., Chan, D. S. H. and Phillips, J. R. (1984). Accurate analytical method for the extraction of solar cell model parameters. *Electronics Letters*, *20*(10), 406-408.

Philipp, H. R. and Taft, E. A. (1960). Optical constants of Silicon in the region 1 to 10 eV. *Phys. Rev.*, *120*(1), 37–38.

Pravettoni, M., Farrell, D. J., Chatten, A. J., Bose, R., Kenny, R. P. and Barnham, K. W. J. (2009). *External quantum efficiency measurements of luminescent solar concentrators: a study of the impact of backside reflector size and shape*. In Proc. 24rd Eur. Photovolt. Solar Energy Conf., Hamburg, Germany.

Rau, U., Einsele, F. and Glaeser, G. C. (2005). Efficiency limits of photovoltaic fluorescent collectors. *Appl. Phys. Lett.*, *87*(17), 171101-171103.

Rowan, B. C., Wilson, L. R. and Richards, B. S. (2008). Advanced material concepts for luminescent solar concentrators. *IEEE Journal of Selected Topics in Quantum Electronics*, *14*(5), 1312-1322.

Shah, D. U. and Schubel, P. J. (2010). Evaluation of cure shrinkage measurement techniques for thermosetting resins. *Polymer Testing*, *29*(6), 629-639.

Sholin, V., Olson, J. D. and Carter, S. A. (2007). Semiconducting polymers and quantum dots in luminescent solar concentrators for solar energy harvesting. *J. Appl. Phys.*, *101*(12), 123114-123122.

Siegel, R. and Howell, J. R. (1972). *Thermal radiation heat transfer.* New York: McGraw-Hill.

Slooff, L. H., Bende, E. E., Burgers, A. R., Budel, T., Pravettoni, M., Kenny, R. P., Dunlop, E. D. and Büchtemann, A. (2008). A luminescent solar concentrator with 7.1% power conversion efficiency. *phys. stat. sol. (RRL)*, *2*(6), 257-259.

Sze, S. M. and Ng, K. K. (1981). *Physics of semiconductor devices*. New York: Wiley.

Tan, S. G., Lim, Y. S., Lo, C. K. and Ramesh, S. (2010). *Research and development of luminescent solar concentrators (LSC) in Malaysia*. In Proceeding of the 2010 International Conference on Green Energy Technology and Management, Chang-hua, Taiwan.

Thomas, G. E. and Stamnes, K. (1996). *Radiative transfer in the atmosphere and ocean*. Cambridge: Cambridge University Press.

Tiggelen, B. A. and Skipetrov, S. E. (2003). *Wave scattering in complex media: From theory to applications*. Dordrecht: Kluwer Academic Publishers.

Van Sark, W. G. J. H. M., Hellenbrand, G. F. M. G., Bende, E., Burgers, A. R. and Slooff, L. H. (2008a). *Annual energy yield of the fluorescent solar concentrator.* In Proc. 23rd Eur. Photovolt. Solar Energy Conf., Valencia, Spain.

Van Sark, W. G., Barnham, K. W. J., Slooff, L. H., Chatten, A. J., Büchtemann, A., Meyer, A., McCormack, S. J., Koole, R., Farrell, D. J. and Bose, R. (2008b). Luminescent solar concentrators – a review of recent results. *Opt. Express*, *16*(26), 21773-21792.

Ward, G. J. (1992). Measuring and modeling anisotropic reflection. *SIGGRAPH Comput. Graph.*, *26*(2), 265-272.

Werts, M. H. V., Hofstraat, J. W., Geurts, F. A. J. and Verhoeven, J. W. (1997). Fluorescein and Eosin as sensitizing chromophores in near-infrared luminescent Ytterbium(III), Neodymium(III) and Erbium(III) chelates. *Chemical Physics Letters*, *276*(3-4), 196-201.

Yablonovitch, E. (1980). Thermodynamics of the fluorescent planar concentrator. *J. Opt. Soc. Am.*, *70*(11), 1362-1363.

Yang, W. J., Ma, Z. Q., Tang, X., Feng, C. B., Zhao, W. G. and Shi, P. P. (2008). Internal quantum efficiency for solar cells. *Solar Energy*, *82*(2), 106-110.

PUBLICATION

The new hybrid simulation algorithm for LSC in Chapter 4 of this thesis was published in the journal "Energies", Volume 3, Issue 12, page 1831-1860, under the special issue "Advances in Solar Energy", with the title "A New Hybrid Algorithm Using Thermodynamic and Backward Ray-Tracing Approaches for Modeling Luminescent Solar Concentrators", on 26 November 2010. The journal manuscript was prepared and revised by Lo Chin Kim, Lim Yun Seng, Tan Seng Gee and Faidz Abd Rahman.

APPENDIX A

VECTOR ROTATION VIA AN AXIS

This appendix shows the detailed derivation of Eq. 4.47 for direction vectors rotation via a rotation axis.

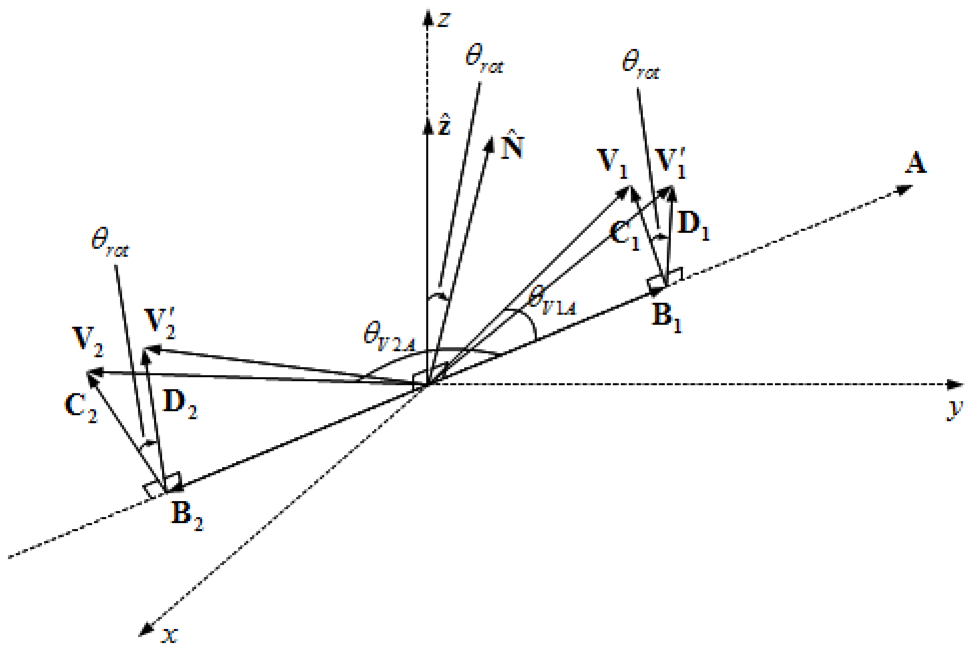

Figure A.1: Vector rotation via the rotation axis A.

In Figure A.1, vectors $\mathbf{V_n}$ are generated on a reference normal vector **z** but the actual surface normal is **N**, so every vector $\mathbf{V_n}$ is rotated by the same angle and via the same axis as **z** rotate into **N**. Therefore, the rotation axis and angle is defined as,

$$\mathbf{A} = \hat{\mathbf{z}} \times \hat{\mathbf{N}} \tag{A.1}$$

$$\theta_{rot} = \cos^{-1}\left(\hat{\mathbf{z}} \cdot \hat{\mathbf{N}}\right) \tag{A.2}$$

Where,

A = Rotation axis,

θ_{rot} = Rotation angle,

$\mathbf{V_n}$ = Original vector to be rotated,

$\mathbf{V'_n}$ = Rotated vector.

Normalize the rotation axis vector,

$$\hat{\mathbf{A}} = \frac{\mathbf{A}}{\|\mathbf{A}\|} \tag{A.3}$$

From Figure A.1, the magnitude of $\mathbf{C_n}$ must be equal to the magnitude of $\mathbf{D_n}$,

$$\|\mathbf{C_n}\| = \|\mathbf{D_n}\| \tag{A.4}$$

Since $\mathbf{B_n}$ has the same direction as **A** or opposite the direction of **A**, it can be written as,

$$\mathbf{B_n} = m\hat{\mathbf{A}} = \begin{bmatrix} m\hat{A}_x & m\hat{A}_y & m\hat{A}_z \end{bmatrix}^T \tag{A.5}$$

A is perpendicular to $\mathbf{V_n}$-$\mathbf{B_n}$, therefore,

$$\hat{\mathbf{A}} \cdot \left(\mathbf{V_n} - \mathbf{B_n}\right) = 0 \tag{A.6}$$

$$\hat{A}_x\left(V_{nx} - B_{nx}\right) + \hat{A}_y\left(V_{ny} - B_{ny}\right) + \hat{A}_z\left(V_{nz} - B_{nz}\right) = 0 \tag{A.7}$$

Substitute Eq. A.5 into Eq. A.7,

$$\hat{A}_x\left(V_{nx} - m\hat{A}_{nx}\right) + \hat{A}_y\left(V_{ny} - m\hat{A}_{ny}\right) + \hat{A}_z\left(V_{nz} - m\hat{A}_{nz}\right) = 0 \tag{A.8}$$

$$\hat{A}_x V_{nx} - m\hat{A}_{nx}^{\ 2} + \hat{A}_y V_{ny} - m\hat{A}_{ny}^{\ 2} + \hat{A}_z V_{nz} - m\hat{A}_{nz}^{\ 2} = 0 \tag{A.9}$$

$$m = \frac{\hat{A}_x V_{nx} + \hat{A}_y V_{ny} + \hat{A}_z V_{nz}}{\hat{A}_{nx}^{\ 2} + \hat{A}_{ny}^{\ 2} + \hat{A}_{nz}^{\ 2}} = \hat{\mathbf{A}} \cdot \mathbf{V_n} \tag{A.10}$$

Therefore,

$$\mathbf{B_n} = \left(\hat{\mathbf{A}} \cdot \mathbf{V_n}\right)\hat{\mathbf{A}} \tag{A.11}$$

When $0<\theta_{VnA}<\pi/2$, as represented by θ_{V1A} in Figure A.1, $\hat{\mathbf{A}} \cdot \mathbf{V_n}$ is positive and therefore **B** has the same direction as **A**. When $\pi/2<\theta_{VnA}<\pi$, as represented by θ_{V2A}, $\hat{\mathbf{A}} \cdot \mathbf{V_n}$ is negative so **B** has the opposite direction as **A**. Hence Eq. A.11 is true in both cases.

Vector $\mathbf{C_n}$ can be found by,

$$\mathbf{C_n} = \mathbf{V_n} - \mathbf{B_n} \tag{A.12}$$

The following 3 equations can be found from Figure A.1 to solve for $\mathbf{D_n}$,

$$\hat{\mathbf{A}} \cdot \mathbf{D_n} = 0 \tag{A.13}$$

$$\begin{aligned} \mathbf{C_n} \cdot \mathbf{D_n} &= \|\mathbf{C_n}\| \|\mathbf{D_n}\| \cos\theta_{rot} \\ &= \|\mathbf{C_n}\|^2 \cos\theta_{rot} \\ &= (\mathbf{C_n} \cdot \mathbf{C_n}) \cos\theta_{rot} \end{aligned} \tag{A.14}$$

$$\begin{aligned} \left(\hat{\mathbf{A}} \times \mathbf{C_n}\right) \cdot \mathbf{D_n} &= \left\|\hat{\mathbf{A}} \times \mathbf{C_n}\right\| \|\mathbf{D_n}\| \cos\left(\frac{\pi}{2} - \theta_{rot}\right) \\ &= \left(\left\|\hat{\mathbf{A}}\right\| \|\mathbf{C_n}\| \sin\frac{\pi}{2} \right) \left(\|\mathbf{D_n}\| \sin\theta_{rot} \right) \\ &= \|\mathbf{C_n}\|^2 \sin\theta_{rot} \\ &= (\mathbf{C_n} \cdot \mathbf{C_n}) \sin\theta_{rot} \end{aligned} \tag{A.15}$$

Rewrite Eq. A.13, Eq. A.14 and Eq. A.15 into matrix form,

$$\begin{bmatrix} D_{nx} \\ D_{ny} \\ D_{nz} \end{bmatrix} = \begin{bmatrix} M_{11} & M_{12} & M_{13} \\ M_{21} & M_{22} & M_{23} \\ M_{31} & M_{32} & M_{33} \end{bmatrix}^{-1} \begin{bmatrix} N_1 \\ N_2 \\ N_3 \end{bmatrix} \tag{A.16}$$

Where,

$$N_1 = 0 \tag{A.17}$$

$$N_2 = (\mathbf{C_n} \cdot \mathbf{C_n}) \cos(\theta_{rot}) \tag{A.18}$$

$$N_3 = (\mathbf{C_n} \cdot \mathbf{C_n}) \sin(\theta_{rot}) \tag{A.19}$$

$$[M_{11} \quad M_{12} \quad M_{13}] = \left(\hat{\mathbf{A}}\right)^T \tag{A.20}$$

$$[M_{21} \quad M_{22} \quad M_{23}] = (\mathbf{C_n})^T \tag{A.21}$$

$$[M_{31} \quad M_{32} \quad M_{33}] = \left(\hat{\mathbf{A}} \times \mathbf{C_n}\right)^T \tag{A.22}$$

Thus, rotated vector can be found by,

$$\mathbf{V_n'} = \mathbf{D_n} - \mathbf{B_n} \tag{A.23}$$

In matrix form,

$$\begin{bmatrix} V'_{nx} \\ V'_{ny} \\ V'_{nz} \end{bmatrix} = \begin{bmatrix} M_{11} & M_{12} & M_{13} \\ M_{21} & M_{22} & M_{23} \\ M_{31} & M_{32} & M_{33} \end{bmatrix}^{-1} \begin{bmatrix} N_1 \\ N_2 \\ N_3 \end{bmatrix} + \begin{bmatrix} B_{\mathrm{n1}} \\ B_{\mathrm{n2}} \\ B_{\mathrm{n3}} \end{bmatrix} \tag{A.24}$$

For the case in Chapter 4.2.2: Trapped Incident light from Ray-tracing Model, replace the subscript n by superscript m, vectors $\mathbf{V_n}$ by $\mathbf{\Theta^m}$ and rotated vectors $\mathbf{V'_n}$ by $\mathbf{\Theta^{m\prime}}$,

$$\begin{bmatrix} \Theta_x^{m\prime} \\ \Theta_y^{m\prime} \\ \Theta_z^{m\prime} \end{bmatrix} = \begin{bmatrix} M_{11} & M_{12} & M_{13} \\ M_{21} & M_{22} & M_{23} \\ M_{31} & M_{32} & M_{33} \end{bmatrix}^{-1} \begin{bmatrix} N_1 \\ N_2 \\ N_3 \end{bmatrix} + \begin{bmatrix} B_{\mathrm{x}} \\ B_{\mathrm{y}} \\ B_{\mathrm{z}} \end{bmatrix} \tag{A.25}$$

Where,

$$\mathbf{A} = [0 \quad -1 \quad 0]^T \tag{A.26}$$

$$\theta_{rot} = 94° \tag{A.27}$$

$$\hat{\mathbf{A}} = \frac{\mathbf{A}}{\|\mathbf{A}\|} \tag{A.28}$$

$$\mathbf{B^m} = \left(\hat{\mathbf{A}} \cdot \mathbf{\Theta}^m\right)\hat{\mathbf{A}} \tag{A.29}$$

$$\mathbf{C^m} = \mathbf{\Theta^m} - \mathbf{B^m} \tag{A.30}$$

$$N_1 = 0 \tag{A.31}$$

$$N_2 = \left(\mathbf{C^m} \cdot \mathbf{C^m}\right)\cos(\theta_{rot}) \tag{A.32}$$

$$N_3 = \left(\mathbf{C^m} \cdot \mathbf{C^m}\right)\sin(\theta_{rot}) \tag{A.33}$$

$$[M_{11} \quad M_{12} \quad M_{13}] = \left(\hat{\mathbf{A}}\right)^T \tag{A.34}$$

$$[M_{21} \quad M_{22} \quad M_{23}] = \left(\mathbf{C^m}\right)^T \tag{A.35}$$

$$[M_{31} \quad M_{32} \quad M_{33}] = \left(\hat{\mathbf{A}} \times \mathbf{C^m}\right)^T \tag{A.36}$$

APPENDIX B

ANALYSIS ON THE RAY DIRECTION VECTOR FOR SPECIAL CASE OF PLANAR LSC

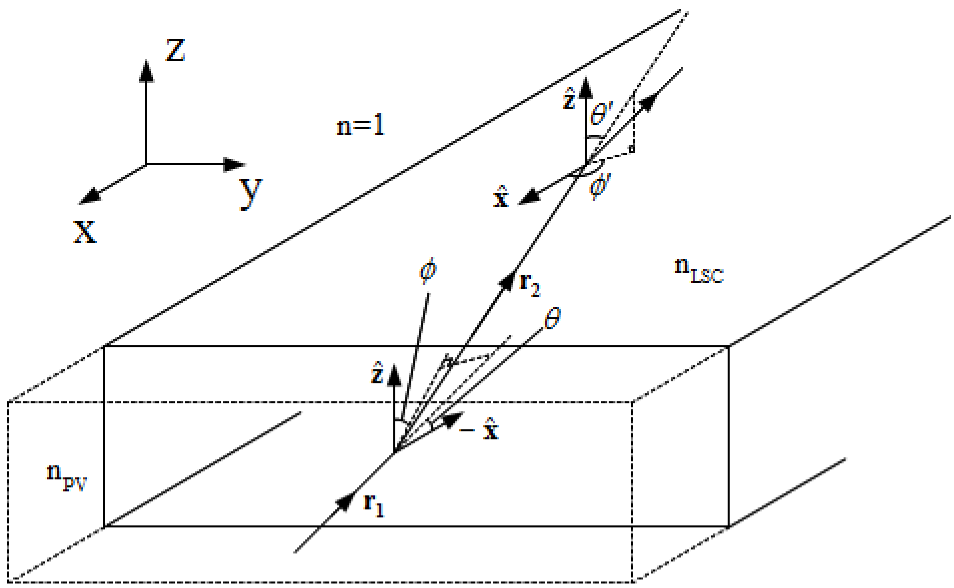

Figure B.1: A ray generated at solar cell surface at arbitrary direction for planar LSC.

Express $\mathbf{r}_1$ and $\mathbf{r}_2$ in Cartesian coordinate in term of θ and ϕ,

$$\mathbf{r}_1 = \begin{bmatrix} -\cos\theta_1 \\ \sin\theta_1 \sin\phi_1 \\ \sin\theta_1 \cos\phi_1 \end{bmatrix} \tag{B.1}$$

$$\mathbf{r}_2 = \begin{bmatrix} -\cos\theta_2 \\ \sin\theta_2 \sin\phi_2 \\ \sin\theta_2 \cos\phi_2 \end{bmatrix} \tag{B.2}$$

Where θ_2 and ϕ_2 can be related to θ_1 and ϕ_1 by Snell's Law,

$$\phi_2 = \phi_1 \tag{B.3}$$

$$\sin\theta_2 = \frac{n_{PV} \sin\theta_1}{n_{LSC}} \tag{B.4}$$

$$\cos\theta_2 = \frac{\sqrt{n_{LSC}^{\ 2} - n_{PV}^{\ 2} \sin^2\theta_1}}{n_{LSC}} \tag{B.5}$$

Substitute Eq. B.3, Eq. B.4 and Eq. B.5 into Eq. B.2,

$$\mathbf{r_2} = \begin{bmatrix} -\dfrac{\sqrt{n_{LSC}{}^2 - n_{PV}{}^2 \sin^2\theta_1}}{n_{LSC}} \\ \dfrac{n_{PV}\sin\theta_1 \sin\phi_1}{n_{LSC}} \\ \dfrac{n_{PV}\sin\theta_1 \cos\phi_1}{n_{LSC}} \end{bmatrix} \tag{B.6}$$

Express $\mathbf{r_2}$ in Cartesian coordinate in term of θ' and ϕ',

$$\mathbf{r_2} = \begin{bmatrix} \sin\theta_2' \cos\phi_2' \\ \sin\theta_2' \sin\phi_2' \\ \cos\theta_2' \end{bmatrix} \tag{B.7}$$

Relate the z component of the two different expressions of $\mathbf{r_2}$,

$$\cos\theta_2' = \frac{n_{PV}\sin\theta_1 \cos\phi_1}{n_{LSC}} \tag{B.8}$$

For a ray to trace backward to the outside of LSC top surface, θ'_2 must be less than the critical angle θ'_C at the top surface,

$$\theta_2' < \theta_C' \tag{B.9}$$

Where the sine and cosine of the critical angle are,

$$\sin\theta_C' = \frac{1}{n_{LSC}} \tag{B.10}$$

$$\cos\theta_C' = \frac{\sqrt{n_{LSC}{}^2 - 1}}{n_{LSC}} \tag{B.11}$$

Since cosine function is a monotonically decreasing function for the range of polar angle $0 \le \theta' \le \pi$, taking cosine of the angles at both sides of the inequality B.9 reverses the inequality sign.

$$\cos\theta_2' > \cos\theta_C' \tag{B.12}$$

$$\frac{n_{PV}\sin\theta_1 \cos\phi_1}{n_{LSC}} > \frac{\sqrt{n_{LSC}{}^2 - 1}}{n_{LSC}} \tag{B.13}$$

Simplify and rearrange,

$$\sin\theta_1 \cos\phi_1 > \frac{\sqrt{n_{LSC}{}^2 - 1}}{n_{PV}} \tag{B.14}$$

The polar angle for the sampling plane is restricted to $0<\theta\leq\pi/2$, in other words, $\sin\theta>0$.

Therefore,

$$\cos\phi_1 > \frac{\sqrt{n_{LSC}^{\;2}-1}}{n_{PV}\sin\theta_1} \tag{B.15}$$

The right hand side of the inequality B.15 is always positive, therefore only the case $\cos\phi_1>0$ is considered in that inequality.

Consider a ray passing through LSC top surface, reflected by the bottom mirror before reaching the solar cell surface. Let $\mathbf{r_3}$ be the reflected ray back-traced to the LSC top surface from the bottom mirror. It is related to $\mathbf{r_2}$ (ray back-traced from the solar cell surface to the bottom mirror) by,

$$\mathbf{r_2} = \begin{bmatrix} \sin(\pi-\theta_2')\cos\phi_2' \\ \sin(\pi-\theta_2')\sin\phi_2' \\ \cos(\pi-\theta_2') \end{bmatrix} \tag{B.16}$$

In this case,

$$\pi-\theta_2' < \theta_C' \tag{B.17}$$

$$\cos(\pi-\theta_2') > \cos\theta_C' \tag{B.18}$$

$$-\cos\theta_2' > \cos\theta_C' \tag{B.19}$$

Therefore,

$$-\frac{n_{PV}\sin\theta_1\cos\phi_1}{n_{LSC}} > \frac{\sqrt{n_{LSC}^{\;2}-1}}{n_{LSC}} \tag{B.20}$$

Similarly, since $\sin\theta>0$,

$$-\cos\phi_1 > \frac{\sqrt{n_{LSC}^{\;2}-1}}{n_{PV}\sin\theta_1} \tag{B.21}$$

Where only the case $\cos\phi_1<0$ is considered in inequality B.21.

Since the range of angle ϕ_1 considered in inequality B.15 and inequality B.21 are mutually exclusive, the two inequalities can be combined as,

$$|\cos\phi_1| > \frac{\sqrt{n_{LSC}^2 - 1}}{n_{PV}\sin\theta_1} \tag{B.22}$$

Eq. B.22 is used in Chapter 5.6.1: Simpler and Faster Calculation for Special Case of Planar LSC to test whether or not the ray can come out from the LSC top surface when traced backward.

Rearrange Eq. B.22,

$$\sin\theta_1 > \frac{1}{|\cos\phi_1|}\frac{\sqrt{n_{LSC}^2 - 1}}{n_{PV}} \tag{B.23}$$

When ϕ_1=0,

$$\theta_{\phi=0} > \sin^{-1}\left(\frac{\sqrt{n_{LSC}^2 - 1}}{n_{PV}}\right) \tag{B.24}$$

Which is consistent with the result of the 2D analysis in Chapter 5.2: Minimum and Maximum Polar Angles on the Sampling Surface.

At other value of ϕ,

$$\sin\theta_1 > \frac{1}{|\cos\phi_1|}\frac{\sqrt{n_{LSC}^2 - 1}}{n_{PV}} \tag{B.25}$$

Since $0 \le |\cos\phi_1| \le 1$, $\frac{1}{|\cos\phi_1|} > 1$,

$$\begin{gathered}\frac{1}{|\cos\phi_1|}\frac{\sqrt{n_{LSC}^2 - 1}}{n_{PV}} > \frac{\sqrt{n_{LSC}^2 - 1}}{n_{PV}} \\ \sin^{-1}\left(\frac{1}{|\cos\phi_1|}\frac{\sqrt{n_{LSC}^2 - 1}}{n_{PV}}\right) > \sin^{-1}\left(\frac{\sqrt{n_{LSC}^2 - 1}}{n_{PV}}\right) \\ \theta_{1(\min)} > \theta_{\phi=0(\min)}\end{gathered} \tag{B.26}$$

In other words, $\theta_{1(\min)}$ has the minimum value at ϕ_1=0.

APPENDIX C

CHANGE OF RAY DIRECTION AT THE SIDE MIRROR

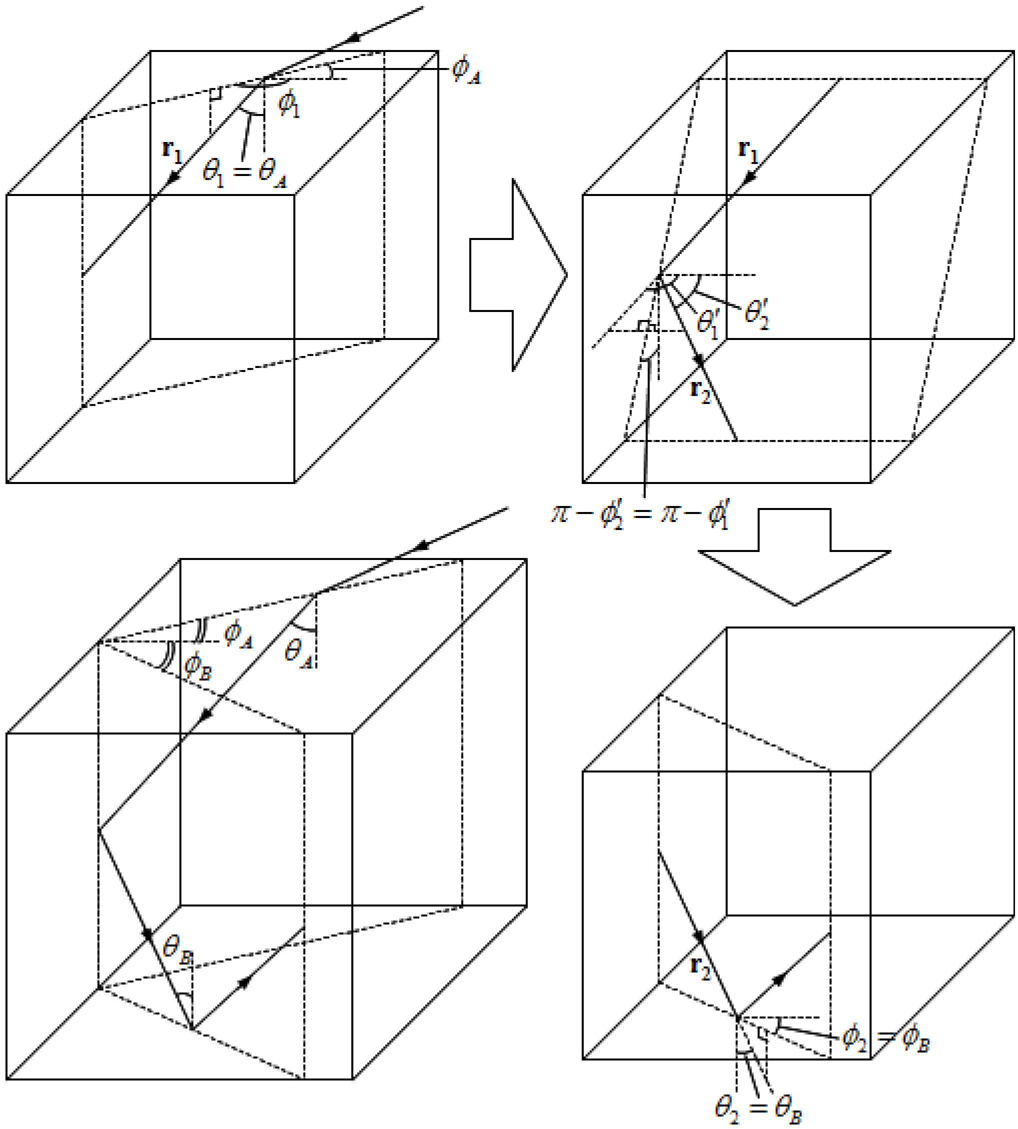

Figure C.1: Explanation of reflection from the side mirror.

Light ray refract or reflect on a plane perpendicular to the top surface or the bottom mirror. After the light ray hit a side mirror, the mirror does not change the polar angle at which the reflected light ray make with the surface normal of the top surface or bottom mirror, the polar angle after hitting the side mirror is the same as the polar angle before that. However, it changes the direction of the plane where refraction or reflection occurs as if the plane has been reflected from the side mirror. This appendix shows the detail analysis on the way light ray changes direction as described above.

In Figure C.1, the light ray is refracted at the top surface boundary, hit the side mirror, then reflected from it, finally hit the bottom mirror and being reflected from the bottom mirror. To simplify the analysis, only the ray just before it reach the side mirror, $\mathbf{r}_1$, and the ray immediate after it has been reflected from the side mirror, $\mathbf{r}_2$, are considered in the analysis. At the top left and bottom right of Figure C.1, $\mathbf{r}_1$ and $\mathbf{r}_2$ are represented by polar and azimuthal angles where the polar axis is the surface normal of the top surface and the azimuthal axis is the surface normal of the side mirror. At the top right of Figure C.1, the ray vectors are represented by another set of polar and azimuthal angles where the polar axis and azimuthal axis are switched. Before analyzing the ray vectors, the relationship of the angles before and after the switch of polar axis and azimuthal axis should be derived as below.

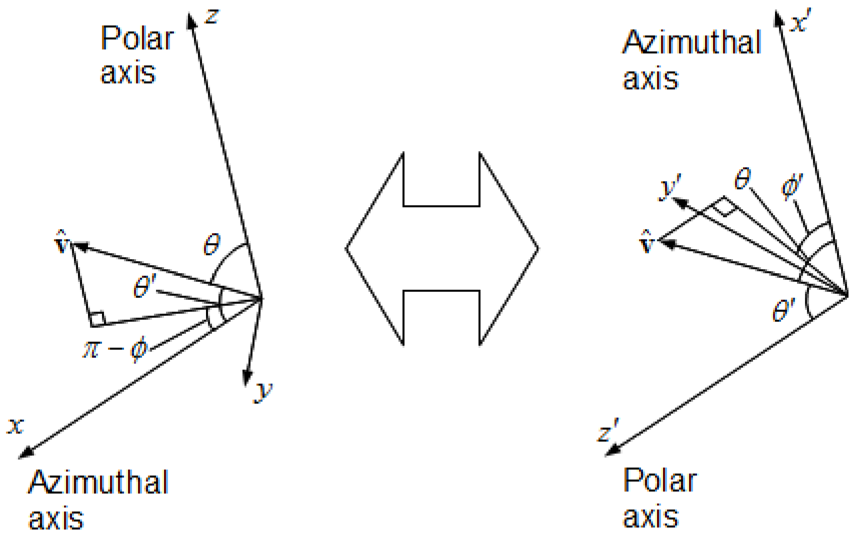

Figure C.2: New polar angle after the polar axis and azimuthal axis are switched.

Consider a normalized vector with arbitrary direction as shown in Figure C.2. The vector in the left hand side is represented in Cartesian coordinate $[x\ y\ z]^T$, where the same vector in the right hand side is represented in term of a new Cartesian coordinate $[x'\ y'\ z']^T$ with its axis rotated from the one in the left hand side in such a way that the polar axis and azimuthal axis are switched.

Represent the normalized vector in term of (θ,ϕ),

$$\hat{\mathbf{v}} = \begin{bmatrix} \sin\theta\cos\phi \\ \sin\theta\sin\phi \\ \cos\theta \end{bmatrix} \tag{C.1}$$

Represent the normalized vector in term of (θ',ϕ'),

$$\hat{\mathbf{v}}' = \begin{bmatrix} \sin\theta'\cos\phi' \\ \sin\theta'\sin\phi' \\ \cos\theta' \end{bmatrix} \tag{C.2}$$

From the left hand side of Figure C.2,

$$\begin{aligned} \cos\theta' &= \hat{\mathbf{v}}\cdot\hat{\mathbf{x}} \\ \cos\theta' &= \sin\theta\cos(\pi-\phi) \\ \cos\theta' &= -\sin\theta\cos\phi \end{aligned} \tag{C.3}$$

Similarly, from the right hand side of Figure C.2,

$$\begin{aligned} \cos\theta &= \hat{\mathbf{v}}'\cdot\hat{\mathbf{x}}' \\ \cos\theta &= \sin\theta'\cos\phi' \end{aligned} \tag{C.4}$$

Back to Figure C.1, represent the ray $\mathbf{r}_1$ in term of switched polar and azimuthal angles, it is related to the polar and azimuthal angles of reflected ray $\mathbf{r}_2$ by,

$$\theta_2' = \pi - \theta_1' \tag{C.5}$$

$$\phi_2' = \phi_1' \tag{C.6}$$

Using Eq. C.4, the polar angle θ_2 for $\mathbf{r_2}$ can be related to its rotated coordinate version of polar and azimuthal angles θ_2' and ϕ_2' by,

$$\cos\theta_2 = \sin\theta_2' \cos\phi_2' \tag{C.7}$$

Substitute Eq. C.5 and Eq. C.6 into Eq. C.7,

$$\cos\theta_2 = \sin(\pi - \theta_1')\cos\phi_1' = \sin\theta_1' \cos\phi_1' \tag{C.8}$$

Express the polar angle θ_1 of $\mathbf{r_1}$ in term of its rotated coordinate version of polar and azimuthal angles θ_1' and ϕ_1',

$$\cos\theta_1 = \sin\theta_1' \cos\phi_1' \tag{C.9}$$

Compare Eq. C.8 and Eq. C.9,

$$\cos\theta_2 = \cos\theta_1 \tag{C.10}$$

By definition, the range of the polar angle is limited to $0<\theta<\pi$. Therefore it can be concluded that,

$$\theta_2 = \theta_1 \tag{C.11}$$

Therefore,

$$\theta_B = \theta_A \tag{C.12}$$

Using Eq. C.3, the rotated coordinate version of polar angle θ_2' of $\mathbf{r_2}$ can be expressed as,

$$\begin{aligned} \cos\theta_2' &= -\sin\theta_2 \cos\phi_2 \\ \cos\phi_2 &= -\frac{\cos\theta_2'}{\sin\theta_2} \end{aligned} \tag{C.13}$$

Substitute Eq. C.5 and Eq. C.11 into Eq. C.13,

$$\begin{aligned} \cos\phi_2 &= -\frac{\cos(\pi - \theta_1')}{\sin\theta_1} \\ \cos\phi_2 &= \frac{\cos\theta_1'}{\sin\theta_1} \end{aligned} \tag{C.14}$$

Express the rotated coordinate version of polar angle θ_1' of $\mathbf{r_1}$ in term of its original polar and azimuthal angles θ_1 and ϕ_1,

$$\begin{aligned} \cos\theta_1' &= -\sin\theta_1 \cos\phi_1 \\ \cos\phi_1 &= -\frac{\cos\theta_1'}{\sin\theta_1} \end{aligned} \tag{C.15}$$

Compare Eq. C.14 and Eq. C.15,

$$\cos\phi_2 = -\cos\phi_1 \tag{C.16}$$

Only the surface facing the box in Figure C.1 is reflective, so the valid range of azimuthal angle ϕ_1 is $\pi/2<\phi_1<3\pi/2$. Therefore, for $\pi/2<\phi_1\leq\pi$,

$$\phi_2 = \pi - \phi_1 \tag{C.17}$$

From Figure C.1,

$$\phi_1 = \pi - \phi_A \tag{C.18}$$

Therefore,

$$\phi_B = \pi - (\pi - \phi_A) = \phi_A \tag{C.19}$$

This is true also for $\pi<\phi_1<3\pi/2$, which can be shown by simply reversing the ray direction in Figure C.1.

In conclusion, the side mirror at the LSC surface does not change the polar angle of the ray after a reflection on it, but the ray will follow a new plane of reflection/refraction where it seems to be reflected from the side mirror, as shown in the bottom left of Figure C.1.

APPENDIX D

CALCULATION OF SINGULARITY POINTS OF INTERNAL QUANTUM EFFICIENCY CONTRIBUTED BY THE SOLAR CELL BASE AND EMITTER REGION

This appendix shows the detailed derivation for Eq. 6.51 and Eq. 6.52 from Chapter 6.4.2.

The value of IQE_b at $\alpha=1/L_b$ can be found by taking the limit $\alpha\to 1/L_b$,

$$\begin{aligned}
\lim_{\alpha\to 1/L_b} IQE_b(\alpha) &= \lim_{\alpha\to 1/L_b}\left\{\begin{array}{l}\dfrac{\alpha L_b}{(\alpha L_b)^2-1}e^{-\alpha\cdot w} \\ \times\left[\alpha L_b-\dfrac{\zeta_b\cosh\frac{w_b}{L_b}+\sinh\frac{w_b}{L_b}+(\alpha L_b-\zeta_b)e^{-\alpha\cdot w_b}}{\zeta_b\sinh\frac{w_b}{L_b}+\cosh\frac{w_b}{L_b}}\right]\end{array}\right\} \\
&= \lim_{\alpha\to 1/L_b}\left[\begin{array}{l}\dfrac{\alpha L_b e^{-\alpha\cdot w}}{\alpha L_b-\frac{1}{\alpha L_b}} \\ -\dfrac{\left[\zeta_b\cosh\frac{w_b}{L_b}+\sinh\frac{w_b}{L_b}+(\alpha L_b-\zeta_b)e^{-\alpha\cdot w_b}\right]e^{-\alpha\cdot w}}{\left(\alpha L_b-\frac{1}{\alpha L_b}\right)\left(\zeta_b\sinh\frac{w_b}{L_b}+\cosh\frac{w_b}{L_b}\right)}\end{array}\right]
\end{aligned} \tag{D.1}$$

Eq. D.1 is in ∞-∞ indeterminate form.

$$\lim_{\alpha\to 1/L_b} IQE_b(\alpha) = \lim_{\alpha\to 1/L_b}\left[\frac{\begin{array}{l}\left(\alpha L_b e^{-\alpha\cdot w}\right)\left(\zeta_b\sinh\frac{w_b}{L_b}+\cosh\frac{w_b}{L_b}\right) \\ -\left[\zeta_b\cosh\frac{w_b}{L_b}+\sinh\frac{w_b}{L_b}+(\alpha L_b-\zeta_b)e^{-\alpha\cdot w_b}\right]e^{-\alpha\cdot w}\end{array}}{\left(\alpha L_b-\frac{1}{\alpha L_b}\right)\left(\zeta_b\sinh\frac{w_b}{L_b}+\cosh\frac{w_b}{L_b}\right)}\right] \tag{D.2}$$

Apply L'Hospital's rule by differentiating both numerator and denominator with respect to α,

$$\lim_{\alpha\to 1/L_b} IQE_b(\alpha) = \lim_{\alpha\to 1/L_b}\left[\frac{\begin{array}{l}\left(-\alpha L_b w e^{-\alpha\cdot w}+L_b e^{-\alpha\cdot w}\right)\left(\zeta_b\sinh\frac{w_b}{L_b}+\cosh\frac{w_b}{L_b}\right) \\ +\left[\zeta_b\cosh\frac{w_b}{L_b}+\sinh\frac{w_b}{L_b}+(\alpha L_b-\zeta_b)e^{-\alpha\cdot w_b}\right]we^{-\alpha\cdot w} \\ -\left[-(\alpha L_b-\zeta_b)w_b e^{-\alpha\cdot w_b}+L_b e^{-\alpha\cdot w_b}\right]e^{-\alpha\cdot w}\end{array}}{\left(L_b+\frac{1}{\alpha^2 L_b}\right)\left(\zeta_b\sinh\frac{w_b}{L_b}+\cosh\frac{w_b}{L_b}\right)}\right] \tag{D.3}$$

Substitute α by $1/L_b$,

$$\lim_{\alpha\to 1/L_b} IQE_b(\alpha)=\left\{\frac{\begin{array}{l}\left(-we^{-w/L_b}+L_b e^{-w/L_b}\right)\left(\zeta_b\sinh\frac{w_b}{L_b}+\cosh\frac{w_b}{L_b}\right)\\ +\left[\zeta_b\cosh\frac{w_b}{L_b}+\sinh\frac{w_b}{L_b}+(1-\zeta_b)e^{-w_b/L_b}\right]we^{-w/L_b}\\ -\left[-(1-\zeta_b)w_b e^{-w_b/L_b}+L_b e^{-w_b/L_b}\right]e^{-w/L_b}\end{array}}{(L_b+L_b)\left(\zeta_b\sinh\frac{w_b}{L_b}+\cosh\frac{w_b}{L_b}\right)}\right\}$$

$$=\left\{\frac{\begin{array}{l}\left(-we^{-w/L_b}+L_b e^{-w/L_b}\right)\left(\zeta_b\sinh\frac{w_b}{L_b}+\cosh\frac{w_b}{L_b}\right)\\ +\left[\begin{array}{l}\zeta_b\left(e^{w_b/L_b}+e^{-w_b/L_b}-2e^{-w_b/L_b}\right)/2\\ +\left(e^{w_b/L_b}-e^{-w_b/L_b}+2e^{-w_b/L_b}\right)/2\end{array}\right]we^{-w/L_b}\\ -\left[-(1-\zeta_b)w_b+L_b\right]e^{-w/L_b}\cdot e^{-w_b/L_b}\end{array}}{(2L_b)\left(\zeta_b\sinh\frac{w_b}{L_b}+\cosh\frac{w_b}{L_b}\right)}\right\}$$

$$=\left\{\frac{\begin{array}{l}\left(-we^{-w/L_b}+L_b e^{-w/L_b}\right)\left(\zeta_b\sinh\frac{w_b}{L_b}+\cosh\frac{w_b}{L_b}\right)\\ +\left[\zeta_b\sinh\frac{w_b}{L_b}+\cosh\frac{w_b}{L_b}\right]we^{-w/L_b}\\ -\left[\zeta_b w_b-w_b+L_b\right]e^{-w/L_b}\cdot e^{-w_b/L_b}\end{array}}{(2L_b)\left(\zeta_b\sinh\frac{w_b}{L_b}+\cosh\frac{w_b}{L_b}\right)}\right\} \qquad \text{(D.4)}$$

$$=\left\{\frac{\begin{array}{l}\left(L_b e^{-w/L_b}\right)\left(\zeta_b\sinh\frac{w_b}{L_b}+\cosh\frac{w_b}{L_b}\right)\\ -\left[\zeta_b w_b-w_b+L_b\right]e^{-w/L_b}\cdot e^{-w_b/L_b}\end{array}}{(2L_b)\left(\zeta_b\sinh\frac{w_b}{L_b}+\cosh\frac{w_b}{L_b}\right)}\right\}$$

$$=\frac{1}{2}e^{-w/L_b}\left\{\frac{\begin{array}{l}(L_b)\left(\zeta_b\sinh\frac{w_b}{L_b}+\cosh\frac{w_b}{L_b}\right)\\ -L_b\left[\frac{\zeta_b w_b-w_b}{L_b}+1\right]\cdot e^{-w_b/L_b}\end{array}}{(L_b)\left(\zeta_b\sinh\frac{w_b}{L_b}+\cosh\frac{w_b}{L_b}\right)}\right\}$$

$$=\frac{1}{2}e^{-w/L_b}\left[1-\frac{\frac{w_b}{L_b}(\zeta_b-1)+1}{\zeta_b\sinh\frac{w_b}{L_b}+\cosh\frac{w_b}{L_b}}e^{-w_b/L_b}\right]$$

Therefore,

$$\lim_{\alpha\to 1/L_b} IQE_b(\alpha)=\frac{1}{2}e^{-w/L_b}\left[1-\frac{1-\frac{w_b}{L_b}\left(1-\zeta_b\right)}{\zeta_b\sinh\frac{w_b}{L_b}+\cosh\frac{w_b}{L_b}}e^{-w_b/L_b}\right] \tag{D.5}$$

Similarly, the value of IQE_e at $\alpha=1/L_e$ can be found by taking the limit $\alpha\to 1/L_e$,

$$\begin{aligned}\lim_{\alpha\to 1/L_e} IQE_e(\alpha)&=\lim_{\alpha\to 1/L_e}\left\{\begin{array}{l}\dfrac{\alpha L_e}{(\alpha L_e)^2-1}\\ \times\left[\begin{array}{l}\dfrac{\zeta_e+\alpha L_e-\left(\zeta_e\cosh\frac{w_e}{L_e}+\sinh\frac{w_e}{L_e}\right)e^{-\alpha\cdot w_e}}{\zeta_e\sinh\frac{w_e}{L_e}+\cosh\frac{w_e}{L_e}}\\ -\alpha L_e e^{-\alpha\cdot w_e}\end{array}\right]\end{array}\right\}\\ &=\lim_{\alpha\to 1/L_e}\left\{\begin{array}{l}\dfrac{\zeta_e+\alpha L_e-\left(\zeta_e\cosh\frac{w_e}{L_e}+\sinh\frac{w_e}{L_e}\right)e^{-\alpha\cdot w_e}}{\left(\alpha L_e-\frac{1}{\alpha L_e}\right)\left(\zeta_e\sinh\frac{w_e}{L_e}+\cosh\frac{w_e}{L_e}\right)}\\ -\dfrac{(\alpha L_e)\left(e^{-\alpha\cdot w_e}\right)}{\alpha L_e-\frac{1}{\alpha L_e}}\end{array}\right\}\end{aligned} \tag{D.6}$$

Eq. D.6 is in ∞-∞ indeterminate form.

$$\lim_{\alpha\to 1/L_e} IQE_e(\alpha)=\lim_{\alpha\to 1/L_e}\left\{\frac{\begin{array}{l}\zeta_e+\alpha L_e-\left(\zeta_e\cosh\frac{w_e}{L_e}+\sinh\frac{w_e}{L_e}\right)e^{-\alpha\cdot w_e}\\ -(\alpha L_e)\left(e^{-\alpha\cdot w_e}\right)\left(\zeta_e\sinh\frac{w_e}{L_e}+\cosh\frac{w_e}{L_e}\right)\end{array}}{\left(\alpha L_e-\frac{1}{\alpha L_e}\right)\left(\zeta_e\sinh\frac{w_e}{L_e}+\cosh\frac{w_e}{L_e}\right)}\right\} \tag{D.7}$$

Apply L'Hospital's rule by differentiating both numerator and denominator with respect to α,

$$\lim_{\alpha\to 1/L_e} IQE_e(\alpha)=\lim_{\alpha\to 1/L_e}\left\{\frac{\begin{array}{l}L_e+\left(\zeta_e\cosh\frac{w_e}{L_e}+\sinh\frac{w_e}{L_e}\right)w_e e^{-\alpha\cdot w_e}\\ -\left(-\alpha L_e w_e e^{-\alpha\cdot w_e}+L_e e^{-\alpha\cdot w_e}\right)\left(\zeta_e\sinh\frac{w_e}{L_e}+\cosh\frac{w_e}{L_e}\right)\end{array}}{\left(L_e+\frac{1}{\alpha^2 L_e}\right)\left(\zeta_e\sinh\frac{w_e}{L_e}+\cosh\frac{w_e}{L_e}\right)}\right\} \tag{D.8}$$

Substitute α by $1/L_e$,

$$\lim_{\alpha\to 1/L_e} IQE_e(\alpha) = \left\{ \frac{\begin{array}{l} L_e + \left(\zeta_e \cosh\frac{w_e}{L_e} + \sinh\frac{w_e}{L_e}\right) w_e e^{-w_e/L_e} \\ + \left(w_e e^{-w_e/L_e} - L_e e^{-w_e/L_e}\right)\left(\zeta_e \sinh\frac{w_e}{L_e} + \cosh\frac{w_e}{L_e}\right) \end{array}}{\left(L_e + L_e\right)\left(\zeta_e \sinh\frac{w_e}{L_e} + \cosh\frac{w_e}{L_e}\right)} \right\}$$

$$= \left\{ \frac{\begin{array}{l} L_e + \\ \left[\zeta_e\left(\cosh\frac{w_e}{L_e} + \sinh\frac{w_e}{L_e}\right) + \left(\sinh\frac{w_e}{L_e} + \cosh\frac{w_e}{L_e}\right)\right] w_e e^{-w_e/L_e} \\ - \left(L_e e^{-w_e/L_e}\right)\left(\zeta_e \sinh\frac{w_e}{L_e} + \cosh\frac{w_e}{L_e}\right) \end{array}}{\left(2L_e\right)\left(\zeta_e \sinh\frac{w_e}{L_e} + \cosh\frac{w_e}{L_e}\right)} \right\} \tag{D.9}$$

$$= \frac{1}{2}\left[\frac{\begin{array}{l} 1 + \left(\zeta_e e^{w_e/L_e} + e^{w_e/L_e}\right)\frac{w_e}{L_e} e^{-w_e/L_e} \\ - \left(e^{-w_e/L_e}\right)\left(\zeta_e \sinh\frac{w_e}{L_e} + \cosh\frac{w_e}{L_e}\right) \end{array}}{\zeta_e \sinh\frac{w_e}{L_e} + \cosh\frac{w_e}{L_e}} \right]$$

Therefore,

$$\lim_{\alpha\to 1/L_e} IQE_e(\alpha) = \frac{1}{2}\left[\frac{1 + \frac{w_e}{L_e}\left(\zeta_e + 1\right)}{\zeta_e \sinh\frac{w_e}{L_e} + \cosh\frac{w_e}{L_e}} - e^{-w_e/L_e} \right] \tag{D.10}$$

To verify the equations for the singularity points, the values of IQE_b and IQE_e at their respective singularity points were evaluated using the parameter values from Chapter 6.4.1, together with several values of IQE_b and IQE_e very near to the singularity points, as shown in Table D.1.

Table D.1. Solar azimuth and zenith distance of the sun at different time.

α	9.9970e3	9.9980e3	9.9990e3	$1/L_b$= 1.0000e4	1.0001e4	1.0002e4	1.0003e4
IQE_b	4.8489e-1	4.8492e-1	4.8494e-1	4.8497e-1	4.8499e-1	4.8502e-1	4.8504e-1
α	6.6647e4	6.6653e4	6.6660e4	$1/L_e$= 6.6667e4	6.6673e4	6.6680e4	6.6687e4
IQE_e	3.1266e-2	3.1269e-2	3.1272e-2	3.1275e-2	3.1278e-2	3.1281e-2	3.1284e-2

Continuously increasing values were observed from the Table D.1 for both cases, therefore confirms that the two equations are correct.